

Journal of
Mechanics of
Materials and Structures

Volume 3, N° 10

December 2008

 mathematical sciences publishers

JOURNAL OF MECHANICS OF MATERIALS AND STRUCTURES

<http://www.jomms.org>

EDITOR-IN-CHIEF Charles R. Steele
ASSOCIATE EDITOR Marie-Louise Steele
Division of Mechanics and Computation
Stanford University
Stanford, CA 94305
USA

BOARD OF EDITORS

D. BIGONI University of Trento, Italy
H. D. BUI École Polytechnique, France
J. P. CARTER University of Sydney, Australia
R. M. CHRISTENSEN Stanford University, U.S.A.
G. M. L. GLADWELL University of Waterloo, Canada
D. H. HODGES Georgia Institute of Technology, U.S.A.
J. HUTCHINSON Harvard University, U.S.A.
C. HWU National Cheng Kung University, R.O. China
IWONA JASIUK University of Illinois at Urbana-Champaign
B. L. KARIHALOO University of Wales, U.K.
Y. Y. KIM Seoul National University, Republic of Korea
Z. MROZ Academy of Science, Poland
D. PAMPLONA Universidade Católica do Rio de Janeiro, Brazil
M. B. RUBIN Technion, Haifa, Israel
Y. SHINDO Tohoku University, Japan
A. N. SHUPIKOV Ukrainian Academy of Sciences, Ukraine
T. TARNAI University Budapest, Hungary
F. Y. M. WAN University of California, Irvine, U.S.A.
P. WRIGGERS Universität Hannover, Germany
W. YANG Tsinghua University, P.R. China
F. ZIEGLER Technische Universität Wien, Austria

PRODUCTION


PAULO NEY DE SOUZA Production Manager
SHEILA NEWBERY Senior Production Editor
SILVIO LEVY Scientific Editor

See inside back cover or <http://www.jomms.org> for submission guidelines.

Regular subscription rate: \$500 a year.

Subscriptions, requests for back issues, and changes of address should be sent to Mathematical Sciences Publishers, 798 Evans Hall, Department of Mathematics, University of California, Berkeley, CA 94720-3840.

©Copyright 2009. Journal of Mechanics of Materials and Structures. All rights reserved.

 mathematical sciences publishers

PREFACE

This issue of the *Journal of Mechanics of Materials and Structures* is dedicated to Pisidhi Karasudhi, Professor Emeritus at the Asian Institute of Technology, Thailand (see next page). It contains invited papers, mainly from authors who spoke at the Tenth East Asia-Pacific Conference on Structural Engineering and Construction, in a symposium entitled Recent Advances in Structural Engineering, Mechanics and Materials (August 4 and 5, 2006). The symposium consisted of six technical sessions and a special session on Modern Engineering Education Strategies and Practices. Thirty-two invited papers were included in the technical program. The authors came from Australia, Canada, Hong Kong, Japan, Singapore, Thailand and the United States of America.

The papers are ordered alphabetically according to first author. The first paper by Borujeni, Maijer and Rajapakse is a numerical investigation of the effects of strain rate and boundary conditions on the overall mechanical response and nucleation/evolution of transformation bands in shape memory alloys. In the next paper, elastodynamic reciprocity relations are developed by Karunasena for wave scattering by flaws, when guided waves are allowed to propagate in fiber-reinforced composite plates. The next two papers are in the area of numerical simulations. Liu, Swaddiwudhipong and Pei discuss numerical simulations of micro and nano indentation tests, while Madurapperuma and Puswewala report on their work on finite element modeling of soil creep. In the next paper Selvadurai, Scarpas and Kringos examine the problem of contact between an isotropic elastic halfspace and a rigid circular indenter, where contact is achieved through a set of Winkler ligaments. The next two papers are in the area of dynamics. The dynamic response of multiple flexible strip foundations resting on a multilayered poroelastic half-plane is considered by Senjuntichai and Kaewjuea while Takemiya uses the thin-layer method to determine the transient ground response due to impulse and moving loads. In the next paper Valliappan and Chee combine degradation evaluation methods, damage mechanics, and the finite element method to examine the safety of mechanical structures with age-related degradation. A study of tsunami propagation using the characteristic-based split method is reported by Wijaya, Bui and Kanok-Nukulchai. The dispersive behavior of waves propagating in a prestressed compressible elastic layer with constrained boundaries is studied by Wijeyewickrema, Ushida and Kayestha. In the last paper of the volume, Yang, Kitipornchai and Liew examine the nonlinear local bending of FGM sandwich plates.

We wish to thank all contributors to this issue and the symposium and the reviewers for their valuable comments. We especially thank Professor Charles R. Steele, the Chief Editor of the *Journal of Mechanics of Materials and Structures*, for agreeing to publish this volume as a special issue and Dr. Silvio Levy, Scientific Editor, for his assistance.

Nimal Rajapakse
The University of British Columbia, Canada
Worsak Kanok-Nukulchai
Asian Institute of Technology, Thailand

Anil C. Wijeyewickrema
Tokyo Institute of Technology, Japan
Teerapong Senjuntichai
Chulalongkorn University, Thailand

BIOGRAPHICAL NOTE

Pisidhi Karasudhi was born on February 2, 1939 in Bangkok, Thailand. He received a Bachelor's Degree in Civil Engineering in 1961 from Chulalongkorn University in Bangkok, and was among the select few admitted that year to the Master's program in Structural Engineering offered by the SEATO (Southeast Asia Treaty Organization) Graduate School of Engineering in Bangkok. He graduated from there in 1963. He did his postgraduate studies at Northwestern University in Evanston, Illinois (USA), under the supervision of the world-renowned academics Seng-Lip Lee and Leon M. Keer. His Ph.D. dissertation in Theoretical and Applied Mechanics, completed in 1968, was one of the first rigorous treatments of a vibrating rigid structure on an elastic half-space.

Dr. Karasudhi joined the Division of Structural Engineering at the Asian Institute of Technology in 1969, and reached the rank of full professor in 1978. A skilled administrator, he also served as Chairman of the Division from 1975 to 1983. He held visiting professorships at the University of Tokyo in 1979 and the National University of Singapore in 1985. In 1993 became the Founding Dean of the School of Civil Engineering at AIT. As the Institute's Vice-President of Development from 1994 till his retirement from AIT to 1999; in that position he was entrusted with raising funds and developing strong relationships with a large group of donors. He was promoted to the rank of Chair Professor, the highest academic rank at AIT, in 1995. He served as Acting President of AIT on multiple occasions and was a member of the Board of Trustees.

Professor Karasudhi was known for very high academic standards and excellent research. He taught a wide range of graduate courses at AIT including courses in elasticity, nonlinear solid mechanics, viscoelasticity, plates, shells and elastic wave propagation. He supervised eleven doctoral students and over a hundred master's students from all over Asia. He has been a continuous source of inspiration to his students and junior colleagues and mentored them with great dedication. Many of his former students now serve in senior positions in academia, government and industry in Asia, Australia and North America.

His early research was in elastostatic and elastodynamic problems of semi-infinite media and the structural dynamics of tall buildings. Later he supervised doctoral and master's theses dealing with load transfer problems, made seminal contributions to the topic, and applied his solutions to practical problems such as negative skin friction analysis of piles and consolidation settlement of piles. In computational mechanics, he made significant contributions to the finite element analysis of plates and shells. He did pioneering research on low-cost construction materials such as ferrocement and rice-husk-ash cement and concrete. In the 1980s and 1990s, he contributed greatly to the development of infinite elements for poroelastic and layered elastic media: his rigorous examination of elastic wave fields in a bimaterial system led to the creation of the first elastodynamic infinite element for layered media.

Over a hundred research papers and monographs bear Karasudhi's name; his graduate textbook *Foundations of Solid Mechanics* (Kluwer, 1991) quickly became a classic. A member of several learned societies, he was honored with the title of Fellow of the Engineering Institute of Thailand, and chaired its civil engineering chapter from 1986 to 1988. He was a sought-after reviewer for specialized journals and an editorial board member of the *International Journal for Computational Mechanics*, the *International Journal of Structures* and the *Journal of Ferrocement*. He was also active as a consultant to industry.



FINITE ELEMENT SIMULATION OF STRAIN RATE EFFECTS ON LOCALIZED UNSTABLE PSEUDOELASTIC RESPONSE OF SHAPE MEMORY ALLOYS

B. AZADI BORUJENI, DAAN M. MAIJER AND R. K. NIMAL D. RAJAPAKSE

A macromechanical total-deformation constitutive model of pseudoelasticity previously developed by the authors is employed within a two-dimensional finite element framework to numerically investigate the effect of strain rate and boundary conditions on the overall mechanical response and nucleation/evolution of transformation bands in NiTi strips during both forward and reverse transformations. The simulation results are compared with the experimental observations previously reported by other researchers, and it is shown that the present method successfully captures the nucleation and propagation of localized deformation bands during both loading and unloading. It is confirmed that the number of propagating fronts plays a key role in the pseudoelastic response of material in nonisothermal conditions. Special attention is paid to the morphology of the transformation fronts and its evolution. The numerical analysis indicates that the predicted morphology of the fronts is highly sensitive to imperfections and misalignments in the boundary conditions, especially during the reverse transformation.

1. Introduction

Owing to their unique mechanical properties, shape memory alloys (SMA) are increasingly being used in many engineering applications such as medical devices, orthodontic wires, microactuators, and vibration control [Otsuka and Wayman 1998; Saadat et al. 2002; Kohl 2004]. The two important characteristics of SMAs are known as *pseudoelasticity* (or *superelasticity*) and *shape memory effect*, which take place over different temperature ranges.

Despite extensive experimental and theoretical research in the past two decades, some aspects of SMA behavior are still subject to intense research. Among these are the instability of the mechanical behavior in some SMAs which leads to macroscale deformation localization (Lüders-like deformation) and sensitivity of their response to loading rate. It has been observed that at low strain rates, the uniaxial pseudoelastic response of NiTi is characterized by a distinct stress plateau and propagation of only one or two transformation fronts. At high strain rates, on the other hand, the stress-strain response maintains a positive slope, and multiple propagating fronts may coexist. Lüders-like deformation in NiTi was first observed by Miyazaki et al. [1981] in wire samples. The subject has been systematically studied through in-situ monitoring of the local variations of temperature and strain by Leo et al. [1993] and Shaw and Kyriakides [1995] in NiTi wires, by Shaw and Kyriakides [1997a] and Pieczyska et al. [2006a] in NiTi strips, and also recently by Feng and Sun [2006] in NiTi microtubes.

Keywords: shape memory alloys, strain rate, localization, phase transformation, pseudoelasticity, martensite reorientation, finite element method.

Various hypotheses have been proposed for the origin of deformation localization in NiTi. Some believe that the severe geometric distortion due to large transformation strain is the only cause for localization. In their view, the stress-strain curve maintains a positive (but small) slope during the transformation [Favier et al. 2002; Sittner et al. 2005]. Other researchers have attributed the deformation localization in NiTi to the intrinsic instability of the material behavior (strain softening) during the phase transformation [Shaw and Kyriakides 1997b; Idesman et al. 2005; Feng and Sun 2006]. This argument is supported by the fact that the large stress drop at the onset of the stress-plateau can not be modeled by geometric instability alone [Shaw and Kyriakides 1997b]. As shown by Iadicola and Shaw [2002], the “real” load drop can be as high as 17% if the stress concentrations at the gripped ends are eliminated.

Regardless of its origin, the localization of deformation in SMAs and its strong rate-dependency can place serious limitations on engineers who wish to design parts made of SMAs and exploit pseudoelastic properties. Therefore, a reliable and easy-to-use thermomechanical constitutive model is desired to enable engineers to predict the local and bulk material response.

Most of the constitutive models developed in the past have focused on the overall response of SMAs which exhibit stable mechanical behavior. Some examples of these models can be found in [Tanaka et al. 1986; Brinson 1993; Boyd and Lagoudas 1994; Lagoudas et al. 1996; Auricchio et al. 1997; Raniecki and Lexcelent 1998; Brocca et al. 2002]. Although these models are often based on detailed thermodynamic considerations, their ability to model the unstable mechanical behavior is not guaranteed. It has been shown through numerical simulations that the ability of a constitutive model to successfully capture the stable pseudoelastic behavior does not automatically ensure the full recovery of inelastic deformation throughout the entire domain during the unstable localized reverse transformation [Azadi et al. 2007; Azadi 2008].

Abeyaratne and Knowles [1993] developed a one-dimensional thermodynamic framework based on the Helmholtz free energy to simulate the isothermal transformation in an SMA bar. The propagating phase boundaries were treated as traveling field discontinuities. Shaw and Kyriakides [1997b] proposed a model based on incremental plasticity to capture the material instability observed in NiTi strips. The material was assumed to behave as an isothermal, rate-independent J_2 -type elasto-plastic solid with isotropic softening. A similar approach has also been recently used by Hu et al. [2007] to simulate the nucleation and propagation of localized helical bands in NiTi tubes. This analysis was extended in [Shaw 2000; Iadicola and Shaw 2004] by considering the thermomechanical coupling of the material with its environment, and investigated the effect of loading rate on the evolution of instabilities. Due to the irreversibility of plastic deformation, the use of incremental plasticity in these models is limited to the forward transformation case, and the reverse transformation upon unloading has been ignored.

Recently, Azadi et al. [2006] developed a one-dimensional phenomenological model to simulate the phase transformation and transformation front propagation in SMA wires. They assumed that the untransformed particles located close to the transformed regions are less stable than those away from the transformed regions. Azadi et al. [2007] extended the one-dimensional model to a multidimensional macromechanical model of localized unstable pseudoelasticity based on the deformation theory of plasticity. In this model, the finite form of transformation strain is expressed in terms of the gradient of a potential function, which allows for the reorientation of the transformation strain tensor with variation of the stress tensor, regardless of the occurrence of a phase transformation. The model is in fact similar to that proposed by Auricchio and Stefanelli [2004], although they did not consider the localization

phenomena and instability of mechanical behavior. Moreover, in the model of [Azadi et al. \[2007\]](#) the effect of temperature and variation of elastic properties upon phase transformation have also been considered. The constitutive model was successfully implemented within a finite element (FE) framework to simulate the isothermal nucleation and propagation of a single transformation front during the reverse transformations, as well as the forward transformation in a short NiTi strip. However, the simulation results were compared with the experimental data only for the forward transformation case. In the present work, the multidimensional analysis of [Azadi et al. \[2007\]](#) is extended to simulate the nucleation and propagation of multiple transformation fronts in longer strips of NiTi by considering the effect of heat generation/consumption occurring during the transformation, and thus the strain rate effects. Moreover, the simulation results are compared with experimental observations for both the forward and reverse transformations, which allows for a better assessment of the performance of the constitutive model. The effect of boundary conditions on the evolution of transformation bands morphology in NiTi strips is also investigated.

2. Constitutive model

A simple macromechanical constitutive model previously developed by [Azadi et al. \[2007\]](#) is used to model the pseudoelastic behavior of polycrystalline NiTi. The constitutive model is inspired by the deformation theory of plasticity, with two sets of yielding criteria for forward and reverse transformations. The model is intended to describe conditions at a local material point subjected to general thermomechanical loading. The equations governing the stress-strain relations and kinetics of transformations from [Azadi et al. \[2007\]](#) are summarized in [Table 1](#). In these equations, ε_{ij} is the total strain tensor, σ_{ij} is the stress tensor, S_{ij} is the deviatoric stress tensor, $\bar{\sigma}$ is the von Mises effective stress, and γ is the volume fraction

Constitutive Relations	Kinetic Relations
<p>Finite form:</p> $\varepsilon_{ij} = D_{ijkl}(\gamma) \sigma_{kl} + \frac{3}{2} \Delta \varepsilon_t (S_{ij} / \bar{\sigma}) \gamma,$ <p>where</p> $D_{ijkl}(\gamma) = \gamma D_{ijkl}^{(M)} + (1 - \gamma) D_{ijkl}^{(A)}.$ <p>Incremental form:</p> $d\varepsilon_{ij} = \bar{D}_{ijkl}(\gamma) d\sigma_{kl} + \left((D_{ijkl}^{(M)} - D_{ijkl}^{(A)}) \sigma_{kl} + \frac{3}{2} \Delta \varepsilon_t \frac{S_{ij}}{\bar{\sigma}} \right) d\gamma,$ <p>where</p> $\bar{D}_{ijkl}(\gamma) = D_{ijkl}(\gamma) + \frac{3}{2} \frac{\Delta \varepsilon_t}{\bar{\sigma}} \left(\delta_{ik} \delta_{jl} - \frac{1}{3} \delta_{ij} \delta_{kl} - \frac{3}{2} \frac{S_{ij} S_{kl}}{\bar{\sigma}^2} \right) \gamma.$	<p>Forward transformation ($d\gamma > 0, \gamma < 1$):</p> $F_{A \rightarrow M}(\sigma_{ij}, \gamma, T) = 0, \quad dF_{A \rightarrow M} = 0,$ <p>where</p> $F_{A \rightarrow M} = \bar{\sigma} - (1 - \gamma) \sigma_{MN}(T) - \gamma \sigma_{MC}(T).$ <p>Reverse transformation ($d\gamma < 0, \gamma > 0$):</p> $F_{M \rightarrow A}(\sigma_{ij}, \gamma, T) = 0, \quad dF_{M \rightarrow A} = 0$ <p>where</p> $F_{M \rightarrow A} = \bar{\sigma} - \gamma \sigma_{AN}(T) - (1 - \gamma) \sigma_{AC}(T).$

Table 1. Summary of the constitutive model.

of martensite; $D_{ijkl}^{(A)}$ and $D_{ijkl}^{(M)}$ are the elastic compliances of the pure austenite and martensite phases, respectively, and $\Delta\varepsilon_t$ is a material parameter, representing the maximum transformation strain that can be achieved during a uniaxial test.

The kinetics of phase transformation in the forward or reverse directions are controlled by a set of yield functions called *martensite nucleation stress* (σ_{MN}), *martensite completion stress* (σ_{MC}), *austenite nucleation stress* (σ_{AN}), and *austenite completion stress* (σ_{AC}). For materials such as NiTi, which exhibit localization of deformation and unstable mechanical behavior, the nucleation stress is higher (lower) than the completion stress during the forward (reverse) transformation. These critical values are temperature-dependent material properties and must be determined through a carefully designed and executed testing setup; see [Iadicola and Shaw 2002], for example.

The heat generation/consumption during the transformation is considered to be a result of inelastic work and enthalpy change due to phase transformation [Shaw 2000]. Therefore, the heat generation may be calculated as

$$\dot{q}_G = (\sigma_{ij}\dot{\varepsilon}_{ij} - \dot{u}^{(e)}) - \dot{h}. \quad (1)$$

In this equation, q_G is the generated heat, $u^{(e)}$ is the elastic energy density, and \dot{h} is the enthalpy change. The elastic energy density is given by

$$u^{(e)} = \frac{1}{2}\sigma_{ij}\varepsilon_{ij}^{(e)}, \quad (2)$$

where $\varepsilon_{ij}^{(e)}$ is the elastic part of the strain given by ([Azadi et al. 2007])

$$\varepsilon_{ij}^{(e)} = (\gamma D_{ijkl}^{(M)} + (1 - \gamma) D_{ijkl}^{(A)}) \sigma_{kl}. \quad (3)$$

It is assumed that the rate of change in enthalpy, \dot{h} , can be approximated by

$$\dot{h} = \begin{cases} \rho \Delta h_{A \rightarrow M} \dot{\gamma} & \text{if } \dot{\gamma} > 0, \\ -\rho \Delta h_{M \rightarrow A} \dot{\gamma} & \text{if } \dot{\gamma} < 0. \end{cases} \quad (4)$$

where ρ is the density and $\Delta h_{A \rightarrow M}$, $\Delta h_{M \rightarrow A}$ are the total changes in enthalpy per unit mass during the forward and reverse transformations at zero-stress. These quantities can be measured by differential scanning calorimetry (DSC). From Table 1 and equations (1) through (4), the heat generation term is obtained as

$$\dot{q}_G = \begin{cases} (\bar{\sigma} \Delta\varepsilon_t + \frac{1}{2}\sigma_{ij}(D_{ijkl}^{(M)} - D_{ijkl}^{(A)})\sigma_{kl} - \rho \Delta h_{A \rightarrow M})\dot{\gamma} & \text{if } \dot{\gamma} > 0, \\ (\bar{\sigma} \Delta\varepsilon_t + \frac{1}{2}\sigma_{ij}(D_{ijkl}^{(M)} - D_{ijkl}^{(A)})\sigma_{kl} + \rho \Delta h_{M \rightarrow A})\dot{\gamma} & \text{if } \dot{\gamma} < 0. \end{cases} \quad (5)$$

A few comments regarding the limitations and validity of the assumptions in this constitutive model are necessary. The current constitutive model is an extension of a mechanical theory (deformation theory of plasticity). Although the model is not derived from explicit thermodynamic considerations, it accounts for the hysteresis behavior and the proper direction of phase transformations and corresponding heat generation terms during loading and unloading, as validated by comparison with experiments. Nevertheless, the reformulation of the proposed constitutive theory in a consistent thermodynamic framework seems to be difficult.

The use of the von Mises effective stress in the yield criteria limits the application of the constitutive model to materials that behave symmetrically under tension and compression. As shown experimentally

(see [Liu et al. 1998], for example), NiTi alloys exhibit tension-compression asymmetry. The tension-compression asymmetry, however, does not impact the current work, which focuses on tension.

It has been shown through experiment that the phase transformation in NiTi may start homogeneously prior to the nucleation of localized deformation bands [Feng and Sun 2006; Daly et al. 2007]. Tan et al. [2004] also reported that the end of the stress plateau in the pseudoelastic response is not the end of the phase transformation, and that the stress-induced transformation continues beyond the stress plateau. The mechanically stable stress-induced phase transformation is not considered in this current analysis. However, it would be straightforward to incorporate into the constitutive model by revising the yield functions $F_{A \rightarrow M}$ and $F_{M \rightarrow A}$ in Table 1.

3. Numerical simulations

The constitutive model has been implemented within a FEM framework to predict the nucleation and propagation of transformation-induced instabilities during the pseudoelastic response of NiTi dog-bone samples at various strain rates. The simulations were run with the aid of an in-house FEM code developed by the authors. The geometry of the sample and FE mesh are shown in Figure 1, left. The sample

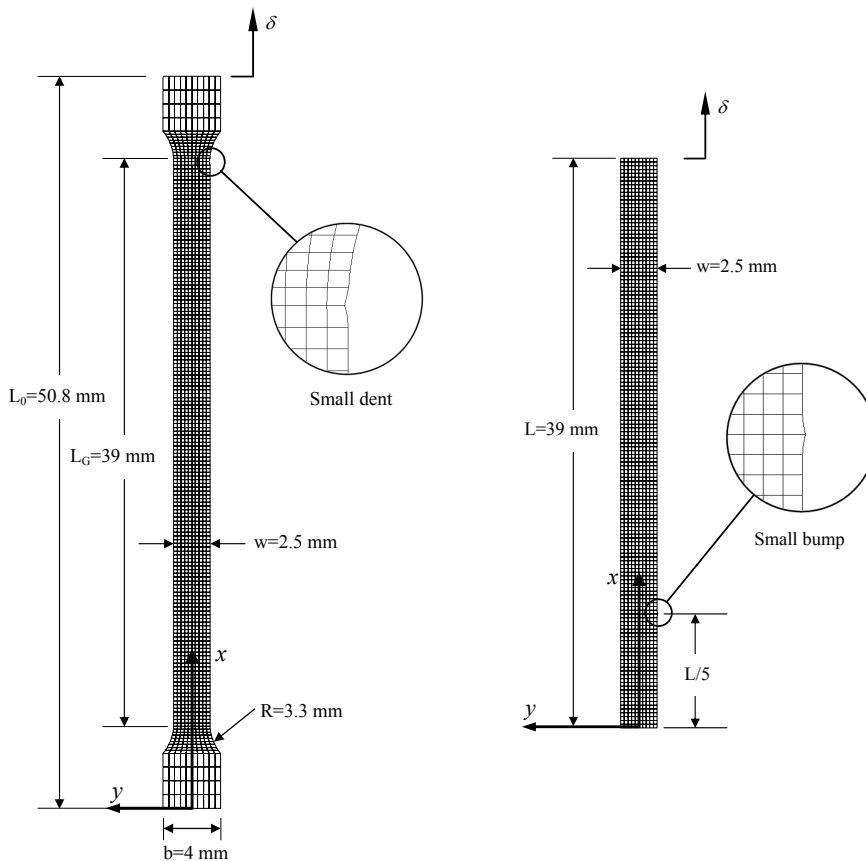


Figure 1. Left: Geometry and finite element discretization of the sample. Right: Geometry and mesh used for calibration of the model in reverse transformation.

dimensions are based on the dog-bone sample used in the experiments of [Shaw and Kyriakides \[1997a\]](#), which has a uniform thickness of 0.4 mm. The two-dimensional spatial domain was discretized with 8-node Serendipity plane-stress elements. The gauge section was discretized with 150 elements along the length and 10 elements across the width. A small dent with a depth of 0.04 mm was introduced at the top right corner of the gauge section as shown in the figure. The purpose of this geometric imperfection was to control the location of the first nucleation.

The nodal displacements along the bottom end of the specimen ($x = 0$) are fixed while those across the top end ($x = L_0$) are pulled at a constant rate. The temperatures of both ends are fixed at the ambient temperature (25 °C). [Shaw \[2000\]](#) rationalized this assumption based on the large size of the metallic grips used in the experiments. The heat loss due to natural convection has been considered by assuming a constant convective film coefficient, $h_{\text{conv}} = 4 \text{ W/m}^2 \text{ K}$, for all the exposed surfaces and free edges of the sample [[Shaw 2000](#)]. The imposed mechanical and thermal boundary conditions are expressed as

$$\begin{aligned} u|_{x=0} = 0, \quad v|_{x=0,y=0} = 0, \quad T|_{x=0} = 25^\circ\text{C}, \quad \dot{q}|_{\text{surface}} = h_{\text{conv}}(T - 25^\circ\text{C}), \\ u|_{x=L_0} = \delta, \quad v|_{x=L_0,y=0} = 0, \quad T|_{x=L_0} = 25^\circ\text{C}, \quad \dot{q}|_{\text{edge}} = h_{\text{conv}}(T - 25^\circ\text{C}), \end{aligned} \quad (6)$$

where u and v are the displacement components in the x - and y -directions, respectively, δ is the applied end displacement, T (°C) is the temperature, and \dot{q} (W/m^2) is the rate of heat loss per unit area.

In the experiments of [Shaw and Kyriakides \[1997a\]](#), the variation in temperature at the moderate strain rate was in the range of +12°C and −5°C. Therefore, heat transfer through radiation was assumed to be negligible. Thermal expansion/contraction was also ignored in the following analysis due to its minor effect on the results.

The sensitivity of the present numerical analysis to mesh size, and the uniqueness of the solution were examined by the authors. Despite the instability of mechanical behavior, only minor mesh sensitivity was observed in the numerical simulations conducted with finer meshes. As pointed out by [Shaw \[2000\]](#), the generation or absorption of heat during the transformation stabilizes the mechanical response. Additionally, the recovery of material stability at the end of phase transformation has an overall stabilizing effect on the solution. As a result, the overall force-displacement response, temperature variation, the number of nucleation events, and the basic features of the front morphology are not affected by mesh size. However, the exact location and timing of nucleation events, and also the orientation of transformation bands ($+\theta$ or $-\theta$) are sensitive to numerical noise.

In the following subsections, the model is first calibrated using data from “isothermal” experiments performed at various temperatures, and then implemented to simulate the “nonisothermal” responses of the specimen at various strain rates.

3A. Material parameters and calibration of the constitutive model. We assume in our analysis that individual solid phases behave as isotropic materials. A set of stress-strain curves derived from the isothermal uniaxial tensile tests on NiTi dog-bone samples reported by [Shaw \[2000\]](#) have been used to find the mechanical parameters of the constitutive model. The mechanical responses of the material at three different temperatures (15, 25, and 35 °C) have been considered for this purpose. The elastic modulus of individual phases (E_A , E_M), and the transformation strain ($\Delta\varepsilon_t$) are the average values measured directly from the experimental results.

In order to find the nucleation and completion stresses during the forward transformation, a set of isothermal simulations at various temperatures were run on the dog-bone sample shown in [Figure 1](#), left. By best fitting the nominal nucleation stress and propagation stress (Maxwell stress) obtained from the numerical analysis to those from the experiments at the above mentioned temperatures, the following linear relationships were established:

$$\begin{aligned}\sigma_{MN}(T) &= 9.4258 T + 189.13 & (\text{MPa}), \\ \sigma_{MC}(T) &= 4.8158 T + 232.73 & (\text{MPa}).\end{aligned}\tag{7}$$

The tapered sections of the sample in [Figure 1](#) experience a lower level of stress. Therefore, some residual austenite remains in those areas at the end of the stress plateau. This effect masks a visible stress valley at the onset of the reverse transformation in the stress-strain response, both in the simulations and experiments. In order to eliminate the end effects, [Shaw and Kyriakides \[1997a\]](#) used straight specimens to measure the nucleation stress during the reverse transformation. During these tests, austenite nucleation upon unloading occurs in the middle of the test section and is accompanied by a distinct stress valley. To calibrate the model for the reverse transformation, a straight specimen was also used in the isothermal simulations, as depicted in [Figure 1](#), right. The dimensions and FE mesh of the specimen are similar to those of the gauge section of the dog-bone sample. A slight side imperfection in the form of a bump was introduced at $x=L/5$ to control the location of the first nucleation ([Figure 1](#), right). The height of the bump was 0.04 mm. The specimen was first loaded until the entire domain was fully transformed into martensite, and then was unloaded.

The following linear relationships were found to best fit the nucleation and propagation stresses of the reverse transformation obtained from the isothermal experiments at different temperatures,

$$\begin{aligned}\sigma_{AN}(T) &= 7.5128 T - 44.22 & (\text{MPa}), \\ \sigma_{AC}(T) &= 10.276 T - 35.31 & (\text{MPa}).\end{aligned}\tag{8}$$

In equations (7) and (8), the temperature is in °C, and stresses are the second Piola–Kirchhoff stresses (Green strains and second Piola–Kirchhoff stresses were employed in the FE formulation in anticipation of future research). The variation of the nucleation and completion stresses with temperature is shown in [Figure 2](#). In this figure, the nominal (engineering) nucleation and propagation stresses as determined by the isothermal simulations are also shown. There is a large difference between the engineering nucleation stress and the second Piola–Kirchhoff nucleation stress during the reverse transformation, which is due to the large amount of strain induced during the forward transformation. In order to show the close fit of the chosen mechanical properties, the overall pseudoelastic responses of the dog-bone sample based on the isothermal simulations are compared to the experimental results in [Figure 3](#).

Thermal parameters of the NiTi strip, including zero-stress enthalpy change, $\Delta h_{A \rightarrow M}$, the thermal conductivity, k , specific heat capacity, C_p , and density, ρ , were taken from [[Shaw 2000](#)]. It was also assumed that the stress-free enthalpy change for the martensite to austenite transformation, $\Delta h_{M \rightarrow A}$, is the negative of that for the austenite to martensite transformation. As an approximation, all thermal parameters were assumed to be independent of phase, temperature, or other state variables. [Table 2](#) summarizes the chosen mechanical and thermal properties.

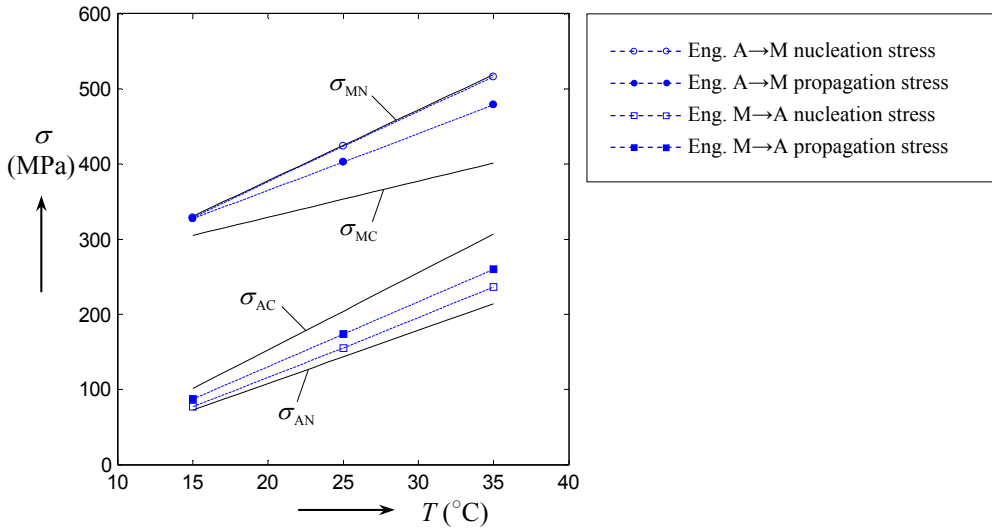


Figure 2. Chosen second Piola–Kirchhoff nucleation and completion stresses, and corresponding engineering values calculated from the isothermal simulations.

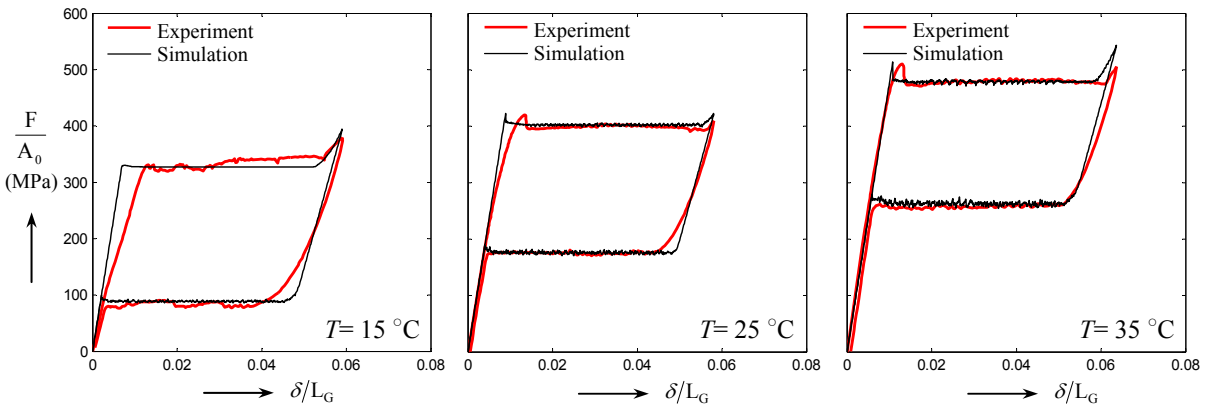


Figure 3. Pseudoelastic response of NiTi strip under isothermal conditions at different temperatures. Experimental curves are adapted from [Shaw 2000].

3B. Simulation of loading-unloading at low strain rate. The pseudoelastic response of the dog-bone sample shown in Figure 1 was simulated for low strain rate displacement-controlled loading-unloading. The ambient air temperature surrounding the sample and the temperature of the grips was 25 °C. The specimen was loaded at a constant rate of $\dot{\delta}/L_G = 10^{-4} \text{ s}^{-1}$. The deformation was paused at $\delta/L_G = 6.4 \%$ for 5 minutes to allow the sample to reach thermal equilibrium, followed by unloading at a constant rate of $\dot{\delta}/L_G = -10^{-4} \text{ s}^{-1}$. The predicted force-displacement response is compared with the experimental measurements of Shaw and Kyriakides [1997a] in Figure 4. A sequence of 14 contour graphs showing the distribution of phase and temperature corresponding to the deformed configurations of the specimen during the forward transformation are provided in Figure 5. The contours are separated by intervals of $\delta/L_G = 0.4 \%$ with the first and last contour corresponding to $\delta/L_G = 0.8 \%$ and $\delta/L_G = 6 \%$, respectively.

Parameter		Value
Elastic modulus of Austenite	E_A (GPa)	57.55
Elastic modulus of Martensite	E_M (GPa)	28.00
Poisson's ratio	ν_A, ν_M	0.3
Transformation strain	$\Delta \varepsilon_t$	0.0429
Martensite nucleation stress	σ_{MN} (MPa)	$9.4258 T(^{\circ}C) + 189.13$
Martensite completion stress	σ_{MC} (MPa)	$4.8158 T(^{\circ}C) + 232.73$
Austenite nucleation stress	σ_{AN} (MPa)	$7.5128 T(^{\circ}C) - 44.22$
Austenite completion stress	σ_{AC} (MPa)	$10.276 T(^{\circ}C) - 35.31$
Enthalpy change at zero-stress	$\Delta h_{A \rightarrow M}, -\Delta h_{M \rightarrow A}$ (J kg ⁻¹)	-12.3×10^3
Thermal conduction coefficient	k (W m ⁻¹ K ⁻¹)	18
Specific heat capacity	C_p (J kg ⁻¹ K ⁻¹)	837
Density	ρ (kg m ⁻³)	6.5×10^3

Table 2. Mechanical and thermal properties of the NiTi strip.

The first region to transform to martensite nucleates at the geometric imperfection described earlier, and a sharp inclined deformation band forms with the well-known angle of 55° to the specimen axis. Upon additional loading, the single, well-defined transformation front evolves into an alternating criss-cross pattern, which is similar to the pattern [Shaw and Kyriakides \[1997a\]](#) observed in their experiments. As loading continues, the temperature at the transformation front increases ([Figure 5](#)), which in turn results in an increase in the nominal stress as shown in [Figure 4](#). At $\delta/L_G \approx 2.7\%$, a second transformation front nucleates at the lower end of the gauge section due to the stress concentration near the round fillet. The second nucleation event causes the drop in the load observed in both the experiment and the simulation results (refer to [Figure 4](#)). As the fronts approach each other, they become straight and inclined across the width with the same orientation to minimize the mismatch between them. At the instant of coalescence,

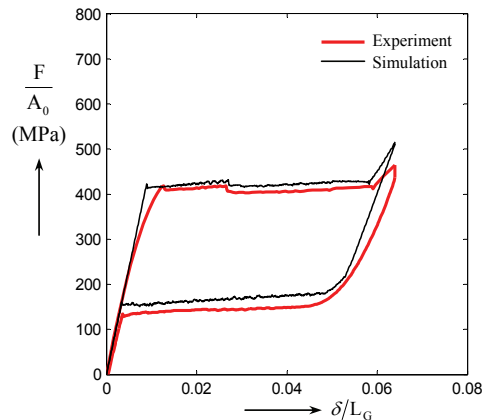


Figure 4. Pseudoelastic response of NiTi strip at $\dot{\delta}/L_G = 10^{-4} \text{ s}^{-1}$. The experimental response is adapted from [Shaw and Kyriakides \[1997a\]](#).

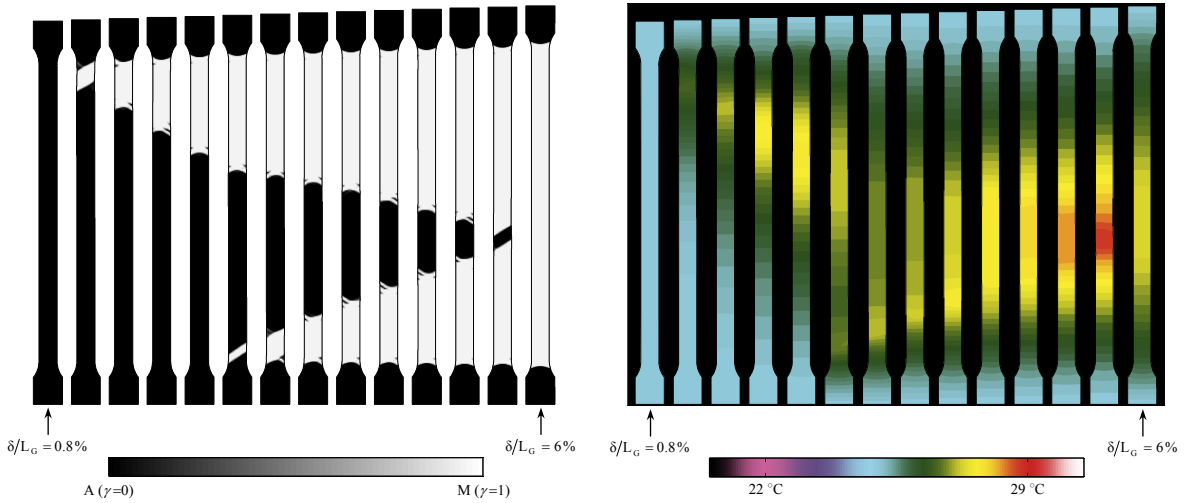


Figure 5. Sequence of events during $A \rightarrow M$ transformation at $\dot{\delta}/L_G = 10^{-4} \text{ s}^{-1}$. Left: Martensitic fraction; right: Temperature.

the fronts make an angle of 57.5° with the loading axis. Overall, the mechanical response, distribution of temperature, evolution of transformation, and details of the transformation front are in good agreement with the experimental observations of [Shaw and Kyriakides \[1997a\]](#).

The sequence of events leading to the initial shape change of the transformation front is particularly interesting. [Figure 6](#) shows a close up view of the transformation front (phase distribution contour) and distorted mesh. The lateral displacement (v) has been multiplied by a factor of 20 to accentuate the lateral deflection in [Figure 6](#), bottom. When the inclined transformation band nucleates at time 1 and begins to spread, the lateral deflection increases continuously at the front. The lateral deflection reaches its maximum between times 5 and 6, where the first finger emanates from the upper front in order to balance the lateral deflection and straighten the specimen. As a result, the lateral deflection decreases from times 6 to 8. The subsequent evolution of the transformation front can be described as successive nucleation and growth of finger patterns in alternative directions in order to keep the lateral deflection minimum.

During the pause between loading and unloading, the temperature of the sample equilibrates prior to returning to the ambient temperature. The evolution of the transformed phase and the temperature distribution during the reverse transformation are shown in [Figure 7](#). As expected, the reverse transformation initiates at the tapered ends of the sample due to the reduced stress at these regions. The two transformation fronts propagate toward each other at the same speed. During most of the unloading part, the converging fronts are predicted to propagate through inverse shrinkage of the finger-type patterns observed during the forward transformation. However, experimental results of [Shaw and Kyriakides \[1997a\]](#) suggested that the fronts during the reverse transformation are quite sharp and straight with an inclination angle of approximately 56° . This discrepancy between the predicted and observed results is probably due to the lack of information on the exact boundary conditions at the gripped ends in the

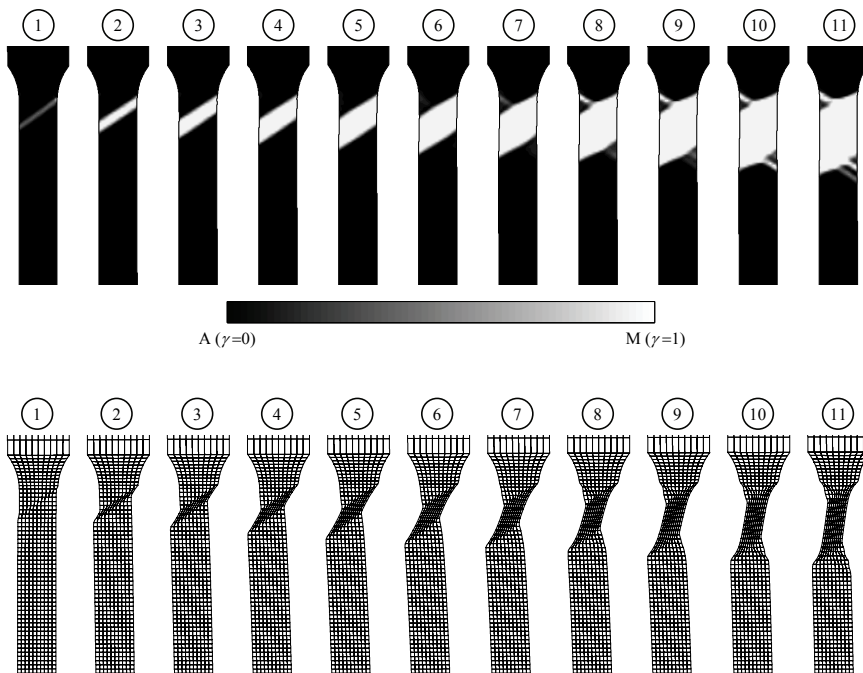


Figure 6. Details of front morphology evolution during A \rightarrow M transformation. Top: distribution of phases; bottom: distorted mesh with lateral displacement multiplied by a factor of 20.

experiment. As will be discussed later, small misalignments in the boundary conditions may result in sharp inclined fronts during the reverse transformation.

In addition to difference in the shape of the transformation front, the magnitude of the predicted temperature drop during the reverse transformation is also different from the measurements of [Shaw and Kyriakides \[1997a\]](#). The maximum temperature drop observed during the experiment was -2°C , whereas in the simulation it was predicted to reach -3.6°C . This discrepancy may be partly due to uncertainties in the thermophysical properties of the specimen and thermal boundary conditions, and/or partly due to the assumption that the zero-stress latent heats associated with the forward and reverse transformations have the same value.

3C. Simulation of loading-unloading at moderate strain rate. The pseudoelastic response of the dog-bone SMA specimen was simulated for a moderate strain rate condition. A constant loading rate of $\dot{\delta}/L_G = 10^{-3} \text{ s}^{-1}$ was applied until $\delta/L_G = 7.65\%$, followed by a 5 minute hold, then unloading at the same constant rate. The ambient air temperature was 25°C . The nominal stress-strain response is shown in [Figure 8](#). The evolution of phase transformation and the distribution of temperature during the forward and reverse transformations are depicted in [Figures 9 and 10](#). The transformation behavior is very similar to the experimental observations of [Shaw and Kyriakides \[1997a\]](#). The localized transformation is first nucleated at the top corner, followed by a second nucleation event at the lower end, then two nucleation events in the mid span. The shape of transformation fronts match those observed in the experiment. For

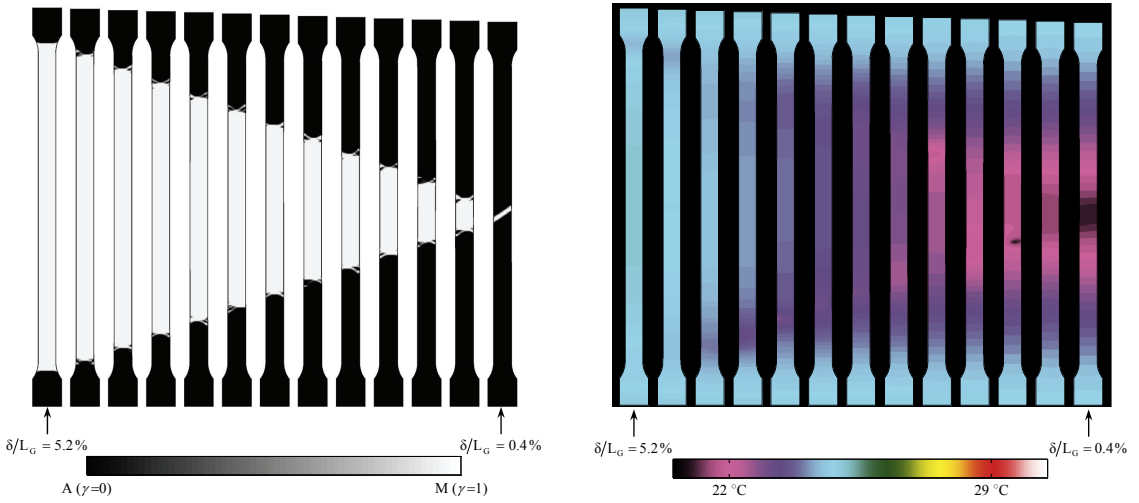


Figure 7. Sequence of events during $M \rightarrow A$ transformation at $\dot{\delta}/L_G = -10^{-4} \text{ s}^{-1}$. Left: martensitic fraction; right: temperature.

the duration of the loading phase, they are sharp and straight, with an inclination angle ranging from 55° to 65° to the vertical axis. Only occasionally will one or two fingers develop at the front. This can be explained by noticing that the lateral deflection developed in each front compensate the lateral deflection in another front, and therefore the sharply inclined fronts can survive without branching and developing crossing fingers.

An interesting feature of the stress-strain response in [Figure 8](#) is the stress-relaxation during the pause between loading and unloading, which can be seen in both the simulation and experimental results. This stress-relaxation is caused by the phase transformation due to the temperature decrease during the pause period [[Pieczyska et al. 2006b](#)].

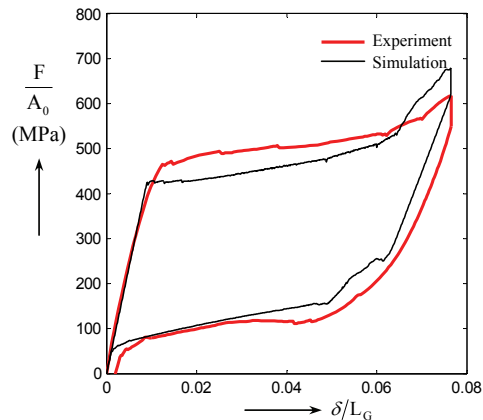


Figure 8. Pseudoelastic response of NiTi strip at $\dot{\delta}/L_G = 10^{-3} \text{ s}^{-1}$. Experimental data are from [Shaw and Kyriakides \[1997a\]](#).

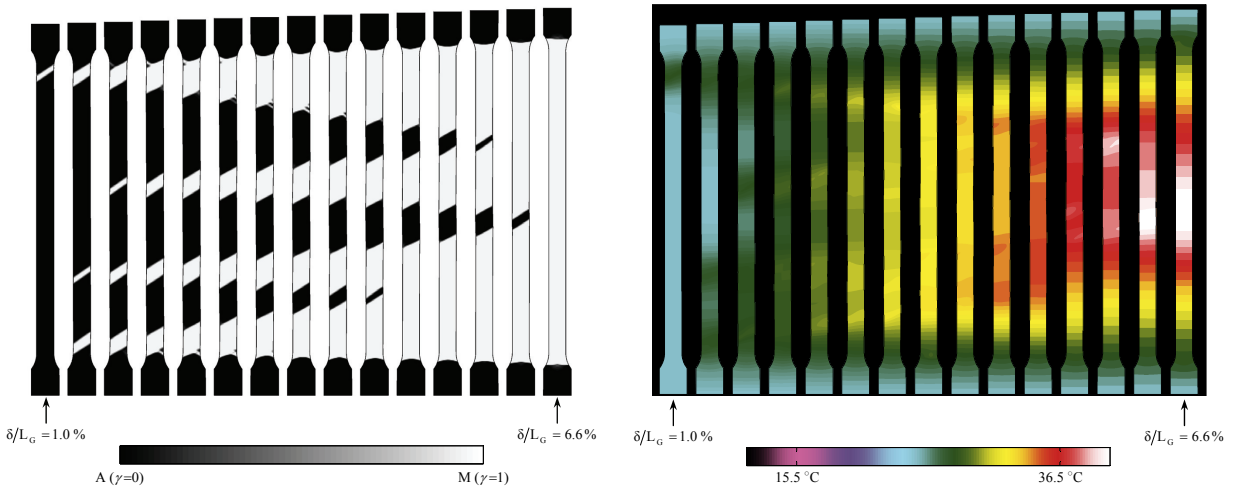


Figure 9. Sequence of events during forward transformation at $\dot{\delta}/L_G = 10^{-3} \text{ s}^{-1}$. Left: martensitic fraction; right: temperature.

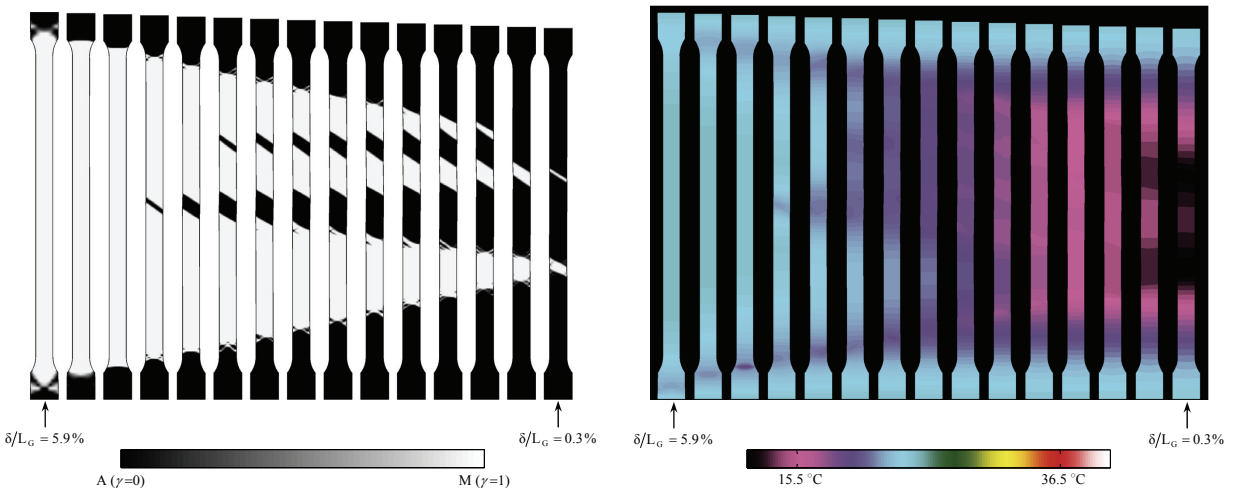


Figure 10. Sequence of events during reverse transformation at $\dot{\delta}/L_G = -10^{-3} \text{ s}^{-1}$. Left: martensitic fraction; right: temperature.

Unlike the low strain rate case, the transformation fronts during unloading at this moderate strain rate are mostly straight, with an inclination between 54° and 62° . The fronts emanating from the sample ends, however, are initially fingered and gradually become straight as they approach the middle fronts.

The temperature distributions during the forward transformation agree with the measurements of [Shaw and Kyriakides \[1997a\]](#). However, as in the previous simulation, the predicted temperatures exhibit a much larger temperature drop (-13°C) during the reverse transformation as compared to the experiments (-5°C). This large deviation from the experimental measurements suggests that the stress-free enthalpy

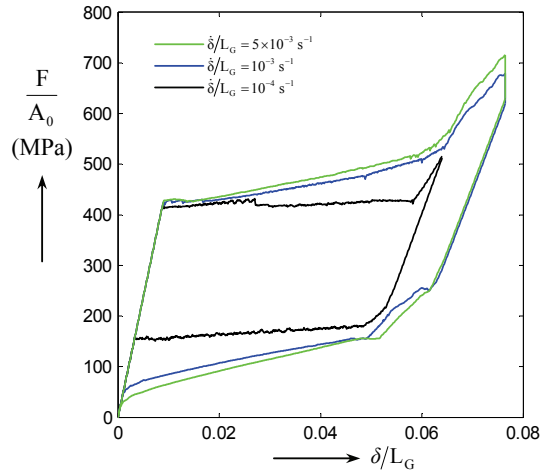


Figure 11. Simulated pseudoelastic response of NiTi strip at various elongation rates.

change during the reverse transformation ($\Delta h_{M \rightarrow A}$) must be substantially smaller than its counterpart during the forward transformation. The DSC measurements reported in Shaw [2000], however, do not show such a large difference. Further investigation is needed to clarify this issue.

3D. Simulation of loading-unloading at high strain rate. The simulation was performed for a high strain rate beyond the loading rates applied in the experiments of Shaw and Kyriakides [1997a]. The elongation rate in this case was $\dot{\delta}/L_G = 5 \times 10^{-3} \text{ s}^{-1}$, which is five times faster than the moderate strain rate case. The loading was stopped at $\delta/L_G = 7.65\%$, followed by a 5 minute hold and subsequent unloading. The predicted nominal stress-strain response at this rate is compared to those at the low and moderate strain rates in Figure 11. The evolution of the phase transformations and temperature during loading and unloading are shown in Figures 12 and 13, respectively.

Similar to previous cases, the first nucleation event occurs at the top end of the gauge section where the geometric imperfection is located. Shortly after that, 7 narrow bands, some parallel and some opposing each other, are nucleated almost simultaneously in the gauge section. The number of nucleation events in this case is substantially larger than those observed in the previous two cases.

Figure 11 indicates that the change in the nominal stress-strain response with strain rate does not exhibit a linear trend. The difference between the stress-strain curves at the low and moderate strain rates is more pronounced than the difference between those at the moderate and high strain rates. As explained earlier, the increase or decrease in stress is caused by the increase or decrease in the temperature of transformation fronts. The magnitude of temperature variation at a front depends on the rate of transformation, which is proportional to the speed at which the transformation front propagates. On the other hand, the propagation speed decreases with the number of coexisting transformation fronts. Consequently, the increase of the transformation front temperature in the high strain rate case is hampered by the increase in the number of transformation fronts, which in turn results in a relatively small increase in the nominal stress.

By increasing the elongation rate, it is seen that the transformation fronts become even sharper, and emanating fingers disappear during the reverse transformation. This is due to the fact that the number

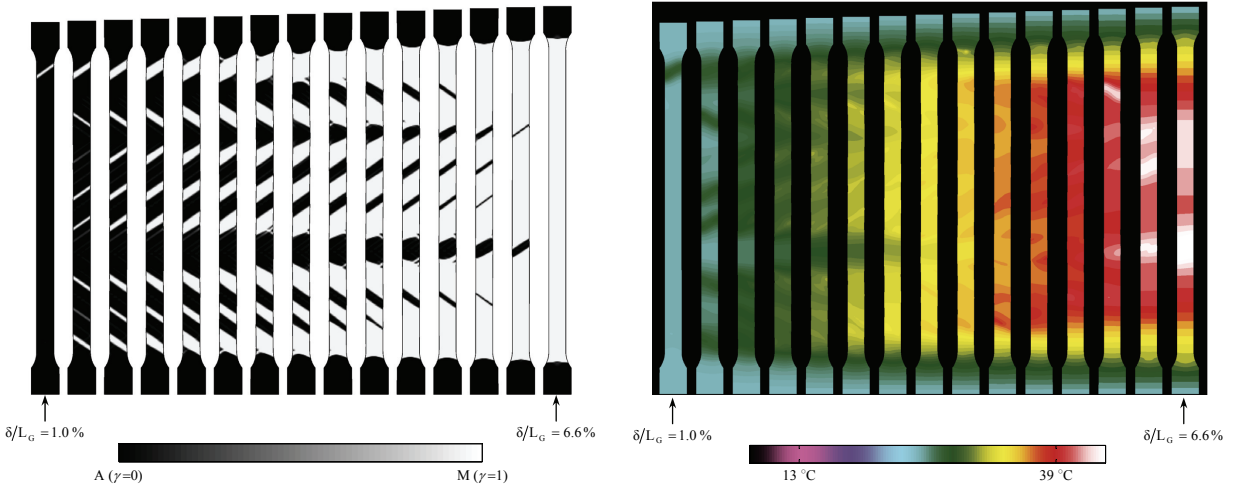


Figure 12. Sequence of events during forward transformation at $\dot{\delta}/L_G = 5 \times 10^{-3} \text{ s}^{-1}$. Left: martensitic fraction; right: temperature.

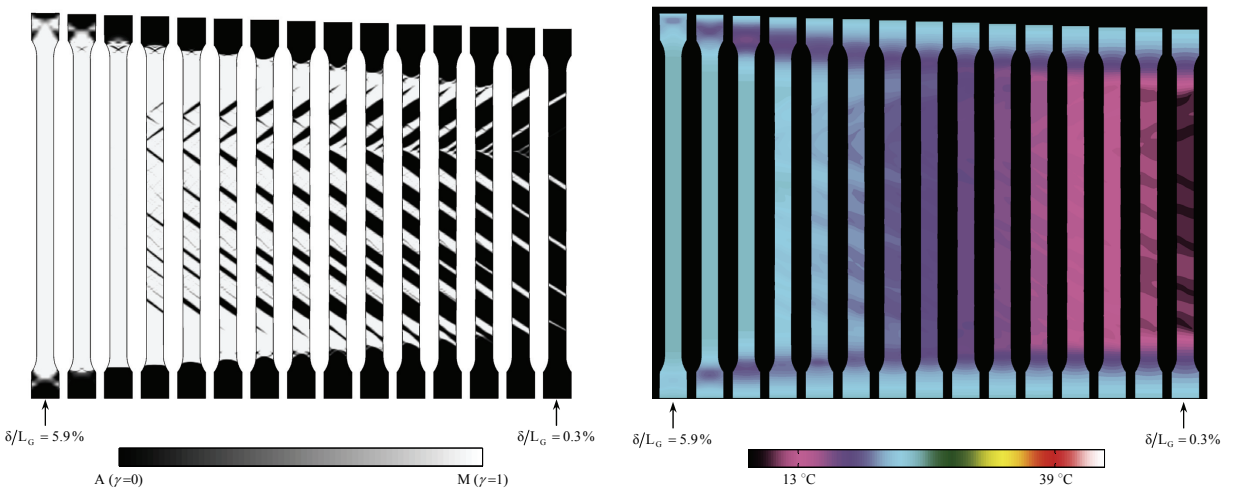


Figure 13. Sequence of events during reverse transformation at $\dot{\delta}/L_G = -5 \times 10^{-3} \text{ s}^{-1}$. Left: martensitic fraction; right: temperature.

of nucleation events increases by an increase in the strain rate. Concurrent transformation fronts help to maintain the overall straightness of the sample by cancelling each other. Hence, the sharp inclined transformation fronts survive for long periods before finally merging.

3E. Effect of boundary conditions. When performing uniaxial tension tests, it is important to minimize grip misalignment in order to reduce the out-of-axis loading. However, in practice, a pure uniaxial test may be difficult to achieve. For most materials which exhibit stable mechanical behavior, the small variation in loading conditions does not usually affect the observed behavior. But it is suspected that the

transformation behavior of NiTi samples undergoing uniaxial tensile tests may be sensitive due to the instability of the mechanical response. The dog-bone simulation has been used to evaluate the possible effects of misalignment on the transformation behavior. A lateral misalignment of 0.35 mm was applied to the lower end of the sample shown in [Figure 1](#). The new displacement boundary conditions are now

$$\begin{aligned} u|_{x=0} &= 0, & v|_{x=0,y=0} &= 0.35 \text{ mm} \\ u|_{x=L_0} &= \delta, & v|_{x=L_0,y=0} &= 0. \end{aligned} \quad (9)$$

All other boundary conditions were applied as previously described. The simulations for the low and moderate strain rate conditions were repeated with new boundary conditions. The overall force-displacement response, the number of transformation fronts, and distribution of temperature were not affected by the new boundary conditions in any of the simulations. The only major change was observed in the morphology of the transformation fronts during the reverse transformation, especially at the low strain rate. [Figure 14](#) shows the evolution of the reverse transformation in this case.

The two transformation fronts in [Figure 14](#) become sharp and straight shortly after they exit the tapered ends of the specimen. As explained earlier, a straight inclined front tends to increase the amount of lateral deflection, which in turn helps to compensate for the misalignment of specimen ends. During the forward transformation, the large axial load acts as a restorative force opposing the growth of lateral deflection; thus the straight inclined fronts eventually convert to criss-cross fronts. During the reverse transformation, the transformation proceeds at a much smaller axial load, and therefore a larger amount of lateral deflection can exist. The kinking of the specimen due to lateral deflection is visible in [Figure 14](#), which can also be observed in the experiments of [Shaw and Kyriakides \[1997a\]](#).

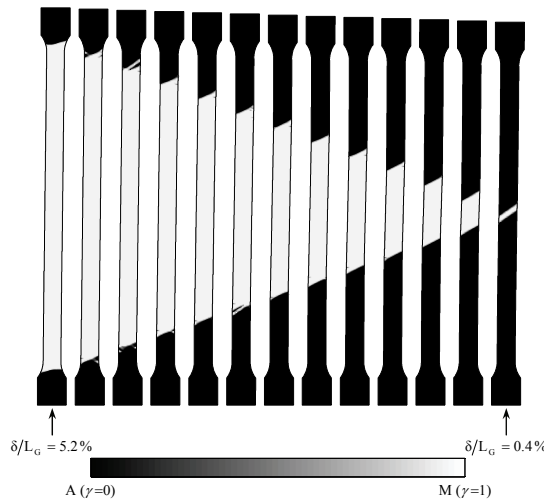


Figure 14. Transformation behavior of the specimen with misaligned grips during reverse transformation at $\dot{\delta}/L_G = -10^{-4} \text{ s}^{-1}$.

4. Summary and conclusions

A numerical study of the nucleation and propagation of transformation bands during unstable pseudoelastic behavior of NiTi dog-bone samples has been presented. A multidimensional macroscopic constitutive model of SMA derived based on the deformation theory of plasticity was implemented within a two-dimensional finite element model to simulate the material response. Unlike similar numerical analyses in the past, the present model is able to capture the localization of transformation during unloading, as well as loading. The constitutive model was calibrated based on isothermal quasi-static uniaxial pseudoelastic experiments available in the literature. The thermomechanical coupling that occurs during the transformation, and the effect of loading rate on the overall mechanical response and evolution of a localized deformation were successfully simulated both during the forward and reverse transformations. The basic features of transformation front morphology and its evolution during forward and reverse transformations were also captured by the numerical analysis.

The following conclusions can be drawn based on the analysis presented in this paper:

- (1) The current macromechanical constitutive model's ability to correctly describe the forward and reverse transformations verifies that the continuum-level phenomena are the major players in the nucleation and propagation of martensitic transformation and its reverse transformation in NiTi shape memory alloys, regardless of the detailed microstructural root of the material instability.
- (2) The comparison between the calculated temperature drop during reverse transformation and experimental measurements clearly indicate that the zero-stress enthalpy change (stress-free latent heat) of the forward transformation must be greater than that of the reverse transformation. This conclusion, however, does not agree with the DSC measurements. Further experimental and theoretical analysis is required to clarify this difference.
- (3) The number of propagating transformation fronts is an important factor in determining the overall mechanical response of the material in nonisothermal conditions. The number of coexisting transformation fronts influences the local variations of temperature at individual fronts, which in turn affects the overall pseudoelastic response.
- (4) A small misalignment in the loading axis during uniaxial loading-unloading of a NiTi sample can dramatically affect the shape of transformation fronts during the reverse transformation. This is due to the lower stress level during the reverse transformation as compared to the forward transformation, which allows the specimen to develop kinks along its span.

The present methodology forms the basis of an analytical tool for use in analyzing SMA components subjected to various thermomechanical loading conditions within the unstable pseudoelastic regime.

References

- [Abeyaratne and Knowles 1993] R. Abeyaratne and J. K. Knowles, "Continuum model of a thermoelastic solid capable of undergoing phase transitions", *J. Mech. Phys. Solids* **41**:3 (1993), 541–571.
- [Auricchio and Stefanelli 2004] F. Auricchio and U. Stefanelli, "Numerical analysis of a three-dimensional super-elastic constitutive model", *Int. J. Numer. Methods Eng.* **61**:1 (2004), 142–155. MR 2005b:74100
- [Auricchio et al. 1997] F. Auricchio, R. Taylor, and J. Lubliner, "Shape-memory alloys: Macromodelling and numerical simulations of the superelastic behavior", *Comput. Methods Appl. Mech. Eng.* **146**:3–4 (1997), 281–312.

- [Azadi 2008] B. Azadi Borujeni, *Constitutive modelling and finite element analysis of the dynamic behavior of shape memory alloys*, Ph.D. dissertation, Department of Mechanical Engineering, University of British Columbia, Vancouver, 2008, Available at <https://circle.ubc.ca/handle/2429/796>.
- [Azadi et al. 2006] B. Azadi, R. K. N. D. Rajapakse, and D. M. Maijer, “One-dimensional thermomechanical model for dynamic pseudoelastic response of shape memory alloys”, *Smart Mater. Struct.* **15**:4 (2006), 996–1008.
- [Azadi et al. 2007] B. Azadi, R. K. N. D. Rajapakse, and D. M. Maijer, “Multi-dimensional constitutive modeling of SMA during unstable pseudoelastic behavior”, *Int. J. Solids Struct.* **44**:20 (2007), 6473–6490.
- [Boyd and Lagoudas 1994] J. Boyd and D. Lagoudas, “A constitutive model for simultaneous transformation and reorientation in shape memory materials”, pp. 159–177 in *Mechanics of phase transformations and shape memory alloys* (Chicago, 1994), edited by L. C. Brinson and B. Moran, AMD **189**, ASME, New York, 1994.
- [Brinson 1993] L. C. Brinson, “One-dimensional constitutive behavior of shape memory alloys: Thermomechanical derivation with non-constant material functions and redefined martensite internal variable”, *J. Intell. Mater. Syst. Struct.* **4**:2 (1993), 229–242.
- [Brocca et al. 2002] M. Brocca, L. C. Brinson, and Z. P. Bazant, “Three-dimensional constitutive model for shape memory alloys based on microplane model”, *J. Mech. Phys. Solids* **50**:5 (2002), 1051–1077.
- [Daly et al. 2007] S. Daly, G. Ravichandran, and K. Bhattacharya, “Stress-induced martensitic phase transformation in thin sheets of Nitinol”, *Acta Mater.* **55**:10 (2007), 3593–3600.
- [Favier et al. 2002] D. Favier, Y. Liu, L. Orgeas, and G. Rio, “Mechanical instability of NiTi in tension, compression and shear”, pp. 205–212 in *IUTAM Symposium on Mechanics of Martensitic Phase Transformation in Solids* (Hong Kong, 2001), edited by Q. P. Sun, Solid Mechanics and its Applications **101**, Kluwer, Dordrecht, 2002.
- [Feng and Sun 2006] P. Feng and Q. P. Sun, “Experimental investigation on macroscopic domain formation and evolution in polycrystalline NiTi microtubing under mechanical force”, *J. Mech. Phys. Solids* **54**:8 (2006), 1568–1603.
- [Hu et al. 2007] Z. Hu, Q. P. Sun, and Z. Zhong, “Numerical simulation for stress-induced phase transformation of SMAs tube under tension”, *Key Eng. Mat.* **340-341** (2007), 1181–1186.
- [Iadicola and Shaw 2002] M. A. Iadicola and J. A. Shaw, “An experimental setup for measuring unstable thermo-mechanical behavior of shape memory alloy wire”, *J. Intell. Mater. Syst. Struct.* **13**:2–3 (2002), 157–166.
- [Iadicola and Shaw 2004] M. A. Iadicola and J. A. Shaw, “Rate and thermal sensitivities of unstable transformation behavior in a shape memory alloy”, *Int. J. Plast.* **20**:4–5 (2004), 577–605.
- [Idesman et al. 2005] A. V. Idesman, V. I. Levitas, D. L. Preston, and J.-Y. Cho, “Finite element simulations of martensitic phase transitions and microstructures based on a strain softening model”, *J. Mech. Phys. Solids* **53**:3 (2005), 495–523. MR 2005h:74060
- [Kohl 2004] M. Kohl, *Shape memory microactuators*, Springer, Berlin, 2004.
- [Lagoudas et al. 1996] D. C. Lagoudas, Z. Bo, and M. A. Qidwai, “A unified thermodynamic constitutive model for SMA and finite element analysis of active metal matrix composites”, *Mech. Compos. Mater. Struct.* **3**:2 (1996), 153–179.
- [Leo et al. 1993] P. H. Leo, T. W. Shield, and O. P. Bruno, “Transient heat transfer effects on the pseudoelastic behavior of shape-memory wires”, *Acta Metall. Mater.* **41**:8 (1993), 2477–2485.
- [Liu et al. 1998] Y. Liu, Z. Xie, J. Van Humbeeck, and L. Delaey, “Asymmetry of stress-strain curves under tension and compression for NiTi shape memory alloys”, *Acta Mater.* **46**:12 (1998), 4325–4338.
- [Miyazaki et al. 1981] S. Miyazaki, T. Imai, K. Otsuka, and Y. Suzuki, “Lüders-like deformation observed in the transformation pseudoelasticity of a Ti–Ni alloy”, *Scr. Metall.* **15**:8 (1981), 853–856.
- [Otsuka and Wayman 1998] K. Otsuka and C. M. Wayman, *Shape memory materials*, Cambridge University Press, Cambridge, 1998.
- [Pieczyska et al. 2006a] E. A. Pieczyska, H. Tobushi, S. P. Gadaj, and W. K. Nowacki, “Superelastic deformation behaviors based on phase transformation bands in TiNi shape memory alloy”, *Mater. Trans. (JIM)* **47**:3 (2006), 670–676.
- [Pieczyska et al. 2006b] E. A. Pieczyska, H. Tobushi, S. P. Gadaj, and W. K. Nowacki, “Stress relaxation during superelastic behavior of TiNi shape memory alloy”, *Int. J. Appl. Electrom.* **23**:1–2 (2006), 3–8.

- [Raniecki and Lexcellent 1998] B. Raniecki and C. Lexcellent, “Thermodynamics of isotropic pseudoelasticity in shape memory alloys”, *Eur. J. Mech. A Solids* **17**:2 (1998), 185–205.
- [Saadat et al. 2002] S. Saadat, J. Salichs, M. Noori, Z. Hou, H. Davoodi, I. Bar-On, Y. Suzuki, and A. Masuda, “An overview of vibration and seismic applications of NiTi shape memory alloy”, *Smart Mater. Struct.* **11**:2 (2002), 218–229.
- [Shaw 2000] J. A. Shaw, “Simulations of localized thermo-mechanical behavior in a NiTi shape memory alloy”, *Int. J. Plast.* **16**:5 (2000), 541–562.
- [Shaw and Kyriakides 1995] J. A. Shaw and S. Kyriakides, “Thermomechanical aspects of NiTi”, *J. Mech. Phys. Solids* **43**:8 (1995), 1243–1281.
- [Shaw and Kyriakides 1997a] J. A. Shaw and S. Kyriakides, “On the nucleation and propagation of phase transformation fronts in a NiTi alloy”, *Acta Mater.* **45**:2 (1997), 683–700.
- [Shaw and Kyriakides 1997b] J. A. Shaw and S. Kyriakides, “Initiation and propagation of localized deformation elasto-plastic strips under uniaxial tension”, *Int. J. Plast.* **13**:10 (1997), 837–871.
- [Sittner et al. 2005] P. Sittner, Y. Liu, and V. Novak, “On the origin of Lüders-like deformation of NiTi shape memory alloys”, *J. Mech. Phys. Solids* **53**:8 (2005), 1719–1746.
- [Tan et al. 2004] G. Tan, Y. Liu, P. Sittner, and M. Saunders, “Lüders-like deformation associated with stress-induced martensitic transformation in NiTi”, *Scr. Mater.* **50**:2 (2004), 193–198.
- [Tanaka et al. 1986] K. Tanaka, S. Kobayashi, and Y. Sato, “Thermomechanics of transformation pseudoelasticity and shape memory effect in alloys”, *Int. J. Plasticity* **2**:1 (1986), 59–72.

Received 14 Oct 2007. Revised 17 Oct 2008. Accepted 24 Oct 2008.

B. AZADI BORUJENI: azadi@mech.ubc.ca

University of British Columbia, Department of Mechanical Engineering, 2054-6250 Applied Science Lane, Vancouver, BC 6T 1Z4, Canada

DAAN M. MAIJER: daan.maijer@ubc.ca

University of British Columbia, Department of Materials Engineering, 309-6350 Stores Road, Vancouver, BC V6T 1Z4, Canada

R. K. NIMAL D. RAJAPAKSE: rajapakse@mech.ubc.ca

University of British Columbia, Department of Mechanical Engineering, 2054-6250 Applied Science Lane, Vancouver, BC 6T 1Z4, Canada

ELASTODYNAMIC RECIPROCITY RELATIONS FOR WAVE SCATTERING BY FLAWS IN FIBER-REINFORCED COMPOSITE PLATES

WARNA KARUNASENA

Due to light weight, high performance, and increased service life, fiber-reinforced composite materials are receiving wide attention as an advanced material in many branches of engineering. Structural integrity of composite structures is affected by the presence of flaws such as cracks and delaminations in the composite material. In this paper, elastodynamic reciprocity relations are developed for wave scattering by flaws, when guided waves are allowed to propagate in fiber-reinforced composite plates. These relations are useful for checking the accuracy of the numerical solution for the scattered wave field in ultrasonic nondestructive evaluation of flaws in composite plate-like structural elements. The classical elastodynamic reciprocity theorem is used to derive simple reciprocity relations for reflected and transmitted wave amplitudes and the corresponding energies associated with the wave modes in a plate with an arbitrary stacking sequence. The derived reciprocity relations are used to check the accuracy of the numerical solution for several example scattering problems.

1. Introduction

In the last two decades, fiber-reinforced composite materials, specially fiber-reinforced plastics (abbreviated as FRPs), have been receiving wide attention in aerospace, civil, and mechanical engineering applications due to their useful properties such as light weight, high strength, corrosion resistance, and long term durability. A state-of-the-art-review of FRP composites for construction applications can be found in [Bakis et al. 2002]. It is well known that structural integrity of facilities made from FRPs are severely affected by flaws such as cracks and delaminations developed within the FRP part of the structure. Guided elastic waves in plate-like composite parts possess characteristics that make them particularly useful for application to the nondestructive evaluation of flaws in composite structures. When excited at a particular location in a plate, guided waves can travel long distances along the plate, and when they meet a flaw along their path, the waves scatter. The scattered wave, which can travel long distances along the plate, will carry information about the size and location of the flaw, thus providing an ultrasonic nondestructive means of inspection of an otherwise inaccessible area of the structure. Ultrasonic nondestructive evaluation methods rely heavily on the solution to the problem of wave scattering at a flaw.

Obtaining closed-form solutions to even simple wave scattering problems in composite plates is impractical if not impossible. Numerical methods for obtaining a solution to the scattered wave field are quite intricate and complicated, and as a result, the accuracy of a numerically obtained solution is questionable. One way of to overcome this problem is to have some indicators, based on sound theories,

Keywords: reciprocity relations, wave scattering, composite plates, cracks, delaminations, finite elements, reflection and transmission coefficients.

to check the accuracy of the numerical solution. Two indicators used in the past are the satisfaction of elastodynamic reciprocity relations and the principle of energy conservation.

Chimenti [1997] has published a comprehensive review of guided waves in composite plates and their use for nondestructive material characterization. Datta [2000] provided a detailed review of the theory of guided waves in composite plates and shells. Although a vast body of work on guided ultrasonic wave propagation in plates and shells now exists, relatively few studies have dealt with scattering of these waves by cracks and delaminations. Moreover, these few studies have been mostly confined to the problems of horizontally polarized shear (SH) waves and plane strain (two-dimensional) waves. The author and his coworkers [Karunasena et al. 1991b] have investigated the two-dimensional wave scattering by a symmetric normal surface-breaking crack in a cross-ply laminated plate by using a hybrid method which combines the finite element method with the wave function expansion procedure. In this work, the authors have used the satisfaction of the reciprocity relations and the principle of energy conservation as checks for accuracy. The two checks are complementary to one other.

Recently, Karunasena [2004] extended the hybrid method to provide a model analysis of the scattering of a guided wave obliquely incident on a long, symmetric, surface-breaking crack in a composite plate. The solution to this problem is the first step towards analyzing the general three-dimensional scattering in a composite plate. As mentioned in the previous paragraph for simple wave scattering problems, satisfaction of the reciprocity relations can be used as one of the two complementary checks for assessing the accuracy of the more complicated oblique wave scattering problem. The focus of this paper is to present the derivation of elastodynamic reciprocity relations for the scattering problem of a guided wave incident obliquely on a long flaw in a composite plate. The analysis is presented for a plate with an arbitrary stacking sequence where each ply can have an arbitrary fiber direction with respect to the global coordinate system. Numerical results for reciprocity relations are provided for four special cases: (i) scattering by a symmetric normal edge crack in a unidirectional, fiber-reinforced, homogeneous, graphite-epoxy composite plate, (ii) scattering by a symmetric normal edge crack in an 8-layer graphite-epoxy cross-ply laminated plate, (iii) scattering by a thin planar crack located at the fixed end of a homogeneous isotropic plate, and (iv) scattering by a thin planar crack located at the fixed end of a unidirectional fiber-reinforced composite plate.

2. Formulation

2.1. Scattering problem. Time harmonic wave scattering of a guided plate wave incident obliquely on a flaw in a composite plate as shown in Figure 1 is considered. The composite material in the plate is uniaxially fiber-reinforced within each layer (or ply or lamina) and possibly laminated, with each ply having an arbitrary fiber direction with respect to the global x -direction. Each layer lies on a plane parallel to the x - y plane. It is assumed that all layers of the plate have equal thickness with transversely isotropic elastic properties. The flaw is located at $x = 0$ and is assumed to be very long (in comparison to the plate thickness) in y -direction. It has a constant cross section in x - z plane. It is assumed that two faces of the plate $z = 0$ and $z = H$ are stress free. Also, the flaw surface is assumed to be open with zero traction. Since the direction of the flaw (that is, the y -direction in this case), in general, is not known *a priori*, it is not always possible to excite the incident wave in the x -direction. Therefore, it is necessary to consider the general case where the incident wave is propagating at an arbitrary angle to

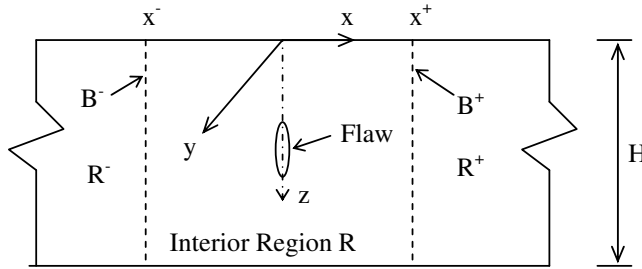


Figure 1. Geometry of the problem.

the x -direction, and the fiber direction is also at an arbitrary angle to global x -direction. Let the incident wave be a guided plate wave mode traveling at a direction making an angle $90^\circ - \phi^{in}$ with the y - z plane, with fibers at an angle θ to the x -direction as shown in Figure 2.

When the incident wave mode strikes the flaw, mode conversion will happen and a scattered field consisting of reflected and transmitted plate wave modes will be generated. The aim of this work is to numerically quantify this scattered field and derive reciprocity relations applicable to converted modes for the purpose of checking the accuracy of the numerical solution for the scattered wave field. In general, the incident and the scattered wave field will have all three displacement components in the x , y , and z directions. Let $u(x, y, z, t)$, $v(x, y, z, t)$, and $w(x, y, z, t)$ denote the displacement quantities in x , y , and z directions, respectively. Here t denotes time.

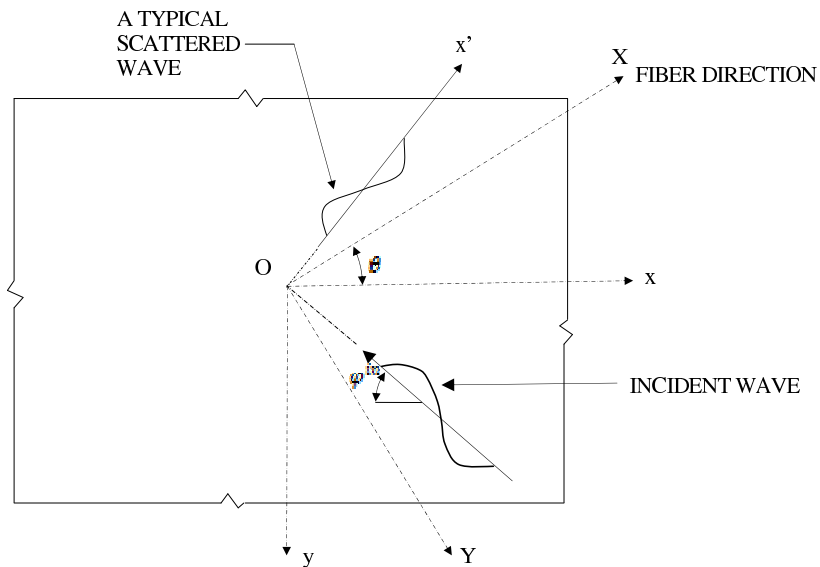


Figure 2. Plan view of a typical lamina (layer) showing fiber orientation and wave normals.

2.2. Solution for scattering problem. We adopt the hybrid method described in [Karunasena et al. 1991b; Karunasena 2004] for solving this scattering problem. The hybrid method combines finite element formulation in a bounded interior region of the plate with a wave function expansion representation in the exterior region. The regions are connected along vertical boundaries B^+ at $x = x^+$, and B^- at $x = x^-$ as shown in Figure 1. Let κ be the wave number of the incident wave in the direction of propagation. Thus, κ should be one of the admissible real roots of the dispersion equation for off-axis propagation. Since the flaw extends to infinity in the y -direction, the scattered field must have the same wave number in the y -direction as the incident field. Thus, each of the scattered wave modes will have a constant wave number $\eta_0 (= \kappa \sin \phi^{in})$ in the negative y direction. Therefore, for time-harmonic waves, y and t variation can be factored out as

$$\begin{Bmatrix} u(x, y, z, t) \\ v(x, y, z, t) \\ w(x, y, z, t) \end{Bmatrix} = \begin{Bmatrix} \hat{u}(x, z) \\ \hat{v}(x, z) \\ \hat{w}(x, z) \end{Bmatrix} \exp[-j(\eta_0 y + \omega t)], \quad (1)$$

where ω is the circular frequency and $j = \sqrt{-1}$.

The procedure for finite element formulation for the interior region R is very similar to that for the plane strain case given in [Karunasena et al. 1991b]. The finite element representation of the interior region should include singular elements at crack tips if the flaw considered is a crack or a delamination. The standard discretization process in the finite element method leads to

$$\delta\{\bar{q}\}^T [S]\{q\} - \delta\{\bar{q}_B\}^T \{P_B\} = 0, \quad (2)$$

where

$$[S] = [K] - \omega^2[M], \quad (3)$$

in which $[K]$ and $[M]$ are, respectively, the global stiffness and mass matrices of the interior region, $\{q\}$ is the nodal displacement vector corresponding to interior nodes, and $\{q_B\}$ and $\{P_B\}$ are, respectively, the nodal displacement vector and the interaction force vector corresponding to the boundary nodes. δ implies first variation and overbar denotes complex conjugate.

The wave field in the exterior regions, R^+ and R^- , is the superposition of the wave fields due to the incident wave and the scattered waves. Using the wave function expansion procedure, the scattered wave field can be expressed in terms of the wave functions (that is, wave modes) supported by the free infinite composite plate with no flaws, and the unknown reflected and transmitted wave amplitudes. The theoretical details of the methodology adopted to obtain wave functions can be found in our work reported in [Karunasena et al. 1991c]. The procedure starts with dividing each layer into several sublayers. The exact dispersion relation of the infinite plate is developed using the propagator matrices as

$$f(\omega, k) = 0, \quad (4)$$

where k denotes the x -direction wave number of a typical wave mode. It is well known that the plate wave modes are dispersive, and at any given frequency ω there are only a finite number of propagating modes that carry energy away from a source of excitation or upon scattering from an inhomogeneity or flaw. However, in order to satisfy the boundary conditions at the source or at a boundary of discontinuity, it is necessary to include also the nonpropagating modes in the modal representation of the displacement field. The wave numbers (k) for the propagating and nonpropagating modes at a given frequency of excitation

can be found by solving the dispersion equation, Equation (4), for the plate. For each wave number k , the corresponding displacement wave function (which is a vector containing the x and z displacements at each sublayer level) can be determined using the propagator matrix for each sublayer. This has been discussed in the references cited above.

The solution to the scattering problem is obtained by imposing the continuity of total (incident plus scattered) displacements and tractions on the boundaries. This is achieved by substituting $\{q_B\}$ and $\{P_B\}$ from the wave function expansion into Equation (2). This leads to a system of linear equations that can be solved for the unknown reflected wave amplitudes (A_m^+) and transmitted amplitudes (A_m^-). These amplitudes are then used to obtain boundary nodal displacements and, in turn, to obtain interior nodal displacements. The reflection coefficient R_{pm} of the m th reflected mode, and transmission coefficient T_{pm} of the m th transmitted mode, due to the p th incident wave mode, are given by

$$R_{pm} = A_m^+ / A_p^{in}, \quad T_{pm} = \begin{cases} A_m^- / A_p^{in}, & \text{for } m \neq p \\ (A_p^{in} + A_m^-) / A_p^{in}, & \text{for } m = p \end{cases} \quad (5)$$

in which A_p^{in} is the amplitude of the incident wave mode. At this stage, numerical solution of all displacement and stress components for the scattered field and, hence for total field, is fully defined. Because the solution process involves numerous intricate computational steps, to check the accuracy of the numerical solution one can test satisfaction of the elastodynamic reciprocity relations developed in the next section.

2.3. Reciprocity relations. The reciprocity relations are derived from the elastodynamic reciprocity theorem [Achenbach 1973; Auld 1973], which may be written using the usual tensor notation in the absence of body forces, as

$$\oint_S (u_j^B \sigma_{jk}^A - u_j^A \sigma_{jk}^B) n_k dS = 0, \quad j, k = x, y, z, \quad (6)$$

where u_j^A and σ_{jk}^A represent the displacements and stresses corresponding to elastodynamic state A , while u_j^B and σ_{jk}^B are the displacements and stresses corresponding to elastodynamic state B in a region V bounded by a surface S . Wave fields corresponding to both elastodynamic states vary harmonically in time with circular frequency ω . When writing Equation (6), Einstein's summation convention of repeated indices has been assumed to hold, and the displacement components u , v , w , have been represented by u_x , u_y , u_z , respectively. In order to derive the reciprocity relations, the orthogonality relations among the wave modes have to be established first.

For convenience in derivation of orthogonality relations, a few notations are introduced first. Let the wave number pair (k_n, ζ_0) denote an admissible wave mode propagating in the first quadrant of the x - y plane in an infinite composite plate with no flaws. Herein, k_n represents the positive x direction wave number and ζ_0 (which is fixed) represents the positive y direction wave number as opposed to the definition of η_0 in Equation (1). Note that $\eta_0 = -\zeta_0$. In a similar manner, let the wave number pairs $(-k_n^*, \zeta_0)$, $(-k_n, -\zeta_0)$, and $(k_n^*, -\zeta_0)$ denote the wave modes corresponding to second, third, and fourth quadrants of the x - y plane, respectively. It should be mentioned here that if the (k_n, ζ_0) th wave mode is an admissible wave mode (of the dispersion relation of the plate), then the $(-k_n, -\zeta_0)$ th wave mode, which is propagating in the opposite direction, is also an admissible wave mode. Similarly, if the $(k_n^*, -\zeta_0)$ th wave mode is admissible, then the $(-k_n^*, \zeta_0)$ th wave mode is also admissible. This point can be explained by visualizing the configuration of the plate with respect to a new coordinate system that is

obtained after rotating the x, y axes by 180° about the z axis. However, when the (k_n, ζ_0) th wave mode is an admissible wave mode, the $(k_n, -\zeta_0)$ th wave mode is not necessarily an admissible wave mode. Due to this reason, a superscript star (*) has been introduced to the x -direction wave numbers of wave modes corresponding to second and fourth quadrants of the x - y plane. Note that the $(k_n, -\zeta_0)$ th wave mode is admissible when the fibers in each layer are aligned either in the x or y directions. This can be visualized by considering the mirror image of the plate with respect to the x - z plane.

The orthogonality relations are derived by applying the reciprocity theorem to the closed region V bounded by planes $z = 0, z = H, x = x_1, x = x_2, y = y_1,$ and $y = y_2$ where $x_1, x_2, y_1,$ and y_2 are coordinates chosen in such a way that $x_2 > x_1$ and $y_2 > y_1$. State A is taken to be the field due to the $(-k_n^*, \zeta_0)$ th wave mode, and state B is taken to be the field due to the $(k_m^*, -\zeta_0)$ th wave mode. The wave fields due to two states can be written as

$$\begin{aligned}
 u_j^A &\rightarrow A_{-n}^{*+} \{u_{-n}^{*+}\} \exp [j(-k_n^* x + \zeta_0 y)], \\
 \sigma_{jk}^A &\rightarrow A_{-n}^{*+} \left\{ \begin{matrix} \{\sigma_{-nx}^{*+}\}, \\ \{\sigma_{-ny}^{*+}\} \end{matrix} \right\} \exp [j(-k_n^* x + \zeta_0 y)], \\
 u_j^B &\rightarrow A_m^{*-} \{u_m^{*-}\} \exp [j(k_m^* x - \zeta_0 y)], \\
 \sigma_{jk}^B &\rightarrow A_m^{*-} \left\{ \begin{matrix} \{\sigma_{mx}^{*-}\}, \\ \{\sigma_{my}^{*-}\} \end{matrix} \right\} \exp [j(k_m^* x - \zeta_0 y)],
 \end{aligned}
 \tag{7}$$

where $A_{-n}^{*+}, \{u_{-n}^{*+}\}, \{\sigma_{-nx}^{*+}\}$ and $\{\sigma_{-ny}^{*+}\}$ represent the amplitude, displacement mode shape vector, mode shape vector of tractions on x face, and the mode shape vector of tractions on y face, respectively, for the $(-k_n^*, \zeta_0)$ th wave mode. $A_m^{*-}, \{u_m^{*-}\}, \{\sigma_{mx}^{*-}\},$ and $\{\sigma_{my}^{*-}\}$ represent the same quantities for the $(k_m^*, -\zeta_0)$ th wave mode. Application of the elastodynamic reciprocity theorem expressed in mathematical form in Equation (6) to the region V for states A and B defined in Equation (7) results in

$$\left\{ \exp [j(k_m^* - k_n^*) x_2] - \exp [j(k_m^* - k_n^*) x_1] \right\} I[(k_m^*, -\zeta_0); (-k_n^*, \zeta_0)] = 0,
 \tag{8}$$

where the notation $I[(k_m^*, -\zeta_0); (-k_n^*, \zeta_0)]$ has been used to represent the integral

$$\int_0^H (\{u_m^{*-}\}^T \{\sigma_{-nx}^{*+}\} - \{u_{-n}^{*+}\}^T \{\sigma_{mx}^{*-}\}) dz.$$

Since x_1 and x_2 are arbitrary, Equation (8) leads to the orthogonality relation

$$I[(k_m^*, -\zeta_0); (-k_n^*, \zeta_0)] = 0 \quad \text{for } k_m^* \neq k_n^*.
 \tag{9}$$

It should be noted that the net contributions from the surface integrals in Equation (6) on planes $y = y_1$ and $y = y_2$ amount to zero.

In a similar manner, choosing states A and B as the fields due to (k_n, ζ_0) th and $(-k_m, -\zeta_0)$ th wave modes, respectively, it can be shown that

$$I[(-k_m, -\zeta_0); (k_n, \zeta_0)] = 0 \quad \text{for } k_m \neq k_n.
 \tag{10}$$

Adopting a similar approach, the following orthogonality relations can be derived:

$$I[(k_m^*, -\zeta_0); (k_n, \zeta_0)] = 0, \quad (11)$$

$$I[(-k_m, -\zeta_0); (-k_n^*, \zeta_0)] = 0. \quad (12)$$

In order to derive reciprocity relations, region V is chosen as the region of the plate surrounding the flaw, and bounded by the planar surfaces $z = 0$, $z = H$, $x = x_3(x_3 \geq x^+)$, $x = x_4(x_4 \leq x^-)$, $y = y_1$, and $y = y_2$ (where y_1 and y_2 are arbitrary, and $y_2 > y_1$). The reciprocity relations among the reflection coefficients can be derived from Equation (6) by choosing state A as the total field due to the $(-k_n, -\zeta_0)$ th incident wave mode, and state B as the total field due to the (k_p^*, ζ_0) th incident wave mode. Let R_{nq} and T_{nq} denote the reflection and transmission coefficients, respectively, due to the $(-k_n, -\zeta_0)$ th incident wave mode, and R_{pm}^* and T_{pm}^* denote the same quantities due to the $(-k_p^*, \zeta_0)$ th incident wave mode. In view of the orthogonality relations given in Equations (9)–(12), the reciprocity relations become (after some algebraic manipulations)

$$R_{pn}^* \varsigma_n = R_{np} \varsigma_p^*, \quad (13)$$

where

$$\varsigma_n = \int_0^H (\{u_n^+\}^T \{\sigma_{-nx}^-\} - \{u_{-n}^-\}^T \{\sigma_{nx}^+\}) dz, \quad (14a)$$

$$\varsigma_p^* = \int_0^H (\{u_p^{*-}\}^T \{\sigma_{-px}^{*-}\} - \{u_{-p}^{*+}\}^T \{\sigma_{px}^{*-}\}) dz. \quad (14b)$$

In Equation (14), $\{u_n^+\}$, $\{u_{-n}^-\}$, $\{u_p^{*-}\}$, and $\{u_{-p}^{*+}\}$ denote the displacement mode shape vectors corresponding to (k_n, ζ_0) th, $(-k_n, -\zeta_0)$ th, $(k_p^*, -\zeta_0)$ th, and $(-k_p^*, \zeta_0)$ th wave modes, respectively, in an infinite plate with no flaw. The corresponding traction mode shape vectors on the x face are denoted by $\{\sigma_{nx}^+\}$, $\{\sigma_{-nx}^-\}$, $\{\sigma_{px}^{*-}\}$, and $\{\sigma_{-px}^{*-}\}$. It should be noted that the net contributions to the surface integral in Equation (6) from surfaces $y = y_1$ and $y = y_2$ becomes zero.

Applying the reciprocity theorem to the same region V , with state A as the total field due to the (k_n, ζ_0) th incident mode, and state B as the total field due to the $(-k_p, -\zeta_0)$ th incident mode, the reciprocity relation among the transmission coefficients can be derived as

$$T_{pn} \varsigma_n = T_{np} \varsigma_p, \quad (15)$$

where ς_p is given by Equation (14a) with n replaced by p . When deriving Equation (15), it has been assumed that the flaw geometry is symmetric with respect to the $x = 0$ plane. It can be shown that when the fibers in each layer are either in x or y direction, the reciprocity relation in Equation (13) degenerates into

$$R_{pn} \varsigma_n = R_{np} \varsigma_p. \quad (16)$$

It is well known that the scattered field consists of both propagating and evanescent (or nonpropagating) wave modes. Wave numbers corresponding to propagating modes have only a real part whereas wave numbers of evanescent modes are in general complex numbers. Reflected and transmitted energies are carried only by the propagating modes. The time-averaged value of the energy flux associated with the n th reflected propagating mode through the plate cross section due to the $(-k_p, -\zeta_0)$ th incident

propagating wave mode is given by

$$I_{pn}^+ = \frac{1}{2}\omega|A_p^{in}|^2|R_{pn}|^2(-j\zeta_n), \quad 1 \leq n \leq N_{pr}, \tag{17}$$

where N_{pr} is the number of propagating wave modes in the reflected wave field. For more information on derivation details of Equation (17), the reader is referred to [Karunasena et al. 1991b]. In a similar manner, the energy flux of the n th transmitted propagating wave mode and the incident wave mode can be written, respectively, as

$$I_{pn}^- = \frac{1}{2}\omega|A_p^{in}|^2|T_{pn}|^2(-j\zeta_n), \quad 1 \leq n \leq N_{pr} \tag{18}$$

$$I_p^{in} = \frac{1}{2}\omega|A_p^{in}|^2(-j\zeta_p). \tag{19}$$

Let E_{pn}^- be the proportion of energy of the $(-k_p, -\zeta_0)$ th incident propagating wave mode transferred into the n th transmitted propagating mode during the scattering process. Then

$$E_{pn}^- = \frac{I_{pn}^-}{I_p^{in}} = |T_{pn}|^2 \frac{\zeta_n}{\zeta_p}. \tag{20}$$

Similarly, if the incident wave mode is the $(-k_n, -\zeta_0)$ th propagating mode, then the proportion of energy transferred into the p th transmitted propagating mode can be expressed as

$$E_{np}^- = \frac{I_{np}^-}{I_n^{in}} = |T_{np}|^2 \frac{\zeta_p}{\zeta_n}. \tag{21}$$

In view of Equations (20) and (21), the reciprocity relation, Equation (15), for transmitted waves simplifies to

$$E_{pn}^- = E_{np}^-, \tag{22}$$

for arbitrary fiber directions in layers. Following a similar procedure, it can be shown that for the reflected waves the reciprocity relation in Equation (16) reduces to

$$E_{pn}^+ = E_{np}^+, \tag{23}$$

when fibers in layers are aligned with the global x, y directions. It is clear from Equations (20) and (21) that for the numerical computation of energy proportions we need to evaluate ζ_n in Equation (14a). $\{u_n^+\}$ and $\{\sigma_{nx}^+\}$ in Equation (14a) can be expressed in components form, respectively, as

$$\{u_n^+\} = \begin{Bmatrix} u_{xn}^+ \\ u_{yn}^+ \\ u_{zn}^+ \end{Bmatrix}, \quad \{\sigma_{nx}^+\} = \begin{Bmatrix} \sigma_{xxn}^+ \\ \sigma_{xyn}^+ \\ \sigma_{xzn}^+ \end{Bmatrix}. \tag{24}$$

It can be shown that $\{u_n^-\}$ and $\{\sigma_{-nx}^-\}$ are given by

$$\{u_n^-\} = \begin{Bmatrix} -u_{xn}^+ \\ -u_{yn}^+ \\ u_{zn}^+ \end{Bmatrix}, \quad \{\sigma_{-nx}^-\} = \begin{Bmatrix} \sigma_{xxn}^+ \\ \sigma_{xyn}^+ \\ -\sigma_{xzn}^+ \end{Bmatrix}. \tag{25}$$

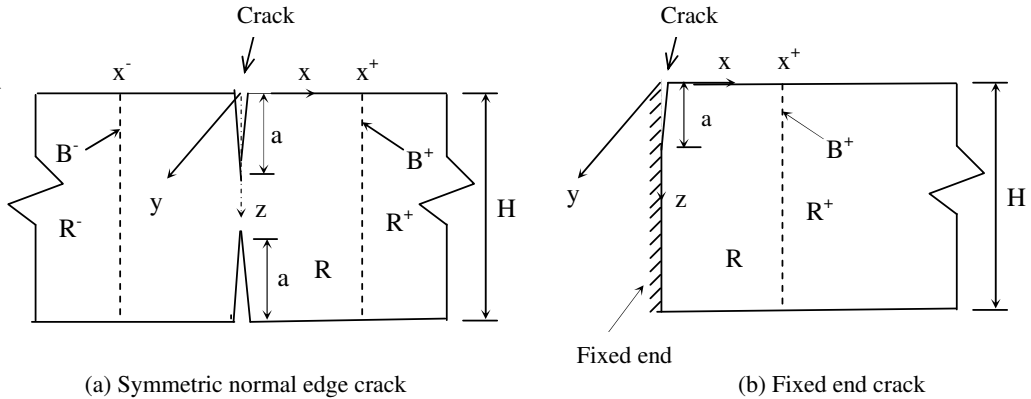


Figure 3. Geometry of the flaws for example problems.

In view of Equations (24) and (25), ζ_n reduces to

$$\zeta_n = 2 \int_0^H \{u_n^+\}^T \{\sigma_{-nx}^-\} dz. \tag{26}$$

After the dispersion relation in Equation (4) is solved for a given ω , the components of the displacement wave function $\{u_{-n}^-\}$ and stress wave function $\{\sigma_{-nx}^-\}$ for wave mode n at each sublayer interface can be determined using the propagator matrices. Then the integral in Equation (26) can be approximated as

$$\zeta_n = -2\{F_n\}^T \{q_n\}, \tag{27}$$

where $\{q_n\}$ is a displacement vector constructed from the displacement components at each sublayer interface and $\{F_n\}$ is a force vector constructed using the stress components at each sublayer interface. Now energy proportion terms in Equations (20) through (23) are fully defined and can be evaluated numerically using the scattering solution results.

3. Results and discussion

The simplified reciprocity relations derived in the previous section have been used to check the accuracy of four example scattering problems described below.

Example 1. Scattering by a thin symmetric normal edge crack in a unidirectional fiber-reinforced homogeneous graphite-epoxy plate. The geometry of the crack is as shown in Figure 3a.

Example 2. Scattering by a thin symmetric normal edge crack in an 8 layer graphite-epoxy plate with the stacking sequence of $0^\circ/90^\circ/0^\circ/90^\circ/90^\circ/0^\circ/90^\circ/0^\circ$. The geometry of the crack is the same as that shown in Figure 3a.

Example 3. Scattering by a thin crack located at the fixed-end of a homogeneous isotropic plate shown in Figure 3b.

Example 4. Scattering by a thin crack located at the fixed-end of a unidirectional fiber-reinforced homogeneous graphite-epoxy plate. The geometry of the crack is same as that shown in Figure 3b.

Lamina	C_{11}	C_{33}	C_{13}	C_{55}
0°	160.73	13.92	6.44	7.07
90°	13.92	13.92	6.92	3.50

Table 1. Elastic constants of graphite-epoxy lamina (in GPa).

The graphite-epoxy composite material in each layer of plates in Examples 1, 2 and 4 are considered to be transversely isotropic. The elastic constants (C_{ij}) for the transversely isotropic graphite-epoxy composite material are given in Table 1. More information on the C_{ij} constants and their relation to the stiffness matrix in Equation (3), and the procedure for their transformation from fiber direction to global x, y directions can be found in [Karunasena et al. 1991a]. The Poisson's ratio for the isotropic material in Example 3 is taken to be 0.25.

Numerical results from the hybrid method for the magnitudes of the reflection and the transmission coefficients ($|R_{pn}|$ and $|T_{pn}|$), and proportions of the reflected and the transmitted energies (E_{pn}^+ and E_{pn}^-) for Example 1 are presented in Table 2. The results correspond to a normalized frequency Ω (given by $\omega H / (2\sqrt{(C_{55}/\rho)_0})$, where ρ is the density of the graphite-epoxy composite) of 2.0 and a normalized crack length (given by $a/(0.5H)$) of 0.1 or 0.5 as given in Table 2. In this table, p and n denote the incident and the scattered wave mode numbers, respectively, and all the incident modes considered are symmetric modes. It should be noted that due to the symmetry of the problem with respect to the mid-plane of the plate, the scattered wave field consists of only symmetric or antisymmetric modes depending on whether the incident mode is a symmetric or an antisymmetric one. It can be seen from this table that the final form of the reciprocity relations among the proportions of energy as given in Equations (22) and (23) are satisfied with negligible errors. Also, it is seen that some reflection and transmission coefficients are quite sensitive to the orientation and depth of the crack, as well as the incident wave mode number. Although not shown here, our computations showed that coefficients are also sensitive to the incident mode frequency. Satisfaction of reciprocity relations can be taken as an indication of the accuracy of the scattering results.

Table 3 shows the scattering results for the 8 layer composite plate in Example 2 at a normalized frequency of 4 and at a normalized crack length of 0.5. The frequency normalization factor for this example is the same as that for Example 1. It is clearly seen that the reciprocity relations in Equations (22) and (23) are satisfied with negligible errors.

The proportion of reflected energy from scattering by the fixed end crack shown in Figure 2b are reported in Tables 4 and 5. Table 4 discusses the isotropic plate (Example 3) and Table 5 addresses a uniaxially fiber-reinforced plate (Example 4). Note that minor modifications to the theory presented in the previous section are required for this problem because the exterior region has only one region which consists of the reflected wave field. The reciprocity relation in Equation (22) does not apply for this fixed end crack scattering problem because there is no transmitted field. The reciprocity relation for the reflected wave modes is given by Equation (23).

For Example 3, the results in Table 4 correspond to a normalized frequency Ω of $3.5\sqrt{3}$, where Ω is given by $\omega H / (2\sqrt{\mu/\rho})$, ρ is the density and μ is the shear modulus of the plate. Five different crack

lengths have been considered. At this frequency ($\Omega = 3.5\sqrt{3}$), the dispersion relation in Equation (4) has three symmetric propagating modes (denoted as 1S, 2S and 3S in Table 4) and four antisymmetric modes (usually denoted as 1A, 2A, 3A and 4A). It is seen from Table 4 that the reciprocity relations among the reflected modes as given in Equation (23) are satisfied with reasonable accuracy for the five different crack lengths considered. In this table, a normalized crack length of 0.0 and 2.0 represent, respectively, the full reflection by a fixed end and reflection by a free end (that is, a crack right through the full thickness of the plate).

For Example 4, the results in Table 5 correspond to a normalized frequency Ω of 6.0. The frequency normalization factor for this example is same as that for Example 1. As in Example 3, five different

p	k_p	$a/(0.5H)$	n	E_{pn}^+	E_{pn}^-	$ R_{pn} $	$ T_{pn} $
1	1.440	0.1	1	0.002	0.993	0.044	0.996
			2	0.001	0.001	0.051	0.048
		0.5	1	0.009	0.821	0.095	0.906
			2	0.127	0.042	0.718	0.409
2	0.324	0.1	1	0.001	0.001	0.012	0.012
			2	0.000	0.999	0.011	0.999
		0.5	1	0.128	0.041	0.178	0.101
			2	0.070	0.760	0.264	0.872
(a) $\theta = 0^\circ$, $\phi^{in} = 45^\circ$, $\eta_0 = 1.440$							
1	1.882	0.1	1	0.000	0.998	0.009	0.999
			2	0.000	0.000	0.062	0.033
		0.5	1	0.002	0.833	0.105	0.913
			2	0.081	0.082	1.357	0.632
2	0.813	0.1	1	0.000	0.000	0.014	0.007
			2	0.000	1.000	0.009	1.000
		0.5	1	0.000	0.082	0.024	0.129
			2	0.075	0.842	0.590	0.918
(b) $\theta = 22.5^\circ$, $\phi^{in} = 22.5^\circ$, $\eta_0 = 0.780$							

Table 2. Scattering results for Example 1 when $\Omega = 2$. p and n denote the incident and scattered wave mode numbers, respectively. Symmetric incident wave modes have been considered.

p	k_p	n	E_{pn}^+	E_{pn}^-	$ R_{pn} $	$ T_{pn} $
1	3.362	1	0.706	0.180	0.840	0.424
		2	0.007	0.108	0.143	0.571
2	0.662	1	0.007	0.108	0.047	0.189
		2	0.543	0.340	0.737	0.583

Table 3. Scattering results for [Example 2](#) when $\Omega = 4$, $a/(0.5H) = 0.5$, θ for 0° lamina = 0° , $\phi^{in} = 45^\circ$, and $\eta_0 = 3.362$.

crack lengths have been considered. At Ω equal to 6.0, the dispersion relation for the uniaxially fiber-reinforced plate has three symmetric propagating modes (denoted as 1S, 2S and 3S in [Table 5](#)) and four antisymmetric modes (denoted as 1A, 2A, 3A and 4A). As in the previous example of scattering problems considered in this paper, it is seen from [Table 5](#) that the reciprocity relations among the proportions of energy in reflected modes are satisfied with reasonable accuracy for all crack lengths considered.

4. Conclusion

By using the classical elastodynamic reciprocity theorem, simplified forms of elastodynamic reciprocity relations applicable to guided wave scattering by flaws in fiber-reinforced composite plates have been developed in this work. These relations are useful when developing ultrasonic nondestructive assessment techniques for flaw characterization in composite structures. A hybrid method combining the finite element method with a wave function expansion procedure has been used to solve the wave scattering problem. The derivation has been presented for a plate with an arbitrary stacking sequence where each ply can have an arbitrary fiber direction. As the scattered field is expressed in wave function expansion, an arbitrary number of layers and thicknesses can be studied without appreciable increase in computational time. Numerical results verifying the derived reciprocity relations have been presented for four example scattering problems – two of them involving scattering by a symmetric normal edge crack in a unidirectional fiber-reinforced composite plate and in an 8-layer cross-ply plate, and other two involving scattering by a fixed-end crack in an isotropic plate and in a unidirectional fiber-reinforced composite plate.

References

- [Achenbach 1973] J. D. Achenbach, *Wave propagation in elastic solids*, North Holland, Amsterdam, 1973.
- [Auld 1973] B. A. Auld, *Acoustic fields and waves in solids*, vol. 2, Wiley-Interscience, New York, 1973.
- [Bakis et al. 2002] C. E. Bakis, L. C. Bank, V. L. Brown, E. Cosenza, J. F. Davalos, J. J. Lesko, A. Machida, S. H. Rizkalla, and T. C. Triantafillou, “Fiber-reinforced polymer composites for construction: State-of-the-art review”, *J. Compos. Constr. (ASCE)* **6:2** (2002), 73–87.
- [Chimenti 1997] D. E. Chimenti, “Guided waves in plates and their use in material characterization”, *Appl. Mech. Rev.* **50** (1997), 247–284.
- [Datta 2000] S. K. Datta, “Wave propagation in composite plates and shells”, Chapter 18, pp. 511–558 in *Comprehensive composite materials*, 1st ed., vol. 1, edited by T.-W. Chou et al., Elsevier, Amsterdam, 2000.

p, n	E_{pn}^+	$a/(0.5 H)$				
		0.0	0.5	1.0	1.5	2.0
$p = 1 = 1S, n = 2 = 2S$	E_{12}^+	0.034	0.075	0.035	0.089	0.109
$P = 2 = 2S, n = 1 = 1S$	E_{21}^+	0.035	0.075	0.035	0.089	0.109
$p = 1 = 1S, n = 3 = 3S$	E_{13}^+	0.230	0.083	0.059	0.039	0.304
$P = 3 = 3S, n = 1 = 1S$	E_{31}^+	0.230	0.083	0.059	0.039	0.303
$p = 1 = 1S, n = 4 = 1A$	E_{14}^+	0.000	0.353	0.170	0.079	0.000
$P = 4 = 1A, n = 1 = 1S$	E_{41}^+	0.000	0.354	0.171	0.081	0.000
$p = 1 = 1S, n = 5 = 2A$	E_{15}^+	0.000	0.030	0.090	0.074	0.000
$P = 5 = 2A, n = 1 = 1S$	E_{51}^+	0.000	0.030	0.090	0.075	0.000
$p = 1 = 1S, n = 6 = 3A$	E_{16}^+	0.000	0.129	0.167	0.213	0.000
$P = 6 = 3A, n = 1 = 1S$	E_{61}^+	0.000	0.129	0.168	0.213	0.000
$p = 1 = 1S, n = 7 = 4A$	E_{17}^+	0.000	0.202	0.368	0.275	0.000
$P = 7 = 4A, n = 1 = 1S$	E_{71}^+	0.000	0.203	0.369	0.277	0.000
$p = 2 = 2S, n = 3 = 3S$	E_{23}^+	0.043	0.053	0.104	0.112	0.022
$P = 3 = 3S, n = 2 = 2S$	E_{32}^+	0.043	0.054	0.105	0.113	0.022
$p = 2 = 2S, n = 4 = 1A$	E_{24}^+	0.000	0.126	0.004	0.013	0.000
$P = 4 = 1A, n = 2 = 2S$	E_{42}^+	0.000	0.126	0.005	0.014	0.000
$p = 2 = 2S, n = 5 = 2A$	E_{25}^+	0.000	0.079	0.057	0.070	0.000
$P = 5 = 2A, n = 2 = 2S$	E_{52}^+	0.000	0.079	0.057	0.070	0.000
$p = 2 = 2S, n = 6 = 3A$	E_{26}^+	0.000	0.622	0.698	0.516	0.000
$P = 6 = 3A, n = 2 = 2S$	E_{62}^+	0.000	0.621	0.698	0.516	0.000
$p = 2 = 2S, n = 7 = 4A$	E_{27}^+	0.000	0.018	0.080	0.075	0.000
$P = 7 = 4A, n = 2 = 2S$	E_{72}^+	0.000	0.018	0.080	0.075	0.000
$p = 3 = 3S, n = 4 = 1A$	E_{34}^+	0.000	0.027	0.006	0.032	0.000
$P = 4 = 1A, n = 3 = 3S$	E_{43}^+	0.000	0.027	0.006	0.032	0.000
$p = 3 = 3S, n = 5 = 2A$	E_{35}^+	0.000	0.015	0.366	0.019	0.000
$P = 5 = 2A, n = 3 = 3S$	E_{53}^+	0.000	0.015	0.364	0.019	0.000
$p = 3 = 3S, n = 6 = 3A$	E_{36}^+	0.000	0.068	0.020	0.094	0.000
$P = 6 = 3A, n = 3 = 3S$	E_{63}^+	0.000	0.067	0.019	0.093	0.000
$p = 3 = 3S, n = 7 = 4A$	E_{37}^+	0.000	0.007	0.187	0.008	0.000
$P = 7 = 4A, n = 3 = 3S$	E_{73}^+	0.000	0.007	0.187	0.008	0.000

Table 4. Reflected energy proportions E_{pn}^+ for [Example 3](#) for different crack lengths when $\Omega = 3.5\sqrt{3}$, $\theta = 0^\circ$, $\phi^{in} = 0^\circ$, $\eta_0 = 0$. S and A denote symmetric and antisymmetric modes, respectively.

Table 4 (cont'd)						
$p = 4 = 1A, n = 5 = 2A$	E_{45}^+	0.063	0.136	0.244	0.407	0.069
$P = 5 = 2A, n = 4 = 1A$	E_{54}^+	0.063	0.136	0.245	0.407	0.070
$p = 4 = 1A, n = 6 = 3A$	E_{46}^+	0.051	0.020	0.074	0.165	0.348
$P = 6 = 3A, n = 4 = 1A$	E_{64}^+	0.051	0.020	0.074	0.163	0.348
$p = 4 = 1A, n = 7 = 4A$	E_{47}^+	0.132	0.010	0.169	0.181	0.093
$P = 7 = 4A, n = 4 = 1A$	E_{74}^+	0.133	0.010	0.169	0.178	0.093
$p = 5 = 2A, n = 6 = 3A$	E_{56}^+	0.159	0.039	0.011	0.002	0.017
$P = 6 = 3A, n = 5 = 2A$	E_{65}^+	0.158	0.039	0.011	0.002	0.017
$p = 5 = 2A, n = 7 = 4A$	E_{57}^+	0.766	0.568	0.084	0.425	0.900
$P = 7 = 4A, n = 5 = 2A$	E_{75}^+	0.766	0.568	0.083	0.421	0.897
$p = 6 = 3A, n = 7 = 4A$	E_{67}^+	0.077	0.116	0.026	0.012	0.005
$P = 7 = 4A, n = 6 = 3A$	E_{76}^+	0.078	0.116	0.026	0.013	0.005

Table 4. (Continued from previous page.)

[Karunasena 2004] W. Karunasena, "Numerical modeling of obliquely incident guided wave scattering by a crack in a laminated composite plate", pp. 181–187 in *Structural integrity and fracture: Proceedings of the international conference, SIF2004* (Brisbane), edited by A. Atrens et al., Australian Fracture Group, Brisbane, 2004.

[Karunasena et al. 1991a] W. M. Karunasena, R. L. Bratton, A. H. Shah, and S. K. Datta, "Elastic wave propagation in laminated composite plates", *J. Eng. Mater. Technol. (ASME)* **113**:4 (1991), 411–418.

[Karunasena et al. 1991b] W. M. Karunasena, A. H. Shah, and S. K. Datta, "Plane-strain-wave scattering by cracks in laminated composite plates", *J. Eng. Mech. (ASCE)* **117**:8 (1991), 1738–1754.

[Karunasena et al. 1991c] W. M. Karunasena, A. H. Shah, and S. K. Datta, "Reflection of plane strain waves at the free edge of a laminated composite plate", *Int. J. Solids Struct.* **27**:8 (1991), 949–964.

Received 29 May 2007. Revised 29 Aug 2007. Accepted 10 Oct 2007.

WARNA KARUNASENA: Karu.Karunasena@usq.edu.au

Faculty of Engineering and Surveying, University of Southern Queensland, Toowoomba, Queensland 4350, Australia

p, n	E_{pn}^+	$a/(0.5 H)$				
		0.0	0.5	1.0	1.5	2.0
$p = 1 = 1S, n = 2 = 2S$	E_{12}^+	0.000	0.033	0.001	0.013	0.014
$P = 2 = 2S, n = 1 = 1S$	E_{21}^+	0.000	0.032	0.001	0.014	0.014
$p = 1 = 1S, n = 3 = 3S$	E_{13}^+	0.014	0.001	0.038	0.006	0.219
$P = 3 = 3S, n = 1 = 1S$	E_{31}^+	0.014	0.001	0.040	0.006	0.224
$p = 1 = 1S, n = 4 = 1A$	E_{14}^+	0.000	0.556	0.567	0.506	0.000
$P = 4 = 1A, n = 1 = 1S$	E_{41}^+	0.000	0.556	0.557	0.513	0.000
$p = 1 = 1S, n = 5 = 2A$	E_{15}^+	0.000	0.288	0.170	0.174	0.000
$P = 5 = 2A, n = 1 = 1S$	E_{51}^+	0.000	0.283	0.176	0.173	0.000
$p = 1 = 1S, n = 6 = 3A$	E_{16}^+	0.000	0.023	0.004	0.020	0.000
$P = 6 = 3A, n = 1 = 1S$	E_{61}^+	0.000	0.024	0.004	0.021	0.000
$p = 1 = 1S, n = 7 = 4A$	E_{17}^+	0.000	0.050	0.158	0.226	0.000
$P = 7 = 4A, n = 1 = 1S$	E_{71}^+	0.000	0.051	0.163	0.230	0.000
$p = 2 = 2S, n = 3 = 3S$	E_{23}^+	0.004	0.151	0.006	0.138	0.009
$P = 3 = 3S, n = 2 = 2S$	E_{32}^+	0.004	0.150	0.006	0.137	0.009
$p = 2 = 2S, n = 4 = 1A$	E_{24}^+	0.000	0.020	0.006	0.016	0.000
$P = 4 = 1A, n = 2 = 2S$	E_{42}^+	0.000	0.020	0.006	0.016	0.000
$p = 2 = 2S, n = 5 = 2A$	E_{25}^+	0.000	0.004	0.027	0.007	0.000
$P = 5 = 2A, n = 2 = 2S$	E_{52}^+	0.000	0.004	0.027	0.007	0.000
$p = 2 = 2S, n = 6 = 3A$	E_{26}^+	0.000	0.631	0.916	0.729	0.000
$P = 6 = 3A, n = 2 = 2S$	E_{62}^+	0.000	0.631	0.916	0.728	0.000
$p = 2 = 2S, n = 7 = 4A$	E_{27}^+	0.000	0.078	0.044	0.049	0.000
$P = 7 = 4A, n = 2 = 2S$	E_{72}^+	0.000	0.078	0.044	0.048	0.000
$p = 3 = 3S, n = 4 = 1A$	E_{34}^+	0.000	0.018	0.019	0.026	0.000
$P = 4 = 1A, n = 3 = 3S$	E_{43}^+	0.000	0.017	0.017	0.027	0.000
$p = 3 = 3S, n = 5 = 2A$	E_{35}^+	0.000	0.006	0.213	0.011	0.000
$P = 5 = 2A, n = 3 = 3S$	E_{53}^+	0.000	0.006	0.212	0.011	0.000
$p = 3 = 3S, n = 6 = 3A$	E_{36}^+	0.000	0.188	0.055	0.147	0.000
$P = 6 = 3A, n = 3 = 3S$	E_{63}^+	0.000	0.189	0.056	0.148	0.000
$p = 3 = 3S, n = 7 = 4A$	E_{37}^+	0.000	0.027	0.598	0.021	0.000
$P = 7 = 4A, n = 3 = 3S$	E_{73}^+	0.000	0.027	0.596	0.021	0.000

Table 5. Reflected energy proportions E_{pn}^+ for [Example 4](#) for different crack lengths when $\Omega = 6.0$, $\theta = 0^\circ$, $\phi^{in} = 0^\circ$, $\eta_0 = 0$. S and A denote symmetric and antisymmetric modes, respectively.

Table 5 (cont'd)						
$p = 4 = 1A, n = 5 = 2A$	E_{45}^+	0.003	0.219	0.266	0.280	0.029
$P = 5 = 2A, n = 4 = 1A$	E_{54}^+	0.003	0.218	0.267	0.278	0.029
$p = 4 = 1A, n = 6 = 3A$	E_{46}^+	0.001	0.010	0.015	0.009	0.054
$P = 6 = 3A, n = 4 = 1A$	E_{64}^+	0.001	0.010	0.015	0.009	0.054
$p = 4 = 1A, n = 7 = 4A$	E_{47}^+	0.003	0.021	0.072	0.001	0.064
$P = 7 = 4A, n = 4 = 1A$	E_{74}^+	0.003	0.021	0.075	0.001	0.064
$p = 5 = 2A, n = 6 = 3A$	E_{56}^+	0.026	0.041	0.009	0.043	0.016
$P = 6 = 3A, n = 5 = 2A$	E_{65}^+	0.026	0.040	0.009	0.043	0.016
$p = 5 = 2A, n = 7 = 4A$	E_{57}^+	0.049	0.020	0.119	0.387	0.451
$P = 7 = 4A, n = 5 = 2A$	E_{75}^+	0.051	0.021	0.119	0.389	0.452
$p = 6 = 3A, n = 7 = 4A$	E_{67}^+	0.000	0.093	0.000	0.046	0.000
$P = 7 = 4A, n = 6 = 3A$	E_{76}^+	0.000	0.093	0.000	0.045	0.000

Table 5. (Continued from previous page.)

SIMULATIONS OF MICRO AND NANOINDENTATIONS

ZISHUN LIU, SOMSAK SWADDIWUDHIPONG AND QINGXIANG PEI

The paper reviews recent research and developments on simulated indentation tests at micron and nanometer levels. For indentation at the maximum depth of several microns or hundreds of nanometer, classical continuum plasticity framework incorporating Taylor dislocation model via strain gradient plasticity embedded in the constitutive equation may be adopted to take care of the size effect. As higher-order stress components and higher-order continuity requirements can be made redundant, only C^0 finite elements incorporating strain gradient plasticity have to be formulated. This results in the significant ease and convenience in finite element implementation requiring minimal additional computational effort and resources. Alternatively, when the indentation depth is lower at nanometer level, either a large scale molecular dynamics model or a hybrid finite element and molecular dynamics simulation has to be adopted. The article includes certain results from the former approach on nanoindentation based on combination of both Morse potential and embedded-atom model potential.

1. Introduction

Numerous experiments including indentation tests [Stelmashenko et al. 1993], twisting of copper wires of micron diameters [Fleck and Hutchinson 1993], fracture toughness tests [Elsner et al. 1994] and microbend tests [Haque and Saif 2003] have demonstrated a strong size effect when the material and deformation length scales are of the same order at micron and submicron levels. Classical continuum mechanics ceases to be valid at this range of deformation. Based on the Taylor [1934] dislocation model (see also [Toupin 1962]), Fleck et al. [1994] proposed the phenomenological theory of strain gradient plasticity. Gao et al. [1999] and Huang et al. [2000] presented a multiscale framework for constructing the mesoscale constitutive laws taking into account the microscale plasticity based on Taylor's work hardening relation. Higher-order stress components, additional governing equations and boundary conditions are required in the formulation, requiring significantly greater formulation and computational efforts. Huang et al. [2004] proposed the conventional mechanism-based strain gradient (CMSG) plasticity theory without involving the higher-order stress components. The approach is appealing as only C^0 continuity is required in the finite element formulation. The concept was adopted by Swaddiwudhipong et al. [2005; 2006a; 2006b] to establish solid, axisymmetric and plane finite elements to simulate Berkovich and conical indentation tests at micron and submicron levels and fracture behavior of elastoplastic materials with strain hardening. In this study, both C^0 solid and axisymmetric finite elements are adopted to demonstrate the necessity of incorporating strain gradient plasticity in the simulation of Berkovich and conical indentation tests at submicron level respectively. The effect of friction at contact surfaces is

Keywords: C^0 finite element, indentation test, molecular dynamics simulation, size effect, strain gradient plasticity.

The supports from the Singapore Ministry of Education's AcRF Tier 1 Funds through grants R-214-000-165-112 and R-214-000-186-112 are greatly appreciated.

also considered in the present numerical model. The results obtained from finite element analyses with and without the strain gradient plasticity including both friction and smooth surfaces are presented and compared.

Molecular dynamics (MD) model is effective in the simulation of behavior of nanostructures, offering the insights into the microscopic properties of materials. MD simulation has recently been used to investigate various aspects of nanomechanics of materials including wear, fracture and characterization of materials at nanometer level. It has been shown that MD simulations can provide a qualitative analysis of discrete plasticity events that are consistent with experimental observations of nanoindentation in single crystals. The approach has become a favorite tool for investigating the physical properties of nano materials at an atomic level [Fang et al. 2001; 2006]. In this study, nanoindentation experiments are simulated using MD simulation adopting embedded-atom model (EAM) potential for target materials and Morse potential for both diamond indenter and interaction between target and indenter materials. The paper covers the mechanisms of nanoindentation on single crystalline substrate using MD simulation. The large scale model is developed for substrate materials in the present MD simulation. Compared with results reported earlier in the literature, the values presented in this article should be less affected by boundary influence.

2. Strain gradient plasticity

The flow stress with Taylor hardening model and the material length scale l for typical values of $M = 3.06$ and $\bar{r} = 1.90$ can be expressed as

$$\sigma_t = \sigma_y \sqrt{f^2(\varepsilon^p) + l\eta^p}, \quad l = \bar{r}b \left(\frac{M\alpha\mu}{\sigma_y} \right)^2 = 18b \left(\frac{\alpha\mu}{\sigma_y} \right)^2,$$

where σ_y is the yield stress, $f(\varepsilon^p)$ represents the stress and plastic strain relation in uniaxial tension, η^p implies the effective plastic strain gradient, \bar{r} is the Nye [1953] factor, M is the Taylor factor, b indicates the magnitude of Burgers vector, μ represents the shear modulus and α is an empirical constant, the value of which varies from 0.2–0.5 depending on the material structures. Based on models of geometrically necessary dislocations associated with the in-plane bending, the torsion of a rod and the spherical or axisymmetric void growth, Gao et al. [1999] expressed the effective plastic strain gradient as

$$\eta^p = \frac{1}{2} \sqrt{\eta_{ijk}^p \eta_{ijk}^p},$$

where $\eta_{ijk}^p = \varepsilon_{ik,j}^p + \varepsilon_{jk,i}^p - \varepsilon_{ij,k}^p$, with the comma (,) in subscripts indicating the differentiation with respect to the index which follows. ε_{ij}^p is the plastic strain tensor $\varepsilon_{ij}^p = \int \dot{\varepsilon}_{ij}^p dt$, where the dot in superscripts implies time derivative. Huang et al. [2004] showed that the constitutive relation for materials with strain gradient plasticity can be expressed as

$$\dot{\sigma}_{ij} = K \dot{\varepsilon}_{kk} \delta_{ij} + 2\mu \left(\dot{\varepsilon}'_{ij} - \frac{3\dot{\varepsilon}}{2\sigma_e} \left(\frac{\sigma_e}{\sigma_f} \right)^m \sigma'_{ij} \right), \quad (2-1)$$

where σ_e is the von Mises effective stress and m is the rate-sensitive exponent. Equation (2-1) degenerates to the constitutive relation for materials with power law hardening when m is large, say $m \geq 20$ as shown earlier in [Huang et al. 2004]. It is interesting to note that higher-order stress components are not

explicitly present in the constitutive relation (2-1) though strain gradient plasticity has been incorporated. This approach facilitates the adoption of conventional continuum mechanic algorithms which are readily available to be employed with minor alterations. Hence, the order of continuity requirement for the finite element model can be reduced from C^1 to C^0 level. This provides a substantial simplification in the formulation and implementation of this powerful numerical tool, resulting in minimal additional computational resources and effort. Though higher-order stress theory is normally required in mechanism-based strain gradient (MSG) plasticity, it was shown in [Shi et al. 2001; Huang et al. 2004] that the results based on CMSG plasticity are practically identical to those on MSG in most part of the domain except in the thin layers near the boundary. As the CMSG framework is much less demanding than the higher-order stress theory, the former serves as an efficient alternative approach producing results without any significant loss of accuracy.

3. Effective strain gradient

The strain gradient tensor of third-order η and the displacement vector u are expressed as

$$\eta = \nabla \nabla u, \quad u = \sum_i u_i \tilde{e}_i,$$

where \tilde{e}_i is the unit vector in the i -th direction. The expressions for effective strain gradient plasticity in Cartesian coordinate system are standard and hence not given herein. The components for axisymmetric case were derived in [Swaddiwudhipong et al. 2006b]:

$$\begin{aligned} \eta'_{rrr} &= \frac{1}{2}\eta_{rrr} - \frac{1}{2}(\eta_{rtt} + \eta_{rzz}) = \frac{1}{2}u_{rcrr} - \frac{1}{2}\left(\left(\frac{u_{rcr}}{r} - \frac{u_{rr}}{r^2}\right) + u_{zczz}\right), \\ \eta'_{rrz} &= \eta_{rrz} = u_{zcrr}, \quad \eta'_{zrz} = \eta_{zrz} = u_{rczz}, \\ \eta'_{ritt} &= \eta'_{trt} = \frac{3}{4}\eta_{ritt} - \frac{1}{4}(\eta_{rrr} + \eta_{rzz}) = \frac{3}{4}\left(\frac{u_{rcr}}{r} - \frac{u_{rr}}{r^2}\right) - \frac{1}{4}(u_{rcrr} + u_{zczz}), \\ \eta'_{rzz} &= \eta'_{zrz} = \frac{3}{4}\eta_{rzz} - \frac{1}{4}(\eta_{rtt} + \eta_{zzz}) = \frac{3}{4}u_{rczr} - \frac{1}{4}\left(\frac{u_{rcz}}{r} + u_{zczz}\right), \\ \eta'_{rzz} &= \eta'_{zrz} = \frac{3}{4}\eta_{rzz} - \frac{1}{4}(\eta_{rrr} + \eta_{rtt}) = \frac{3}{4}u_{zczz} - \frac{1}{4}\left(u_{rcrr} + \left(\frac{u_{rcr}}{r} - \frac{u_{rr}}{r^2}\right)\right), \\ \eta'_{tir} &= \eta_{tir} = \frac{u_{rcr}}{r} - \frac{u_{rr}}{r^2}, \quad \eta'_{tiz} = \eta_{tiz} = \frac{u_{zcr}}{r}, \\ \eta'_{tzt} &= \eta'_{ztt} = \frac{3}{4}\eta_{tzt} - \frac{1}{4}(\eta_{zrr} + \eta_{zzz}) = \frac{3}{4}\frac{u_{rcz}}{r} - \frac{1}{4}(u_{rcrz} + u_{zczz}), \\ \eta'_{zzz} &= \frac{1}{2}\eta_{zzz} - \frac{1}{2}(\eta_{zrr} + \eta_{ztt}) = \frac{1}{2}u_{zczz} - \frac{1}{2}\left(u_{rcrz} + \frac{u_{rcz}}{r}\right), \end{aligned}$$

where subscript r, θ and z denote orthogonal cylindrical coordinates.

4. C^0 elements with strain gradient plasticity

The coordinates of C^0 solid elements are usually expressed as

$$x = \sum_{i=1}^n N_i(g, h, r) x_i, \quad y = \sum_{i=1}^n N_i(g, h, r) y_i, \quad z = \sum_{i=1}^n N_i(g, h, r) z_i,$$

and the displacements of C^0 solid elements are usually expressed as

$$u = \sum_{i=1}^n N_i(g, h, r) u_i, \quad v = \sum_{i=1}^n N_i(g, h, r) v_i, \quad w = \sum_{i=1}^n N_i(g, h, r) w_i,$$

and the Jacobian matrix which is essential for the transformation of coordinates is obtained from

$$J = \frac{\partial(x, y, z)}{\partial(g, h, r)} = \begin{pmatrix} x_{,g} & x_{,h} & x_{,r} \\ y_{,g} & y_{,h} & y_{,r} \\ z_{,g} & z_{,h} & z_{,r} \end{pmatrix}.$$

In each element, n is the number of nodes; x_i, y_i, z_i and u_i, v_i, w_i are the nodal coordinates and nodal displacement components in the x, y and z directions respectively while g, h and r are the corresponding natural coordinates.

The derivative of the strain vector with respect to x is given by

$$\{\varepsilon\}_{,x} = \left(\frac{\partial^2 u}{\partial x^2}, \frac{\partial^2 v}{\partial y \partial x}, \frac{\partial^2 w}{\partial y \partial x}, \frac{\partial^2 u}{\partial y \partial x} + \frac{\partial^2 v}{\partial x^2}, \frac{\partial^2 v}{\partial z \partial x} + \frac{\partial^2 w}{\partial y \partial x}, \frac{\partial^2 w}{\partial x^2} + \frac{\partial^2 u}{\partial z \partial x} \right)^T = [B]_{,x} \{\delta\},$$

while the coordinate transformation of the derivatives of finite element displacement functions of the actual and master elements is stipulated by

$$\frac{\partial(N_{i,x}, N_{i,y}, N_{i,z})}{\partial(x, y, z)} = (J^{-1})^T \frac{\partial(N_{i,g}, N_{i,h}, N_{i,r})}{\partial(g, h, r)} J^{-1}.$$

Details of the derivation were presented earlier in [Swaddiwudhipong et al. 2005]. Similar derivations of strain gradient measures and coordinate transformation for axisymmetric and plane elements are presented in [Swaddiwudhipong et al. 2006b; 2006a], respectively. The concept is implemented as a user subroutine in a commercial finite element package, ABAQUS [ABAQUS 2002].

5. Molecular dynamics simulation

In this study, the standard MD technology as described in details in [Rapaport 2004] is used to simulate the motion of the atoms of the materials. Equations of motions are integrated using Verlet method. In MD simulations, the force acting on an individual atom is obtained by summing up the forces contributed by the surrounding atoms. The interatomic forces are calculated from the potential energy function U :

$$\mathbf{f}_i = -\nabla U(\mathbf{r}_1, \mathbf{r}_2, \dots, \mathbf{r}_N).$$

The main problem for modeling the material in MD simulations is to find a suitable potential function $U(\mathbf{r}_1, \mathbf{r}_2, \dots, \mathbf{r}_N)$. The pair potential is relatively simple and computational inexpensive, but it is less accurate compared to the embedded-atom model (EAM) potential. The EAM potential is based upon the recognition that the cohesive energy of a metal is governed not only by the pairwise potential of the nearest neighbor atoms, but also by the embedding energy related to the electron sea in which the atoms are embedded. The total energy E_{tot} which can be written as a unique function of the electron density r_{ij} is mainly the energy to embed the atoms into the electron sea of the neighboring atoms,

and supplemented by a short-range doubly screened pair interaction, which accounts for the core-core repulsions. Consequently, the total atomic potential energy of a system [Pei et al. 2006] is given by

$$E_{tot} = \frac{1}{2} \sum_{i,j} \Phi_{ij}(r_{ij}) + \sum_i F_i(\bar{\rho}_i),$$

where Φ_{ij} is the pair-interaction energy between the i -th and the j -th atoms, F_i represents the embedding energy of atom i , and $\bar{\rho}_i$ indicates the host electron density at site i induced by all other atoms in the system. In this paper, the EAM potential is used for the atomic interaction among the nickel (Ni) atoms of the target substrate materials. The Morse potential is, however, adopted for the interaction between the atoms of nickel substrate and those of diamond indenter. The Morse type pair potential is given by

$$\phi(r_{ij}) = D(e^{-2\beta(r_{ij}-r_0)} - 2e^{-\beta(r_{ij}-r_0)}),$$

where $\phi(r_{ij})$ is the pair potential energy function, D is the cohesion energy, β represents the elastic modulus, and r_{ij} and r_0 are the instantaneous and equilibrium distances between atoms i and j , respectively. The Morse potential is also employed for the interaction among the atoms of the diamond indenter. The latter is usually assumed as a rigid body since the diamond is substantially harder than the nickel substrate. This implies that the interactive forces among the indenter atoms have no bearing on the accuracy of the simulated force results.

6. Numerical examples

6A. Simulation of indentation at micron level via finite elements with strain gradient plasticity. Both conventional finite elements and those incorporating mechanism-based strain gradient plasticity are employed by Pethica et al. [1983] to simulate the Berkovich indentation on electropolished nickel. The following material properties adopted earlier in [Bhattacharya and Nix 1988] to simulate this test are employed in the study. The Young's modulus of elasticity $E = 207$ GPa, the yield strength $Y = 350$ MPa, $n = 0.03$ in the power law, and the Poisson's ratio $\nu = 0.33$. The friction coefficient of 0.15 which is typical for contact surfaces of metallic materials and diamond indenter is adopted in the analyses. The intrinsic material length scale of 5 micron for nickel as stipulated in [Wang et al. 2003] is used in the analyses. These finite element analyses include both friction and smooth contact surfaces. The typical computing time required for each simulation carried out in this study using Sun Blade 2000 Workstation 2@900 MHz with 1 GB RAM are about 6 and 30 hours for conical and Berkovich indentation tests respectively.

Figure 1 compares the solutions obtained from finite element analyses with and without the strain gradient effects are compared with the experimental data reported in [Pethica et al. 1983]. The comparison demonstrates clearly the hardening effects of materials subject to indentation at micron and submicron levels. Numerical results obtained from the finite element model incorporating CMSG plasticity theory agree rather well with indentation test results. In contrast, conventional finite element solutions deviate significantly from the test results conducted at submicron level. The numerical results obtained from the proposed axisymmetric and solid finite elements are by and large identical.

6B. Molecular dynamics simulation for nanoindentation. In this study, the simulations of the nanoindentation on a fcc crystalline nickel substrate by a covalently bonded hemisphere diamond tip has been carried out. The positions and velocities of both the tip and the substrate atoms were obtained as functions

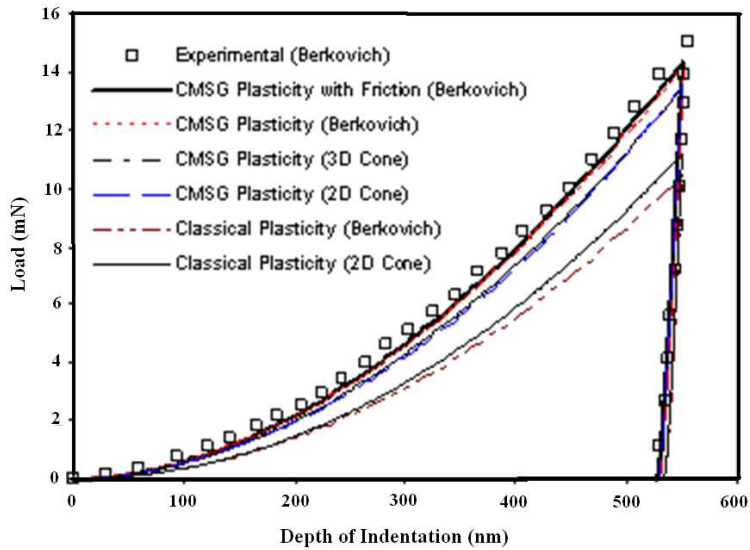


Figure 1. Comparison of indentation test results at micron level.

of time using the MD method. It is assumed that the heat generated in the system during the indentation process was dissipated by the thermal baths of the tip and of the substrate at a high rate that is much faster than the indentation speed. Therefore, in the simulations the nano scale tip and substrate were controlled at the same temperatures during the indentations, that is, the indentations are considered as isothermal processes.

The configuration of the simulated tip and substrate is shown in [Figure 2](#). The substrate material is nickel having fcc lattice with a lattice constant of 3.52 \AA . The substrate sizes are $35.2 \text{ nm} \times 35.2 \text{ nm} \times 35.2 \text{ nm}$ containing 4,000,000 atoms. A hemisphere (radius = 10.5 nm) diamond indenter is used. The

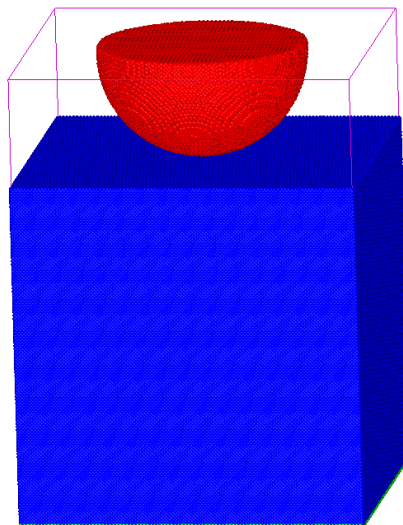


Figure 2. Large scale MD simulation model containing more than 4 million atoms.

latter contains 289,235 carbon atoms. The typical CPU time required for each MD simulation carried out in the present study is about 200 hours based on IBM p575 supercomputer. The boundary conditions of the substrate include:

- (1) The two layers of atoms at the bottom of the substrate are fixed in space while the top surface of the substrate is free.
- (2) Periodic boundary conditions are applied at the four side surfaces of the substrate. The indentation is on the (001)-surface of the fcc lattice.

The load-displacement curve obtained from the MD simulated indentation test on nickel as depicted in Figure 3 shows as expected that the indentation depth increases with loading. The load-displacement response, which depicts the force required to push the indenter tip a certain distance into the substrate, demonstrates characteristic discontinuities. Examining the load-displacement curve in detail, we find the first significant drop occurs at the indentation depth of about 1 nm. This drop, representing a transition from elastic to plastic deformation, is attributed to the nucleation of a dislocation. It can be further observed that the initial loading region of the load-displacement curve can be assumed to be linear and the reduced Young's modulus of elasticity can be determined through the relationship $F = 2E_r r_a h$, where F is the loading force, E_r is the reduced Young's modulus, r_a is the radius of contact area, and h is the penetration depth. The atomic configuration at about 1.3 nm indentation depth, the associated Von Mises stress contours in the nanoindentation process are illustrated in Figure 4, left, while the dislocations in the substrate materials are shown in Figure 4, right. The results demonstrate that plastic deformation takes place near the contact area and the dislocations of substrate materials occur beneath the contact

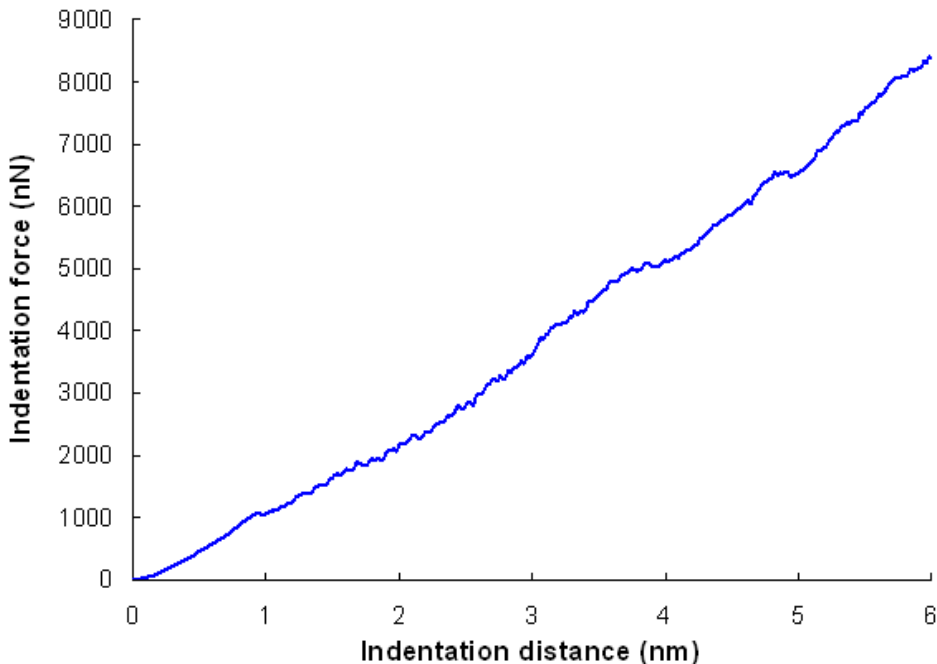


Figure 3. Variation of indentation force against indentation distance.

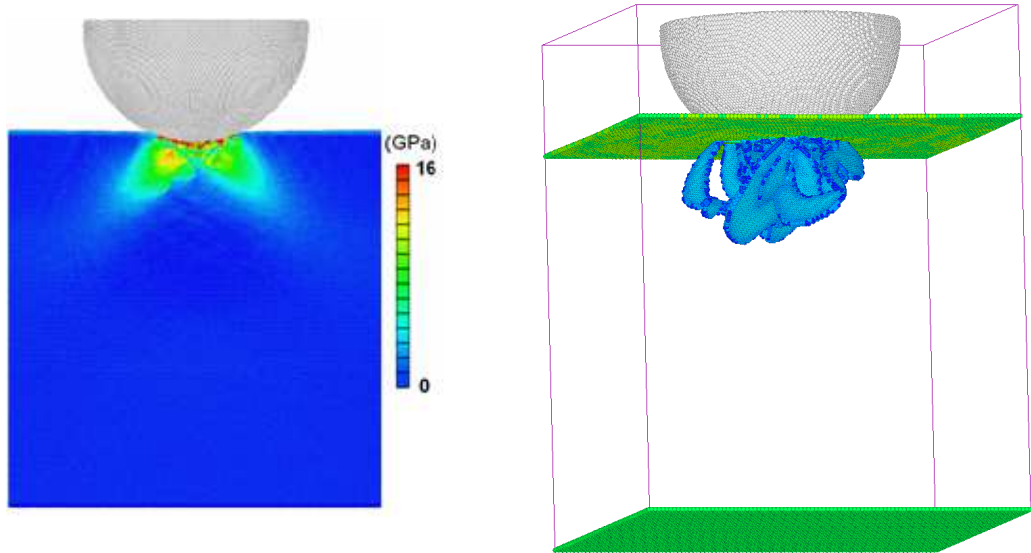


Figure 4. Left: Stress (von Mises) distribution in the substrate during nanoindentation simulation. Right: Dislocations in nickel substrate during indentation.

surface. These phenomena are consistent with the MD simulated results of copper as reported in [Saraev and Miller 2005].

7. Conclusions

A C^0 finite element approach for materials with strain gradient plasticity is proposed in the simulation of indentation tests at the micron and hundreds of nanometers levels. As only the constitutive condition is affected, higher-order stress and hence higher-order continuity requirements are no longer necessary. The elements were adopted to simulate the Berkovich indentation on electropolished nickel. Comparison of finite element results with other existing analytical solutions demonstrates that when the material length scale and the nonuniform plastic deformation are of the same order at micron or submicron level, the effects of strain gradient plasticity have to be considered. A large scale study using molecular dynamics method to simulate nanoindentation of nickel substrate was also carried out. The load-displacement response, stress variation and the plastic dislocations in the nickel substrate are presented. The paper provides appropriate numerical tools for the simulations of indentation tests at both micron and a few nanometer levels.

References

- [ABAQUS 2002] *ABAQUS user's manual*, Version 6.3, Hibbit and Karlsson and Sorensen, Pawtucket, RI, 2002.
- [Bhattacharya and Nix 1988] A. K. Bhattacharya and W. D. Nix, “Finite element simulations of indentation experiments”, *Int. J. Solids Struct.* **24**:9 (1988), 881–891.
- [Elssner et al. 1994] G. Elssner, D. Korn, and M. Rühle, “The influence of interface impurities on fracture energy of UHV diffusion bonded metal-ceramic bicrystals”, *Scr. Metall. Mater.* **31**:8 (1994), 1037–1042.

- [Fang et al. 2001] T. H. Fang, C. I. Weng, J. G. Chang, and C. C. Hwang, “Nanotribology of amorphous hydrogenated carbon films using scanning probe microscopy”, *Thin Solid Films* **396**:1–2 (2001), 167–173.
- [Fang et al. 2006] T. H. Fang, W. J. Chang, and C. I. Weng, “Nanoindentation and nanomachining characteristics of gold and platinum thin films”, *Mater. Sci. Eng. A* **430**:1–2 (2006), 332–340.
- [Fleck and Hutchinson 1993] N. A. Fleck and J. W. Hutchinson, “A phenomenological theory for strain gradient effects in plasticity”, *J. Mech. Phys. Solids* **41**:12 (1993), 1825–1857. MR 94g:73020
- [Fleck et al. 1994] N. A. Fleck, G. M. Muller, M. F. Ashby, and J. W. Hutchinson, “Strain gradient plasticity: Theory and experiment”, *Acta Metall. Mater.* **42**:2 (1994), 475–487.
- [Gao et al. 1999] H. Gao, Y. Huang, W. D. Nix, and J. W. Hutchinson, “Mechanism-based strain gradient plasticity, I: Theory”, *J. Mech. Phys. Solids* **47**:6 (1999), 1239–1263. MR 2000k:74014
- [Haque and Saif 2003] M. A. Haque and M. T. A. Saif, “Strain gradient effect in nanoscale thin films”, *Acta Mater.* **51**:11 (2003), 3053–3061.
- [Huang et al. 2000] Y. Huang, H. Gao, W. D. Nix, and J. W. Hutchinson, “Mechanism-based strain gradient plasticity, II: Analysis”, *J. Mech. Phys. Solids* **48**:1 (2000), 99–128. MR 2000k:74015
- [Huang et al. 2004] Y. Huang, S. Qu, K. C. Hwang, M. Li, and H. Gao, “A conventional theory of mechanism-based strain gradient plasticity”, *Int. J. Plast.* **20**:4–5 (2004), 753–782.
- [Nye 1953] J. Nye, “Some geometrical relations in dislocated crystals”, *Acta Metall.* **1**:2 (1953), 153–162.
- [Pei et al. 2006] Q. X. Pei, C. Lu, F. Z. Fang, and H. Wu, “Nanometric cutting of copper: A molecular dynamics study”, *Comput. Mater. Sci.* **37**:4 (2006), 434–441.
- [Pethica et al. 1983] J. B. Pethica, R. Hutchings, and W. C. Oliver, “Hardness measurement at penetration depths as small as 20 nm”, *Philos. Mag. A* **48**:4 (1983), 593–606.
- [Rapaport 2004] D. C. Rapaport, *The art of molecular dynamics simulation*, 2nd ed., Cambridge University Press, Cambridge, 2004.
- [Saraev and Miller 2005] D. Saraev and R. E. Miller, “Atomistic simulation of nanoindentation into copper multilayers”, *Model. Simul. Mater. Sci. Eng.* **13**:7 (2005), 1089–1099.
- [Shi et al. 2001] M. Shi, Y. Huang, H. Jiang, K. C. Hwang, and M. Li, “The boundary-layer effect on the crack tip field in mechanism-based strain gradient plasticity”, *Int. J. Fract.* **112**:1 (2001), 23–41.
- [Stelmashenko et al. 1993] N. A. Stelmashenko, A. G. Walls, L. M. Brown, and Y. V. Milman, “Microindentation on W and Mo oriented single crystals: An STM study”, *Acta Metall. Mater.* **41**:10 (1993), 2855–2865.
- [Swaddiwudhipong et al. 2005] S. Swaddiwudhipong, J. Hua, K. K. Tho, and Z. S. Liu, “ C^0 solid elements for materials with strain gradient effects”, *Int. J. Numer. Methods Eng.* **64**:10 (2005), 1400–1414.
- [Swaddiwudhipong et al. 2006a] S. Swaddiwudhipong, J. Hua, K. K. Tho, and Z. S. Liu, “Finite element modelling for materials with size effect”, *Model. Simul. Mater. Sci. Eng.* **14**:7 (2006), 1127–1137.
- [Swaddiwudhipong et al. 2006b] S. Swaddiwudhipong, K. K. Tho, J. Hua, and Z. S. Liu, “Mechanism-based strain gradient plasticity in C^0 axisymmetric element”, *Int. J. Solids Struct.* **43**:5 (2006), 1117–1130.
- [Taylor 1934] G. I. Taylor, “The mechanism of plastic deformation of crystals, I: Theoretical”, *Proc. R. Soc. Lond. A* **145**:855 (1934), 362–387.
- [Toupin 1962] R. A. Toupin, “Elastic materials with couple-stresses”, *Arch. Ration. Mech. An.* **11**:1 (1962), 385–414. MR 26 #2056
- [Wang et al. 2003] W. Wang, Y. Huang, K. J. Hsia, K. X. Hu, and A. Chandra, “A study of microbend test by strain gradient plasticity”, *Int. J. Plast.* **19**:3 (2003), 365–382.

Received 5 Jul 2007. Revised 15 Nov 2007. Accepted 6 Dec 2007.

ZISHUN LIU: liuzs@ihpc.a-star.edu.sg

Institute of High Performance Computing, 1 Science Park Road, # 01-01, Singapore 117528

SOMSAK SWADDIWUDHIPONG: cvesomsa@nus.edu.sg

Department of Civil Engineering, National University of Singapore, E1A-07-03, 1 Engineering Drive 2, Singapore 119260
<http://www.eng.nus.edu.sg/civil/people/cvesomsa/somsa.html>

QINGXIANG PEI: peiqx@ihpc.a-star.edu.sg

Institute of High Performance Computing, 1 Science Park Road, # 01-01, Singapore 117528

NUMERICAL IMPLEMENTATION OF A CONSTITUTIVE MODEL FOR SOIL CREEP

M. A. K. M. MADURAPPERUMA AND U. G. A. PUSWEWALA

We discuss the numerical implementation of a creep constitutive model to facilitate the modeling of long-term soil creep. Multidimensional soil creep models are generalized from the one-dimensional soil creep model proposed by Bjerrum in 1967, which was based on field test data and was later modified for transient loading conditions by Vermeer et al. in 1998. Here this differential form of one-dimensional creep model is extended to two- and three-dimensional states of stress and strain by incorporating concepts from viscoplasticity. The devised multidimensional creep model takes into account both volumetric and deviatoric creep strain, with creep deformation of the soil defined by several material parameters. The model is incorporated as a plane strain element subroutine in a nonlinear, time-incrementing finite element program, along with iterative corrections within each time step. Numerical analyses are conducted to demonstrate soil creep by using published experimental data. The verified computer code will be a useful research tool for estimating settlements in structures founded on soils exhibiting creep.

1. Introduction

Many theories have been proposed to explain the time-dependent deformation of soils under load. Bjerrum [1967], in his study of settlement of 3000 years old deposits of Norwegian clay, proposed the concept that deformation of such soils can be decomposed into two parts: “instant compression” and “delayed compression”, or soil creep. This was a departure from the view where soil is understood to undergo “primary consolidation” followed by “secondary consolidation or compression” [Terzaghi 1931]. Bjerrum’s argument was that under constant load, creeping soils continue to experience strain with time, thus causing an increase of its critical pressure. The term critical pressure is used to define a specific effective pressure (preconsolidation pressure) in the classical void ratio versus log pressure graph for a soil medium [Balasubramaniam and Brenner 1981]. Thus if the soil is allowed to creep under a particular load over a long period and if the load is suddenly increased thereafter, the soil behaves as if it had been subjected to a much greater pressure than the previous maximum pressure it physically sustained.

Bjerrum gave examples of buildings founded on Norwegian clay undergoing creep settlements. Similar creep settlements can take place under other structures like roads, river embankments and dams, built on creeping media. Apart from the foundation-related problems usually considered, creep plays an important role in slope stability; gradual geometric changes due to creep and the associated reduction of strength due to the smoothening of soil particles may then lead to slope slides. The different problems that relate to soil creep have made it necessary to develop a stress-strain relation that takes two- and three-dimensional situations into account.

Keywords: constitutive model, finite element analysis, soil creep, numerical simulation, soil-structure interaction.

As mentioned, Bjerrum's original creep model was a comprehensive one-dimensional model based on the behavior of Norwegian clays with a sedimentation history of 3000 years. It was based on an expression for creep rate for constant effective stress; it was modified for transient loading conditions by Vermeer et al. [1998] and later generalized to three dimensions [Vermeer and Neher 1999]. However, the generalized constitutive model is not in a form that can be implemented in finite element formulation for numerical simulation of soil creep. Adachi and Okano [1974] proposed a rate-formulated elastoviscoplastic constitutive model, later generalized in [Adachi and Oka 1982] based on the overstress type viscoplastic theory. However, this model has not been verified for predicting the time-dependent long-term behavior of soft soils. [Borja and Kavazvjian 1985] proposed a constitutive model to describe time dependent elasto-plastic strains based on Bjerrum's concept. The validity of this model was not properly verified through realistic experimental approaches and its long-term predictive capability has not been comprehensively reported in the literature.

On the other hand, numerical implementation by using the finite element method has taken into account creep of soil using nonlinear constitutive equations; see, for example, [Iizuka and Ohta 1987; Stolle et al. 1997; Brinkgreve 2002]. A detailed description of numerical implementation of advanced constitutive models is presented in [Stolle et al. 1997; Wheeler et al. 2003]. The long term prediction of soft soil settlement is dependent on the constitutive model that describes the soil creep behavior and the finite element formulation which involves solution algorithms, iteration schemes, time increments and numerical stability. Therefore, a simple creep model that could describe all aspects of actual field behavior to sufficient accuracy would be highly useful and suitable for practical applications. Based on an extensive literature review, we found the constitutive model proposed by Vermeer et al. [1998] based on Bjerrum's one-dimensional model to be one of the most appropriate for generalization and numerical implementation. Its ability to predicting long-term time-dependent soil behavior and the evaluation of model parameters through conventional tests in the laboratory are the main reasons to select this model.

Here we extend the model of [Vermeer et al. 1998] to multidimensional state of stress and strain by incorporating concepts of viscoplasticity. A nonlinear, time incrementing finite element program, with iterative corrections within each time step, developed earlier to model creep in geomaterials [Puswewala et al. 1992], is modified to incorporate the present model as an element subroutine under conditions of plane strain. Numerical analyses are conducted for two soil-structure interaction problems by using this program and published experimental data to demonstrate the creep behavior of soils predicted by the model.

2. The differential form of one-dimensional creep model

In his Rankine Lecture, Bjerrum [1967] described the compression of clays exhibiting creep under constant effective stress. Building on this work, Garlanger [1972] proposed a creep equation of the form

$$e = e_c - C_\alpha \log \frac{\tau_c + t'}{\tau_c}, \quad (1)$$

where e is the void ratio, e_c is the void ratio at the end of consolidation, $t' > 0$ is the effective creep time, and C_α is the slope of the e versus log time curve. The time scale parameter τ_c depends on the history

of compression and the geometry of the sample. Janbu [1969] developed a construction for evaluating τ_c from experimental data.

This expression was later modified by Butterfield [1979] to fit into the framework of critical state soil mechanics. He introduced the concept of logarithmic strain. The expression of the total volumetric strain, ε_v , is

$$\varepsilon_v = \varepsilon_v^c + \mu^* \ln \frac{\tau_c + t'}{\tau_c}, \tag{2}$$

where the deformation during primary consolidation is given by ε_v^c and consists of the elastic settlement and a part of the delayed settlement, following Bjerrum. The modified secondary compression index μ^* describes the secondary compression per logarithmic time increment. Equation (2) can be rewritten by including the components of ε_v^c as

$$\varepsilon_v = \varepsilon_v^c + \varepsilon_v^{cr} = k^* \ln \frac{\sigma'}{\sigma'_0} + (\lambda^* - k^*) \ln \frac{\sigma'_{pc}}{\sigma'_{p0}} + \mu^* \ln \frac{\tau_c + t'}{\tau_c}, \tag{3}$$

where

- ε_v is the total volumetric strain due to an increase in mean effective stress from σ'_0 to σ' in a time period of $(\tau_c + t')$,
- σ'_{p0} and σ'_{pc} represent the preconsolidation pressure corresponding to before-loading state and end-of-consolidation state respectively,
- k^* , λ^* , μ^* are the Modified Cam Clay Model parameters [Roscoe and Burland 1968], called respectively the (modified) swelling index, compression index and creep index, and having the values

$$\lambda^* = \frac{C_c}{2.3(1 + e_0)}, \quad k^* \approx \frac{3}{2.3} \frac{(1 - \nu)}{(1 + \nu)} \frac{C_r}{1 + e_0}, \quad \mu^* = \frac{C_\alpha}{2.3(1 + e_0)}, \tag{4}$$

where C_r is the slope on an e versus $\log \sigma'$ diagram of the compression line from σ'_0 to σ'_c , C_c is the slope of the instant line, C_α is the slope of the e versus \log time curve, ν is the Poisson's ratio, e_0 is the initial void ratio and σ'_c is the preconsolidation pressure [Vermeer et al. 1998].

Equation (3) is valid for a constant mean effective stress, but for transient or continuous loading problems it is necessary to formulate a constitutive law in differential form. Moreover there is still the question of how to express the time scale parameter τ_c analytically. By adopting Bjerrum's concept that the secondary compression increases the critical pressure (preconsolidation pressure), by eliminating σ'_{pc} and τ_c from (3), Vermeer et al. proposed a differential form of expression that accounts for creep of soft soil, of the form

$$\dot{\varepsilon}_v = \dot{\varepsilon}_v^e + \dot{\varepsilon}_v^c = \kappa^* \frac{\dot{\sigma}'}{\sigma'} + \frac{\mu^*}{\tau} \left(\frac{\sigma'}{\sigma'_p} \right)^{(\lambda^* - \kappa^*)/\mu^*} \quad \text{in which } \sigma'_p = \sigma'_{p0} \exp \frac{\varepsilon_v^c}{\lambda^* - \kappa^*}, \tag{5}$$

where the parameter τ , which is not the same as τ_c , is introduced to provide a time scale and an additional degree of freedom in the soil creep model. For example, in the conventional consolidation test each load is kept for one day and at the end of the day the isotropic consolidation line with $\sigma'_p = \sigma'$ is obtained (overconsolidation ratio = 1). Therefore, in the case of conventional consolidation test the time scale parameter τ can be taken as precisely 1 day. The quantity ε_v^c is the accumulated volumetric creep strain.

3. Generalization of the one-dimensional model to three dimensions

The expression for volumetric creep strain rate ($\dot{\epsilon}_v^c$) in (5) is extended for a general state of stress and strain. Well-known stress invariant quantities are adopted for pressure p and deviatoric stress q as $p = \sigma_{\text{oct}}$ and $q = 3\tau_{\text{oct}}/\sqrt{2}$, where σ_{oct} and τ_{oct} are the octahedral normal stress and octahedral shear stress. In terms of the principal stresses $\sigma_1, \sigma_2, \sigma_3$, the pressure p and the deviatoric stress q can be expressed as

$$p = \frac{1}{3}(\sigma_1 + \sigma_2 + \sigma_3) \quad \text{and} \quad q = \sqrt{\frac{1}{2}((\sigma_1 - \sigma_2)^2 + (\sigma_2 - \sigma_3)^2 + (\sigma_3 - \sigma_1)^2)}. \quad (6)$$

The extension of (6) to a state of general stress and strain yields

$$p = \frac{1}{3}(\sigma_{ii}) \quad \text{and} \quad q = \sqrt{\frac{3}{2}(s_{ij}s_{ij})}, \quad (7)$$

where summation is implied over the indices $i, j = 1, 2, 3$ and s_{ij} denotes the deviatoric stress tensor in terms of multidimensional states of stress quantities as

$$s_{ij} = \sigma_{ij} - \frac{1}{3}\sigma_{ii}\delta_{ij}, \quad (8)$$

where δ_{ij} is Kronecker's delta. The invariants p and q [Roscoe and Burland 1968] can be used to define a new stress measure [Vermeer and Neher 1999]

$$p^{\text{eq}} = p + \frac{q^2}{M^2 p}, \quad (9)$$

called *equivalent pressure* and having the dimension of pressure. The soil parameter M represents the slope of the critical state line and can be computed by using the critical state friction angle (ϕ_{cs}) as

$$M = \frac{6 \sin \phi_{\text{cs}}}{3 - \sin \phi_{\text{cs}}}. \quad (10)$$

(see [Vermeer et al. 1998]). For principal stress quantities yield function is defined as

$$f = p^{\text{eq}} - p_p^{\text{eq}}, \quad (11)$$

where p_p^{eq} is the apparent equivalent preconsolidation pressure. The yield function f in (11) can be described as ellipses in p - q space when the principal stress quantities are used to calculate p and q in (6). The equivalent pressure p^{eq} is constant on ellipses and the peaks of the ellipses are located on the critical state line which is given by the model of [Roscoe and Burland 1968] in p - q space.

Together with p and q in (7), the equivalent pressure p^{eq} in (9) leads to

$$p^{\text{eq}} = \frac{1}{3}\sigma_{ii} + \frac{9s_{ij}s_{ij}}{2M^2\sigma_{ii}}. \quad (12)$$

By considering the volumetric creep strain rate part ($\dot{\epsilon}_v^c$) in (5) and introducing the new equivalent pressure p^{eq} and the apparent equivalent preconsolidation pressure p_p^{eq} the expression for volumetric creep strain rate can be written as

$$\dot{\epsilon}_v^c = \frac{\mu^*}{\tau} \left(\frac{p^{\text{eq}}}{p_p^{\text{eq}}} \right)^{(\lambda^* - \kappa^*)/\mu^*}, \quad \text{with } p_p^{\text{eq}} = p_{p0}^{\text{eq}} \exp \frac{\epsilon_v^c(t)}{\lambda^* - \kappa^*}, \quad (13)$$

where $\varepsilon_v^c(t)$ denotes the accumulated volumetric creep up to the current time t . The coefficient of lateral earth pressure K_0^{NC} is used to estimate the initial value of equivalent preconsolidation pressure p_{p0}^{eq} using initial preconsolidation pressure σ_{p0} as given in [Vermeer and Neher 1999; Vermeer et al. 1998].

4. Formulation of the soil creep problem

The basic concept used here is that the total strain vector consists of an elastic strain component and a creep strain component:

$$\boldsymbol{\varepsilon}(t) = \boldsymbol{\varepsilon}^e(t) + \boldsymbol{\varepsilon}^c(t), \quad (14)$$

where $\boldsymbol{\varepsilon}(t)$ is the current total strain vector, $\boldsymbol{\varepsilon}^e(t)$ the current elastic strain vector, $\boldsymbol{\varepsilon}^c(t)$ the current creep strain vector, and t denotes the current time. The elastic strain component can be related to the stress vector $\boldsymbol{\sigma}(t)$ through the use of a constitutive matrix \mathbf{D} as

$$\boldsymbol{\varepsilon}^e(t) = \mathbf{D}^{-1}\boldsymbol{\sigma}(t). \quad (15)$$

In the present analysis \mathbf{D} is composed of Young's modulus E and Poisson's ratio ν , which implies that the elastic strain is related to stress according to isotropic linear elasticity. In order to introduce general creep strain, one can adopt the view that creep strain is simply a time-dependent plastic strain. Then it is logical to assume a flow rule for the creep rate component and equivalent pressure p^{eq} is introduced as the plastic potential function [Vermeer et al. 1998]. Assuming the same yield function as in (11) the total strain rate can then be obtained as

$$\dot{\boldsymbol{\varepsilon}}(t) = \mathbf{D}^{-1}\dot{\boldsymbol{\sigma}}(t) + \lambda \frac{\partial p^{eq}}{\partial \boldsymbol{\sigma}(t)}, \quad (16)$$

where the plastic multiplier λ can be eliminated from (16) by adopting the concept that the creep strain rate is proportional to partial derivative of the plastic potential function with respect to the corresponding stress component, i.e.,

$$\lambda = \frac{\dot{\boldsymbol{\varepsilon}}_v^c}{\boldsymbol{\alpha}}, \quad (17)$$

where λ can be evaluated for multidimensional situation as

$$\dot{\boldsymbol{\varepsilon}}_v^c = \dot{\varepsilon}_{11}^c + \dot{\varepsilon}_{22}^c + \dot{\varepsilon}_{33}^c \quad \text{and} \quad \boldsymbol{\alpha} = \left(\frac{\partial p^{eq}}{\partial \sigma_{11}} + \frac{\partial p^{eq}}{\partial \sigma_{22}} + \frac{\partial p^{eq}}{\partial \sigma_{33}} \right). \quad (18)$$

Equations (14)–(18) yield

$$\dot{\boldsymbol{\varepsilon}}^c(t) = \frac{\dot{\boldsymbol{\varepsilon}}_v^c}{\boldsymbol{\alpha}} \frac{\partial p^{eq}}{\partial \boldsymbol{\sigma}(t)}. \quad (19)$$

By combining (13) and (19) we obtain

$$\dot{\boldsymbol{\varepsilon}}^c(t) = \frac{1}{\alpha} \frac{\mu^*}{\tau} \left(\frac{p^{eq}}{p_p^{eq}} \right)^{(\lambda^* - \kappa^*)/\mu^*} \frac{\partial p^{eq}}{\partial \boldsymbol{\sigma}(t)}, \quad \text{with } p_p^{eq} = p_{p0}^{eq} \exp \frac{\varepsilon_v^c(t)}{\lambda^* - \kappa^*}. \quad (20)$$

Note that the subscript 0 is used in the equations to denote initial conditions and that $\varepsilon_v^c = 0$ for time $t = 0$. The derivative quantities of p^{eq} and the components of strain rate vector $\dot{\boldsymbol{\varepsilon}}^c$ are given in the [Online Supplement](#).

5. Finite element algorithm for creep model

A finite element algorithm was developed for the purpose of incorporating the devised creep model under plane strain conditions, based on [Puswewala et al. 1992]. At any point within a material domain of volume V and surface S , discretized by finite elements, the displacement vector field will be denoted by \mathbf{u} , the strain vector by $\boldsymbol{\varepsilon}$, and the stress vector by $\boldsymbol{\sigma}$. From the principle of virtual work, equilibrium of the material domain at the time t_k , which is reached after the accumulation of k time steps starting from $t = 0$, can be expressed as

$$\int_v \mathbf{B}^T \boldsymbol{\sigma}_k dv + \mathbf{f}_k = \mathbf{0}, \quad (21)$$

where \mathbf{f}_k is the known force vector consisting of body forces and surface traction forces. Vectors \mathbf{B} , \mathbf{u} , $\boldsymbol{\varepsilon}$ and the nodal displacement vector \mathbf{a} hold the following relationships, i.e.,

$$\boldsymbol{\varepsilon} = \mathbf{L}\mathbf{u}, \quad \mathbf{u} = \mathbf{N}\mathbf{a} \quad \text{and} \quad \boldsymbol{\varepsilon} = \mathbf{L}\mathbf{N}\mathbf{a} = \mathbf{B}\mathbf{a}, \quad (22)$$

where \mathbf{N} is the shape function matrix and \mathbf{L} is a differential operator matrix. It is necessary to evaluate \mathbf{a}_{k+1} and $\boldsymbol{\sigma}_{k+1}$ at the end of the next time interval Δt_k , provided $\boldsymbol{\varepsilon}_k$, \mathbf{a}_k and $\boldsymbol{\sigma}_k$ at the time t_k are known. In order to evaluate the accumulated volumetric creep strain (ε_v^c) at the time t_k , Equations (14) and (15) are used since $\boldsymbol{\varepsilon}_k$, \mathbf{D}^{-1} and $\boldsymbol{\sigma}_k$ are known quantities at the time t_k . Together with (14), (15) and (22), the expression for the difference between the stress vectors $\boldsymbol{\sigma}_{k+1}$ and $\boldsymbol{\sigma}_k$ can be obtained as

$$\boldsymbol{\psi}_{k+1} \equiv \boldsymbol{\sigma}_{k+1} - \boldsymbol{\sigma}_k - \mathbf{D}\mathbf{B}\{\mathbf{a}_{k+1} - \mathbf{a}_k\} + \mathbf{D}\Delta t_k \boldsymbol{\beta}(\boldsymbol{\sigma}_{k+\theta}) = \mathbf{0}. \quad (23)$$

In the above, the following relationship has been used

$$\boldsymbol{\varepsilon}_{k+1}^c - \boldsymbol{\varepsilon}_k^c = \boldsymbol{\beta}(\boldsymbol{\sigma}_{k+\theta}) \Delta t_k, \quad (24)$$

where $\boldsymbol{\beta}$ denotes the strain rate vector given by (20), and

$$\boldsymbol{\sigma}_{k+\theta} = (1 - \theta)\boldsymbol{\sigma}_k + \theta\boldsymbol{\sigma}_{k+1}, \quad \text{where} \quad 0 \leq \theta \leq 1. \quad (25)$$

For $\theta \geq \frac{1}{2}$ (i.e., to have an unconditionally stable scheme), Newton–Raphson procedure is used to iterate within the time interval Δt_k for the unknowns $\boldsymbol{\sigma}_{k+1}$ and \mathbf{a}_{k+1} . The iterate number is denoted by a superscript numeral. After successive iterations, the iteration cycle n can be reached, while the convergence criterion may not yet be satisfied. At this point, (21) and (23) can be written using the appropriate current stress and displacement values, but these expressions would now not reduce to zero since convergence has not yet been achieved. Using the curtailed Taylor expansion on the latter expressions, the following two equations are obtained to yield the unknown incremental corrections $\Delta \boldsymbol{\sigma}_{k+1}^n$ and $\Delta \mathbf{a}_{k+1}^n$ upon solution (this is the $(n + 1)$ -th iterate):

$$\Delta \boldsymbol{\sigma}_{k+1}^n = \bar{\mathbf{D}}^n [\mathbf{B} (\Delta \mathbf{a}_{k+1}^n + \mathbf{a}_{k+1}^n - \mathbf{a}_k) - \mathbf{D}^{-1} (\boldsymbol{\sigma}_{k+1}^n - \boldsymbol{\sigma}_k) - \Delta t_k \boldsymbol{\beta} (\boldsymbol{\sigma}_{k+\theta}^n)], \quad (26)$$

$$\begin{aligned} & \int_v \mathbf{B}^T \bar{\mathbf{D}}^n \mathbf{B} \Delta \mathbf{a}_{k+1}^n dv \\ &= \int_v \mathbf{B}^T \bar{\mathbf{D}}^n \{ \mathbf{D}^{-1} (\boldsymbol{\sigma}_{k+1}^n - \boldsymbol{\sigma}_k) - \mathbf{B} (\mathbf{a}_{k+1}^n - \mathbf{a}_k) + \Delta t_k \boldsymbol{\beta} (\boldsymbol{\sigma}_{k+\theta}^n) \} dv - \int_v \mathbf{B}^T \boldsymbol{\sigma}_{k+1}^n dv, \quad (27) \end{aligned}$$

where $\sigma_{k+\theta}^n$ is obtained from (25) by replacing σ_{k+1} with σ_{k+1}^n , and

$$\bar{D}^n = [D^{-1} + \Delta t_k S^n \theta]^{-1}, \tag{28}$$

where the matrix

$$S^n = \left(\frac{\partial \beta}{\partial \sigma} \right), \tag{29}$$

is evaluated for $\sigma_{k+\theta}^n$. In (27) the right-hand side does not include provisions for increasing body forces. If convergence occurs at the above $(n + 1)$ -the iterate, we set $\sigma_{k+1} = \sigma_{k+1}^{n+1}$ (note that $\sigma_{k+1}^{n+1} = \sigma_{k+1}^n + \Delta \sigma_{k+1}^n$) and $a_{k+1} = a_{k+1}^{n+1}$, and proceed to the next time step; otherwise iteration is continued. The components of the matrix S^n and the expressions for the element stiffness matrix and the stress increments are given in the [Online Supplement](#).

There are several possibilities that can be followed for convergence study, depending on the values of θ and n (for example, $\theta \neq 0$ and $n = 1$). The value of θ used in the analysis is $\frac{1}{2}$, which guarantees the numerical stability of the algorithm. As an approximation has already been incorporated at the stage of writing (24), the iteration solution is generally curtailed after one or two cycles. Use of sufficiently small time steps would compensate for these approximations. As per the constitutive model in (20), the solution process is initiated by obtaining the instantaneous elastic deformation and stress distribution at the time of application of the initial load ($t = 0$). These displacement and stress vectors are used to obtain the incremental displacement and stress vectors during the first time interval Δt_0 by solving (26) and (27). The solution process is repeated for each time interval, until the termination of analysis. The flow diagram for FEM algorithm is given in [Figure 1](#).

6. Numerical analysis and discussion

The sensitivity analysis of material parameters used in the model is carried out by simulating a concrete strip foundation on a soil layer. Numerical analyses were carried out by a finite element mesh composed of 40 eight-node serendipity elements representing an 8 m deep layer of soft soil underlain by a hard surface like rock ([Figure 2](#)). The simulation was done under simplified plane strain conditions, with the top of the surface subjected to a uniform load of 120 kPa applied over the strip footing. The strip footing materials were selected as concrete and the basic material properties of the soil were selected similar to Haney clay investigated by [Vaid and Campanella \[1977\]](#), and the corresponding material parameters are as follows:

Foundation material parameters: Young’s modulus $E = 2.1 \times 10^7$ kPa; Poisson’s ratio $\nu = 0.23$

Soil properties for the problem configuration in Figures 2 and 6:

$$E = 2.1 \times 10^4 \text{ kPa}, \quad \nu = 0.25, \quad \sigma_{p0} = 350 \text{ kPa}, \quad \phi_{cs} = 32.1, \tag{30}$$

$$\kappa^* = 0.016, \quad \lambda^* = 0.105, \quad \mu^* = 0.004 \quad \tau = 1 \text{ day}$$

[Figure 3](#) shows the settlement behavior at the center of the foundation predicted by the constitutive model for different combinations of Young’s modulus and Poisson’s ratio. The settlement reduces when Poisson’s ratio is equal to 0.45, which is as expected since incompressible behavior is represented by the case where Poisson’s ratio equals 0.5. The figure shows the significant effect of parameters E and ν on the time dependent deformation of the creeping soil medium, implying that these parameters indicate the

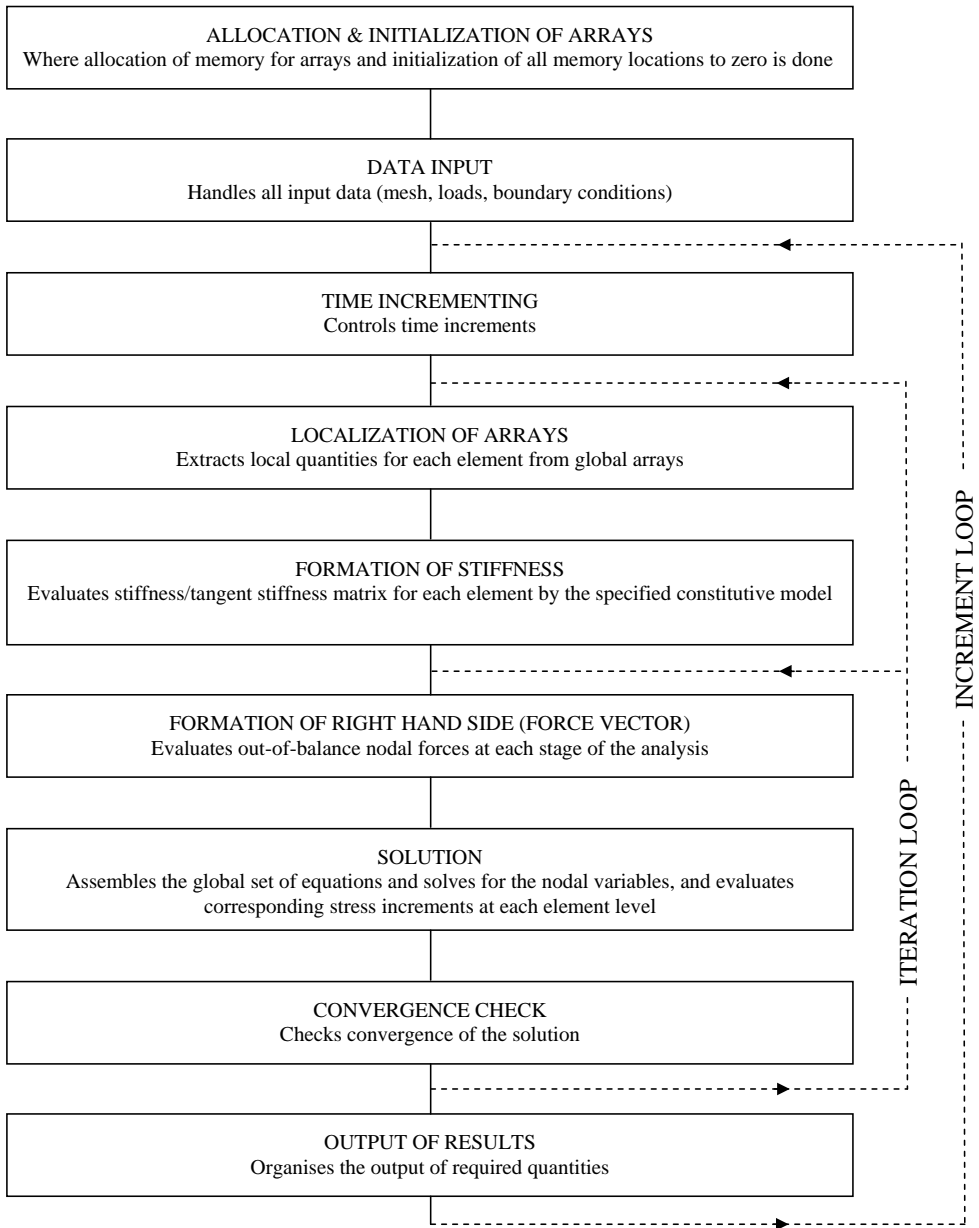


Figure 1. Flow diagram for FEM algorithm.

overall stiffness of the soil modeled as a solid continuum in this work. The effect of modified secondary compression index, μ^* , on the settlement is shown in [Figure 4](#); the settlement with time at the center point under the surface load of 120 kN/m^2 is shown for three different values of μ^* , with all other parameters as given in (30). [Figure 4](#) clearly indicates that the settlement increases with the increase of modified secondary compression index. The effect of preconsolidation pressure (σ_{p0}) on the settlement is shown in the [Figure 5](#); the settlement with time at the center point under the surface load of 120 kN/m^2 is

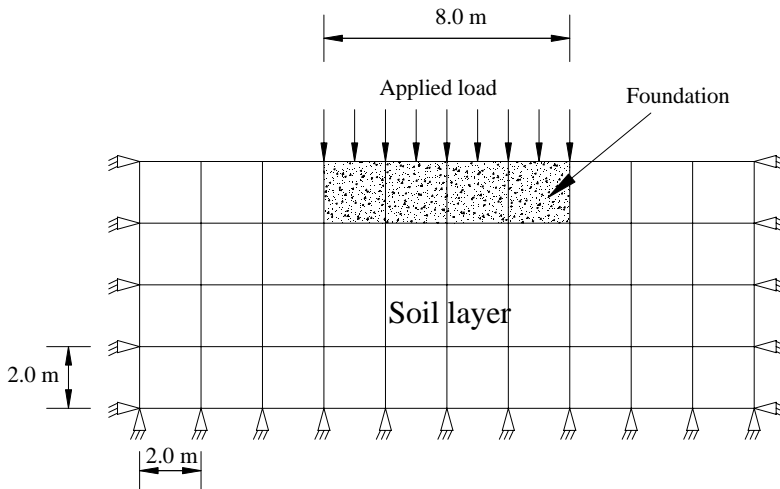


Figure 2. Finite element mesh and loading arrangement for the problem considered for sensitivity analysis.

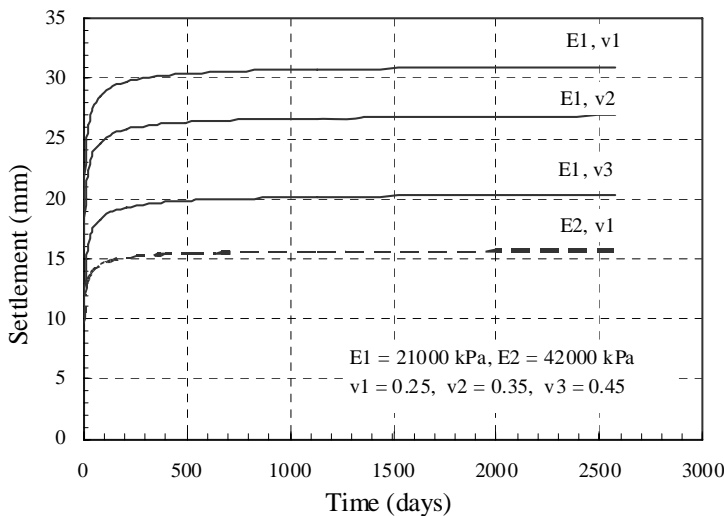


Figure 3. Settlement behavior of the center point with Young's modulus and Poisson's ratio.

shown for three different values of σ_{p0} , with all other parameters as given in (30). With the decrease of preconsolidation pressure, the figure indicates higher settlements which confirm Bjerrum's. If the preconsolidation pressure is less than the applied pressure then the settlement could be appreciable, but the problem does not work for those values due to numerical complications inherent in the model.

Another soil-structure interaction problem, where a strip footing is placed on a thick clay stratum, is considered for numerical simulation. The simulation is carried out by a finite element mesh composed of 445 eight-node serendipity elements under simplified plane strain conditions (Figure 6). Load is transferred to the soil through a wall of thickness 0.4 m on a foundation 2.4 m wide and 0.4 m high. The configuration has symmetry, and the far boundaries of the soil domain are considered at distances

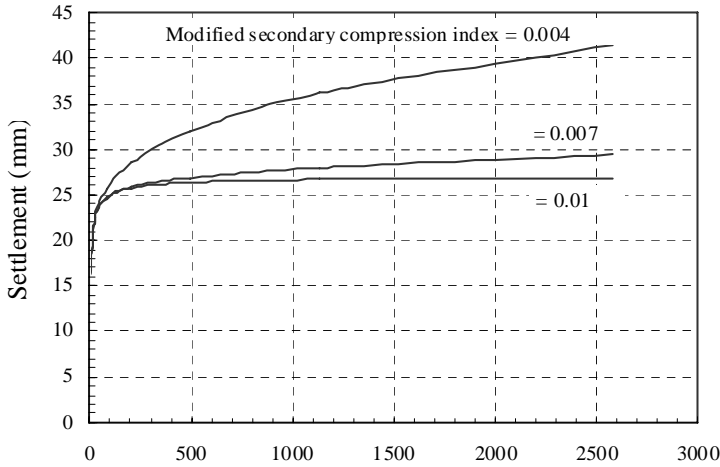


Figure 4. Settlement behavior of the center point with modified secondary compression index.

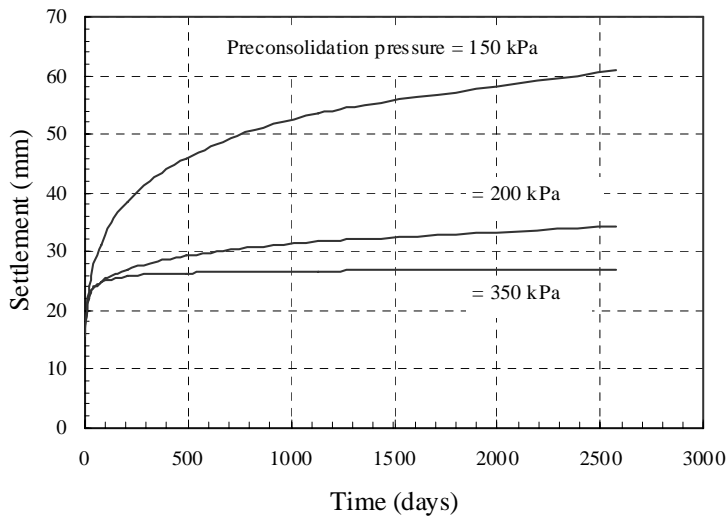


Figure 5. Settlement behavior of the center point with preconsolidation pressure.

sufficiently far from the foundation to render the boundary effects on the interaction problem insignificant. A structural load of 300 kN/m is assumed to act along the wall, equivalent to a load of 125 kPa transferred to the soil through the foundation. The wall and the footing materials were selected as concrete and the material properties of the soil are given in (30).

The problem configuration shown in Figure 6 deals with a soil-structure interaction that can often exist in the real field. By taking L as the ratio of distance to the point from the center of the loaded area to the half the total foundation width (1.2 m), the total settlement with time is shown in Figure 7 for three selected points at the foundation base level. According to this figure, the rate of settlement

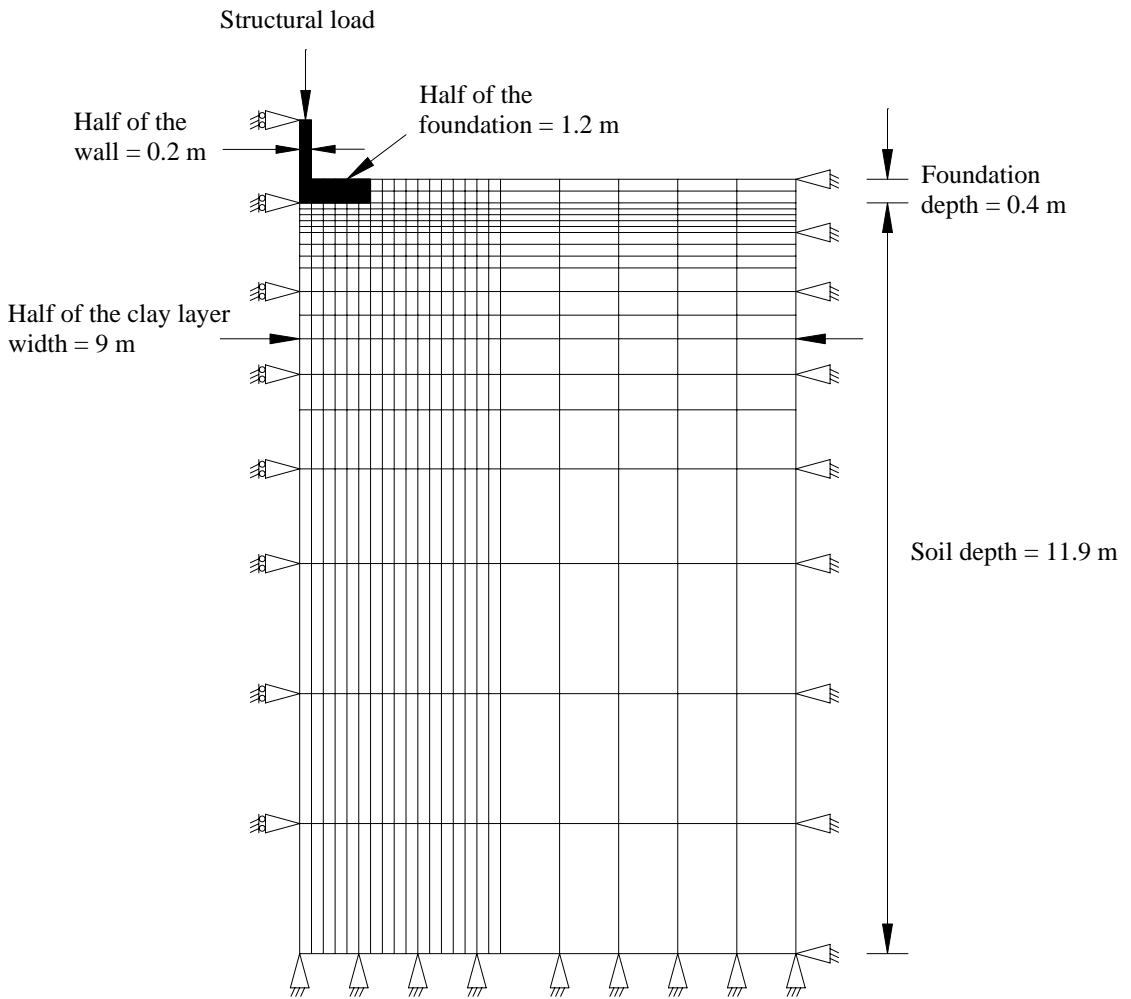


Figure 6. Finite element mesh and loading arrangement for the problem considered for numerical simulation.

decreases, whereby during the first year it has a rate of 4 mm per year while after eight years it has a rate of 1mm per year. The settlement of the foundation base with time is shown in [Figure 8](#), which indicates that delayed settlement is several times the instant settlement. The predicted instant (elastic) settlement is about 7.5 mm and delayed settlement is about 29 mm underneath the loaded foundation after approximately eight years.

The vertical average normal stress distribution in the soil along vertical sections at distances of 0.1 m, 0.5 m, 1.1 m and 2.1 m away from the centerline with time are shown in [Figures 9–12](#), respectively. [Figures 9–11](#) show the time dependent variation of vertical average normal stress in the creeping material along three vertical sections underneath the loaded foundation, and indicate that stresses increase with time along the depth, towards the applied average stress at the base. This is equivalent to the geological phenomena whereby rocks undergoing creep over time reach lithostatic states of stress in the long term.

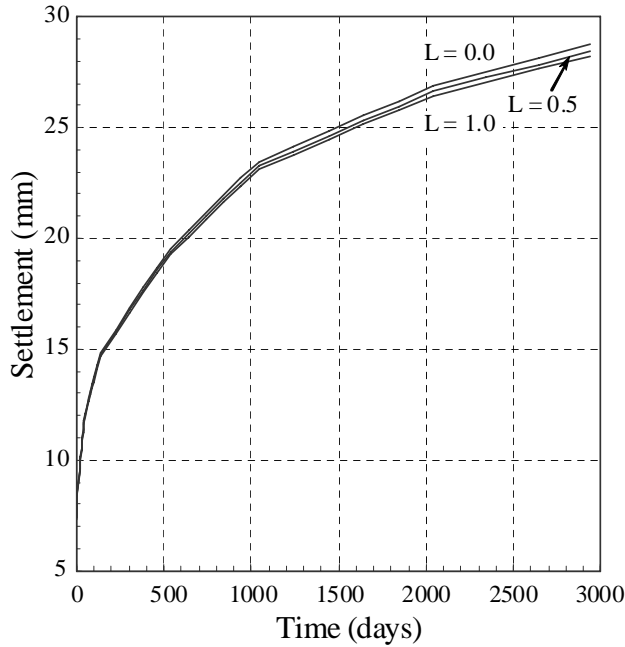


Figure 7. Settlement behavior of three selected points at the foundation level with time. $L = (\text{distance from center point})/1.2 \text{ m}$.

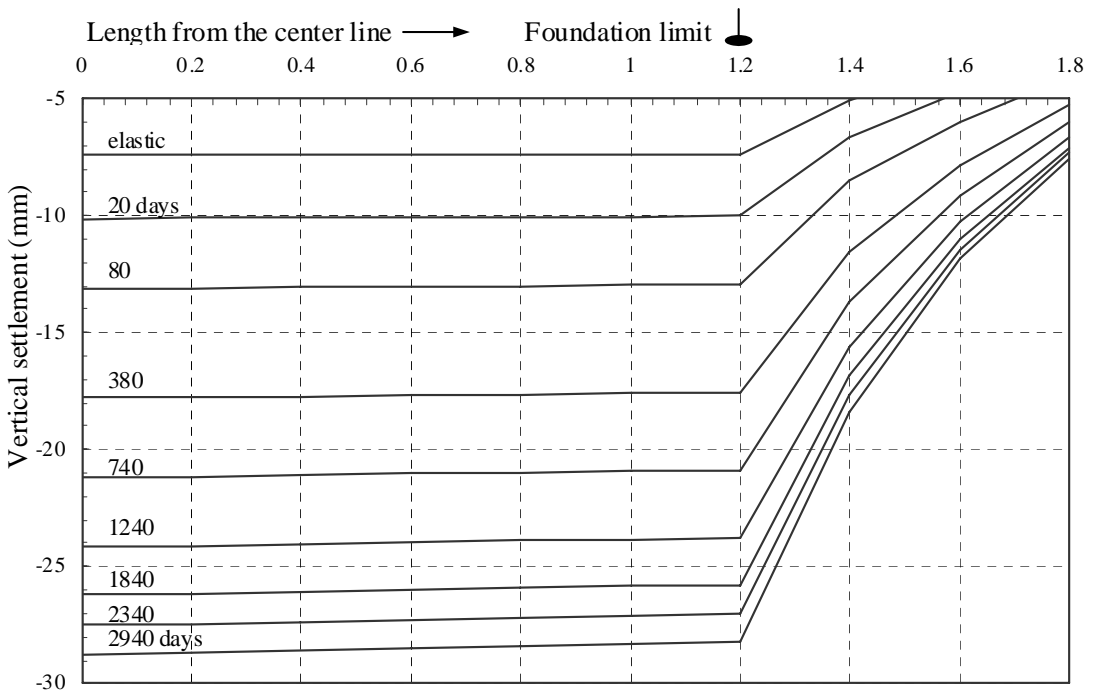


Figure 8. Total settlement behavior at the foundation level with time.

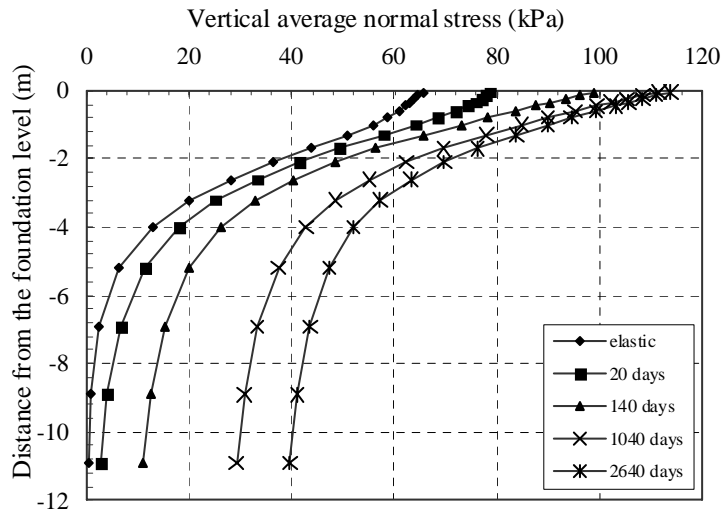


Figure 9. Average normal stress distribution at a distance of 0.1 m from the centerline (underneath the foundation) with time.

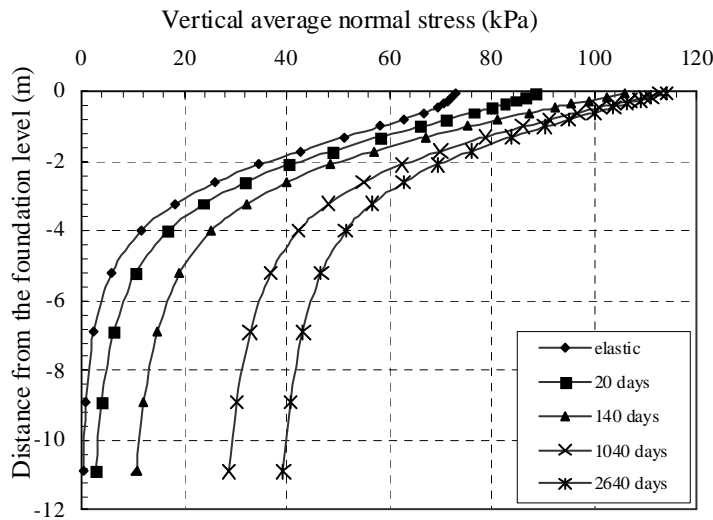


Figure 10. Average normal stress distribution at a distance of 0.5 m from the centerline (underneath the foundation) with time.

The stress distribution at a vertical section outside the foundation width is shown in Figure 12. The time dependent average shear stress distributions in the soil along vertical sections at distances of 0.5 m and 1.1 m away from the centerline are shown in Figures 13 and 14, respectively. A general reduction in average shear stress with time underneath the loaded foundation can be seen (under the ultimate lithostatic state expected, shear stress tend to vanish). Figures 12, 13 and 14 show that the far field effects are insignificant in the general case. A similar trend is shown by the elastic solution indicated on Figures 9, 10 and 11. However, under the loaded patch, the normal vertical stress in the soil medium

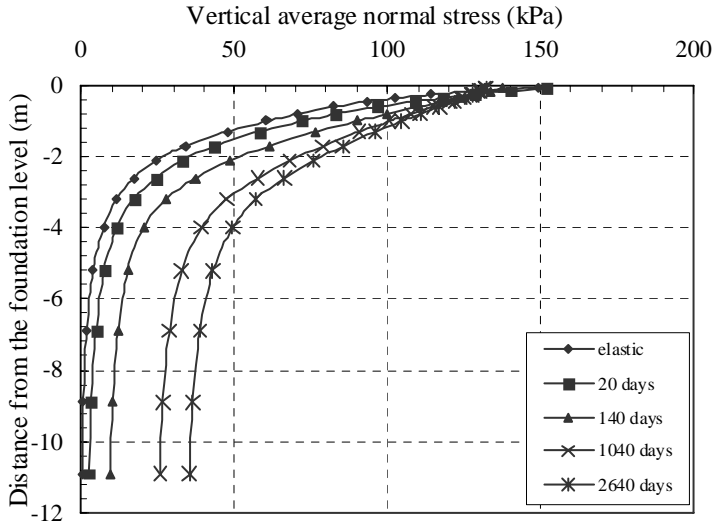


Figure 11. Average normal stress distribution at a distance of 1.1 m from the centerline (underneath the foundation) with time.

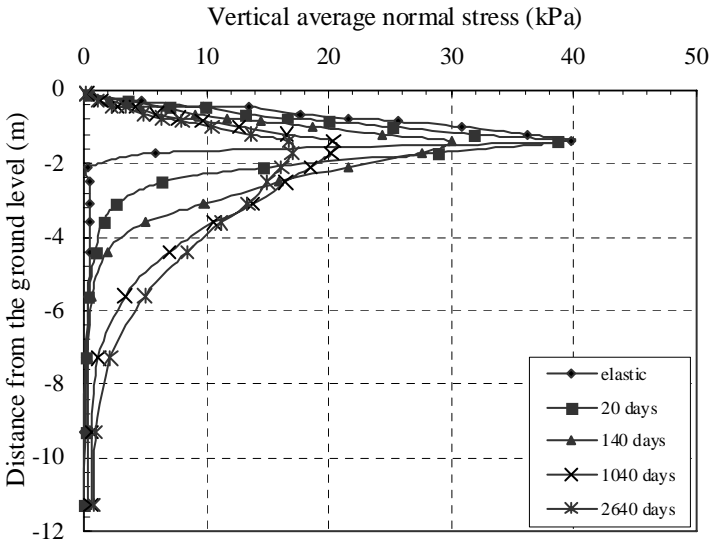


Figure 12. Average normal stress distribution at a distance of 2.1 m from the centerline (outside the foundation) with time.

keeps on increasing with time towards the magnitude of the pressure applied on the footing as a result of the creep of the material, regardless of the depth of the far boundary.

It is noted that the numerical values presented in this analysis are dependent on the selected material parameters which are similar to Haney clay [Vaid and Campanella 1977]. However, the numerically predicted results of the present research compares well with those monitored in the field as reported by Bjerrum [1967]. The numerically predicted results for the soil-structure interaction problem (given by

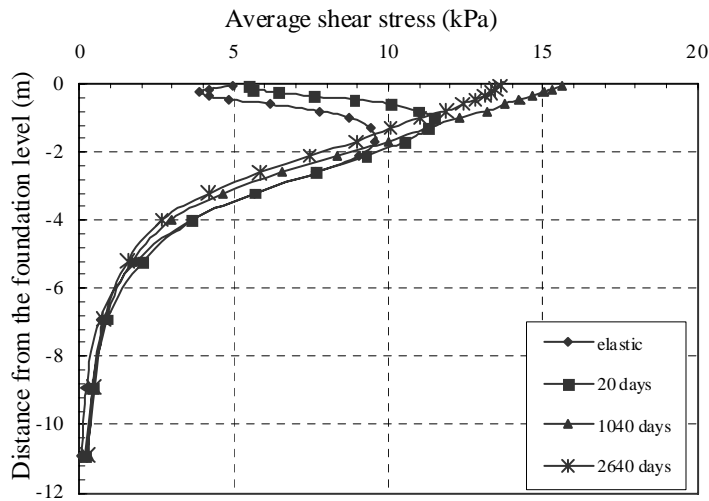


Figure 13. Average shear stress distribution at a distance of 0.5 m from the centerline (underneath the foundation) with time.

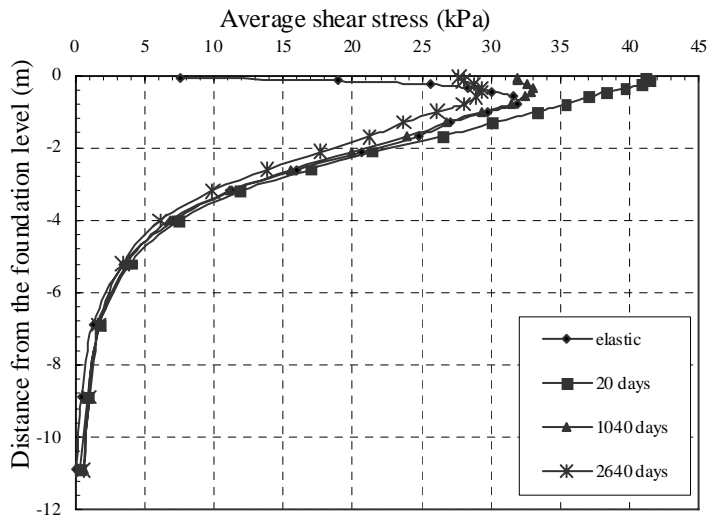


Figure 14. Average shear stress distribution at a distance of 1.1 m from the centerline (underneath the foundation) with time.

Figure 6) are shown in Figure 15, which depicts the time-dependent settlement under the mid-point of the foundation. This time-settlement curve in this last figure shows a behavior qualitatively similar to the monitored behavior of two buildings: Skoger Sparebank Building, Norway and Konnerud Gate 16 Building, Norway, given by Bjerrum [1967], and reproduced approximately in Figure 16.

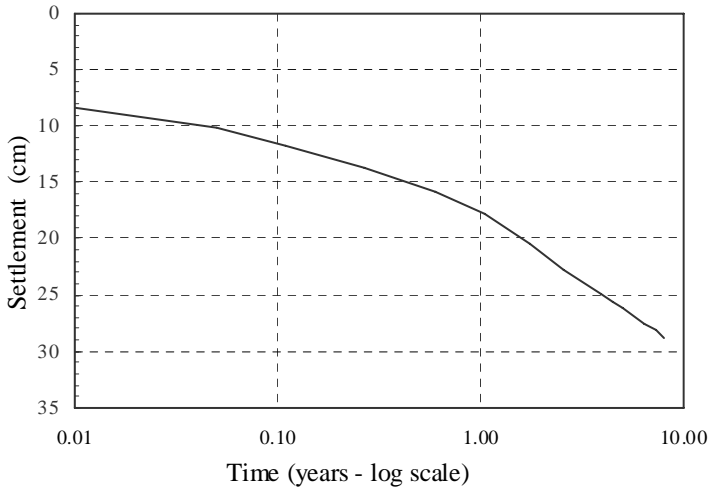


Figure 15. Settlement predicted for the mid-point of foundation depicted in Figure 5 by the finite element analysis.

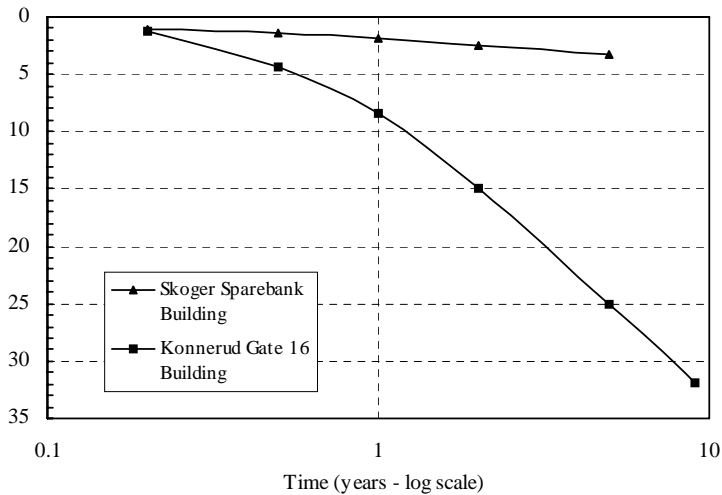


Figure 16. The monitored settlement behavior of the Skoger Sparebank Building, Norway and the Konnerud Gate 16 Building, Norway. From Bjerrum [1967, Figures 23, 25].

7. Conclusion

The modified soil creep model of Bjerrum [1967] has been generalized to multidimensions and implemented in a time-incrementing, iterative, nonlinear finite element code. Analyses were conducted for two cases of a loaded strip footing placed on a clay stratum, under the assumption of simplified plane strain conditions. The sensitivity of settlement predicted by the model to various material parameters is demonstrated. The model predicts that delayed (creep) settlement can be several times the instant (elastic) settlement. The vertical normal stresses under the loaded foundations increase with time towards the

applied vertical pressure magnitude and the shear stress under the loaded foundation decreases with time. This predicted behavior is in confirmation with the tendency of a creeping material to reach a lithostatic state of stress in the long term. The predicted numerical values, while dependent on the selected magnitudes of material parameters, compare qualitatively with reported field data given by Bjerrum. Due to the complications of nonlinear relationships involved in the model, the numerical algorithm experiences some difficulties if arbitrary material parameters are selected. The developed model can be extended by incorporating nonlinear elasticity for elastic strains which was not considered in the present study. But it was seen to function and yield results that capture the essential trends shown by test data for valid material parameters. The computer code developed here, when further developed and verified with field data, would be a useful research tool for estimating settlements in structures founded on soils exhibiting creep.

Acknowledgments

The authors extend their gratitude to the Science and Technology Personnel Development Project of the Ministry of Science and Technology, Sri Lanka, and the Asian Development Bank, who funded this research program. This work was carried out while Madurapperuma was at the Department of Civil Engineering, University of Moratuwa, Sri Lanka.

References

- [Adachi and Oka 1982] T. Adachi and F. Oka, "Constitutive equation for normally consolidated clays based on elasto-viscoplasticity", *Soils Found.* **22** (1982), 57–70.
- [Adachi and Okano 1974] T. Adachi and F. Okano, "A constitutive equation for normally consolidated clay", *Soils Found.* **14** (1974), 55–73.
- [Balasubramaniam and Brenner 1981] A. S. Balasubramaniam and R. P. Brenner, "Consolidation and settlement of soft clay", pp. 480–560 in *Soft clay engineering*, edited by E. W. Brand and R. P. Brenner, Elsevier, New York, 1981.
- [Bjerrum 1967] L. Bjerrum, "Engineering geology of Norwegian normally consolidated marine clays as related to settlements of buildings", *Géotechnique* **17** (1967), 81–118.
- [Borja and Kavazanjian 1985] R. I. Borja and E. Kavazanjian, "A constitutive model for the σ - ϵ - t behavior of wet clays", *Géotechnique* **35** (1985), 283–298.
- [Brinkgreve 2002] R. B. J. Brinkgreve, *PLAXIS finite element code for soil and rock analyses: user manual*, Balkema, Rotterdam, 2002.
- [Butterfield 1979] R. Butterfield, "A natural compression law for soils (an advance on e - $\log p'$)", *Géotechnique* **29** (1979), 469–480.
- [Garlanger 1972] J. E. Garlanger, "The consolidation of soils exhibiting creep under constant effective stress", *Géotechnique* **22** (1972), 71–78.
- [Iizuka and Ohta 1987] A. Iizuka and H. Ohta, "A determination procedure of input parameters in elasto-viscoplastic finite element analysis", *Soils Found.* **27** (1987), 71–87.
- [Janbu 1969] N. Janbu, "The resistance concept applied to soils", pp. 191–196 in *Proceedings of the 7th ICSMFE* (Mexico City, 1969), vol. 1, Sociedad Mexicana de Mecánica de Suelos, Mexico City, 1969.
- [Puswewala et al. 1992] U. G. A. Puswewala, R. K. N. D. Rajapakse, L. Domaschuk, and R. P. Lach, "Finite element modelling of pressuremeter tests and footings on frozen soils", *Int. J. Numer. Anal. Methods Geomech.* **16**:5 (1992), 351–375.
- [Roscoe and Burland 1968] K. H. Roscoe and J. B. Burland, "On the generalized stress-strain behavior of 'wet' clay", pp. 535–609 in *Engineering plasticity*, edited by J. Heyman and F. A. Leckie, Cambridge, Cambridge, 1968.

- [Stolle et al. 1997] D. F. E. Stolle, P. G. Bonnier, and P. A. Vermeer, “A soft soil model and experiences with two integration schemes”, pp. 123–128 in *Numerical models in geomechanics, NUMOG VI: Proceedings of the 6th International Symposium on Numerical Models in Geomechanics* (Montréal, 1997), edited by S. Pietruszczak and G. N. Pande, Balkema, Rotterdam, 1997.
- [Terzaghi 1931] K. Terzaghi, “The static rigidity of plastic clays”, *J. Rheol.* **2**:3 (1931), 253–262.
- [Vaid and Campanella 1977] Y. Vaid and R. G. Campanella, “Time-dependent behavior of undisturbed clay”, *J. Geotech. Eng. (ASCE)* **103**:7 (1977), 693–709.
- [Vermeer and Neher 1999] P. A. Vermeer and H. P. Neher, “A soft soil model that accounts for creep”, pp. 249–261 in *Beyond 2000 in computational geotechnics: 10 years of PLAXIS International* (Amsterdam, 1999), edited by R. B. J. Brinkgreve, Balkema, Rotterdam, 1999.
- [Vermeer et al. 1998] P. A. Vermeer, D. F. E. Stolle, and P. G. Bonnier, “From the classical theory of secondary compression to modern creep analysis”, pp. 2469–2478 in *Computer methods and advances in geomechanics: proceedings of the Ninth International Conference on Computer Methods and Advances in Geomechanics* (Wuhan, 1997), vol. 4, edited by J.-X. Yuan, Balkema, Rotterdam, 1998.
- [Wheeler et al. 2003] S. J. Wheeler, M. Cudny, H. Neher, and C. Wiltafsky, “Some developments in constitutive modeling of soft clays”, pp. 3–22 in *International Workshop on Geotechnics of Soft Soils: theory and practice* (Noordwijkerhout, 2003), edited by P. A. Vermeer et al., VGE, Verlag Glückauf, Essen, 2003.

Received 30 May 2007. Revised 18 Nov 2008. Accepted 20 Nov 2008.

M. A. K. M. MADURAPPERUMA: ma.k.aa@m.titech.ac.jp

Department of Civil Engineering, Tokyo Institute of Technology, M-19, 2-12-1, O-okayama, Meguro-ku, Tokyo 152-8552, Japan

<http://www.cv.titech.ac.jp/~anil.lab/>

U. G. A. PUSWEWALA: head@earth.mrt.ac.lk

Department of Civil Engineering, University of Moratuwa, Katubedda, Moratuwa, Western Province, Sri Lanka

<http://www.civil.mrt.ac.lk/>

ON A WINKLER LIGAMENT CONTACT BETWEEN A RIGID DISC AND AN ELASTIC HALFSPACE

A. P. S. SELVADURAI, T. SCARPAS AND N. KRINGOS

This paper presents a variational solution to the problem of the contact between an isotropic elastic halfspace and a rigid circular indenter, where the contact is achieved through a set of ligaments modeled by a continuously distributed layer of Winkler elements. The problem is of interest to the modeling of the ligament-type contact mechanics between a rigid cylinder and a substrate. The limiting solution for Boussinesq indentation is modified to take into consideration small but finite influences of the elastic stiffness of the ligaments forming the interface layer.

1. Introduction

The mechanics of contact between a component and a substrate is of interest to many areas of materials engineering and materials science. The classical definition of adhesive contact between two material regions assumes the complete compatibility of displacements between the two regions. Other forms of nonclassical contacts include interacting surfaces that exhibit limited adhesion, frictional constraints and slip. The developments, both fundamental and applied, in this area are too numerous to cite individually. We mention [Duvaut and Lions 1976; Selvadurai 1979; 2003; 2007; Gladwell 1980; Haslinger and Janovský 1983; Johnson 1985; Ciarlet 1988; Frémond 1988; Moreau et al. 1988; Curnier 1992; Klarbring 1993; Selvadurai and Boulon 1995] for further reviews of the topic. The idealization of the nature of adhesion is in itself a complex problem, where the fine structure and properties of the media/processes contributing to the generation of the adhesion need to be taken into consideration in developing a plausible model that can determine the onset of debonding [Plueddemann 1974; Anderson et al. 1977; de Lollis 1985; Pizzi and Mittal 1994; Mittal 1995]. Furthermore, depending on the nature of the interacting regions, the contact between the bodies in adhesive contact can in fact be induced at discrete regions at the micromechanical scale, which can contribute to the formation of a *structural model* of the adhesion zone as opposed to a *continuum model*. A model of this type was first introduced by Barenblatt [1959; 1962] in the discussion of brittle fracture and separation at material surfaces and the concepts were adopted and extended in [Dugdale 1960; Goodier 1968; Goodier and Field 1963; Goodier and Kanninen 1966; Kanninen 1970] in their studies of the ductile fracture problems, where cohesive forces of finite magnitude are present at the extremities of a decohesion zone. A key feature in these models is the structural or reduced continuum representation of the decohesion zone. The linear and nonlinear ligament models also allow for the interpretation of intermolecular and surface forces at adhesive zones [Tonck et al. 1988; Israelachvili 1992]. In this paper, we adopt the basic concepts expounded in the structural model of contact zone response and apply it to the modeling of a contact

Keywords: Winkler ligaments, contact problem, variational method, adhesive contact, compliance of indenter, rigid circular indenter, variational solution, elastic halfspace indentation.

between an isotropic elastic halfspace region and a rigid cylindrical indenter, which is achieved through a continuously distributed set of ligament connections. The term *bonded* or *adhesive* is avoided in the present discussion since these specifically refer to phenomena where complete continuity of displacements is established at the connecting zone. In particular, we restrict attention to the modeling of the interface as a series of Winkler elements, although the approach can be extended to include more advanced structural contacts represented by either Vlazov- and Reissner-type layers [Selvadurai 1979], which provide shear interaction between the Winkler elements, or the constrained elastic layer, where certain traction boundary conditions at the edges of the ligament zones are satisfied in an integral sense. A more appropriate terminology that describes this type of contact is *structural bonding*. An alternative to this approach is to consider the connecting layer as an elastic continuum itself. An example of such an application with relevance to nanorheological analysis of the contact between an elastic sphere and a plane separated by an interfacial elastic layer is given by Trifa et al. [2002] in connection with the compressive load transfer at a ligament zone. The Winkler ligament approach adopted here is perhaps not the most all-encompassing treatment of the contact process, but it allows the incorporation of the influences of a material characteristic that could be attributed to the zones that generate the bonding mechanism. In particular, the deformability characteristics of the substrate are accounted for in the modeling.

In this paper we consider the axisymmetric problem of the contact between a rigid cylinder and an isotropic elastic halfspace region, where the structural bonding zone corresponds to a series of closely spaced Winkler ligaments. The conventional approach to the solution of the resulting mixed boundary-value problem is to reduce the analysis to the solution of a Fredholm integral equation of the second kind, which can only be solved in an approximate fashion either by reducing it to a matrix equation or through the introduction of a series representation of the solution or through a variational technique itself. Here, we present a much simpler solution that is based on the application of a direct variational technique. The variational technique has been successfully applied to the study of the mechanics of contact between elastic continua and between structural elements and elastic continua [Kalker 1977; Selvadurai 1979; 1980; 1984; Karasudhi 1991]. This latter approach is a suitable approximation, in the sense that it yields results in closed form, which can be used to establish the influence of the idealized ligament zone in the load transfer mechanism between the rigid cylinder and the elastic halfspace as well as in the development of ligament adhesive stresses between the two regions.

2. The Winkler ligament contact problem

We consider the problem of a rigid circular cylinder of radius a and with a flat base, which is connected to an isotropic elastic halfspace region. The connectivity is provided by a set of Winkler elements that establishes continuity of displacements between the rigid cylinder and the elastic halfspace (Figure 1). The Winkler elements are characterized by a linear load-displacement relationship, although the analysis can be easily extended to include a nonlinear Winkler model with no provision for energy dissipation. The rigid cylinder is subjected to an axisymmetric force of magnitude P which induces rigid body displacement of the cylinder, a deformation of the set of Winkler ligaments and the displacements of the surface of the halfspace region.

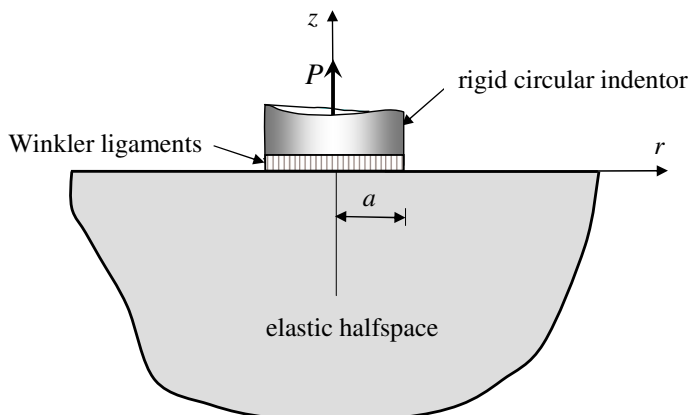


Figure 1. Contact problem for a rigid cylinder achieved through a layer of Winkler ligaments

In the variational approach adopted here, we assume that the vertical displacements of the surface of the halfspace region, within the contact region, can be approximated by a kinematically admissible displacement of the form

$$u_z^{HS}(r, 0) = a \left(C_1 - C_2 \left(\frac{r}{a} \right)^2 \right); \quad r \in (0, a), \tag{1}$$

where C_1 and C_2 are arbitrary constants. Similarly, we assume that due to the loading of the rigid disc, the Winkler ligaments experience a displacement

$$u_z^W(r, 0) = a \left(C_3 + C_2 \left(\frac{r}{a} \right)^2 \right); \quad r \in (0, a), \tag{2}$$

where C_3 is an arbitrary constant. The displacement fields (1) and (2) satisfy the kinematic constraints necessary for the compatibility of the displacements between the elastic halfspace, the Winkler layer and the rigid disc. The prescribed displacement field in the system is therefore indeterminate to within the constants C_i ($i = 1, 2, 3$).

In order to apply the variational procedure, we need to evaluate the total energy of the system consistent with the displacement fields defined by Equations (1) and (2). The total energy of the systems consists of the strain energy of the halfspace region, the strain energy of the Winkler layer and the potential energy of the applied load. In order to calculate the strain energy of the halfspace region, we require the solution to a mixed boundary value problem where displacements are prescribed over the contact region. We consider the mixed boundary-value problem related to a halfspace region where the boundary plane $z = 0$ is subjected to the boundary conditions

$$u_z^{HS}(r, 0) = w(r) \quad \text{for } r \in (0, a), \tag{3}$$

$$\sigma_{zz}(r, 0) = 0 \quad \text{for } r \in (a, \infty), \tag{4}$$

$$\sigma_{rz}(r, 0) = 0 \quad \text{for } r \in (0, \infty), \tag{5}$$

where u_z^{HS} is the axial displacement of the halfspace region and σ_{zz} and σ_{rz} are the stress components referred to the cylindrical polar coordinate system (r, θ, z) . In addition, the displacements and stress fields should satisfy regularity conditions, which ensure that the displacement and stress fields decay uniformly to zero as $(r, z) \rightarrow \infty$. The solution of the mixed boundary-value problem defined by Equations (3)–(5) is standard and is given in the classical texts [Sneddon 1951; 1966; Green and Zerna 1968; Selvadurai 1979; 2000a; Gladwell 1980]. Following Green and Zerna [1968] it can be shown that when the shear traction vanishes on the plane $z = 0$, the solution to the elasticity problem can be expressed in terms of a single potential function $\phi(r, z)$, such that

$$2Gu_z(r, z) = z \frac{\partial^2 \phi}{\partial u^2} - 2(1-\nu) \frac{\partial \phi}{\partial z}, \quad \sigma_{zz}(r, z) = z \frac{\partial^3 \phi}{\partial z^3} - \frac{\partial^2 \phi}{\partial z^2}, \quad \sigma_{rz}(r, z) = z \frac{\partial^2 \phi}{\partial r \partial z},$$

where G and ν are the linear elastic shear modulus and Poisson's ratio for the halfspace material. Using results of potential theory we use a representation of $\partial \phi / \partial z$ in the form

$$\frac{\partial \phi}{\partial z} = \frac{1}{2} \int_{-a}^a \frac{g(t) dt}{\sqrt{\{r^2 + (z + it)^2\}}},$$

where $g(t)$ is an arbitrary function. For this representation in terms of the potential function, the boundary condition (5) is explicitly satisfied and the remaining boundary conditions (3) and (4) are equivalent to an Abel integral equation of the form

$$w(r) = \int_0^r \frac{g(t) dt}{\sqrt{r^2 - t^2}}$$

which can be solved [Sneddon 1966; Gladwell 1980; Gorenflo and Vessella 1991; Selvadurai 2000a] in the exact form

$$g(t) = \frac{2}{\pi} \frac{d}{dt} \int_0^t \frac{r w(r) dr}{\sqrt{t^2 - r^2}}.$$

The stresses within the contact region can be expressed as

$$\sigma_{zz}(r, 0) = -\frac{G}{1-\nu} \frac{1}{r} \frac{\partial}{\partial r} \int_r^a \frac{t g(t) dt}{\sqrt{t^2 - r^2}}.$$

Considering the assumed form of the displacement of the halfspace region within the contact zone, defined by (1), it can be shown that the induced stresses are given by

$$\sigma_{zz}(r, 0) = \frac{2G}{\pi(1-\nu)} \left[\frac{C_1}{\sqrt{a^2 - r^2}} + \frac{2C_2}{a^2} \left(\sqrt{a^2 - r^2} - \frac{r^2}{\sqrt{a^2 - r^2}} \right) \right]. \quad (6)$$

The strain energy of the halfspace region can be obtained by calculating the work done by the normal tractions in the contact zone, that is,

$$U_{\text{HS}} = \frac{1}{2} \int_0^{2\pi} \int_0^a u_z^{\text{HS}}(r, 0) \sigma_{zz}(r, 0) r dr d\theta.$$

Similarly, the strain energy of the Winkler ligament zone can be obtained from the result

$$U_W = \frac{1}{2} \int_0^{2\pi} \int_0^a k [u_z^W(r, 0)]^2 r dr d\theta,$$

where k is the stiffness of the Winkler ligament per unit area. The work of the applied force P is given by $W_P = -P[u_z^{\text{HS}}(0, 0) + u_z^W(0, 0)]$. The total potential energy function for the system can be evaluated in the form

$$U = \frac{2Ga^3}{(1-\nu)} \left[C_1^2 - \frac{4}{3}C_1C_2 + \frac{4}{5}C_2^2 \right] + \frac{\pi ka^4}{2} \left[\frac{1}{3}C_2^2 + C_2C_3 + C_3^2 \right] - Pa[C_1 + C_3].$$

Considering the principle of minimum total potential energy for a conservative system, the arbitrary constants are determined from the conditions

$$\frac{\partial U}{\partial C_1} = \frac{\partial U}{\partial C_2} = \frac{\partial U}{\partial C_3} = 0$$

which gives the undetermined parameters C_1 , C_2 and C_3 . The constants take the forms

$$[C_1; C_2; C_3] = \frac{\bar{P}}{(16 + 15\Omega)} \left[3(7 + 5\Omega); \frac{15}{2}; \frac{4}{\Omega} \right], \quad (7)$$

where $\bar{P} = P(1-\nu)/4Ga^2$ and $\Omega = \pi ka(1-\nu)/16G$. The formal variational solution for the contact problem associated with a set of Winkler ligaments is given by (1), (2), (6) and (7). Both the state of stress within the halfspace region and within the zone of Winkler ligaments can be determined from these results in conjunction with Boussinesq's solution for the loading of a halfspace region by a concentrated normal force [Timoshenko and Goodier 1970; Davis and Selvadurai 1996; Selvadurai 2001].

3. The role of the Winkler ligament zone

An inspection of the variational solution indicates that as the relative stiffness of the Winkler ligament zone (as defined by the parameter Ω) increases, the terms incorporating C_2 and C_3 will have a diminishing influence on the load transfer process. In the limit as $\Omega \rightarrow \infty$, $C_1 \rightarrow \bar{P}$ and the displacement of the rigid cylinder is given by $w(0) = P(1-\nu)/4Ga$, and the contact stress within the circular region is

$$\sigma_{zz}(r, 0) = P/2\pi a\sqrt{a^2 - r^2},$$

which is Boussinesq's classical result for the indentation of a halfspace by a rigid circular indenter with a flat base. In terms of the contact problem, a ligament zone of high relative stiffness will invariably result in the development of a singular stress state at the boundary of the circular cylinder, which would represent a potential location for the development of delamination. For a finite value of the relative stiffness parameter Ω , the displacement of the rigid cylinder as well as the stresses in the ligament zone are influenced by the Winkler ligament stiffness k . Figure 2 illustrates the variation in the normalized displacement of the rigid disc $\bar{\Delta}$ (defined as $4G\Delta a/P(1-\nu)$, where Δ is the displacement of the rigid disc) as a function of the relative stiffness parameter Ω . As can be observed, the reduction to the case of the classical Boussinesq rigid punch problem is achieved for a value of $\Omega > 5$. The contact stress at the cylinder-Winkler ligament layer can similarly be evaluated in explicit form. From (6) and (7) we obtain

$$\bar{\sigma} = \frac{\sigma_{zz}(r, 0)}{\sigma_0} = \frac{1}{2(15\Omega + 16)} \left[\frac{(15\Omega + 21)}{\sqrt{1 - \rho^2}} + 15 \left(\sqrt{1 - \rho^2} - \frac{\rho^2}{\sqrt{1 - \rho^2}} \right) \right]; \quad \rho \in (0, 1), \quad (8)$$

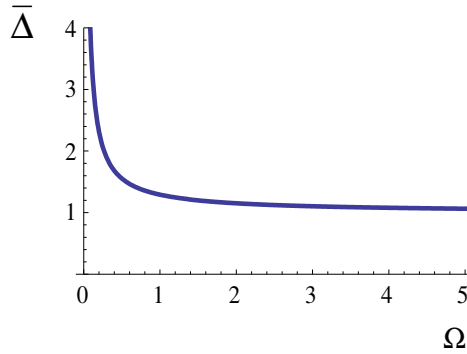


Figure 2. Influence of the relative stiffness parameter on the displacement of the bonded disc

where $\sigma_0 = P/\pi a^2$ and $\rho = r/a$. **Figure 3** illustrates the variation in the contact stress as a function of the relative stiffness parameter Ω . As $\Omega \rightarrow 0$, the normal stresses exhibit a nonuniform distribution at the adhesive zone, but maintain the singular character, derived from the appropriate terms in (8). As $\Omega \rightarrow \infty$, the adhesive stresses reduce to the Boussinesq-type distribution, with singular behaviour as $\rho \rightarrow 1$. It is of interest to examine the influence of the relative stiffness parameter Ω in moderating the stress intensity factor at the boundary of the ligament zone, which can be compared with the critical stress intensity factor necessary to initiate brittle fracture at the boundary of the adhesion zone. Considering the definition of the Mode I stress intensity factor we have

$$K_I^a = \lim_{r \rightarrow a^-} [2(a - r)]^{1/2} \sigma_{zz}(r, 0). \tag{9}$$

Considering (8) and (9) we obtain

$$K_I^a = \frac{\sigma_0 \sqrt{a}}{2} \frac{15\Omega + 6}{15\Omega + 16}.$$

Again as $\Omega \rightarrow \infty$, we recover from the above equation the classical result for the stress intensity factor associated with the axisymmetric problem of an elastic medium of infinite extent with an intact region of radius a and subjected to a far-field stress that is equivalent to a total force P [Kassir and Sih 1968]. Also, as $\Omega \rightarrow 0$, the stress intensity factor approaches the value $K_I^a = 3\sigma_0\sqrt{a}/16$. This result is consistent with the observation made by Selvadurai [2000b] with regard to the Mode I stress intensity factor for a penny-shaped crack that is located at the interface of a functionally graded material where the elastic modulus exhibits a bounded exponential variation in the axial direction. In the case where the linear elastic shear modulus at the plane of the crack is lower than the finite value of the far-field shear modulus, the Mode I stress intensity factor is lower than the corresponding value applicable to the problem of a penny-shaped crack located in homogeneous elastic solid.

4. Concluding remarks

This paper presents a relatively elementary study of the mechanics of a Winkler ligament zone that forms the structural bonding between a rigid cylinder and an isotropic elastic substrate of semi-infinite extent. The variational approach presented here is an approximation to the more complex formulation that would involve a complete analysis of a Fredholm integral equation of the second kind, which will invariably

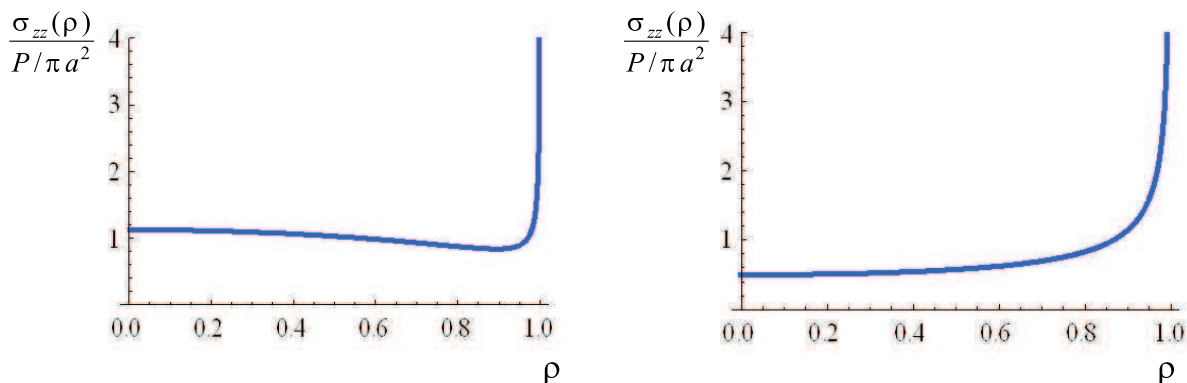


Figure 3. Adhesive stresses at the bonded zone [$\Omega \rightarrow 0$] (left) and [$\Omega \rightarrow \infty$] (right).

entail a numerical solution technique. The variational procedure provides a convenient approach for examining the particular influences of the Winkler ligament zone that provides the structural bonding between the rigid cylinder and the halfspace region. The displacement functions chosen satisfy the kinematic constraints and the range of the polynomial expressions used can be extended to include further terms. Such a treatment is perhaps unwarranted in view of the elementary nature of the modeling of the ligament zone as a continuous distribution of unconnected spring elements. The elementary analysis nonetheless illustrates trends that are important to the understanding of the mechanics of load transfer at ligament zones. The form of the displacement functions chosen for the variational treatment still maintains the singular behaviour of the stress states in the ligament zone for $\Omega \in (0, \infty)$, although such an interpretation should be viewed with some caution, since at the outset the stiffness of the ligament zone is assumed to be finite. In particular, it is noted that the presence of a ligament zone of low relative stiffness has a tendency to moderate the stress intensity factor at the boundary of the ligament zone. It should also be borne in mind that structural adherents with lower stiffness generally tend to possess lower resistance to fracture, indicative of low values of the critical stress intensity factors. Finally, the variational approach for the solution of contact problems of this nature would be most effective when the ligaments exhibit nonlinear force-displacement relationships. In such a case, the conventional integral equation approach leads to nonlinear forms that are not easily solved, except through the use of either perturbation schemes or a method of successive approximations. The variational approach with improved representations for the deflected shapes can lead to compact results in exact closed forms.

Acknowledgements

The first author thanks the Delft University of Technology for an appointment as Guest Professor in the Faculty of Civil Engineering and Geosciences, which provided the opportunity to collaborate with members of the Structural Mechanics Section. The work was supported in part by the Max Planck Forschungspreis in the Engineering Sciences awarded to A. P. S. Selvadurai by the Max Planck Gesellschaft, Germany. The authors are grateful to the comments made by a reviewer.

References

- [Anderson et al. 1977] G. P. Anderson, S. J. Bennet, and K. L. de Vries, *Analysis and testing of adhesive bonds*, Academic Press, New York, 1977.
- [Barenblatt 1959] G. I. Barenblatt, “The formation of equilibrium cracks during brittle fracture: General ideas and hypotheses: Axially-symmetric cracks”, *Prikl. Mat. Mech.* **23**:3 (1959), 434–444. In Russian; translation in *J. Appl. Math. Mech.* **23**:3, 1959, 622–636.
- [Barenblatt 1962] G. I. Barenblatt, “The mathematical theory of equilibrium cracks in brittle fracture”, pp. 55–129 in *Advances in applied mechanics*, vol. 7, edited by H. L. Dryden and T. von Karman, Academic Press, New York, 1962.
- [Ciarlet 1988] P. G. Ciarlet, *Mathematical elasticity, I: Three-dimensional elasticity*, Studies in Mathematics and its Applications **20**, North Holland, Amsterdam, 1988.
- [Curnier 1992] A. Curnier (editor), *Proceedings of the International Symposium on Contact Mechanics* (Lausanne, 1992), Presses Polytechniques et Universitaires Romandes, Lausanne, 1992.
- [Davis and Selvadurai 1996] R. O. Davis and A. P. S. Selvadurai, *Elasticity and geomechanics*, Cambridge University Press, Cambridge, 1996.
- [Dugdale 1960] D. S. Dugdale, “Yielding of steel sheets with slits”, *J. Mech. Phys. Solids* **8**:2 (1960), 100–104.
- [Duvaut and Lions 1976] G. Duvaut and J.-L. Lions, *Inequalities in mechanics and physics*, Springer, Berlin, 1976.
- [Frémond 1988] M. Frémond, “Contact with adhesion”, pp. 157–185 in *Topics in non-smooth mechanics*, edited by J. J. Moreau et al., Birkhäuser, Basel, 1988.
- [Gladwell 1980] G. M. L. Gladwell, *Contact problems in the classical theory of elasticity*, Sijthoff and Noordhoff, Alphen aan den Rijn, 1980.
- [Goodier 1968] J. N. Goodier, “Mathematical theory of equilibrium cracks”, Chapter 1, pp. 1–66 in *Fracture — an advanced treatise, 2: Mathematical fundamentals*, edited by H. Liebowitz, Academic Press, San Diego, 1968.
- [Goodier and Field 1963] J. N. Goodier and F. A. Field, “Plastic energy dissipation in crack propagation”, pp. 103–118 in *Fracture of solids* (Maple Valley, WA, 1962), edited by D. C. Drucker and J. J. Gilman, Metallurgical Society Conferences **20**, Wiley Interscience, New York, 1963.
- [Goodier and Kanninen 1966] J. N. Goodier and M. F. Kanninen, “Crack propagation in a continuum model with non-linear atomic separation laws”, Technical report 165, Division of Engineering Mechanics, Stanford University, Stanford, CA, 1966.
- [Gorenflo and Vessella 1991] R. Gorenflo and S. Vessella, *Abel integral equations: Analysis and applications*, Lecture Notes in Mathematics **1461**, Springer, Berlin, 1991.
- [Green and Zerna 1968] A. E. Green and W. Zerna, *Theoretical elasticity*, 2nd ed., Clarendon Press, Oxford, 1968.
- [Haslinger and Janovský 1983] J. Haslinger and V. Janovský, “Contact problem with friction”, pp. 74–100 in *Trends in applications of pure mathematics to mechanics* (Bratislava, 1981), vol. IV, edited by J. Brilla, Monographs and Studies in Mathematics **20**, Pitman, Boston, 1983.
- [Israelachvili 1992] J. N. Israelachvili, *Intermolecular and surface forces*, Academic Press, New York, 1992.
- [Johnson 1985] K. L. Johnson, *Contact mechanics*, Cambridge University Press, Cambridge, 1985.
- [Kalker 1977] J. J. Kalker, “Variational principles of contact elastostatics”, *J. Inst. Math. Appl.* **20**:2 (1977), 199–219.
- [Kanninen 1970] M. F. Kanninen, “Plane deformation of the loaded straight edge of a semi-infinite linearly elastic body suspended on a Winkler layer”, *J. Appl. Mech. (ASME)* **37** (1970), 524–526.
- [Karasudhi 1991] P. Karasudhi, *Foundations of solid mechanics*, Solid Mechanics and its Applications **3**, Kluwer Academic Publishers, Dordrecht, 1991.
- [Kassir and Sih 1968] M. K. Kassir and G. C. Sih, “External elliptic crack in elastic solid”, *Int. J. Fract.* **4**:4 (1968), 347–356.
- [Klarbring 1993] A. Klarbring, “Mathematical programming in contact problems”, Chapter 7, pp. 233–263 in *Computational methods in contact mechanics*, edited by M. H. Aliabadi and C. A. Brebbia, Computational Mechanics, Southampton, 1993.
- [de Lollis 1985] N. J. de Lollis, *Adhesives, adherends, adhesion*, Krieger, Malabar, FL, 1985.
- [Mittal 1995] K. K. Mittal (editor), *Adhesion measurements of films and coatings*, VSP BV, Utrecht, 1995.

- [Moreau et al. 1988] J. J. Moreau, P. D. Panagiotopoulos, and G. Strang (editors), *Topics in non-smooth mechanics*, Birkhäuser, Basel, 1988.
- [Pizzi and Mittal 1994] A. Pizzi and K. L. Mittal (editors), *Handbook of adhesive technology*, Dekker, New York, 1994.
- [Plueddemann 1974] E. P. Plueddemann (editor), *Interfaces in polymer matrix composites*, Composite Materials **6**, Academic Press, New York, 1974.
- [Selvadurai 1979] A. P. S. Selvadurai, *Elastic analysis of soil-foundation interaction*, Developments in Geotechnical Engineering **17**, Elsevier, Amsterdam, 1979.
- [Selvadurai 1980] A. P. S. Selvadurai, “Elastic contact between a flexible circular plate and a transversely isotropic elastic halfspace”, *Int. J. Solids Struct.* **16**:2 (1980), 167–176.
- [Selvadurai 1984] A. P. S. Selvadurai, “A contact problem for a Reissner plate and an isotropic elastic halfspace”, *J. Méc. Théor. Appl.* **3** (1984), 181–196.
- [Selvadurai 2000a] A. P. S. Selvadurai, *Partial differential equations in mechanics, 2: The biharmonic equation, Poisson’s equation*, Springer, Berlin, 2000.
- [Selvadurai 2000b] A. P. S. Selvadurai, “The penny-shaped crack at a bonded plane with a localized elastic non-homogeneity”, *Eur. J. Mech. A Solids* **19**:3 (2000), 525–534.
- [Selvadurai 2001] A. P. S. Selvadurai, “On Boussinesq’s problem”, *Int. J. Eng. Sci.* **39**:3 (2001), 317–322.
- [Selvadurai 2003] A. P. S. Selvadurai, “On an invariance principle for unilateral contact at a bimaterial elastic interface”, *Int. J. Eng. Sci.* **41**:7 (2003), 721–739.
- [Selvadurai 2007] A. P. S. Selvadurai, “The analytical method in geomechanics”, *Appl. Mech. Rev.* **60**:3 (2007), 87–106.
- [Selvadurai and Boulon 1995] A. P. S. Selvadurai and M. J. Boulon (editors), *Mechanics of geomaterial interfaces*, Studies in Applied Mechanics **42**, Elsevier, Amsterdam, 1995.
- [Sneddon 1951] I. N. Sneddon, *Fourier transforms*, McGraw-Hill, New York, 1951.
- [Sneddon 1966] I. N. Sneddon, *Mixed boundary value problems in potential theory*, North Holland, Amsterdam, 1966.
- [Timoshenko and Goodier 1970] S. P. Timoshenko and J. N. Goodier, *Theory of elasticity*, McGraw-Hill, New York, 1970.
- [Tonck et al. 1988] A. Tonck, J. M. Georges, and J. L. Loubet, “Measurements of intermolecular forces and the rheology of dodecane between alumina surfaces”, *J. Colloid Interface Sci.* **126**:1 (1988), 150–163.
- [Trifa et al. 2002] M. Trifa, F. Auslender, and F. Sidoroff, “Nanorheological analysis of the sphere plane contact problem with interfacial films”, *Int. J. Eng. Sci.* **40**:2 (2002), 163–176.

Received 23 Jul 2007. Revised 8 Dec 2007. Accepted 10 Dec 2007.

A. P. S. SELVADURAI: patrick.selvadurai@mcgill.ca

Department of Civil Engineering and Applied Mechanics, McGill University, 817 Sherbrooke Street West, Montréal QC H3A 2K6, Canada

<http://www.mcgill.ca/civil/faculty/selvadurai/>

T. SCARPAS: a.scarpas@tudelft.nl

Section of Structural Mechanics, Faculty of Civil Engineering and Geosciences, Delft University of Technology, The Netherlands

N. KRINGOS: n.kringos@tudelft.nl

Section of Structural Mechanics, Faculty of Civil Engineering and Geosciences, Delft University of Technology, The Netherlands

DYNAMIC RESPONSE OF MULTIPLE FLEXIBLE STRIPS ON A MULTILAYERED POROELASTIC HALF-PLANE

TEERAPONG SENJUNTICHAJ AND WICHAIRAT KAEWJUEA

We study the dynamic response of multiple flexible strip foundations resting on a multilayered poroelastic half-plane subjected to time-harmonic vertical loading. The contact surface between the strip foundations and the half-plane is assumed to be smooth and either fully permeable or impermeable. The half-plane under consideration consists of a number of layers with different thicknesses and material properties, and is governed by Biot's poroelastodynamic theory. The vertical deflection of the strip foundation is represented by an admissible function containing a set of generalized coordinates. Solutions for generalized coordinates are obtained by establishing the equations of motion of the foundation through the application of Lagrange's equations of motion. Selected numerical results are presented to demonstrate the influence of foundation rigidity, hydraulic boundary conditions, layer properties and configuration, and distance of adjacent foundations on dynamic interaction between flexible strip foundations and a multilayered poroelastic half-plane.

1. Introduction

The study of dynamic interaction between a strip foundation and an elastic medium has received considerable attention over the past forty years due to its useful applications for analysis and design of foundations subjected to dynamic loading. Mixed-boundary value problems related to vibrations of a strip foundation have been considered in the past by employing a variety of analytical, semianalytical, and numerical techniques. [Karasudhi et al. \[1968\]](#) derived analytical solutions for vertical, horizontal, and rocking vibrations of a rigid smooth strip resting on an elastic half-plane in terms of Fredholm integral equations. The integral equation solutions were also presented by [Luco and Westmann \[1972\]](#) for dynamic response of a surface rigid strip bonded to an elastic half-plane. [Gazetas and Roesset \[1976\]](#) employed a semianalytical technique to obtain dynamic compliances of a rigid strip on a layered elastic medium. Dynamic interaction between a system of flexible strips and an elastic half-plane was studied by [Wang et al. \[1991\]](#) by employing a coupled variational-Green's function technique. Several researchers have employed numerical approaches to study vibrations of a strip foundation. For example, [Chang-Liang \[1974\]](#) presented a finite element model of a strip footing on an elastic layer with rigid base. A boundary element method was used by [Israil and Ahmad \[1989\]](#) to study dynamic interaction between a rigid strip and a layered viscoelastic medium. In addition, a number of studies related to vibrations of flexible strips have been presented [[Spyrakos and Beskos 1986](#); [Kokkinos and Spyrakos 1991](#); [Spyrakos and Xu 2004](#)] by employing a hybrid BEM-FEM technique.

Keywords: multiple strip foundations, layered systems, poroelasticity, soil-structure interaction, vibrations.

The work presented in this paper was partially supported by CHE and AUN/SEED-Net Scholarships. This support is gratefully acknowledged.

All studies mentioned above considered a half-plane as a single-phase elastic medium. However, geomaterials are often two-phased materials with a solid skeleton and pores filled with water, commonly known as poroelastic materials in mechanics literature. The first theory of elastic wave propagation in a poroelastic medium was established by Biot [1956] by adding inertia terms to his quasistatic theory [Biot 1941]. A limited number of studies related to vibrations of a rigid strip foundation on a poroelastic medium have appeared in the literature by employing Biot's poroelastodynamic theory despite their relevance to geotechnical engineering and earthquake engineering [Kassir and Xu 1988; Bougacha et al. 1993; Japón et al. 1997]. In addition, dynamic response of a rigid strip bonded to a multilayered poroelastic half-plane was also studied by Senjuntichai and Rajapakse [1996] by employing an exact stiffness matrix scheme [Rajapakse and Senjuntichai 1995] and a discretization technique. In practice, there exists a situation of a closely spaced foundation system where one needs to consider not only the interaction between the foundations and the supporting medium but also the interaction that occurs between the adjacent foundations through the supporting medium. A review of literature indicates that this structure-soil-structure interaction problem has been investigated in the past for dynamic interaction between elastic media and rigid circular foundations [Warburton et al. 1971; Wong and Luco 1986], and flexible strip foundations [Wang et al. 1991]. To our knowledge, the dynamic interaction between a system of foundations and a poroelastic medium has never been reported in the literature.

In this paper, the dynamic response of a system of flexible strip foundations resting on a multilayered poroelastic half-plane subjected to time-harmonic vertical loading as shown in Figure 1 is studied. The interaction problem is analyzed by adopting the coupled variational Green's function scheme [Wang et al. 1991] together with a discretization technique. The contact surface between the foundations and the half-plane is assumed to be smooth. Two extreme fluid flow conditions at the strip-half-plane contact surface are considered, that is, fully permeable and impermeable contact surfaces. Each layer of the half-plane is governed by Biot's theory of poroelastodynamics. The transverse deflection of a strip foundation is represented by an admissible function containing a set of generalized coordinates. Contact traction and pore pressure jump under each strip foundation are expressed in terms of the generalized coordinates through the solutions of the flexibility equations based on the influence functions. These influence functions correspond to the solid and fluid displacements of a multilayered half-plane under a vertical load and pore pressure loading at the surface level. The generalized coordinates are determined by establishing the Lagrange equations of motion for the foundation system. Convergence and accuracy of the present numerical scheme are established through comparison with existing studies. Selected numerical results are presented to illustrate the influence of poroelastic material parameters, layering, foundation rigidity, hydraulic boundary conditions, frequency of excitation, and presence of adjacent foundations on vertical displacement, contact traction, and pore pressure profiles, and bending moment of the strip foundation system.

2. Basic equations and influence functions

Consider a poroelastic medium with a Cartesian coordinate system (x, y, z) defined such that the z -axis is perpendicular to the free surface as shown in Figure 1. It is assumed that the deformations are plane strain in the xz -plane, that is, $\varepsilon_{xy} = \varepsilon_{yy} = \varepsilon_{yz} = 0$. Let u_i and w_i denote the average displacement of the solid matrix and the fluid displacement relative to the solid matrix in the i -direction ($i = x, z$) respectively.

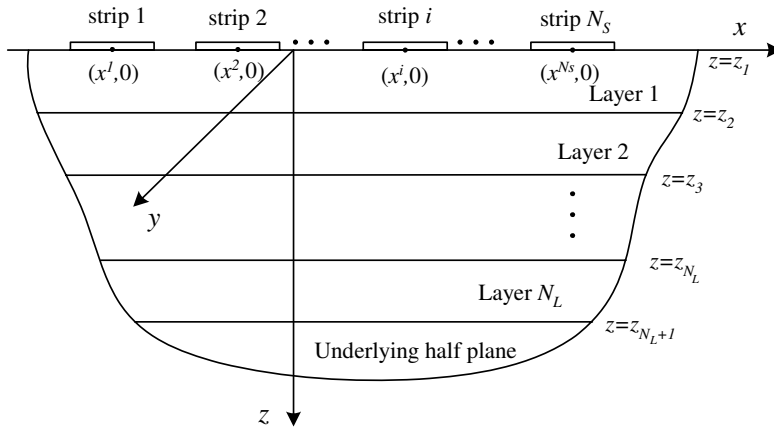


Figure 1. Flexible strip foundations on a multilayered poroelastic half-plane.

The constitutive relations for a homogeneous poroelastic material [Biot 1941] can be expressed by using standard indicial notations as $\sigma_{ij} = 2\mu\varepsilon_{ij} + \lambda\delta_{ij}\varepsilon_{kk} - \alpha\delta_{ij}p$, with $i, j = x, z$, and $p = -\alpha M\varepsilon_{kk} + M\zeta$. In the above equations, σ_{ij} and ε_{ij} denote the stresses and strains of the bulk material respectively, μ and λ are Lamé’s constants of the bulk material, p is the excess pore fluid pressure (suction is considered negative), ζ is the variation of the fluid content per unit reference volume defined as $\zeta = -w_{,i,i}$, and δ_{ij} denotes the Kronecker delta. In addition, α and M are Biot’s parameters accounting for the compressibility of the two-phase material.

The equations of motion for a poroelastic medium in the absence of body forces (solid and fluid) and a fluid source can be expressed in terms of displacements u_i and w_i as [Biot 1962]

$$\begin{aligned} \mu u_{i,jj} + (\lambda + \alpha^2 M + \mu)u_{j,ji} - \alpha M w_{j,ji} &= \rho \ddot{u}_i + \rho_f \ddot{w}_i, \\ \alpha M u_{j,ji} + M w_{j,ji} &= \rho_f \ddot{u}_i + m \ddot{w}_i + b \dot{w}_i. \end{aligned} \tag{1}$$

Here ρ and ρ_f are the mass densities of the bulk material and the pore fluid respectively, m is a density parameter that depends on ρ_f and the geometry of the pores, and b is the parameter accounting for the internal friction due to the relative motion between the solid matrix and the pore fluid. If the internal friction is neglected, then $b = 0$. In addition, the superscript dot denotes the derivative with respect to time.

The motion under consideration is time-harmonic with a factor $e^{i\omega t}$ where ω is the frequency of motion and $i = \sqrt{-1}$. The term $e^{i\omega t}$ is hereafter omitted from all expressions for brevity.

The Fourier integral transform of a function $f(x, z)$ and its inverse relationship with respect to the x -coordinate are given by [Sneddon 1951]

$$\bar{f}(\zeta, z) = \frac{1}{\sqrt{2\pi}} \int_{-\infty}^{\infty} f(x, z) e^{-i\zeta x} dx, \quad f(x, z) = \frac{1}{\sqrt{2\pi}} \int_{-\infty}^{\infty} \bar{f}(\zeta, z) e^{i\zeta x} d\zeta, \tag{2}$$

where ζ denotes the Fourier transform parameter.

An exact stiffness matrix method proposed by Rajapakse and Senjuntichai [1995] is employed in the derivation of the influence functions required for analysis of the interaction problem shown in Figure 1.

In this method, the exact stiffness matrices for the n th layer and an underlying half-plane are derived from the general solutions of a homogeneous poroelastic material in the Fourier transform space [Senjuntichai and Rajapakse 1994]. The global stiffness matrix of a multilayered poroelastic half-plane is then obtained by assembling the layer and half-plane stiffness matrices together with the continuity of traction and fluid flow at the layer interfaces. The global equation system can be expressed as

$$KU = F, \tag{3}$$

where K is the global stiffness matrix, U and F are the global vectors of generalized displacements and generalized forces defined as

$$U = [u^{(2)} \ u^{(2)} \ \dots \ u^{(n)} \ \dots \ u^{(N)} \ u^{(N+1)}]^T, \quad F = [f^{(1)} \ f^{(2)} \ \dots \ f^{(n)} \ \dots \ f^{(N)} \ f^{(N+1)}]^T,$$

in which

$$u^{(n)} = [i\bar{u}_x^{(n)} \ \bar{u}_z^{(n)} \ \bar{p}^{(n)}]^T, \quad f^{(n)} = [i\bar{\sigma}_{zx}^{(n)} \ \bar{\sigma}_{zz}^{(n)} \ \bar{w}_z^{(n)}]^T,$$

and the superscript n denotes the quantities at the n th interface. Details on the formulation of the exact stiffness matrix method including the explicit expression of the layer and half-plane stiffness matrices are given elsewhere [Rajapakse and Senjuntichai 1995].

To determine the influence functions, a boundary value problem corresponding to a multilayered poroelastic half-plane subjected to a uniform strip load at the surface is solved. The global generalized force vector can then be expressed as

$$F = \left[0 \quad -\sqrt{\frac{2}{\pi}} \frac{\sin(\zeta a)}{\zeta} \quad 0 \ \dots \ 0 \right]^T,$$

where a is half the width of the loading strip. The solutions for displacements and pore pressure at layer interfaces can be obtained by solving (3) for discrete value of ζ together with the application of numerical quadrature to evaluate the inverse Fourier transforms defined in (2). In the analysis of the interaction problem shown in Figure 1, only vertical solid and fluid displacements (u_z and w_z) at the surface level are required to establish the flexibility equation for the derivation of the contact stress and pore pressure jump, which are employed in the formulation presented in the next section.

3. Formulation of interaction problem

Consider a system of N_S flexible foundations resting on a multilayered poroelastic medium as shown in Figure 1. For a foundation with its length much longer than its width subjected to dynamic loading that is uniform along the longitudinal direction, it is reasonable to consider the foundation as a strip foundation under plane strain condition. For the i -th strip foundation with a width of $2a^i$, it is convenient to define a local coordinate η as $\eta = (x - x^i)/a^i$, with $i = 1, 2, 3, \dots, N_S$, where x^i is the x -coordinate at the center of the i -th foundation. The vertical deflection of the i -th foundation, denoted by w_{st}^i , can then be expressed as

$$w_{st}^i(\eta) = \sum_{n=0}^{N_T} \alpha_n^i \eta^n, \quad i = 1, 2, 3, \dots, N_S, \tag{4}$$

where $\alpha_0^i, \alpha_1^i, \dots, \alpha_{N_T}^i$ are a set of generalized coordinates. In view of (4), the bending moment per unit length acting on the i -th foundation is given by

$$M_{st}^i(\eta) = -D^i \sum_{n=0}^{N_T} n(n-1)\alpha_n^i \eta^{n-2}, \quad i = 1, 2, 3, \dots, N_S, \quad \text{where} \quad D^i = \frac{E_{st}^i (h_{st}^i)^3}{12[1 - (\nu_{st}^i)^2]},$$

and h_{st}^i, E_{st}^i , and ν_{st}^i are the thickness, Young’s modulus, and Poisson’s ratio of the i -th foundation.

In this paper, it is assumed that the contact surface between the strip foundation and the multilayered half-plane is smooth and either fully permeable or impermeable. For an impermeable strip foundation, the vertical loading is resisted by contact traction and pore pressure generated at the bottom surface of the foundation. The resultants of the contact traction and pore pressure of the i -th foundation can be represented by traction $T_z^i(\eta)$ and pore pressure jump $T_p^i(\eta)$ acting on the contact surface between the i -th foundation and the half-plane.

To determine T_z^i and T_p^i , the contact surface between the i -th strip foundation ($i = 1, 2, 3, \dots, N_S$) and the half-plane is discretized into the total number of N_E^i strip elements. The width of each element is denoted by Δ_k^i where $k = 1, 2, \dots, N_E^i$ (see Figure 2). The vertical displacement compatibility and the impermeable condition are then imposed at the contact surface between the strip foundation and the half-plane. This is done by taking each term of the deflection approximation of the i -th foundation, (4) with $\alpha_n^i = 1$ ($i = 1, 2, 3, \dots, N_S; n = 0, 1, 2, \dots, N_T$). Thereafter, the resulting deflection variation and zero flow condition are imposed on the nodal locations at the contact surface of the half-plane by applying contact traction T_{znk}^i and pore pressure jump T_{pnk}^i at the k -th node of the i -th strip foundation. It is assumed that contact traction and pore pressure jump are constant within each strip element. The following flexibility equation system can be established to determine the intensities of T_{znk}^i and T_{pnk}^i at each strip element:

$$\begin{bmatrix} G_{zz}^{11} & G_{zp}^{11} & \dots & G_{zr}^{1j} & \dots & G_{zz}^{1N_S} & G_{zp}^{1N_S} \\ G_{pz}^{11} & G_{pp}^{11} & \dots & G_{pr}^{1j} & \dots & G_{pz}^{1N_S} & G_{pp}^{1N_S} \\ \vdots & \vdots & \ddots & \vdots & \ddots & \vdots & \vdots \\ G_{qz}^{i1} & G_{qp}^{i1} & \dots & G_{qr}^{ij} & \dots & G_{qz}^{iN_S} & G_{qp}^{iN_S} \\ \vdots & \vdots & \ddots & \vdots & \ddots & \vdots & \vdots \\ G_{zz}^{N_S1} & G_{zp}^{N_S1} & \dots & G_{zr}^{N_Sj} & \dots & G_{zz}^{N_SN_S} & G_{zp}^{N_SN_S} \\ G_{pz}^{N_S1} & G_{pp}^{N_S1} & \dots & G_{pr}^{N_Sj} & \dots & G_{pz}^{N_SN_S} & G_{pp}^{N_SN_S} \end{bmatrix} \begin{bmatrix} T_{zn}^1 \\ T_{pn}^1 \\ \vdots \\ T_{qn}^i \\ \vdots \\ T_{zn}^{N_S} \\ T_{pn}^{N_S} \end{bmatrix} = \begin{bmatrix} u_{zn}^1 \\ u_{pn}^1 \\ \vdots \\ u_{qn}^i \\ \vdots \\ u_{zn}^{N_S} \\ u_{pn}^{N_S} \end{bmatrix}, \quad (5)$$

where

$$G_{qr}^{ij} = \begin{bmatrix} G_{qr,11}^{ij} & G_{qr,12}^{ij} & \dots & G_{qr,1N_E}^{ij} \\ G_{qr,21}^{ij} & G_{qr,22}^{ij} & \dots & G_{qr,2N_E}^{ij} \\ \vdots & \vdots & G_{qr,kl}^{ij} & \vdots \\ G_{qr,N_E1}^{ij} & G_{qr,N_E2}^{ij} & \dots & G_{qr,N_EN_E}^{ij} \end{bmatrix}.$$

In this equation, the element $G_{qr,kl}^{ij}$ ($i, j = 1, 2, 3, \dots, N_S; k, l = 1, 2, 3, \dots, N_E$) denotes the vertical displacement ($q = z$) and the fluid displacement ($q = p$) at the center of the k -th strip element of the i -th foundation due to a vertical load ($r = z$) and fluid pressure ($r = p$) applied over the l -th strip element of

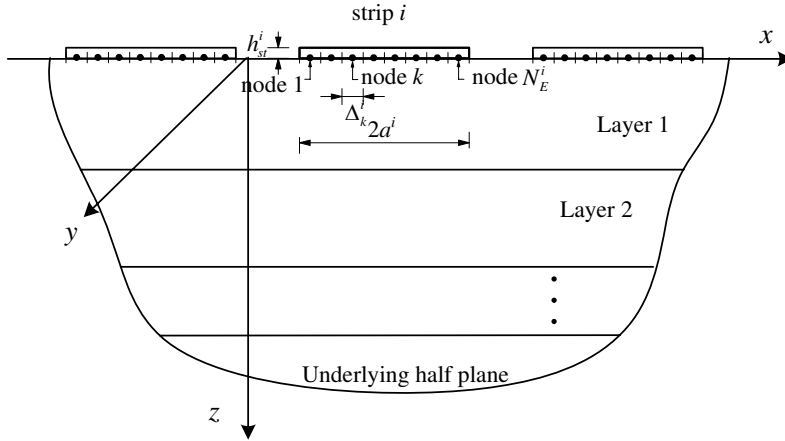


Figure 2. Dcretization of the strip-half-plane contact surface.

the j -th foundation. In addition,

$$\begin{aligned} \mathbf{T}_{zn}^i &= [T_{zn1}^i \ T_{zn2}^i \ \cdots \ T_{znk}^i \ \cdots \ T_{znN_E}^i]^T, & \mathbf{T}_{pn}^i &= [T_{pn1}^i \ T_{pn2}^i \ \cdots \ T_{pnk}^i \ \cdots \ T_{pnN_E}^i]^T, \\ \mathbf{u}_{zn}^i &= [u_{zn1}^i \ u_{zn2}^i \ \cdots \ u_{znk}^i \ \cdots \ u_{znN_E}^i]^T, & \mathbf{u}_{pn}^i &= [0 \ 0 \ \cdots \ 0 \ \cdots \ 0]^T. \end{aligned}$$

The contact traction and pore pressure jump at the k -th strip element of the i -th foundation that are required to satisfy the displacement compatibility and the impermeability condition at the contact surface can be expressed respectively as

$$\mathbf{T}_{zk}^i = \sum_{n=0}^{N_T} \alpha_n^i T_{znk}^i, \quad \mathbf{T}_{pk}^i = \sum_{n=0}^{N_T} \alpha_n^i T_{pnk}^i, \tag{6}$$

where T_{znk}^i and T_{pnk}^i ($n = 0, 1, 2, \dots, N_T; k = 1, 2, 3, \dots, N_E$) denote the intensities of contact traction and pore pressure jump respectively acting on the k -th strip element of the i -th foundation when $u_{znk}^i = \eta_k^n$, in which η_k is the local coordinate at the center of the k -th strip element.

For a fully permeable strip foundation, since no pore pressure jump is generated under the foundation, the flexibility matrix (5) is then reduced to

$$\begin{bmatrix} \mathbf{G}_{zz}^{11} & \mathbf{G}_{zz}^{12} & \cdots & \mathbf{G}_{zz}^{1N_S} \\ \mathbf{G}_{zz}^{12} & \mathbf{G}_{zz}^{22} & \cdots & \mathbf{G}_{zz}^{2N_S} \\ \vdots & \vdots & \mathbf{G}_{zz}^{ij} & \vdots \\ \mathbf{G}_{zz}^{N_S 1} & \mathbf{G}_{zz}^{N_S 2} & \cdots & \mathbf{G}_{zz}^{N_S N_S} \end{bmatrix} \begin{bmatrix} \mathbf{T}_{zn}^1 \\ \mathbf{T}_{zn}^2 \\ \vdots \\ \mathbf{T}_{zn}^{N_S} \end{bmatrix} = \begin{bmatrix} \mathbf{u}_{zn}^1 \\ \mathbf{u}_{zn}^2 \\ \vdots \\ \mathbf{u}_{zn}^{N_S} \end{bmatrix}. \tag{7}$$

The Lagrangian function Π of the system of N_S flexible strip foundations resting on a multilayered poroelastic half-plane as shown in Figure 1 can be expressed as

$$\Pi = \sum_{i=1}^{N_S} \left\{ v^i - U^i - \int_{-1}^1 \left[\frac{1}{2} \{ T_z^i(\eta) + \alpha T_p^i(\eta) \} - f^i(\eta) \right] w_{st}^i(\eta) d\eta \right\}, \tag{8}$$

where V^i and U^i denote the kinetic and strain energies of the i -th strip foundation respectively and

$$V^i = \dot{\alpha}^i M_{st}^i (\dot{\alpha}^i)^T, \quad U^i = \alpha^i H_{st}^i (\alpha^i)^T, \quad i = 1, 2, 3, \dots, N_S,$$

in which α^i is a row vector whose elements are the generalized coordinates of the i -th foundation, that is, $\alpha^i = [\alpha_0^i \ \alpha_1^i \ \alpha_2^i \ \dots \ \alpha_{N_T}^i]$. The elements M_{mn}^i and H_{mn}^i of the matrices M_{st}^i and H_{st}^i are given by

$$M_{mn}^i = \frac{\rho_{st}^i h_{st}^i (a^i)^{m+n-1}}{2(m+n-1)} [1 - (-1)^{m+n-1}],$$

$$H_{mn}^i = \frac{E^i (h_{st}^i)^2 (a^i)^{m+n-5}}{24[1 - (v_{st}^i)^2]} \frac{(m-1)(m-2)(n-1)(n-2)}{(m+n-5)} [1 - (-1)^{m+n-5}],$$

where ρ_{st}^i is the density of the i -th foundation. In addition, $f^i(\eta)$ denotes the external loading acting on the i -th foundation and can be written as

$$f^i(\eta) = \sum_{m=0}^{N_L} \varphi_m^i \eta^m,$$

where φ_m^i is the coefficient of the loading function.

The Lagrange's equations of motion for the interaction problem shown in Figure 1 are given by

$$\frac{d}{dt} \left(\frac{\partial \Pi}{\partial \dot{A}} \right) - \frac{\partial \Pi}{\partial A} = 0, \tag{9}$$

where $A = [\alpha^1 \ \alpha^2 \ \alpha^3 \ \dots \ \alpha^{N_S}]^T$. Substitution of (8) in (9) results in the following equations of motion to determine α^i ($i = 1, 2, 3, \dots, N_S$):

$$QA = B, \tag{10}$$

where

$$Q = -\omega^2(M_{st} + M_{st}^T) + H_{st} + H_{st}^T + S + S^T,$$

and

$$M_{st} = \text{diag}[M_{st}^i], \quad H_{st} = \text{diag}[H_{st}^i], \quad S = \text{diag}[S^i], \quad B = [B^1 \ B^2 \ B^3 \ \dots \ B^{N_S}]^T.$$

The elements of S_{mn}^i and B_m^i of the matrices S^i and B^i ($i = 1, 2, \dots, N_S; m, n = 1, 2, \dots, N_T + 1$) are given by

$$S_{mn}^i = \frac{1}{2} \sum_{k=1}^{N_E} \Delta_k^i (\eta_k)^{m-1} (T_{z(n-1)k}^i + \alpha T_{p(n-1)k}^i), \quad B_m^i = \sum_{k=1}^{N_L} \frac{\varphi_k^i (a^i)^{m+k-1}}{(m+k-1)} [1 - (-1)^{m+k-1}],$$

where Δ_k^i denotes the width of the k -th strip element of the i -th foundation.

The solution of a linear simultaneous equation system given by (10) yields the numerical values of the generalized coordinates α_n^i ($n = 0, 1, 2, \dots, N_T; i = 1, 2, 3, \dots, N_S$) for a given foundation-half-plane system. Finally, vertical displacements, contact traction, and pore pressure jump can then be obtained by back substituting the generalized coordinates in (4) and (6) respectively.

4. Numerical results and discussion

Numerical results for dynamic interaction between a system of strip foundations subjected to vertical loading resting on a multilayered poroelastic half-plane are presented in this section. For impermeable strip foundations, the first step is to solve the system of linear simultaneous equations given by (5) to obtain the unknown contact traction T_{znk}^i and pore pressure jump T_{pnk}^i at each strip element of the i -th foundation ($i = 1, 2, 3, \dots, N_S$) for each n value. For fully permeable foundations, (7) is solved for the unknown T_{znk}^i . This involves the computation of the influence functions $G_{qr,kl}^{ij}$ by solving (3). Since (3) is established in the Fourier transform space, it has to be solved for discrete values of ζ . The required influence functions are then determined by numerically integrating the inverse Fourier transform given by (2).

To perform the numerical integration, it is important to examine the singularities of the integrands. The main singularities are the branch points and poles that are complex-valued quantities with negative imaginary parts for all poroelastic materials due to the presence of some internal friction ($b \neq 0$). Therefore, the real ζ -axis is free from any singularities and the influence functions can be evaluated by direct numerical integration along the real ζ -axis when $b \neq 0$. For poroelastic materials with $b = 0$ and ideal elastic materials, 1% attenuation is used to ensure that the real ζ -axis is free from any singularity. In the present study, the numerical evaluation of the influence functions is performed by employing a globally adaptive numerical quadrature scheme [Piessens et al. 1983]. This scheme subdivides the interval of integrand and uses a 21-point Gauss–Kronrod rule to estimate the integral over each interval.

Convergence and numerical stability of the solution scheme were investigated with respect to the number of terms, N_T , in (4), and the number of strip elements, N_E , used to discretize the contact surface between the strip foundation and the half-plane. It was found that converged numerical solutions are obtained when $N_T \geq 8$ and $N_E \geq 20$.

The accuracy of the present solution scheme is verified by comparing with the existing solutions. The left side of Figure 3 shows a comparison of vertical compliance, $C_V = w_{st}(0)\mu^{(1)}/af_0$, of a rigid strip of width $2a$ subjected to a uniform load f_0 resting on a layered elastic half plane consisting of one homogeneous layer with a thickness of $2a$ and an underlying half-plane. Numerical solutions from the present scheme are compared with those presented by Israil and Ahmad [1989] for different values of $\mu^{(1)}/\mu^{(2)}$. The nondimensional frequency $\delta = \omega a \sqrt{\rho^{(1)}/\mu^{(1)}}$ is used in the comparison in this figure and all numerical results presented in this paper. It can be seen from the left side of Figure 3 that the two solutions agree very closely for all values of $\mu^{(1)}/\mu^{(2)}$.

The right side of Figure 3 presents a comparison of vertical impedance $K_V = F_0/\mu a w_{st}(0)$ of a permeable rigid strip of width $2a$ on a homogenous poroelastic half-plane subjected to a time-harmonic vertical force F_0 . It is evident from the right side of Figure 3 that the solutions from the present scheme are in very good agreement with those given by Kassir and Xu [1988]. Note that the half-plane in the present study consists of 10 layers of equal thickness $0.2a$ and an underlying half-plane. A comparison of vertical impedance $K_V = f_0 a / \mu w_{st}(0)$ of a flexible strip on a homogenous elastic half-plane subjected to a uniform load of intensity f_0 is shown in Figure 4. The nondimensional relative rigidity, $\gamma = E_{st} h_{st}^3 / 12(1 - \nu_{st}^2) a^3 \mu^{(1)}$, is used in the comparison. Excellent agreement is noted between the present solution and the solution given by Wang et al. [1991]. The accuracy of the present solution scheme is therefore verified by these independent comparisons.

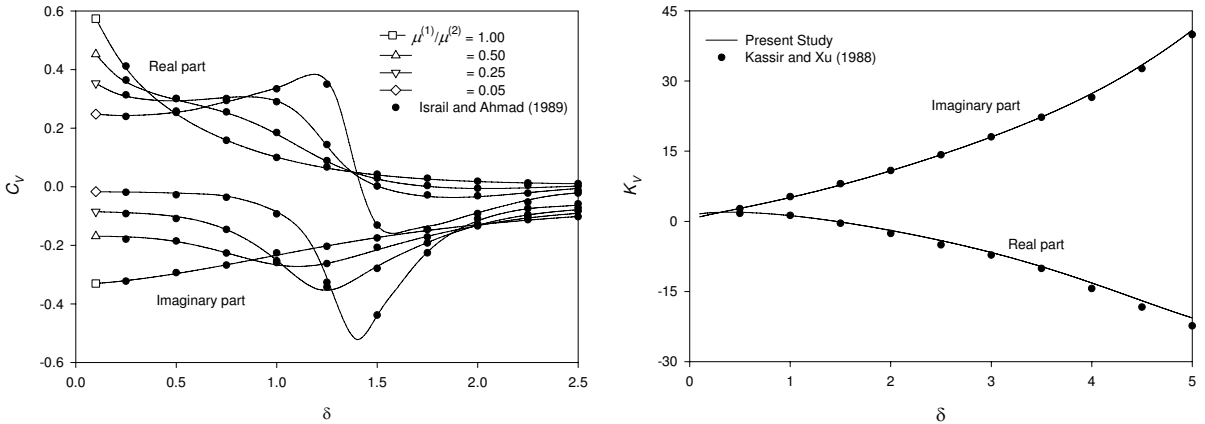


Figure 3. Comparison of (left) compliance of a rigid strip on a layered elastic half-plane, and (right) vertical impedance of a rigid strip on a homogenous poroelastic half-plane.

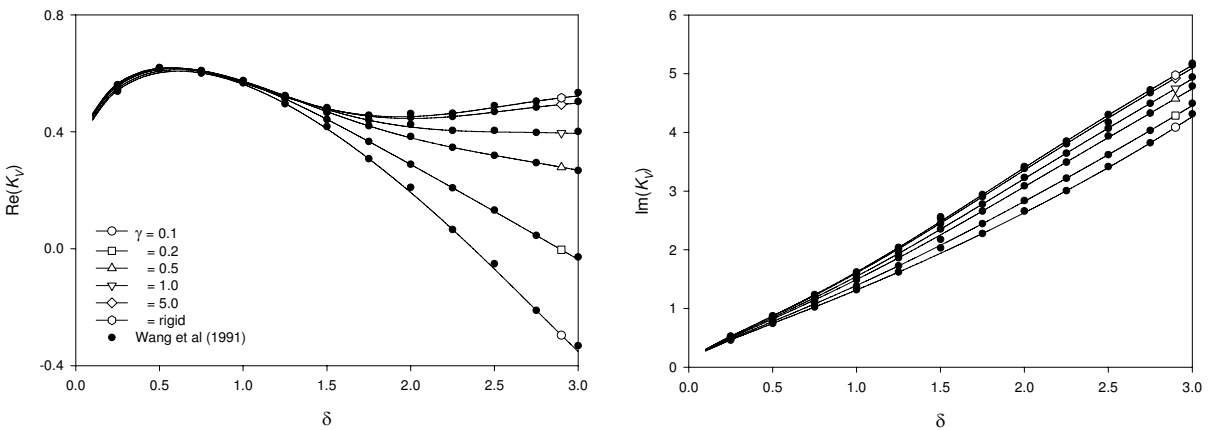


Figure 4. Comparison of vertical impedance of a flexible strip on an elastic half-plane.

Next, vertical vibrations of strip foundations resting on a multilayered poroelastic half-plane as shown in Figure 5 are studied. The strip foundations under consideration are either fully permeable or impermeable. The half-plane consists of two poroelastic layers bonded to an underlying poroelastic half-plane. The material properties of both layers and the underlying half-plane are given in Table 1. The first set of solutions corresponds to vertical vibrations of a single strip foundation on a multilayered poroelastic half-plane subjected to a uniform load of intensity f_0 as shown on the left side of Figure 5. Nondimensional vertical displacement at the center of the strip foundation, $w_{st}^*(0) = w_{st}(0)\mu^{(1)}/f_0a$, is presented in Figure 6. Both fully permeable and impermeable foundations with different relative rigidity ratio $\gamma = 0.2, 0.5, 1.0, 5.0$, and 100 are considered to investigate the influence of strip foundation rigidity and hydraulic boundary conditions at the contact surface. Numerical results presented in Figure 6 indicate that the variation of $w_{st}^*(0)$ with frequency is quite similar for fully permeable and impermeable strips although both real and imaginary parts of $w_{st}^*(0)$ are larger for the impermeable strip. Both real and imaginary parts of $w_{st}^*(0)$ decrease with increasing relative rigidity γ . The real part of $w_{st}^*(0)$ shows a

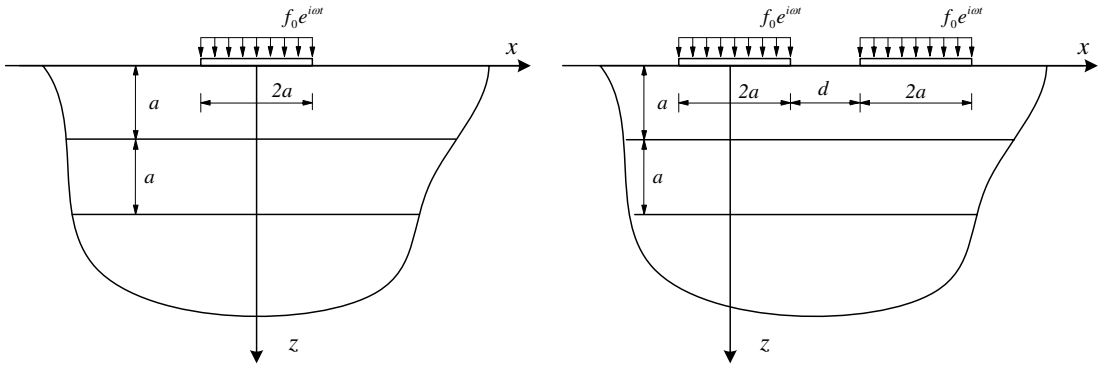


Figure 5. Flexible strip foundation systems considered in numerical study: (left) single strip and (right) two strips.

	μ	λ	M	ρ	ρ_f	m^\dagger	α	b
First layer	2.5	5.0	25.0	2.0	1.0	3.0	0.95	1.50
Second layer	1.25	1.88	18.8	1.6	1.0	1.8	0.98	0.75
Underlying half-plane	10.0	10.0	20.0	2.4	1.0	4.8	0.90	4.50

Table 1. Material properties of the layered systems considered in numerical study. Units: μ , λ and M in 10^8 N/m²; ρ , ρ_f and m in 10^3 kg/m³; b in 10^6 Ns/m⁴.

change in sign within the frequency range $1.0 < \delta < 1.5$. The imaginary part of $w_{st}^*(0)$ remains negative throughout the frequency range $0 < \delta < 3.0$ and it is maximum when the corresponding real part of the solution is equal to zero. In addition, the strip foundation becomes virtually rigid when $\gamma \geq 100$.

Comparison of nondimensional central bending moment $M_{st}^*(0) = M_{st}(0)/f_0 a^3$ shown in Figure 7 indicates that the bending moment of a strip foundation depends significantly on the relative rigidity γ and the hydraulic boundary condition at the contact surface. The bending moment at the center of the strip varies smoothly with frequency and the maximum values of real and imaginary parts of $M_{st}^*(0)$ are found when $1.0 < \delta < 1.5$. As expected, the magnitudes of both real and imaginary parts of $M_{st}^*(0)$ increase with increasing γ , and the bending moment at the center of an impermeable foundation is higher than that of the permeable one.

Figure 8 presents profiles of nondimensional displacement w_{st}^* of an impermeable strip foundation on the multilayered half-plane for $\gamma = 0.2, 0.5, 1.0, 5.0$, and 100 , and $\delta = 0.5$ and 2.0 . It can be seen from the left side of Figure 8 that both real and imaginary parts of displacement profiles depend significantly on relative rigidity and frequency. Both $\text{Re}[w_{st}^*]$ and $\text{Im}[w_{st}^*]$ are maximal at the center of the strip before monotonically decreasing at the strip edge. In addition, the displacements decrease with decreasing the relative rigidity γ , and the effect of γ is negligible when $\gamma > 100$.

Profiles of nondimensional contact traction $T_z^* = T_z/f_0$ and pore pressure jump $T_p^* = T_p/f_0$ under an impermeable strip foundation on the multilayered half-plane are presented in Figure 9 to investigate the load transfer mechanism between the strip and the half-plane. It is found that the contact traction under a flexible strip is distributed more uniformly than that under a rigid strip. Numerical results for

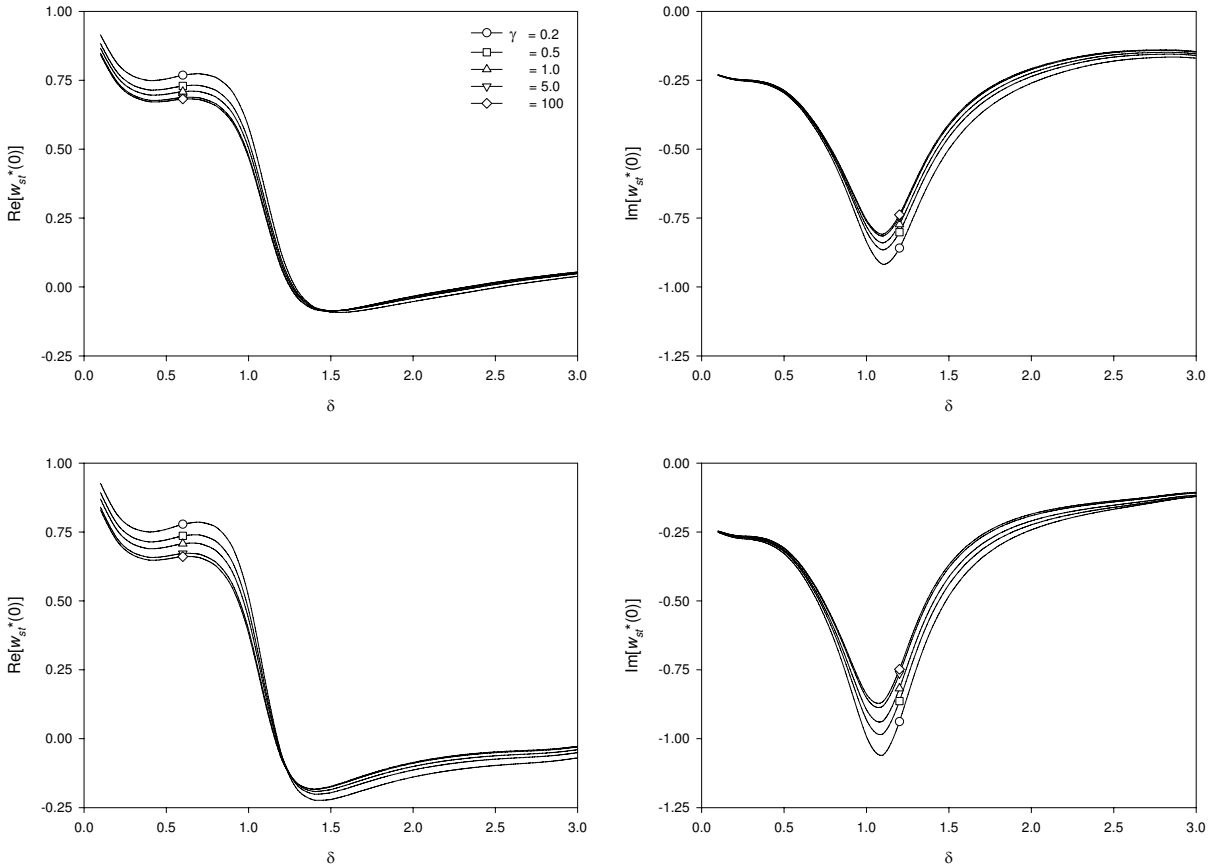


Figure 6. Displacement at the center of a flexible strip on a multilayered poroelastic half-plane: (top row) permeable strip and (bottom row) impermeable strip.

the contact traction presented in Figure 9 confirm the presence of classical singular behavior in both real and imaginary parts of T_z^* near the edge of the strip. Similar behavior was also observed for a rigid strip [Hryniewicz 1981] and a flexible strip [Wang et al. 1991] on a homogeneous elastic half plane. A comprehensive review on investigations of the exact local behavior of the contact traction in the vicinity of the foundation edge was given by Selvadurai [1979]. On the contrary, the pore pressure jump presented in Figure 9 is not singular near the strip edge. Its real and imaginary parts approach zero near the edge of both rigid and flexible strips. It is also found that larger pore pressure jump occurs at a higher frequency ($\delta = 2.0$) than at low frequency ($\delta = 0.5$). This implies that the load is carried by both solid and fluid phases at higher frequency, whereas at low frequency, the load transfer takes place through the solid skeleton. Similar behavior was also observed for the load transfer mechanism of a circular plate in a poroelastic medium [Zeng and Rajapakse 1999; Senjuntichai and Sapsathiam 2003].

Figure 10 shows nondimensional central displacement $w_{st}^*(0)$ of an impermeable flexible strip foundation ($\gamma = 1.0$) on different poroelastic systems. Four poroelastic systems, namely a homogenous half plane, a homogenous layer of thickness a with an impermeable rigid base, and multilayered systems A

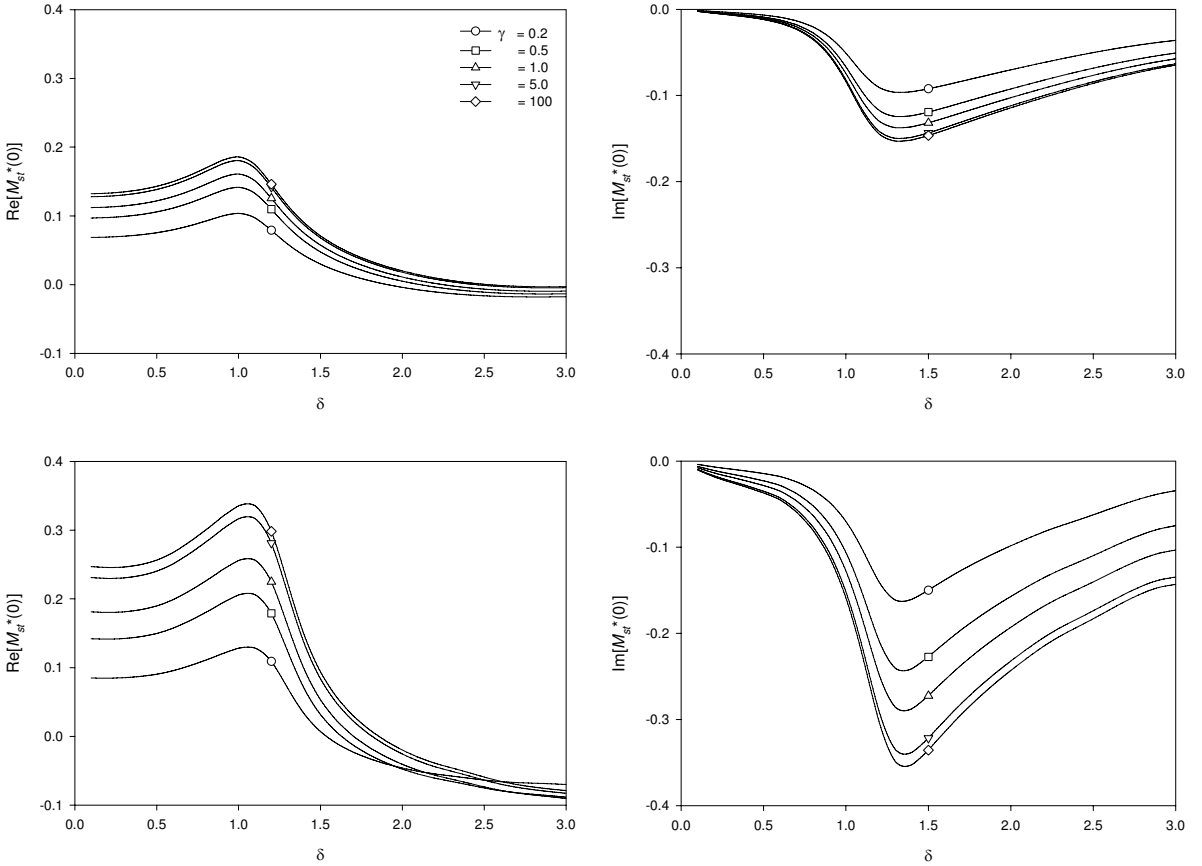


Figure 7. Bending moment at the center of a flexible strip on a multilayered poroelastic half-plane: (top row) permeable strip and (bottom row) impermeable strip.

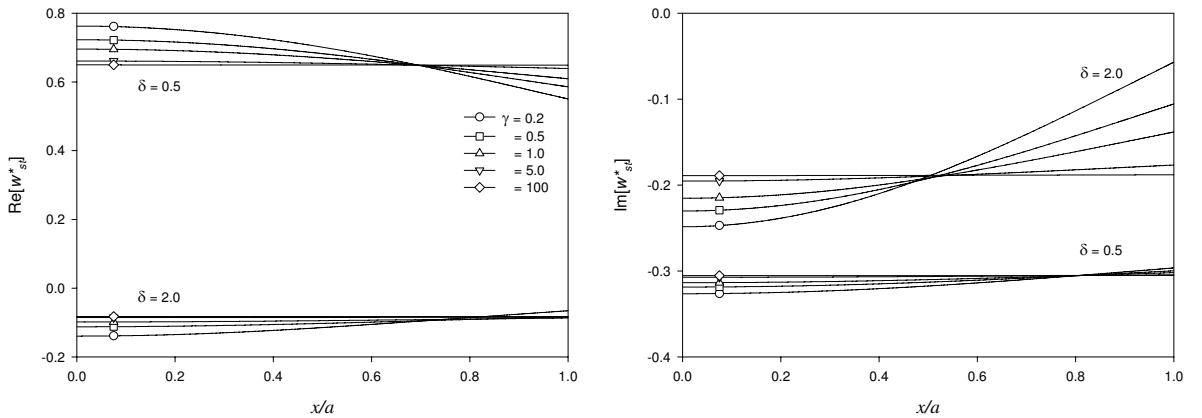


Figure 8. Displacement profiles of an impermeable strip on a multilayered poroelastic half-plane.

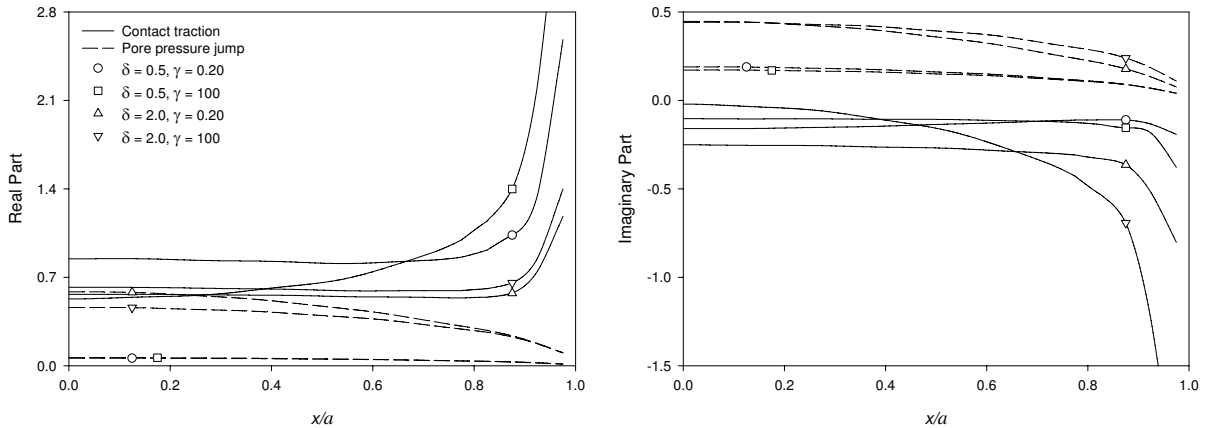


Figure 9. Profiles of contact traction and pore pressure jump under an impermeable strip on a multilayered poroelastic half-plane.

and B , are considered in this figure to investigate the influence of layering and poroelastic material parameters. The material properties of the homogeneous half-plane and the homogeneous layer are identical to those of the first layer defined in Table 1. The geometries of the multilayered systems A and B are identical to those shown in Figure 5. The material properties of both systems are given in Table 1 except the internal friction between solid and fluid is neglected for both layers and the half-plane of system B ($b = 0$). The comparison of $w_{st}^*(0)$ presented in Figure 10 indicates substantial differences among three poroelastic systems. Both real and imaginary parts of $w_{st}^*(0)$ for the strip on the homogeneous half-plane vary smoothly with δ whereas the strip displacement on the homogeneous layer shows oscillatory variation over the frequency range due to the standing wave generated between the surface and the rigid base. The difference in strip displacements corresponding to the multilayered systems A and B is mainly due to the parameter b . Note that all layers in system B have zero internal friction ($b = 0$) whereas system A consists of materials with nonzero b values. It is found that both real and imaginary parts of $w_{st}^*(0)$ in system A are smaller due to the presence of the internal friction between solid and fluid phases that makes this layered system more stiff and damped.

Numerical results corresponding to vertical vibrations of two impermeable strip foundations of width $2a$ subjected to uniform loading resting on a multilayered poroelastic half-plane as shown on the right side of Figure 5 with the properties given by Table 1 are presented next. The two strip foundations are identical and the distance between them is denoted by d . Variations of nondimensional displacement and nondimensional bending moment at the center of the left foundation with respect to nondimensional frequency are presented in Figures 11 and 12 respectively. Two values of the normalized distance between the two foundations $d/a = 1$ and 5 and the relative rigidity $\gamma = 0.2, 0.5, 1.0, 5.0,$ and 100 are considered in these two figures. It should be noted that the influence of the normalized distance d/a was investigated by preparing plots similar to those shown in Figures 11 and 12 for different values of d/a . It was found that the effect of d/a on displacement and bending moment becomes negligible when $d/a > 15$.

Numerical results presented in Figures 11 and 12 indicate that the presence of the adjacent foundation significantly influences both displacement and bending moment. Both real and imaginary parts of $w_{st}^*(0)$ for the two-foundation systems ($d/a = 1.0$ and 5.0) presented in Figure 11 show more oscillatory variation

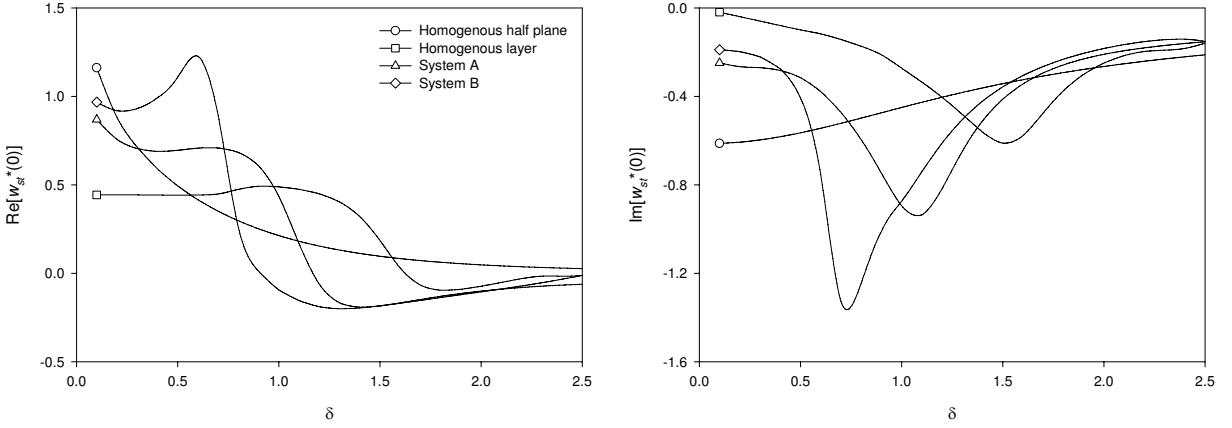


Figure 10. Displacement at the center of an impermeable strip ($\gamma = 1.0$) on different poroelastic systems.

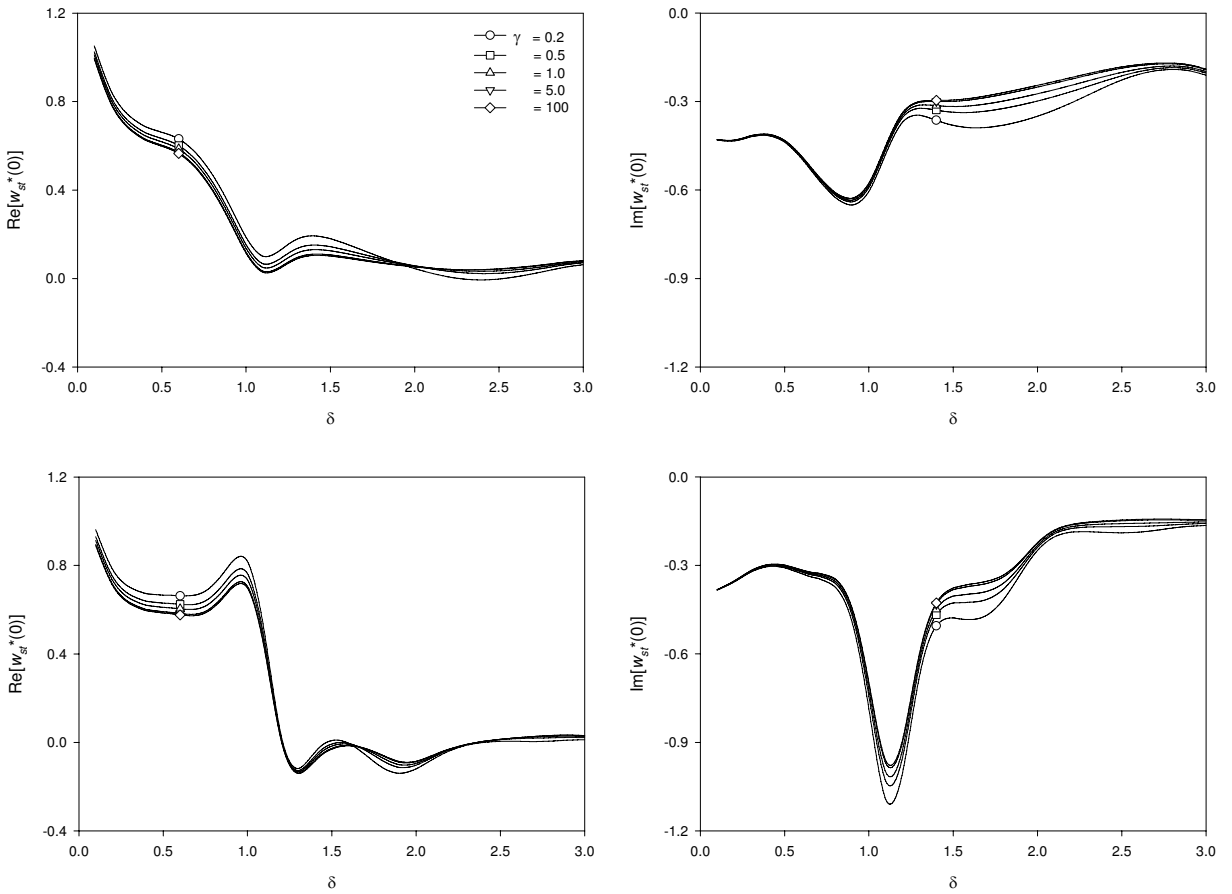


Figure 11. Displacement at the center of the left strip of two impermeable strip systems (see [Figure 5](#), right side): (top row) $d/a = 1.0$ and (bottom row) $d/a = 5.0$.

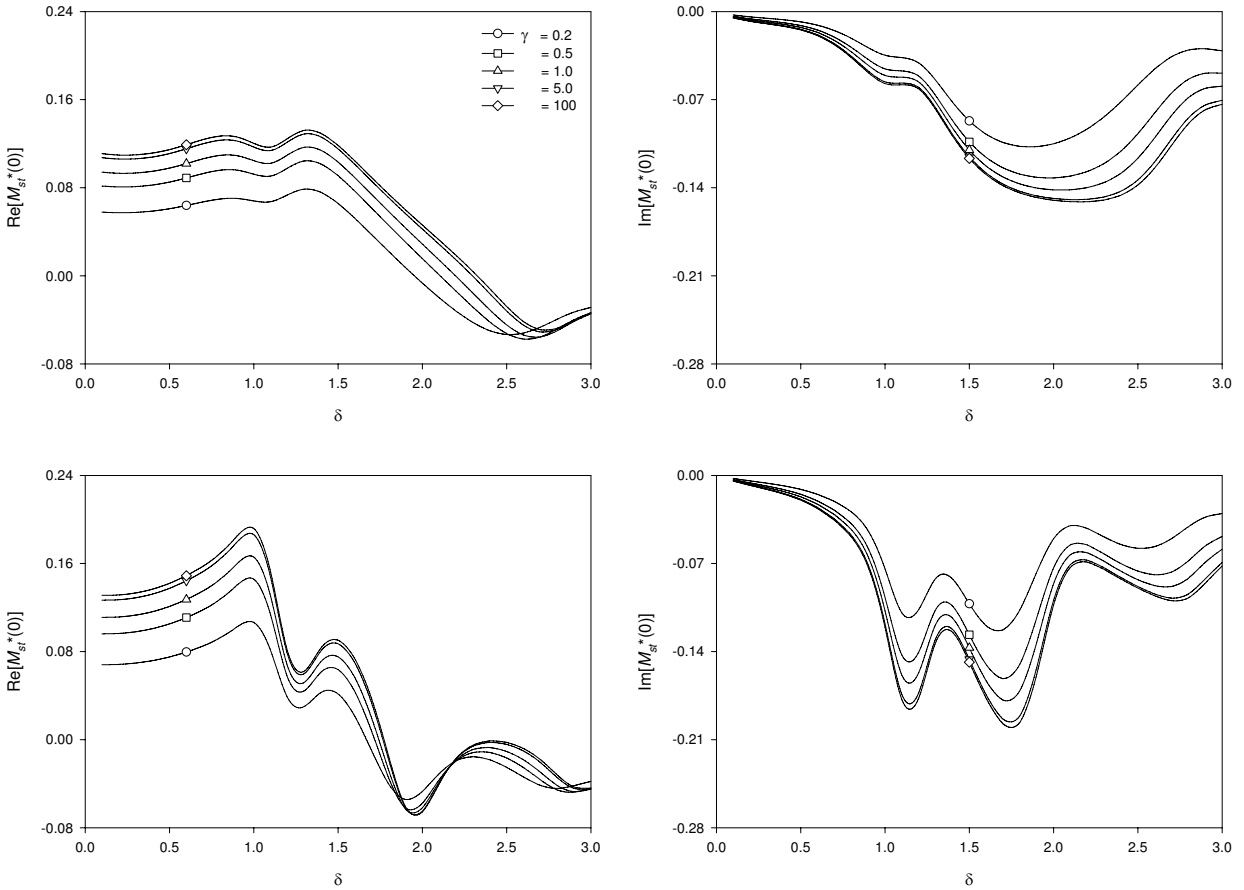


Figure 12. Bending moment at the center of the left strip of two impermeable strip systems (see Figure 5, right side) : (top row) $d/a = 1.0$ and (bottom row) $d/a = 5.0$.

with frequency when compared to smooth variations observed for a single strip foundation presented in Figure 6. The comparison of nondimensional displacement in Figure 11 for both two-foundation systems indicates differences in both magnitude and shape of $w_{st}^*(0)$. The real part of $w_{st}^*(0)$ for $d/a = 5.0$ shows a change sign near $\delta = 1.2$ whereas $\text{Re}[w_{st}^*(0)]$ for the two-foundation system with $d/a = 1.0$ remains positive throughout the frequency range $0 < \delta < 3.0$. The imaginary part of $w_{st}^*(0)$ remains negative for $0 < \delta < 3.0$ and the maximum values are found near $\delta = 1.0$ for both $d/a = 1.0$ and 5.0 . In addition, both real and imaginary parts of $w_{st}^*(0)$ decrease with increasing γ and the foundations become virtually rigid when $\gamma \geq 100$ similar to what observed for a single strip foundation in Figure 6.

The nondimensional bending moment shown for the two-foundation systems in Figure 12 indicates that both $\text{Re}[M_{st}^*(0)]$ and $\text{Im}[M_{st}^*(0)]$ exhibit more oscillatory variation with frequency than those observed for a single strip foundation in Figure 7. An important feature of the bending moment results revealed from Figure 12 is the notable dependence of both $\text{Re}[M_{st}^*(0)]$ and $\text{Im}[M_{st}^*(0)]$ on the distance d/a . The variation of both $\text{Re}[M_{st}^*(0)]$ and $\text{Im}[M_{st}^*(0)]$ with δ for the two-foundation system with $d/a = 5.0$ shows considerable oscillations, and it is quite different from that of a two-foundation system

with $d/a = 1.0$. Numerical results presented in Figure 12 also indicates that the relative rigidity γ has more significant influence on the bending moment than on the displacement, similar to what is observed in Figures 6 and 7 for a single strip foundation. Both real and imaginary parts of $M_{st}^*(0)$ for the two-foundation systems increase with increasing the relative rigidity γ and their magnitudes are lower than the corresponding solutions presented in Figure 7.

5. Conclusion

The dynamic interaction between a flexible strip foundation system under time-harmonic vertical loading resting on a multilayered poroelastic half plane is presented in this paper by using the coupled variational Green's function scheme together with a discretization technique. Both fully permeable and impermeable conditions at the contact surface between the foundations and the multilayered half-plane are considered. The required influence functions, which are computed by using the exact stiffness matrix method, correspond to a vertical strip load and fluid source applied at the surface of a multilayered poroelastic half-plane. The present numerical solutions are computationally stable and are in very good agreement with the existing solutions for both rigid and flexible foundations. Numerical results indicate that the dynamic response of the strip foundations depends significantly on the frequency of excitation, hydraulic boundary conditions, relative rigidity γ , poroelastic material properties and the distance between adjacent foundations. Both permeable and impermeable strip foundations show similar variations of displacement and bending moment with frequency, and higher magnitudes are observed in the impermeable one. With increasing the relative rigidity γ , the displacements of both single and multiple strip foundations decrease whereas their bending moments increase. The effect of the relative rigidity is negligible when $\gamma > 100$. In addition, the displacement and bending moment of the two-foundation system show significant dependence on both the distance between adjacent foundations and the frequency. It is also found that variations of displacement and bending moment with frequency show more considerable oscillations when $\delta > 1.5$.

References

- [Biot 1941] M. A. Biot, "General theory of three-dimensional consolidation", *J. Appl. Phys.* **12**:2 (1941), 155–164.
- [Biot 1956] M. A. Biot, "Theory of propagation of elastic waves in a fluid-saturated porous solid, I: Low-frequency range", *J. Acoust. Soc. Am.* **28**:2 (1956), 168–178. MR 24 #B110a
- [Biot 1962] M. A. Biot, "Mechanics of deformation and acoustic propagation in porous media", *J. Appl. Phys.* **33**:4 (1962), 1482–1498. MR 27 #2218
- [Bougacha et al. 1993] S. Bougacha, J. M. Roesset, and J. L. Tassoulas, "Dynamic stiffness of foundations on fluid-filled poroelastic stratum", *J. Eng. Mech. (ASCE)* **119**:8 (1993), 1649–1662.
- [Chang-Liang 1974] V. Chang-Liang, *Dynamic response of structures in layered soils*, Ph.D. Thesis, MIT, Cambridge, MA, 1974, Available at <http://nisee.berkeley.edu/elibrary/Text/200612062>.
- [Gazetas and Roesset 1976] G. Gazetas and J. M. Roesset, "Forced vibrations of strip footings on layered soils", pp. 115–131 in *Methods of structural analysis: Proceedings of the National Structural Engineering Conference* (Madison, WI, 1976), edited by W. E. Saul and A. H. Peyrol, ASCE, New York, 1976.
- [Hryniewicz 1981] Z. Hryniewicz, "Dynamic response of a rigid strip on elastic half-space", *Comput. Methods Appl. Mech. Eng.* **25**:3 (1981), 355–364.
- [Israil and Ahmad 1989] A. S. M. Israil and S. Ahmad, "Dynamic vertical compliance of strip foundations in layered soils", *Earthquake Eng. Struct. Dyn.* **18**:7 (1989), 933–950.

- [Japón et al. 1997] B. R. Japón, R. Gallego, and J. Domínguez, “Dynamic stiffness of foundations on saturated poroelastic soils”, *J. Eng. Mech. (ASCE)* **123**:11 (1997), 1121–1129.
- [Karasudhi et al. 1968] P. Karasudhi, L. M. Keep, and S. L. Lee, “Vibratory motion of a body on an elastic half plane”, *J. Appl. Mech. (ASME)* **35** (1968), 697–705.
- [Kassir and Xu 1988] M. K. Kassir and J. Xu, “Interaction functions of a rigid strip bonded to saturated elastic half-space”, *Int. J. Solids Struct.* **24**:9 (1988), 915–936.
- [Kokkinos and Spyrakos 1991] F. T. Kokkinos and C. C. Spyrakos, “Dynamic analysis of flexible strip-foundations in the frequency domain”, *Comput. Struct.* **39**:5 (1991), 473–482.
- [Luco and Westmann 1972] J. E. Luco and R. A. Westmann, “Dynamic response of rigid footing bonded to an elastic half space”, *J. Appl. Mech. (ASME)* **39** (1972), 527–534.
- [Piessens et al. 1983] R. Piessens, E. de Doncker-Kapenga, C. W. Überhuber, and Kahaner, *QUADPACK: A subroutine package for automatic integration*, Springer Series in Computational Mathematics **1**, Springer, Berlin, 1983. MR 85b:65022
- [Rajapakse and Senjuntichai 1995] R. K. N. D. Rajapakse and T. Senjuntichai, “Dynamic response of a multi-layered poroelastic medium”, *Earthquake Eng. Struct. Dyn.* **24**:5 (1995), 703–722.
- [Selvadurai 1979] A. P. S. Selvadurai, *Elastic analysis of soil-foundation interaction*, Elsevier, Amsterdam, 1979.
- [Senjuntichai and Rajapakse 1994] T. Senjuntichai and R. K. N. D. Rajapakse, “Dynamic Green’s functions of homogeneous poroelastic half-plane”, *J. Eng. Mech. (ASCE)* **120**:11 (1994), 2381–2404.
- [Senjuntichai and Rajapakse 1996] T. Senjuntichai and R. K. N. D. Rajapakse, “Dynamics of a rigid strip bonded to a multi-layered poroelastic medium”, pp. 353–370 in *Mechanics of poroelastic media*, edited by A. P. S. Selvadurai, Solid Mechanics and its Applications **41**, Kluwer, Dordrecht, 1996.
- [Senjuntichai and Sapsathiarn 2003] T. Senjuntichai and Y. Sapsathiarn, “Forced vertical vibration of circular plate in multilayered poroelastic medium”, *J. Eng. Mech. (ASCE)* **129**:11 (2003), 1330–1341.
- [Sneddon 1951] I. Sneddon, *Fourier transform*, McGraw-Hill, New York, 1951.
- [Syrakos and Beskos 1986] C. C. Spyrakos and D. E. Beskos, “Dynamic response of flexible strip-foundations by boundary and finite elements”, *Soil Dyn. Earthq. Eng.* **5**:2 (1986), 84–96.
- [Syrakos and Xu 2004] C. C. Spyrakos and C. Xu, “Dynamic analysis of flexible massive strip-foundations embedded in layered soils by hybrid BEM–FEM”, *Comput. Struct.* **82**:29–30 (2004), 2541–2550.
- [Wang et al. 1991] Y. Wang, R. K. N. D. Rajapakse, and A. H. Shah, “Dynamic interaction between flexible strip foundations”, *Earthquake Eng. Struct. Dyn.* **20**:5 (1991), 441–454.
- [Warburton et al. 1971] G. B. Warburton, J. D. Richardson, and J. J. Webster, “Forced vibrations of two masses on an elastic half space”, *J. Appl. Mech. (ASME)* **38** (1971), 148–156.
- [Wong and Luco 1986] H. L. Wong and J. E. Luco, “Dynamic interaction between rigid foundations in a layered half-space”, *Soil Dyn. Earthq. Eng.* **5**:3 (1986), 149–158.
- [Zeng and Rajapakse 1999] X. Zeng and R. K. N. D. Rajapakse, “Vertical vibrations of a rigid disk embedded in a poroelastic medium”, *Int. J. Numer. Anal. Methods Geomech.* **23**:15 (1999), 2075–2095.

Received 12 Jul 2007. Revised 29 Jun 2008. Accepted 22 Sep 2008.

TEERAPONG SENJUNTICHAJ: fcetsj@eng.chula.ac.th

Department of Civil Engineering, Chulalongkorn University, Bangkok 10330, Thailand

WICHAIRAT KAEWJUEA: iwichairat@yahoo.com

Department of Civil Engineering, Chulalongkorn University, Bangkok 10330, Thailand

TIME-DOMAIN THIN LAYER METHOD FOR COMPUTING TRANSIENT RESPONSE DUE TO SUDDEN/MOVING LOADS

HIROKAZU TAKEMIYA

In this study, the author applied the thin-layer method (TLM) for developing explicit time domain solutions for the ground response due to impulse and moving loads. The Fourier and Laplace transforms for space and time, respectively, are applied to derive the transformed domain solution that satisfies given boundary conditions. The eigenvalue decomposition in the Laplace parameter domain and the discrete wave number superposition for the horizontal wave field description lead to an accurate and efficient strategy for a stable time-space domain solution. Some demonstrations are given: The first example is a fundamental problem relating to interpretation of the causal transient responses of the P, S, and Rayleigh waves due to an impact loading. The second example is also fundamental, and treats the description of a compound wave field produced by a single moving load, detailing the kinematic as well as the inertial effects, with the speed being an important parameter. The third example is an engineering application that demonstrates the track response due to train passage in order to interpret the wave generation in ground by the high-speed passage. A comparison to measurement data is presented for validation.

1. Introduction

In the 1950s, the importance of studies on the transient and stationary responses of an elastic medium under impact/moving loads was recognized, and analytical solutions to these problems were derived under special conditions. These solutions have provided information to learn about the relevant wave field. Further, they can lead to fundamental solutions to solve the more complicated engineering problem by the modern numerical methods.

Regarding fixed position loading on an elastic halfspace medium, there exists a classical work by [Lamb \[1904\]](#) for a time harmonic problem which includes an attempt for a transient response by using the Fourier series expansion. An impulse problem of a vertical point load was solved by [Pekeris \[1955\]](#) for the surface response by applying the Laplace transform and the inverse of the transform solution in the complex plane. [Mitra \[1964\]](#) applied the same method for a disc-type impulse load. [Eason \[1966\]](#) applied the inverse Laplace transform by a suitable complex number contour integration, leaving some infinite integrals that contain the Bessel function for all points of the solid. In the wave fields, the causality of respective wave propagation is of primary interest. By using those obtained Green functions, the initial-boundary value problems have been solved in the time domain boundary method step-by-step [[Takemiya and Steinfeld 1993](#); [Takemiya and Fujiwara 1994](#); [Takemiya et al. 1994](#)].

Regarding moving loads on an elastic halfspace medium, classical work has been done by applying the integral transform method. [Eason \[1965\]](#) considered a three-dimensional problem for a moving force

Keywords: transient response, causality, impulse load, moving load, thin layer method, Laplace–Fourier transform, time domain solution, high-speed train.

This work was done while the author worked at Okayama University, Okayama, Japan.

with a constant speed on a homogeneous semi-infinite space (halfspace), deriving the stationary solution in the range less than the Rayleigh wave speed. Using the Betti–Rayleigh reciprocal theorem, [Payton \[1964\]](#) dealt with a transient problem of the sudden application of a load and subsequent movement at constant velocity on an elastic halfspace. [Gakenheimer and Miklowitz \[1969\]](#) employed the Laplace transform for time and then applied the Cagniard method for the inversion of the transformed solution. They discussed the transient response for three different states in terms of the speed ratio of the moving load velocity against the seismic P and S wave velocities. A constant moving velocity constitutes a stationary problem with the relative coordinates of $x - ct$ where x is distance, t is time and c is the velocity of the moving load. Recently, such a moving load problem has been advanced in the study of ground motions induced by a high-speed train [[Dieterman and Metrikine 1997](#); [Sheng et al. 1999](#); [Lombaert et al. 2001](#); [Takemiya 2003](#); [Takemiya and Bian 2005](#)].

As an idealization of the ground, a halfspace has been employed for the sake of closed form solution that allows for the interpretation of surface wave propagation. However, in view of actual situations in which soft surface soil is deposited on hard soil, a layer or a layered halfspace may be a more useful model for interpreting the observed dispersive wave field. In the studies of seismic wave synthesis, a vertically heterogeneous model has been proposed. The finite element discretization is taken in the direction of depth by [Lysmer and Drake \[1972\]](#) for the Rayleigh wave analysis.

For the three-dimensional problem, [Olson et al. \[1984\]](#) attempted to apply the wave number decomposition for the horizontal dependence of the wave motion to the layered system. This formulation, specially termed a *thin layer method* (TLM) by [Kausel et al. \[1975\]](#), is used to evaluate the extending soil effects in the soil-foundation dynamic analysis. The frequency domain formulation results in a set of algebraic governing equations of wave numbers. If a rigid base underlies the layers, general eigenvalue determination programs are straightforwardly available for the solution. The eigenvalue decomposition enables the wave number integral operation in a closed form by residue theory. This corresponds to solving the locked modes in the layered halfspace, as stated in [Harvey \[1981\]](#), discarding the leaking modes that [Haddon \[1987\]](#) discussed.

For the former situation, an alternative approach is shown by [Kausel \[1994\]](#) and [Touhei \[1995\]](#) by taking the closed form inverse Fourier transform for time with a set of discrete wave number superimpositions for space. To fulfill the required causality of wave propagation, [Takemiya and Goda \[2000\]](#) applied the Laplace transform instead in the seismic fault rupture problem.

In this paper, by applying the Fourier and Laplace transforms to time and space, respectively, to the layered ground model, the direct time domain solution is obtained with special attention paid to the initial condition for the wave propagation. The Laplace transform scheme surpasses the Fourier transform regarding the causality arguments [[Takemiya and Guan 1993](#)].

Firstly, the response of a halfspace medium under a sudden loading on the surface is investigated with respect to the wave front propagation in time. The accuracy of the thin layer solution is checked by comparison to the closed form solution. Secondly, the moving load problem on an elastic stratum with the initial condition and the stationary without it are compared. We focus on the effect of the moving speed on the predominant wave velocity of the medium as a crucial parameter. The causal wave generation, given a starting position, is discussed in reference to the frequency domain solution. Thirdly, for validating the present procedure, wave synthesis is attempted for train loading to compare to the measurement data under the low- and high-speed passages.

2. Solution method by Fourier–Laplace transform

The equation of motion governing elastodynamics is given by

$$\mu u_{i,jj} + (\lambda + \mu)u_{j,ji} + \rho \ddot{u}_i = f_i, \tag{1}$$

where λ and μ define the Lamé constants, ρ is the density, u is the displacement, f is the body force action, and \ddot{u} denotes the double differentiation of u with respect to time t . The subscripts i and j correspond to the Cartesian coordinates x , y , and z . Equation (1) can be reformulated in the Fourier transform technique as

$$\tilde{\tilde{u}}(\xi_x, \xi_y, z, s) = \int_{-\infty}^{\infty} \int_{-\infty}^{\infty} \int_0^{\infty} u(x, y, z, t) \exp(-st) \exp(i\xi_x x) \exp(i\xi_y y) dt dx dy, \tag{2}$$

$$u(x, y, z, t) = \frac{1}{8\pi^3 i} \int_{-\infty}^{\infty} \int_{-\infty}^{\infty} \int_{\sigma-i\infty}^{\sigma+i\infty} \tilde{\tilde{u}}(\xi_x, \xi_y, z, s) \exp(pt) \exp(-i\xi_x x) \exp(-i\xi_y y) ds d\xi_x d\xi_y, \tag{3}$$

where the symbols $\tilde{\tilde{}}$ and $\tilde{\tilde{}}$ define the Fourier transform with respect to space coordinates and the Laplace transform with respect to time, respectively; the notations ξ_x and ξ_y are the wave numbers along the x and y directions respectively; and i is an imaginary unit.

The associated equation is then coordinate transformed by

$$\begin{Bmatrix} \tilde{\tilde{u}}_x \\ \tilde{\tilde{u}}_y \\ \tilde{\tilde{u}}_z \end{Bmatrix} = \begin{bmatrix} i\xi_x/\xi & 0 & -i\xi_y/\xi \\ i\xi_y/\xi & 0 & i\xi_x/\xi \\ 0 & 1 & 0 \end{bmatrix} \begin{Bmatrix} \tilde{\tilde{u}}_1 \\ \tilde{\tilde{u}}_2 \\ \tilde{\tilde{u}}_3 \end{Bmatrix}, \quad \text{or} \quad \tilde{\tilde{u}}_{x,y,z} = D\tilde{\tilde{u}}_{1,2,3}, \tag{4}$$

where $\xi = \sqrt{(\xi_x^2 + \xi_y^2)}$. The subscripts 1, 2, and 3 correspond to the new orientations after the coordinate transformation. The associated vector transformation holds for the forces also.

$$\tilde{\tilde{f}}_{x,y,z} = D\tilde{\tilde{f}}_{1,2,3}. \tag{5}$$

The coordinate transformation of (4) polarizes the three-dimensional governing (1) into an expression for the in-place wave field comprising the P and SV waves and one for the out-of-plane wave field comprising the SH wave. Then, the respective governing equations are

$$\begin{bmatrix} \mu & 0 \\ 0 & \lambda+2\mu \end{bmatrix} \begin{Bmatrix} \frac{d^2 \tilde{\tilde{u}}_{1n}}{dz^2} \\ \frac{d^2 \tilde{\tilde{u}}_{2n}}{dz^2} \end{Bmatrix} + \begin{bmatrix} 0 & -(\lambda+\mu)\xi \\ (\lambda+\mu)\xi & 0 \end{bmatrix} \begin{Bmatrix} \frac{d\tilde{\tilde{u}}_{1n}}{dz} \\ \frac{d\tilde{\tilde{u}}_{1n}}{dz} \end{Bmatrix} + \begin{bmatrix} (\lambda+2\mu)k_\alpha^2 & 0 \\ 0 & -\mu k_\beta^2 \end{bmatrix} \begin{Bmatrix} \tilde{\tilde{u}}_{1n} \\ \tilde{\tilde{u}}_{2n} \end{Bmatrix} + \begin{Bmatrix} \tilde{\tilde{f}}_{1n} \\ \tilde{\tilde{f}}_{2n} \end{Bmatrix} = \begin{Bmatrix} 0 \\ 0 \end{Bmatrix}, \tag{6}$$

$$\mu \frac{d^2 \tilde{\tilde{u}}_{3n}}{dz^2} - \mu k_\beta^2 \cdot \tilde{\tilde{u}}_{3n} + \tilde{\tilde{f}}_{3n} = 0, \tag{7}$$

where the notations $k_\alpha = \sqrt{\xi^2 + (p/V_p)^2}$ for the P wave number and $k_\beta = \sqrt{\xi^2 + (p/V_s)^2}$ for the S wave number are used.

The discretization of the displacement is employed by the thin layer elements. The use of a linear interpolation function Φ for the displacements of neighboring nodes leads to the matrix equations

$$(\mathbf{A}^{\text{P-SV}} \zeta^2 + \mathbf{B}^{\text{P-SV}} \zeta + \mathbf{C}^{\text{P-SV}} + s^2 \mathbf{M}^{\text{P-SV}}) \tilde{\mathbf{U}}_{123}^{\text{P-SV}} = \tilde{\mathbf{F}}_{123}^{\text{P-SV}}, \tag{8}$$

$$(\mathbf{A}^{\text{SH}} \zeta^2 + \mathbf{C}^{\text{SH}} + s^2 \mathbf{M}^{\text{SH}}) \tilde{\mathbf{U}}_{123}^{\text{SH}} = \tilde{\mathbf{F}}_{123}^{\text{SH}}, \tag{9}$$

where $\tilde{\mathbf{U}}$ denotes the nodal displacements and $\tilde{\mathbf{F}}$ the nodal forces. The superscripts P-SV and SH indicate the wave field concerned; namely, the former refers to the in-plane motion of the P and SV waves and the latter to the out-of-plane motion of the SH wave. Note here that the above decoupled equations coincide with those formulated in cylindrical coordinates in such a way that the subscripts 1, 2, and 3 correspond to r , z , and θ , respectively. Therefore, the coefficient matrices \mathbf{A} , \mathbf{B} , \mathbf{C} , \mathbf{M} are described in detail in the original paper [Kausel et al. 1975]. Equations (8) and (9) can be taken as eigenvalue problems with respect to the Laplace parameter s , whose general expression is cast as

$$\{\hat{\mathbf{A}}^{\text{P-SV}} + s^2 \mathbf{M}^{\text{P-SV}}\} \Phi_m^{\text{P-SV}} = 0, \tag{10}$$

$$\{\hat{\mathbf{A}}^{\text{SH}} + s^2 \mathbf{M}^{\text{SH}}\} \Phi_m^{\text{SH}} = 0, \tag{11}$$

where $\hat{\mathbf{A}}^{\text{P-SV}} = \mathbf{A}^{\text{P-SV}} \zeta^2 + \mathbf{B}^{\text{P-SV}} \zeta + \mathbf{C}^{\text{P-SV}}$ and $\hat{\mathbf{A}}^{\text{SH}} = \mathbf{A}^{\text{SH}} \zeta^2 + \mathbf{C}^{\text{SH}}$.

Equation (10) defines the generalized Rayleigh function for the in-plane wave and (11) the generalized Love waves for the out-of-plane wave by referring to the superscripts. The decomposed eigenvectors Φ satisfy the orthogonal condition:

$$\Phi_i^{\text{P-SV}} \mathbf{M}^{\text{P-SV}} \Phi_j^{\text{P-SV}} = \delta_{ij}, \tag{12}$$

$$\Phi_i^{\text{SH}} \mathbf{M}^{\text{SH}} \Phi_j^{\text{SH}} = \delta_{ij}, \tag{13}$$

$$(\Phi^{\text{P-SV}})^T \mathbf{A}^{\text{P-SV}} \Phi^{\text{P-SV}} = \mathbf{\Lambda}^{\text{P-SV}}, \tag{14}$$

$$(\Phi^{\text{SH}})^T \mathbf{A}^{\text{SH}} \Phi^{\text{SH}} = \mathbf{\Lambda}^{\text{SH}}, \tag{15}$$

$$\Phi^{\text{P-SV}} = [\phi_1^{\text{P-SV}} \phi_2^{\text{P-SV}} \dots \phi_{2n}^{\text{P-SV}}], \tag{16}$$

$$\Phi^{\text{SH}} = [\phi_1^{\text{SH}} \phi_2^{\text{SH}} \dots \phi_n^{\text{SH}}], \tag{17}$$

$$\mathbf{\Lambda}^{\text{P-SV}} = \text{diag}[-(s_i^{\text{P-SV}})^2], \quad (i = 1, 2, \dots, 2n), \tag{18}$$

$$\mathbf{\Lambda}^{\text{SH}} = \text{diag}[-(s_i^{\text{SH}})^2], \quad (i = 1, 2, \dots, n). \tag{19}$$

Therefore, using the eigenvectors above, the displacement and force vectors are represented as follows (where we've replaced superscript P-SV on Φ by subscript 1 and 2, and superscript SH by subscript 3):

$$\begin{Bmatrix} \tilde{\mathbf{U}}_1 \\ \tilde{\mathbf{U}}_2 \end{Bmatrix} = \begin{bmatrix} \Phi_1 \bar{\mathbf{E}}^{\text{P-SV}} \Phi_1^T \Phi_1 \bar{\mathbf{E}}^{\text{P-SV}} \Phi_1^T \Phi_1 \bar{\mathbf{E}}^{\text{P-SV}} \Phi_2^T \\ \Phi_2 \bar{\mathbf{E}}^{\text{P-SV}} \Phi_1^T \Phi_2 \bar{\mathbf{E}}^{\text{P-SV}} \Phi_1^T \Phi_2 \bar{\mathbf{E}}^{\text{P-SV}} \Phi_2^T \end{bmatrix} \begin{Bmatrix} \tilde{\mathbf{F}}_1 \\ \tilde{\mathbf{F}}_2 \end{Bmatrix}, \tag{20}$$

$$\mathbf{U}_3 = \left[\Phi_3 \bar{\mathbf{E}}^{\text{SH}} \Phi_3^T \Phi_3 \bar{\mathbf{E}}^{\text{SH}} \Phi_3^T \right] \begin{Bmatrix} \tilde{\mathbf{F}}_3 \end{Bmatrix}, \tag{21}$$

where

$$\tilde{\mathbf{E}}^{\text{P-SV}} = \text{diag} \left\{ \frac{1}{(-s_j^{\text{P-SV}2} + s^2)} \cdot \tilde{\mathbf{T}}(\zeta_y, s) \right\}, \quad j = 1 \sim 2n, \tag{22}$$

$$\tilde{\mathbf{E}}^{\text{SH}} = \text{diag} \left\{ \frac{1}{(-s_j^{\text{SH}2} + s^2)} \cdot \bar{T}(\zeta_y, s) \right\}, \quad j = 1 \sim n. \quad (23)$$

The term $\tilde{T}(\zeta_y, s)$ defines the load effect, whose detailed description is given later. the wave number domain expressions for the load vectors are

$$\tilde{\mathbf{F}}_1 = \left[-i \frac{\zeta_x}{\zeta} \mathbf{I} - i \frac{\zeta_y}{\zeta} \mathbf{I} \right] \begin{Bmatrix} \tilde{\mathbf{F}}_x(\zeta_x, \zeta_y) \\ \tilde{\mathbf{F}}_y(\zeta_x, \zeta_y) \end{Bmatrix}, \quad (24)$$

$$\tilde{\mathbf{F}}_2 = \tilde{\mathbf{F}}_z(\zeta_x, \zeta_y), \quad (25)$$

$$\tilde{\mathbf{F}}_3 = \left[-i \frac{\zeta_y}{\zeta} \mathbf{I} - i \frac{\zeta_x}{\zeta} \mathbf{I} \right] \begin{Bmatrix} \tilde{\mathbf{F}}_x(\zeta_x, \zeta_y) \\ \tilde{\mathbf{F}}_y(\zeta_x, \zeta_y) \end{Bmatrix}, \quad (26)$$

where \mathbf{I} denotes a unit matrix. The expressions in (20) and (21) are now back transformed into the original Cartesian coordinates by using the transpose of the coefficient matrix of (4).

$$\begin{Bmatrix} \tilde{U}_x \\ \tilde{U}_y \\ \tilde{U}_z \end{Bmatrix} = \begin{bmatrix} \frac{\zeta_x^2}{\zeta^2} \Phi_1 \tilde{\mathbf{E}}^{\text{P-SV}} \Phi_1^T + \frac{\zeta_y^2}{\zeta^2} \Phi_3 \tilde{\mathbf{E}}^{\text{SH}} \Phi_3^T & \frac{\zeta_x \zeta_y}{\zeta^2} \Phi_1 \tilde{\mathbf{E}}^{\text{P-SV}} \Phi_1^T - \frac{\zeta_x \zeta_y}{\zeta^2} \Phi_3 \tilde{\mathbf{E}}^{\text{SH}} \Phi_3^T & i \frac{\zeta_x}{\zeta^2} \Phi_1 \tilde{\mathbf{E}}^{\text{P-SV}} \Phi_2^T \\ \frac{\zeta_x \zeta_y}{\zeta^2} \Phi_1 \tilde{\mathbf{E}}^{\text{P-SV}} \Phi_1^T - \frac{\zeta_x \zeta_y}{\zeta^2} \Phi_3 \tilde{\mathbf{E}}^{\text{SH}} \Phi_3^T & \frac{\zeta_y^2}{\zeta^2} \Phi_1 \tilde{\mathbf{E}}^{\text{P-SV}} \Phi_1^T + \frac{\zeta_x^2}{\zeta^2} \Phi_3 \tilde{\mathbf{E}}^{\text{SH}} \Phi_3^T & i \frac{\zeta_y}{\zeta^2} \Phi_1 \tilde{\mathbf{E}}^{\text{P-SV}} \Phi_2^T \\ -i \frac{\zeta_x}{\zeta^2} \Phi_2 \tilde{\mathbf{E}}^{\text{P-SV}} \Phi_1^T & -i \frac{\zeta_y}{\zeta^2} \Phi_2 \tilde{\mathbf{E}}^{\text{P-SV}} \Phi_1^T & \Phi_2 \tilde{\mathbf{E}}^{\text{P-SV}} \Phi_2^T \end{bmatrix} \times \begin{Bmatrix} \tilde{\mathbf{F}}_x(\zeta_x, \zeta_y) \\ \tilde{\mathbf{F}}_y(\zeta_x, \zeta_y) \\ \tilde{\mathbf{F}}_z(\zeta_x, \zeta_y) \end{Bmatrix}. \quad (27)$$

The horizontal loading generates the P-SV and SH waves while the vertical loading generates the P-SV but not the SH wave. The explicit expression for the analytical inverse Laplace transforms of the concerned elements $\tilde{\mathbf{E}}^{\text{P-SV}}$ and $\tilde{\mathbf{E}}^{\text{SH}}$ are given in the next section for given loading time functions $T(t)$.

The inverse Fourier transform of (3) can be replaced by the following stepwise numerical integration:

$$\mathbf{u}(x, y, z, N \Delta t) = \frac{1}{(2\pi)^2} \int_{-\infty}^{\infty} \int_{-\infty}^{\infty} \tilde{\mathbf{u}}(\zeta_x, \zeta_y, z, N \Delta t) e^{-i\zeta_x x} e^{-i\zeta_y y} d\zeta_x d\zeta_y, \quad (28)$$

where N is the number of the time increments Δt used for response duration. The odd and even nature of $\tilde{\mathbf{u}}(\zeta_x, \zeta_y, z, N \Delta t)$, when multiplied by $e^{-i\zeta_x x} e^{-i\zeta_y y}$, is used to our advantage to carry out the integral computation over $-\infty$ to $+\infty$ efficiently. The cylindrical coordinate transformation is employed further to make the integral operation more convenient since the wave number range over the distance ζ_r is truncated by certain discrete wave numbers, while that over the angle ζ_θ is limited to $0 \sim \pi/2$. Therefore,

$$\begin{aligned} \mathbf{u}(x, y, z, n \Delta t) &= \frac{1}{(2\pi)^2} \int_0^\infty \int_0^{2\pi} \tilde{\mathbf{u}}(\zeta_r, \zeta_\theta, z, n \Delta t) e^{-\zeta_r \cos \zeta_\theta} e^{\zeta_r \sin \zeta_\theta} \zeta_r d\zeta_r d\zeta_\theta \\ &\cong \frac{1}{(2\pi)^2} \sum_{m=0}^{\pi/2} \sum_{n=0}^L \tilde{U}(\zeta_{rn}, \zeta_{\theta m}, z, N \Delta t) e^{-\zeta_{rn} \cos \zeta_{\theta n}} e^{\zeta_{rn} \sin \zeta_{\theta n}} \Delta \zeta_r \Delta \zeta_\theta, \end{aligned} \quad (29)$$

where L is the fundamental wavelength, $\Delta \xi_r = 2\pi/L$ and $\Delta \xi_\theta = \pi/2N$ are the wave number increments for the radius and angle, respectively, for which the total numbers N and M are used for superposition.

3. Modal transient responses due to certain surface loads

3.1. Space distribution. Consider a uniformly distributed surface load of unit intensity over $2b_x$ by $2b_y$ in the x - y plane which is either suddenly applied or impulsively applied at a fixed position. We can say that the the distribution along the x direction is given by $F_x(x)$, along the y direction by $F_y(x)$, and along the z direction by $\delta(z)$, and the intensity time variation is given by $T(t)$. Then,

$$F_i(x, y, z; t) = F_x(x)F_y(y)\delta(z) \cdot T(t). \tag{30}$$

The Fourier–Laplace transform of (30) is given by

$$\tilde{F}_i(\xi_x, \xi_y, s) = \tilde{F}_x(\xi_x)\tilde{F}_y(\xi_y) \cdot \tilde{T}(s). \tag{31}$$

(a) *Uniform load.* A uniform load on the rectangular area is defined as

$$F_x(x) = [H(x + b_x) - H(x - b_x)] \iff \tilde{F}_x(\xi_x) = \frac{\sin(\xi_x b_x)}{\xi_x b_x}, \tag{32}$$

$$F_y(y) = [H(y + b_y) - H(y - b_y)] \iff \tilde{F}_y(\xi_y) = \frac{\sin(\xi_y b_y)}{\xi_y b_y}, \tag{33}$$

where the notation $H()$ defines a Heaviside function and the symbol \iff indicates Fourier transform pairs.

(b) *Load proportional to the deflection of an elastically supported beam.* Consider an elastically supported beam of the bending rigidity EI on Winkler springs whose stiffness is k per unit length along the y -axis but constant in width $2b_x$ in the x -direction. The base reaction of the Winkler springs is

$$F_z(x, y) = F_x(x) \cdot F_y(y) = \frac{1}{\sqrt{2}L_c} \exp\left(-\left|\frac{y}{L_c}\right|\right) \sin\left(\left|\frac{y}{L_c}\right| + \frac{\pi}{4}\right) \times \{H(x + b_x) - H(x - b_x)\}, \tag{34}$$

where $L_c = \sqrt[4]{4EI/k}$.

The Fourier transform of (34) is given by

$$F_z(\xi_x, \xi_y) = F_z(\xi_x) \cdot F_z(\xi_y) = \frac{4}{4 + (\xi_y L_c)^4} \cdot \frac{2 \sin \xi_x b_x}{\xi_x b_x}. \tag{35}$$

3.2. Time function.

(a) *Dirac type loading.* An impulse loading is defined by a Delta function $\delta()$. The Laplace transform pair is

$$T(t) = \delta(t) \iff \tilde{T}(s) = 1. \tag{36}$$

(b) *Heaviside type loading.* A suddenly applied loading is expressed by a Heaviside function $H(t)$. The corresponding Laplace transform pair is

$$T(t) = H(t) \iff \tilde{T}(s) = \frac{1}{s}. \tag{37}$$

(c) *Moving load.* A moving load with a space distribution $F_y(y)$ moving at constant speed c along the y -direction is considered. The mathematical expression is then

$$F_z(y - ct) \iff \tilde{F}(\xi_y) \tilde{T}(\xi_y, s), \tag{38}$$

where

$$\tilde{T}(\xi_y, s) = \frac{1}{s - i\xi_y c}. \tag{39}$$

The Laplace domain representation of the moving load has a similar nature as the modified Heaviside type loading but with a phase shift such that

$$\tilde{T}(\xi_y, t) = e^{i\xi_y ct}. \tag{40}$$

This expression indicates a specific periodicity in time by the train speed under a given site condition.

A loading consisting of N consecutive loads of intensities F_n ($n = 1, 2, \dots, N$) is expressed as

$$F_z(y - ct) = \sum_{n=0}^N F_n \delta(y - c \cdot n \Delta t), \tag{41}$$

so that the frequency domain counterpart becomes $\tilde{T}(\xi_y, n \Delta t) = e^{i\xi_y c \cdot n \Delta t}$. Further, in the case of a moving load accompanied by a harmonic oscillation of frequency ω_0 , the following expression holds:

$$F(y - ct) \exp(i\omega_0 t) \iff \tilde{F}_z(\xi_y) \tilde{T}(\xi_y, s), \tag{42}$$

where

$$\tilde{T}(\xi_y, s) = \frac{1}{s - i(\xi_y c - \omega_0)}. \tag{43}$$

The inverse Laplace transform is

$$\tilde{T}(\xi_y, t) = e^{i(\xi_y c - \omega_0)t}. \tag{44}$$

3.3. Eigenmode response. The transient responses of the decomposed modes are obtained from the inverse Laplace transforms of Equations (22) and (23) as

$$\mathbf{E}^{P-SV/SH} = \frac{1}{2\pi i} \int_{\gamma i - \infty}^{\gamma i + \infty} \text{diag} \left\{ \frac{1}{(-(s_j^{P-SV/SH})^2 + s^2)} \cdot \tilde{T}(s) \right\} e^{st} ds, \tag{45}$$

which is evaluated from the residue theory for the respective loading types in the previous section. (Here $\mathbf{E}^{P-SV/SH}$ means that either subscript may be taken consistently across the equation.)

(a) *Dirac type loading.* Introducing Equation (45) for $\tilde{T}(s)$ from Equation (36) results in the time domain solution. The damping effect is now taken into account by introducing the damping ratio β_j into each decomposed mode, taken as a system with a single degree of freedom. Then

$$\mathbf{E}^{P-SV/SH} = \text{diag} \left[\exp(-\beta_j s_j^{P-SV/SH} t) \frac{\sin(s_j^{P-SV/SH} t)}{s_j^{P-SV/SH}} \right]. \tag{46}$$

(b) *Heaviside type loading.* The response due to a suddenly applied (Heaviside type) loading is straightforwardly obtained by introducing $\bar{T}(s)$ from (36) into (45). However, we can alternatively evaluate it by integrating the Dirac's impulse response of (46). The result for the initial condition at rest is then:

$$\mathbf{E}_H^{P-SV/SH}(t) = \text{diag} \left[\frac{1 - \exp(-\beta s_j^{P-SV/SH} t) \{ \beta \sin(s_j^{P-SV/SH} t) + \cos(s_j^{P-SV/SH} t) \}}{(\beta s_j^{P-SV})^2 + (s_j^{P-SV})^2} \right]. \quad (47)$$

(c) *Moving load.* For a moving oscillating load of a constant speed c in the y -direction with the frequency ω_0 , the inverse Laplace transform gives, after substituting (45) for $\bar{T}(\zeta_y, s)$ from (43):

$$\begin{aligned} \mathbf{E}^{P-SV/SH} = \text{diag} & \frac{1}{(s_j^{P-SV/SH})^2 + (\beta s_j^{P-SV/SH} + i(\zeta_y c - \omega_0))^2} \\ & \times \left(-\exp(-\beta s_j^{P-SV/SH} t) \beta \sin(s_j^{P-SV/SH} t) + \cos(s_j^{P-SV/SH} t) + \cos((\zeta_y c - \omega_0)t) \right. \\ & \left. - i \left(\frac{\zeta_y c - \omega_0}{s_j^{P-SV/SH}} \exp(-\beta s_j^{P-SV/SH} t) \sin(s_j^{P-SV/SH} t) - \sin((\zeta_y c - \omega_0)t) \right) \right), \quad (48) \end{aligned}$$

which has a dominant contribution along the line $\zeta_y c = \omega_0$. Comparing (48) with (47) suggests that the latter response is reduced to the former response on this line. Therefore, at this resonant situation, the response due to a moving load turns out to be like that caused by a sudden Heaviside-type loading at the temporal position by the moving speed.

4. Laplace transform versus Fourier transform

We now discuss the correspondence between the Laplace transform and the Fourier transform. This will assist the interpretation of the results obtained using the first method described above. The formal conversion follows by substituting the Laplace parameter “ s ” with another parameter “ $i\omega$ ” of frequency ω multiplied by an imaginary unit i . Then, (30) becomes

$$F_i(x, y, z; \omega) = F_x(x) F_y(y) \delta(z) \cdot \bar{T}(\omega), \quad (49)$$

where the time function for the moving load (43) is expressed, after some manipulation, by

$$\bar{T}(\zeta_y, \omega) = \frac{1}{c} \frac{i}{\left(\zeta_y - \frac{\omega - \omega_0}{c} \right)} = \frac{2\pi}{c} \delta \left(\zeta_y - \frac{\omega - \omega_0}{c} \right). \quad (50)$$

The $\delta()$ function involved indicates that the wave number along the moving direction of the load can be selected from the wave number-frequency domain solution as follows:

$$\zeta_y = (\omega - \omega_0)/c. \quad (51)$$

The homogeneous equations (10) and (11) are replaced by

$$\{ \hat{\mathbf{A}}^{P-SV} - \omega^2 \mathbf{M}^{P-SV} \} \Phi_m^{P-SV} = 0, \quad (52)$$

$$\{ \hat{\mathbf{A}}^{SH} - \omega^2 \mathbf{M}^{SH} \} \Phi_m^{SH} = 0. \quad (53)$$

The solutions corresponding to in-plane and out-of-plane motions provide information on the wave number versus frequency characteristics of the respective eigenmodes. The inverse Fourier transforms with respect to wave numbers and frequency yield, in view of (51), the solution

$$\mathbf{u}(x, y, z, t) = \frac{1}{(2\pi)^2 c} \int_{-\infty}^{\infty} \int_{-\infty}^{\infty} \mathbf{u}\left(\xi_x, \frac{\omega - \omega_0}{c}, z, \omega\right) e^{-i\xi_x x} \cdot e^{i\left(\frac{\omega_0 y}{c}\right)} \cdot e^{i\omega\left(t - \frac{y}{c}\right)} d\xi_x d\omega. \quad (54)$$

Hence, the solution is characterized by the crossings of the wave number versus frequency diagrams of dispersive wave modes and the speed line of (51).

5. Computational results

5.1. Fundamental problem I: Transient response of a halfspace under a sudden loading. Investigated first is the transient response of an elastic isotropic homogeneous halfspace when a uniform disk load of a unit radius is impulsively applied (a Dirac-type loading) on the free surface. The schematic model is shown on the right. The properties are defined by the density ρ , the P wave and S wave velocities c_1 and c_2 , respectively, and the Poisson ratio ν . For the sake of the present TLM computation the halfspace is approximated by a stratum of the rigid base at 228 m deep, which is discretized by sub-layers as 10@0.4 m + 5@0.8 m + 10@1.0 m \times 10 + 10@2.0 m + 10@4.0 m \times 10 + 15@10 m. The fundamental wavelength is set to 700 m for the analysis. The discrete wave numbers for superposition are then set to 700. The time increment for response computation is $\Delta t = 10^{-3}$ [s]. The wave modes employed are 40 for in-plane motion and 20 for out-of-plane motion. These values yield a reliable solution with less computational time. The response observation points are as indicated in the figure to the right.

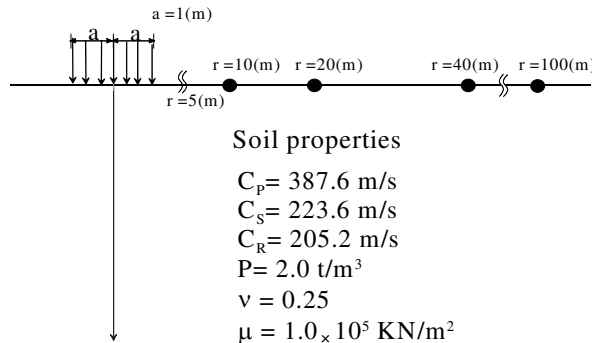


Figure 1. A halfspace under an impulse load.

The transient responses that reach the static displacements computed by the present method are depicted by symbols in Figure 2 in the dimensionless form. The response U_{ij} can be identified by the subscript ij with i indicating the response direction and j the loading direction. They are compared with analytical halfspace solutions by lines (denoted by HS) that are obtained by the author by following Eason’s formulation [1966] for the vertical loading. Since the Eason solution is limited to times after the S wave arrival, the author improved it as valid for all times. Further, the author extended it to the horizontal loading case to give an excellent match, when the loaded area is assumed small enough, with Pekeris’ solution [1955] for a point loading. The letters P , S and R are designated to indicate the wave front arrivals of the P , S and Rayleigh waves, respectively. A unit of dimensionless time corresponds to the arrival of the S wave at a focused point. The wave causality is noted to be clearly fulfilled in view of the respective wave front arrival times. An excellent agreement is attained between the present and the closed form solutions, as the focused point is at a far distance from the loading center. In Figure 2, the Rayleigh wave dominates the vertical and horizontal responses, whereas the P wave contribution appears small.

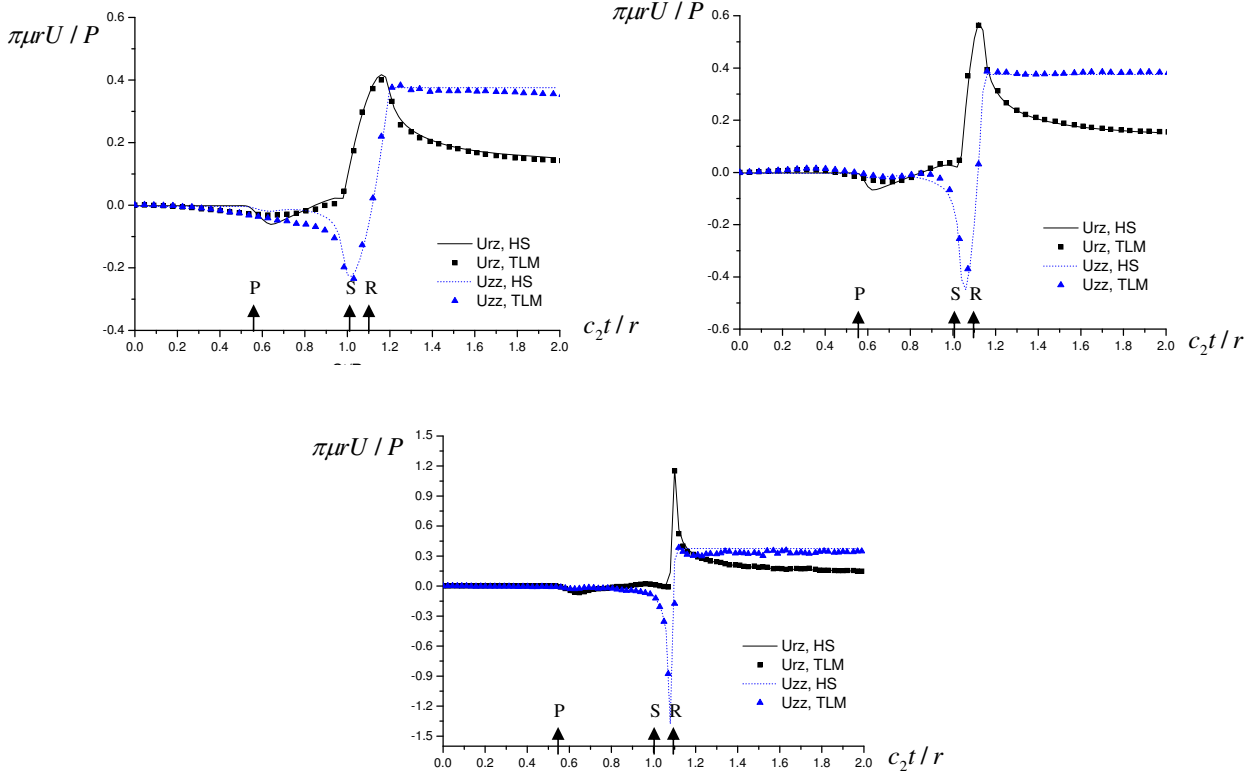


Figure 2. Transient response of a halfspace under a vertical disk load: horizontal (radial) and vertical at distances of 10 m (top left), 20 m (top right), and 100 m (bottom).

5.2. Fundamental problem II: Causality in a transient response for a moving load on a stratum. Comparison of the ground surface response is made between the moving Green functions from the Fourier Transform method [Takemiya 2001; Takemiya et al. 2001] that uses the wave propagation matrix across layers and the present direct Time Domain TLM. In order to investigate the wave field for a suddenly applied and then moving load, a simple stratum, as described in Figure 3, is employed for the model. The load and stratum properties are provided there. The sublayer division is made such that $20\text{ m} = 50 @ 0.4\text{ m}$, which guarantees roughly the shortest wavelength of 2 m at the frequency 100 Hz since there exist 5 nodal points within it. A key consideration in the design of this investigation is the placement of the observation point at a location which allows the initial effect to be distinguished from the moving effect of the load.

First, the site characteristics are investigated by computing the wave dispersion curves in the form of the wave number versus frequency, and the group velocity versus frequency. They are depicted in Figure 4 (left and right, respectively). In layered soils, the wave generation is significantly affected by the so-called Airy phase frequency. These frequencies are noted at 4 Hz, 13 Hz, and 12 Hz, respectively, for the first, second, and third modes of the in-plane motions. The speed of the moving load is also important for the wave generation. Here, three representative situations, as defined by the speed ratio α of the moving load against the S wave velocity of the medium, are demonstrated: $\alpha < 1$ is the subseismic

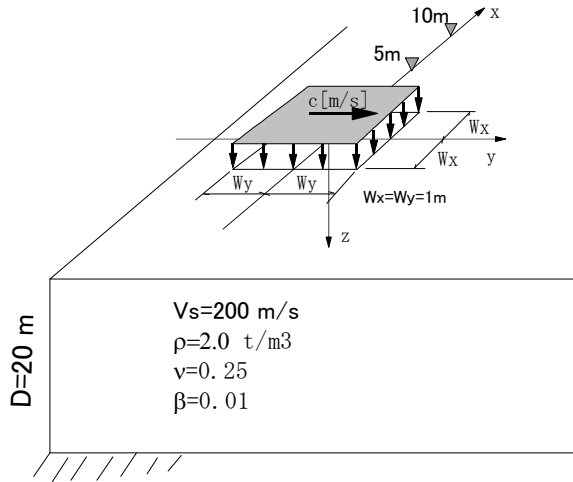


Figure 3. Stratum model for analysis under a moving load.

condition, $\alpha = 1$ the seismic condition, and $\alpha > 1$ the superseismic condition. These are indicated in Figure 4 by the dashed lines as a parameter to locate which frequency is most associated with the wave generation. For the speed ratio $\alpha < 1$, there is no crossing with the dispersion curves; for $\alpha = 1$, the crossing of the speed line with the 1st mode occurs at 6 Hz; and for $\alpha = 2$, it occurs at 4 Hz.

The TLM computed responses at the ground surface are depicted in Figures 5–7. The distance between the starting position of the load and the observation point is taken as 40 m along the direction of motion, with an offset of either 5 m or 10 m perpendicular to the direction of motion. The numbers of wave

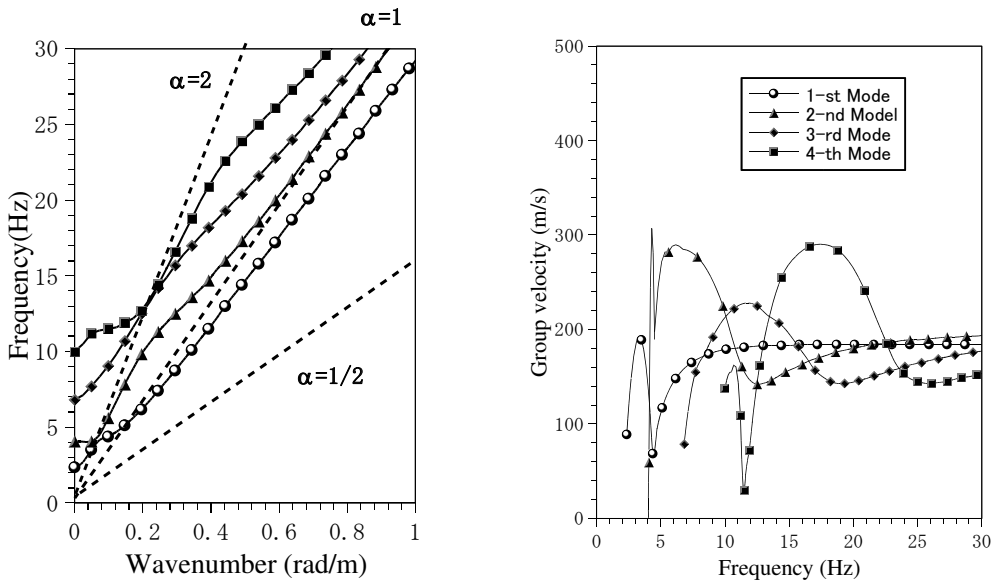


Figure 4. Wave dispersion characteristic for in-plane wave. Frequency-wave number curve (left) and group velocity-frequency curve (right).

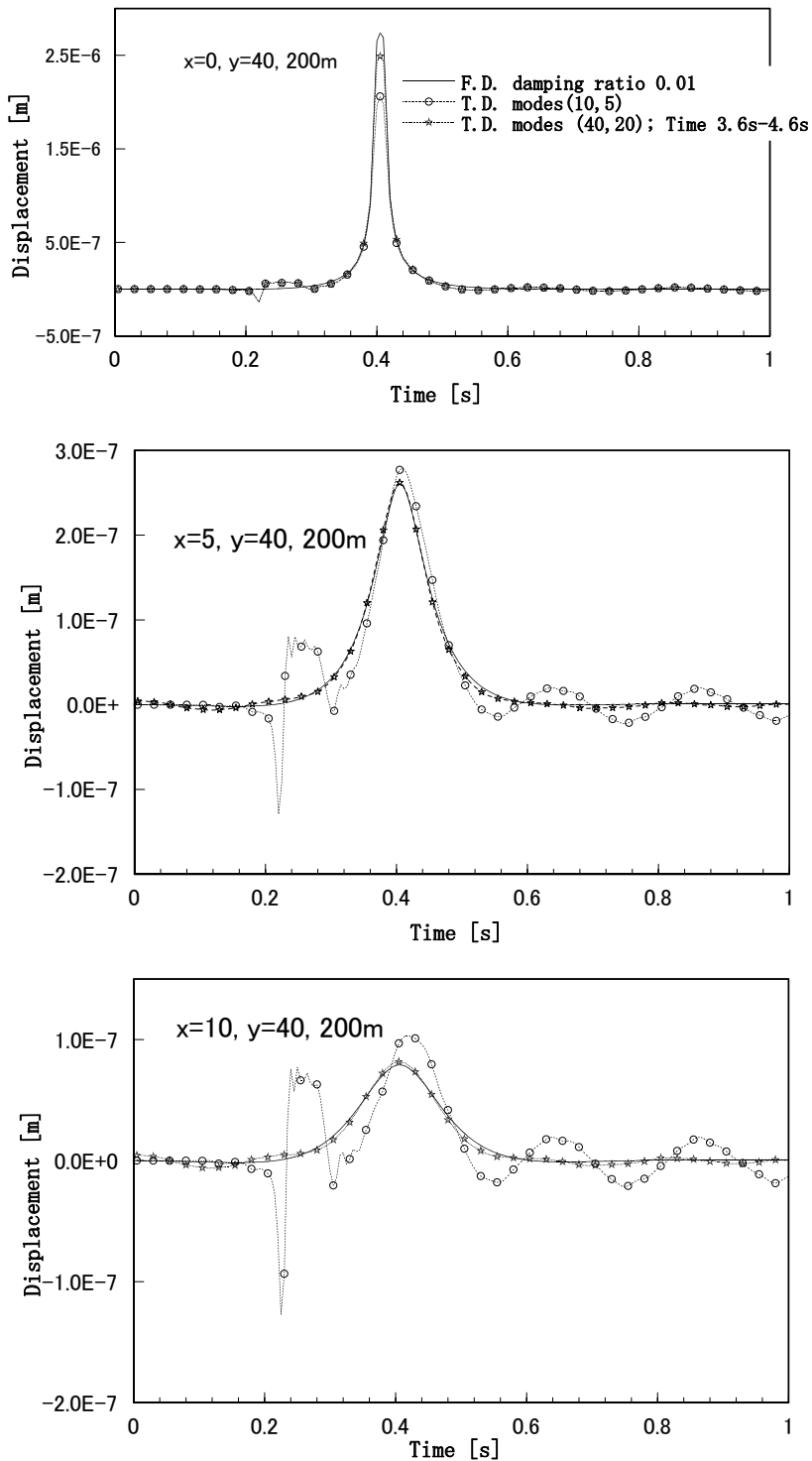


Figure 5. Transient response under a moving load for the $\alpha = 0.5$ subseismic situation.

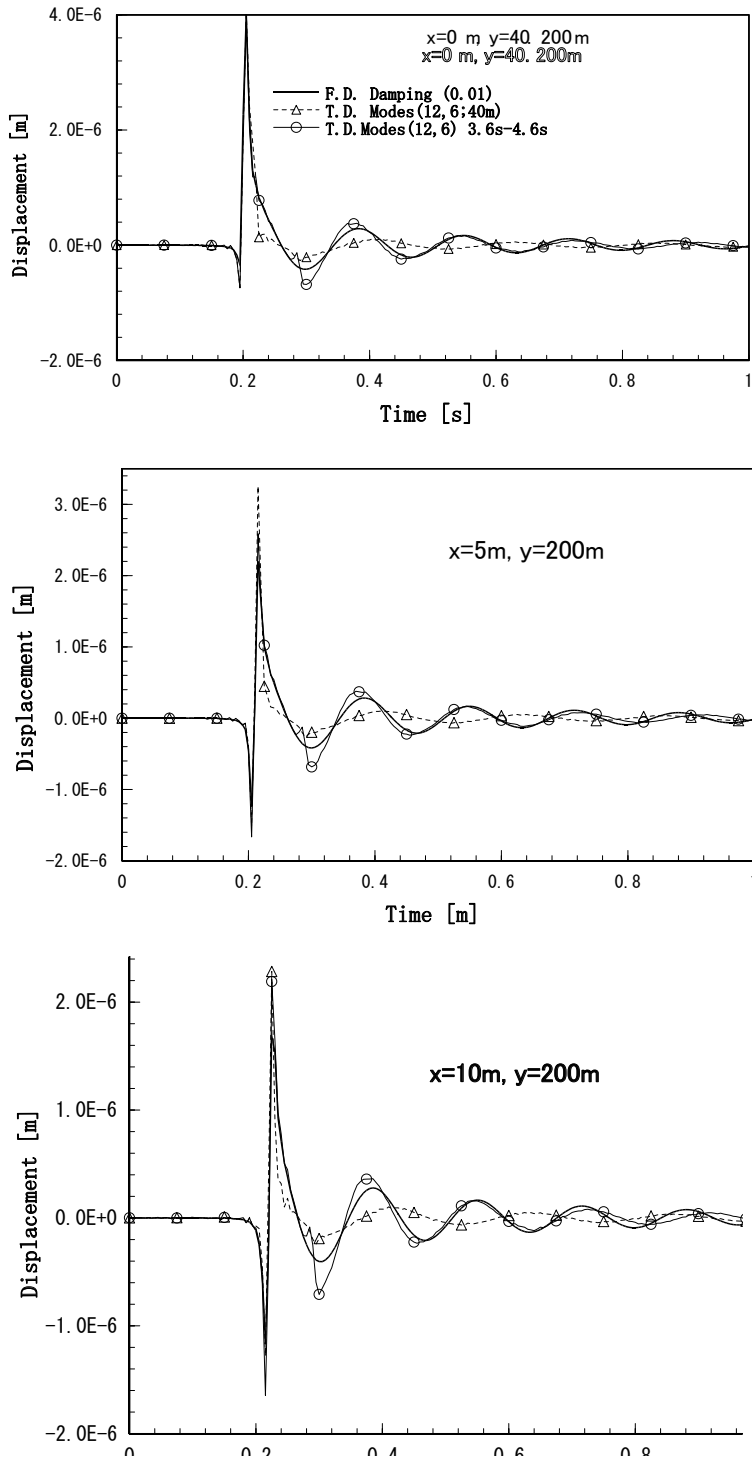


Figure 6. Transient response under a moving load for the $\alpha = 1.0$ seismic situation.

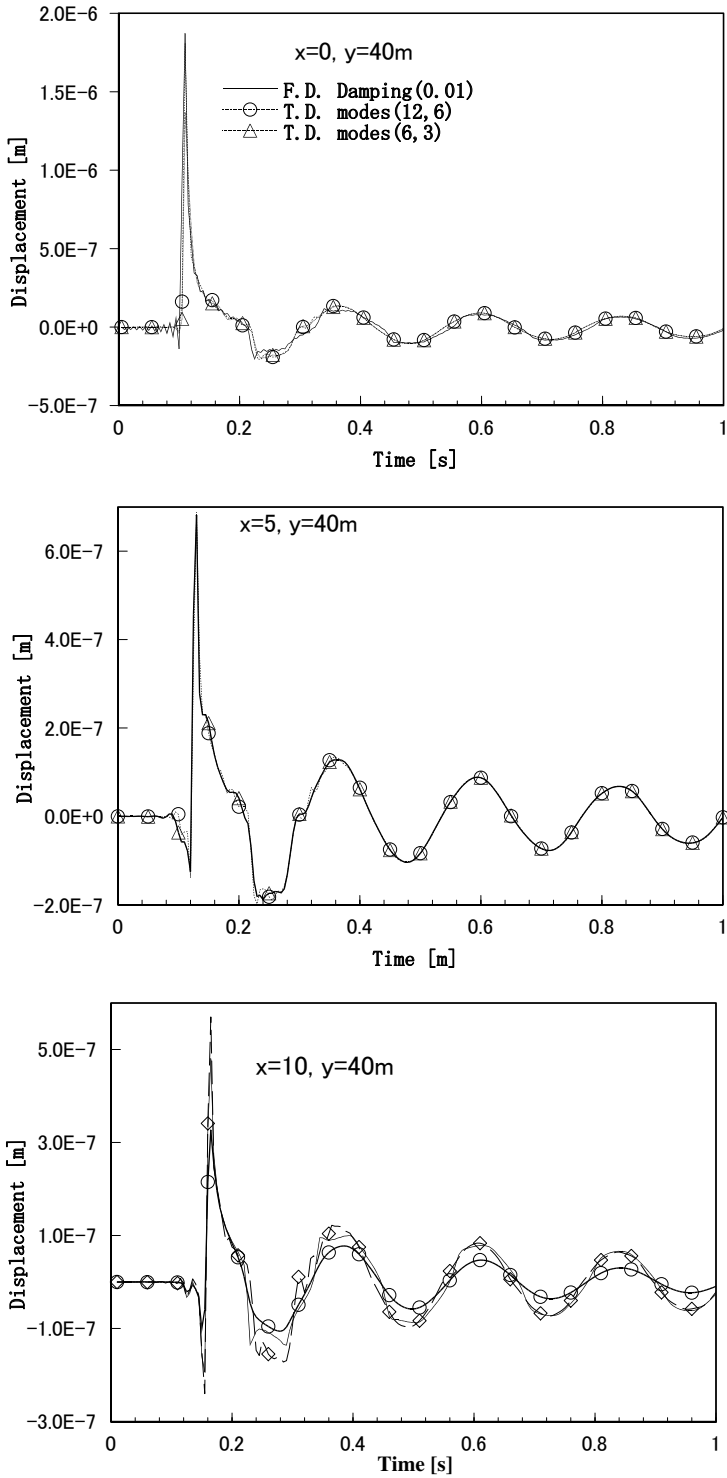


Figure 7. Transient response under a moving load for the $\alpha = 2.0$ superseismic situation.

modes used are indicated in the figure: the first number refers to the number of in-plane modes and the second number to the number of out-of-plane mode. By referring to (40), we note that the moving load has a velocity-dependent periodic nature in addition to that of the Laplace transform for the Heaviside type loading. The consequences are drastically different response features for different speeds of the moving load. For the subseismic situation with speed ratio $\alpha = 1/2$, the initial impact effect appears at an observation point ahead of the moving load at the time of seismic wave arrivals. The fronts of the P , SV , and Rayleigh waves are clearly detectable. Therefore, the former can be separated from the latter by taking a long approach, for instance 200 m, from the starting point to the observation point. The total response time histories, after the initial effect is excluded by an appropriate time window, are also depicted. They are denoted by TD with a specific time indicated. The frequency domain solutions, indicated as FD [Takemiya 2001; 2003], are also depicted in the figure for comparison. These include a nominal small damping ratio $\beta = 0.01$ for the sake of a stable computation. All the resulting FD responses, regardless of the distance off the moving line, look like kinematic ground deformations; the responses attain a maximum at the moment the load passes the observation point, with almost symmetric variation before and after it.

Next, for the seismic resonance situation of the speed ratio $\alpha = 1$, the response features are described as an impulsive response, as for a δ -type loading at the temporal position of the load, with small successive fluctuations with a specific period. This periodicity is distorted in comparison with the frequency domain solution if the observation point lies in a short distance. However, if the observation point is set as far as 200 m, then the periodicity agrees well with the 6 Hz periodicity from the frequency domain solution. This frequency was predicted from the crossing of the speed line with the first wave mode curve.

Lastly, for the superseismic situation of the speed ratio $\alpha = 2$, the direct effect of the moving load precedes the wave fronts due to the initial loading. Because of the small contribution, they are embedded in the dynamic response within the chosen time window in the figure. The respective peak values are quite similar to those in the seismic resonance case, but smaller. In contrast, the harmonic fluctuations are more conspicuous in the superseismic situation. This phenomenon may be reasoned as follows: the periodicity of the tailing response is estimated as 4 Hz, which coincides with the crossing frequency of the speed line with the first mode wave curve and furthermore corresponds to the Airy phase frequency of this wave mode.

The Fourier amplitudes of the transient responses in Figure 5–7 are depicted in Figure 8. For the speed ratio $\alpha = 0.5$, the amplitudes are almost constant in the frequency range up to several Hz. For $\alpha = 1$ or 2, it is interesting to note that a peak response due to the moving speed of the load occurs at different frequencies. For the former case it is at 5.5 Hz and for the latter case it is at 4.5 Hz. In the above low frequency range or below the peak, a significant response reduction results as the distance increases off the moving axis. This fact has been already pointed out in [Takemiya and Goda 2000] as a consequence of the cut-off frequency to be determined by the stratum depth.

5.3. Application: Track response under train passage. Another application of the TLM is applied to an actual problem to predict the response of a ballast type train track under the passage of trains. The train geometry is illustrated in Table 1 and Figure 9. The wave fields of layered soils due to the Swedish X-2000 trains of different speeds have already been analyzed in the frequency domain solution method [Takemiya 2001; Takemiya and Bian 2005]. The site condition is prescribed for the equivalent soil properties in

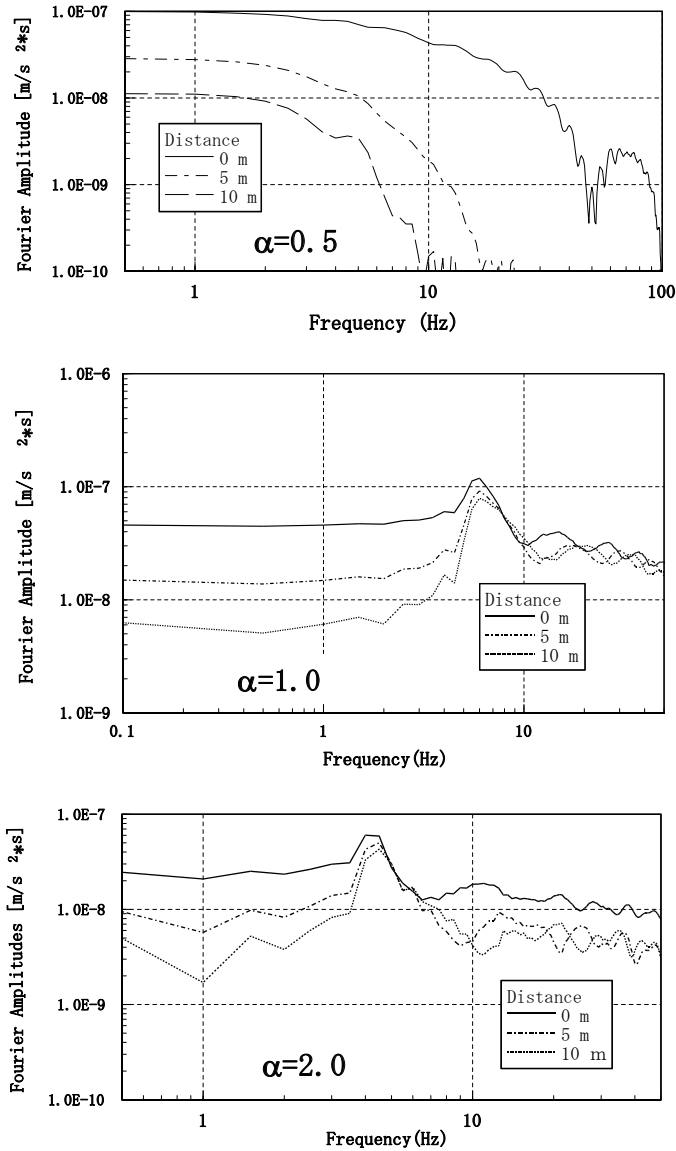


Figure 8. Fourier amplitudes of transient responses.

Train Car No (Southbound)	5	4	3	2	1
P_{n2}, P_{n1} (kN)	181.5, 180.0	122.5, 122.5	122.5, 122.5	122.5, 122.5	117.5, 160
a_n (m)	2.9	2.9	2.9	2.9	2.9
b_n (m)	6.6	14.8	14.8	14.8	11.6
L_n (m)	17.17	24.4	24.4	24.4	22.17

Table 1. Swedish X-2000 train geometry (see also Figure 9).

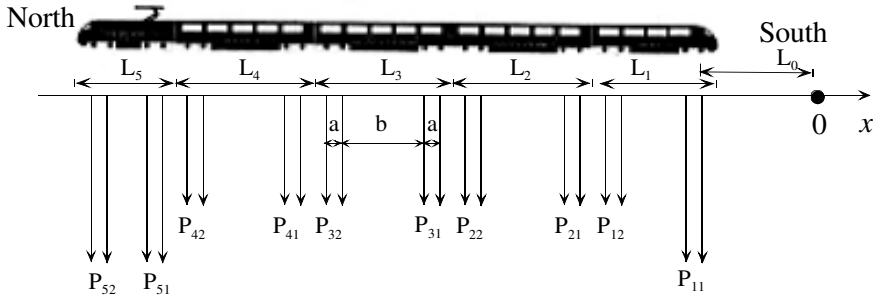


Figure 9. A train geometry, Swedish X-2000.

Table 2. Herein a stacked layered soil model is considered for the sake of the TLM computation. An additional layer of 1.4 m thickness is put at the top to approximate the track portion, and the fictitious rigid bottom base is set at 45 m depth. The employed subdivision is $4 + 10 + 9 + 12 + 45 = 80$ layers in total. An equal sublayer thickness is employed within the respective original geological layers.

The axle loading due to train passage onto the ground beneath is presumed in the form of (34) with $q = (3\pi/4)L_c = 6.2$ m [Takemiya 2001], which means that 9 sleepers of 2 m long are involved together for a track deflection under the given rigidities of rails and ballast. This set of adjusted loads gives rise to a train load when the phase distances associated with the train geometry are properly taken into account. Since these are taken as in a stationary moving state, the causal response due to the initial condition should be excluded. For this requirement, first, the starting position of the axle load is set at 80 m in front of the focused position for the moving speed of 70 km/h, and 400 m for the moving speed of 200 km/h. The response time windows are then picked up to exclude the transient response due to the initial condition by inspection of the duration of these response time histories. Figure 10 shows the results after superposition of individual responses by following (41) for the given axle loads in Table 1. The kinematic response at low train speed is reproduced in the computation and shows a good fitting with the measurement data, although smaller peak values are predicted at the passage of the first and final axles. A dynamic response at high speed is attained which approximates the measured data quite acceptably, except for the final response to the passage of the last bogie and thereafter. This discrepancy may be caused by the track modeling in view of [Takemiya and Bian 2005] and the associated nonlinear behavior. The mechanism of the wave generation and propagation in the ground is interpreted from the wave dispersion characteristics that show the frequency versus wave number [Takemiya 2001]. In the

No	Properties	Shear Velocity (m/s)		Density (t/m^3)	Poisson ratio	Layer thickness (m)
		19.4 m/s	55.6 m/s			
1	Crust	72.0	65.0	1.5	0.49	1.1
2	Original Clay	41.0	33.0	1.26	0.49	3.0
3	Clay	65.0	60.0	1.475	0.49	4.5
4	Clay	87.0	85.0	1.475	0.49	6.0

Table 2. Soil properties at Ledsgard.

low speed situation, the train speed line is off-set lower than the fundamental wave mode line, whereas in the latter situation it indicates the crossing of the speed line with the fundamental wave mode line at 2.5 Hz, the corresponding wavelength is 16.7 m. These facts are confirmed in Figure 10.

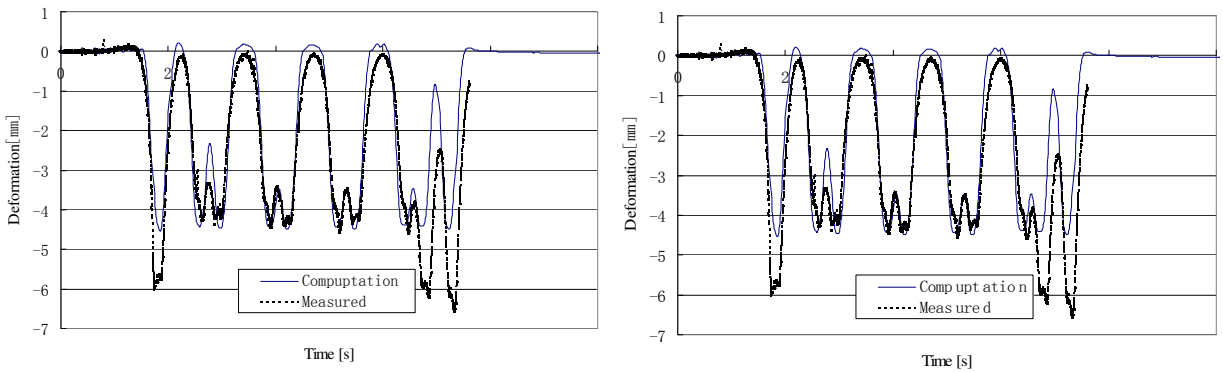


Figure 10. Track response due to the X2000 train passage at (left) 70 km/h (19.4 m/s) and (right) 200 km/h (55.6 m/s).

6. Conclusions

The transient responses due to moving loads, initially at rest, have been dealt with by the Laplace–Fourier transform scheme with respect to time and space, respectively. The TLM is applied for discretization along the depth of the ground. The wave field can be decomposed into the eigenmodes of wave numbers in the horizontal dependence once it is decoupled into in-plane and out-of-plane motions. A variety of space distributions and time variations are considered for loading profiles.

Firstly, an illustrative study is demonstrated for the transient response of a uniform halfspace due to sudden vertical loading on the surface. The causal responses of the TLM are validated in comparison with the closed form solution.

Secondly, the transient response due to a constant moving (quasistatic) load is investigated for a stratum model. The causality features are discussed depending on the speed ratio of the moving load against the shear velocity of the layer. From the computed results, it is noted that in the case of a short distance from a starting position to an observation position, the wave field includes the initial touch down effect as well as the moving load effect. However, as the distance is increased, the former response becomes substantially separated from the latter response. Regarding the speed ratio of the moving load against the seismic S wave velocity, distinct response features result. Those are interpreted in the time as well as in the frequency domains. The wave dispersion characteristics are helpful to give a fundamental knowledge for predicting the ground borne vibration.

Thirdly, a practical application is attempted to predict train-induced vibration. Since the stationary response is focused on a constant speed passage, the superposition is taken for a set of responses due to axle loads, with special care to exclude the causal effects from the initial condition. The validation is made from the measured data at the site.

Notation

A, B, C	coefficient matrices
$c_{\text{P-SV}}$	train speed
$\tilde{\mathbf{E}}^{\text{P-SV}}, \tilde{\mathbf{E}}^{\text{SH}}$	diagonal matrices defined in (19) and (20)
$\tilde{\mathbf{F}}_1, \tilde{\mathbf{F}}_2, \tilde{\mathbf{F}}_3$	force vectors in the Fourier transformed domain
$H(t)$	Heaviside step function
L	fundamental wavelength
M	mass matrix
s	Laplace parameter
s_j	wave number eigenvalue
$T(t)$	time function
$\tilde{T}(s)$	Laplace transform of time function
\mathbf{U}	nodal displacement vector
$\tilde{\mathbf{U}}_1, \tilde{\mathbf{U}}_2, \tilde{\mathbf{U}}_3$	Fourier–Laplace transformed displacements
β	damping ratio
$\Lambda^{\text{P-SV}}, \Lambda^{\text{SH}}$	diagonal matrices eigenwave numbers for waves field as P-SV and SH
ζ	wave number
Φ	mode shape matrix
$\delta(\)$	Dirac delta function
ρ	density
ω	circular frequency
–	Laplace transform with respect to time
~	Fourier transform with respect to space coordinate

Acknowledgement

The author expresses his thanks to S. Yagi for implementing the theory involved into a computer code, and also to Dr. F. Chen for some recomputation of examples shown here.

References

- [Dieterman and Metrikine 1997] H. A. Dieterman and A. V. Metrikine, “Steady-state displacements of a beam on an elastic half-space due to a uniformly moving constant load”, *Eur. J. Mech. A Solids* **6**:2 (1997), 295–306.
- [Eason 1965] G. Eason, “The stresses produced in a semi-infinite solid by a moving surface force”, *Int. J. Eng. Sci.* **2**:6 (1965), 581–609.
- [Eason 1966] G. Eason, “The displacements produced in an elastic half-space by a suddenly applied surface force”, *J. Inst. Math. Appl.* **2** (1966), 299–326. [MR 34 #5361](#)
- [Gakenheimer and Miklowitz 1969] D. C. Gakenheimer and J. Miklowitz, “Transient excitation of an elastic halfspace by a point load traveling on the surface”, *J. Appl. Mech. (ASME)* **36**:3 (1969), 505–515.
- [Haddon 1987] R. A. W. Haddon, “A simple exact method for Green’s functions for SH motion in a layered elastic medium using leaking modes”, *Geophys. J. Int.* **88**:2 (1987), 379–392.
- [Harvey 1981] D. J. Harvey, “Seismogram synthesis using normal mode superposition: The locked mode approximation”, *Geophys. J. Int.* **66**:1 (1981), 37–69.
- [Kausel 1994] E. Kausel, “Thin-layer method: Formulation in the time domain”, *Int. J. Numer. Methods Eng.* **37**:6 (1994), 927–941.

- [Kausel et al. 1975] E. Kausel, J. M. Roesset, and G. Waas, “Dynamic analysis of footings on layered media”, *J. Eng. Mech. (ASCE)* **101**:5 (1975), 679–693.
- [Lamb 1904] H. Lamb, “On the propagation of tremors over the surface of an elastic solid”, *Philos. Tr. R. Soc. S. A* **203** (1904), 1–42.
- [Lombaert et al. 2001] G. Lombaert, G. Degrande, and D. Clouteau, “The influence of the soil stratification on free field traffic-induced vibrations”, *Arch. Appl. Mech.* **71**:10 (2001), 661–678.
- [Lysmer and Drake 1972] J. Lysmer and L. A. Drake, “A finite element method for seismology”, *Methods Comput. Phys.* **11** (1972), 181–216.
- [Mitra 1964] M. Mitra, “Disturbance produced in an elastic half-space by impulsive normal pressure”, *Proc. Camb. Philos. Soc.* **60** (1964), 683–696. [MR 29 #5458](#)
- [Olson et al. 1984] A. H. Olson, J. A. Orcutt, and G. A. Frazier, “The discrete wavenumber/finite element method for synthetic seismograms”, *Geophys. J. Int.* **77**:2 (1984), 421–460.
- [Payton 1964] R. G. Payton, “An application of the dynamic Betti–Rayleigh reciprocal theorem to moving-point loads in elastic media”, *Quart. Appl. Math.* **21**:4 (1964), 299–313. [MR 27 #5411](#)
- [Pekeris 1955] C. L. Pekeris, “The seismic buried pulse”, *Proc. Nat. Acad. Sci. U.S.A.* **41**:9 (1955), 629–639. [MR 17,320e](#)
- [Sheng et al. 1999] X. Sheng, C. J. C. Jones, and M. Petyt, “Ground vibration generated by a harmonic load acting on a railway track”, *J. Sound Vib.* **225**:1 (1999), 3–28.
- [Takemiya 2001] H. Takemiya, “Noise and vibration from high-speed trains”, Chapter 12, pp. 347–393 in *Ground vibrations alongside tracks induced by high-speed trains: Prediction and mitigation*, edited by V. V. Krylov, Thomas Telford, London, 2001.
- [Takemiya 2003] H. Takemiya, “Simulation of track-ground vibrations due to a high-speed train: The case of X-2000 at Ledsgard”, *J. Sound Vib.* **261**:3 (2003), 503–526.
- [Takemiya and Bian 2005] H. Takemiya and X. C. Bian, “Substructure simulation of inhomogeneous track and layered ground dynamic interaction under train passage”, *J. Eng. Mech. (ASCE)* **131**:7 (2005), 699–711.
- [Takemiya and Fujiwara 1994] H. Takemiya and A. Fujiwara, “Wave propagation/impediment in a stratum and wave impeding block (WIB) measured for SSI response reduction”, *Soil Dyn. Earthq. Eng.* **13**:1 (1994), 49–61.
- [Takemiya and Goda 2000] H. Takemiya and K. Goda, “Thin layer method simulation of near source ground motions due to discretized dislocation in layered soils”, *J. Struct. Mech. Earthq. Eng. (JSCE)* **640**:50 (2000), 89–98.
- [Takemiya and Guan 1993] H. Takemiya and F. Guan, “Transient Lamb’s solution for surface strip impulses”, *J. Eng. Mech. (ASCE)* **119**:12 (1993), 2385–2403.
- [Takemiya and Steinfeld 1993] H. Takemiya and B. Steinfeld, “Transient 3D Lamb’s solution by classical approach and direct boundary element method”, pp. 307–314 in *Proceedings of the Second European Conference on Structural Dynamics (EURODYN ’93)* (Trondheim), edited by T. Moan et al., Balkema, Rotterdam, 1993.
- [Takemiya et al. 1994] H. Takemiya, F. Guan, and Y. Sukeyasu, “2-D transient soil-surface foundation interaction and wave propagation by time domain BEM”, *Earthquake Eng. Struct. Dyn.* **23**:9 (1994), 931–945.
- [Takemiya et al. 2001] H. Takemiya, S. Satonaka, and W. P. Xie, “Train-track-ground dynamics due to high speed moving source and ground vibration transmission”, *J. Struct. Mech. Earthq. Eng. (JSCE)* **882**:56 (2001), 299–309.
- [Touhei 1995] T. Touhei, “Propagation of normal modes due to impulsive loading to 3-D medium on a rigid basement”, *Earthquake Eng. Struct. Dyn.* **24**:7 (1995), 937–949.

Received 1 Jun 2007. Revised 23 Nov 2007. Accepted 6 Dec 2007.

HIROKAZU TAKEMIYA: takemiya@ed-techno.org
E&D Techno-design, Inc., Haga 5303, Okayama, Japan

AGING DEGRADATION OF MECHANICAL STRUCTURES

SOMASUNDARAM VALLIAPPAN AND CALVIN K. CHEE

A numerical approach is proposed in this paper for safety assessment of mechanical structures with age-related degradation. Deterioration occurs in mechanical structures due to various environmental attacks and operation conditions which leads to changes in structural performance and structural resistance capacity. By combining techniques such as degradation evaluation methods, damage mechanics, and the finite element method, the proposed numerical method can be used to analyse the responses and damages of mechanical structures with age-related degradation. Ageing degradation effects can be taken into account by introducing degradation factor into formulations of finite element method and damage mechanics. The numerical results for a notched bar and a plate with a central hole are provided to validate the proposed numerical method.

1. Introduction

The ageing of mechanical structures can be defined as partial or total loss of their capacity to achieve the purpose for which they were constructed via a slow, progressive and irreversible process that occurs over a period of time. Ageing can lead to changes in engineering properties and may affect the static and dynamic responses, structural resistance/capacity, failure mode, and location of failure initiation. The ageing effects may impact the ability of mechanical system to withstand various challenges from operation, environment, and natural events.

Although engineering materials such as steel and concrete are inherently durable, some engineering structures may need to be improved because of deficiencies in their design and manufacture or as a result of environmental attacks. The ageing process can directly affect mechanical structures by changing the characteristics of the materials of which they are made and leading to a loss in their resistance capacity. Corrosion, irradiation, elevated temperature, or fatigue effects are the main problems for mild steel. Common problems to concrete include alkali-aggregate reaction (AAR), freezing and thawing, leaching, sulphate attack, cracking due volume changes led by temperature variation, corrosion of concrete, debonding of steel, etc.

The safety of existing aged mechanical structures is an important research topic owing to ageing processes altering their strength and stiffness as well as revised predictions of the maximum loads associated with severe operation conditions and environmental attacks. Probabilistic degradation evaluation approaches, damage/fracture mechanics methods, nondestructive detection methods, etc., can be used for this purpose.

Time dependent changes in engineering structures are random in nature. Safety evaluation of new and existing structures can be conducted rationally within a probabilistic framework [Shinozuka 1983].

Keywords: mechanical structures, ageing, age-related degradation, finite element method, damage mechanics, numerical analysis.

Probability methods are widely used for condition assessment of existing structures. The mathematical formalism of a probabilistic risk assessment (PRA) provides a means for identifying ageing structural components that may play a significant role in mitigating structural risk. Structural condition assessments supporting a decision regarding continued service can be rendered more sufficient if guided by the logic of a PRA.

Degradation effects can be quantified with fragility curves developed for both undegraded and degraded components. Fragility analysis is a technique for assessing, in probabilistic terms, the capability of an engineered system to withstand a specified event. Fragility modelling requires a focus on the behavior of the system as a whole and specifically on things that can go wrong with the system. The fragility modelling process leads to a median-centered (or likely) estimate of system performance coupled with an estimate of the variability or uncertainty in performance. [Braverman et al. \[2004\]](#) reported on a fragility analyses performed for concrete structural members and other passive components of nuclear power plants (NPPs). Structural performance in the presence of uncertainties is depicted by a fragility curve (or conditional probability of failure). [Ellingwood \[1998\]](#) addressed the issues related to structural ageing in probabilistic risk assessment of NPPs and proposed a probabilistic framework to assess degradation in certain critical structural components or system capacities due to reinforcement corrosion or concrete deterioration from aggressive environmental influences. [Naus et al. \[1999\]](#) summarized the research program addressing the ageing of nuclear power plant concrete structures. A reliability-based methodology was developed that can be used to facilitate quantitative assessments of current and future structural reliability and performance of concrete structures in NPPs. The methodology is able to take into account the nature of past and future loads, and randomness in strength and in degradation results from environmental factors. A methodology was presented by [Tekie and Ellingwood \[2003\]](#) for developing fragilities of concrete gravity dams to assess their performance against seismic hazards. A robust system reliability evaluation method was proposed for ageing redundant structures by [Wang et al. \[1997\]](#). Using the advanced first-order second-moment reliability method, the element-level reliability indices are calculated for individual piles for several strength limit states. The system-level reliability indices of the pile group are calculated considering the lateral and vertical deflection limit states. An alternative method to evaluate the safety of engineering structures is by using damage/fracture methods. When engineering materials are subjected to unfavourable conditions such as cold and hot working processes, temperature variations, chemical actions, radiation, mechanical loading, or environmental conditions, microscopic defects and cracks may develop inside the materials. Such damage causes reduction in strength and stiffness that may lead to failure and shorten the operating life of the structures. Such deterioration in mechanical properties of a material is known as a damage process [[Valliappan et al. 1990](#)].

Because of the significant influence of damage on engineering material properties, a number of studies have been carried out on modelling and numerical methods for crack growth in structures under various loading conditions. Valliappan and his coworkers have been one of the pioneers in developing numerical methods for the analysis of engineering structures using damage mechanics. For example, from the viewpoint of continuum damage mechanics concept, [Valliappan and Zhang \[1996\]](#) addressed the problem of the effect of microscopic defects and cracks within materials in order to study the behavior of structural components under different loading conditions. A formulation for elasto-plastic analysis of damage mechanics problems was developed based on the principles of thermodynamics and the associated finite element method. A theoretical formulation for isotropic and anisotropic elasto-plastic analysis of static

and dynamic damage mechanics problems was developed by Zhang and Valliappan [1998a]. The formulations were based on the combination of concepts between the internal energy dissipation and the damage elasto-plasticity energy potential in terms of a set of internal state variables to explain microstructural changes in damaged materials. And the formulations were introduced into numerical algorithms of the finite element techniques for static and dynamic analysis of structures including the effect of damage [Zhang and Valliappan 1998b].

This paper presents a numerical approach for the safety assessment of mechanical structures with age-related degradation by combining techniques such as degradation evaluation methods, damage mechanics, and the finite element method. A notched bar and a plate with a central hole are solved as the examples in the numerical analysis using the proposed method. The results of the analysis validate that the proposed method is an efficient tool for safety assessment of aged mechanical structures.

2. Numerical method for safety assessment of aged mechanical structures

A dynamic two-dimensional finite element method coupled with damage mechanics is developed to evaluate damage initiation and propagation for aged mechanical structures. To take into account the effect of aged-related degradation on the safety of aged mechanical structures, ageing degradation is quantified according to various mechanical and environmental attacks under various operation conditions. The quantified age-related degradation factor is then included in the damage model and the finite element formulation.

2.1. Quantification of ageing degradation of engineering materials. Age-related degradation of engineering materials such as steel and concrete is a complicated process. Degradation of aged steel can be classified as either material or physical damage. Material damage occurs when the microstructure of the metal is modified causing changes in its mechanical properties. For example, degradation mechanisms that can potentially cause material damage to containment steels include: (i) low-temperature exposure, (ii) high-temperature exposure, (iii) intergranular corrosion, (iv) dealloying corrosion, (v) hydrogen embrittlement, and (vi) neutron irradiation. Primary degradation mechanisms that potentially can cause physical damage to containment pressure boundary components include: (i) general corrosion (atmospheric, aqueous, galvanic, stray-electrical current, and general biological); (ii) localized corrosion (filiform, crevice, pitting, and localized biological); (iii) mechanically assisted degradation (erosion, fretting, cavitation, corrosion fatigue, surface flaws, arc strikes, and overload conditions); (iv) environmentally induced cracking (stress-corrosion and hydrogen-induced); and (v) fatigue. Degradation of mild steel reinforcing concrete can occur as a result of corrosion, irradiation, elevated temperature, or fatigue effects. Prestressing concrete is susceptible to the same degradation mechanism as mild steel concrete, primarily due to tendon relaxation and concrete creep and shrinkage.

Ageing is a time-dependent process. Ageing degradation of engineering materials, which accumulates over time by various processes depending on the operating environment and service conditions, will reduce the strength of structures or their components. Generally, the ageing degradation of the strength of a structure or a structural component can be expressed by

$$R(t) = R_0G(t) \quad (1)$$

in which R_0 is the component capacity in the undegraded (original) state and $G(t)$ is a time dependent degradation function defining the fraction of initial strength remaining at time t . The degradation mechanisms are uncertain, experimental data are lacking, and thus the function $G(t)$ should be treated as stochastic. However, as it has been found that the variability in $G(t)$ is of minor importance when compared to mean degradation and local process characteristics, it is assumed that $G(t)$ is deterministic and equal to mean $E[g(t)] = G(t)$ [Mori and Ellingwood 1993].

Corrosion is one of the main reasons for degradation of aged steel. In this research time-dependent ageing degradation function for steel is assumed to be given by Broomfield [1997]

$$G(t) = 1 - \frac{1}{1 + Ae^{-Bt}} \quad (2)$$

in which A and B are constant parameters and t is the age of the structure.

It is worth pointing out that Equation (1) is applicable to all structural materials whereas (2) is specifically for steel. However, similar to (2) expressions are available for other materials such as concrete. In fact, the authors have adopted one such function for the stability evaluation of aged concrete gravity dams.

2.2. Dynamic finite element analysis of aged mechanical structures using damage mechanics. Since the safety margin reserved in the critical mechanical structures is large, they are considered to be safe even against hostile loadings larger than expected in their design. However, past experience shows that engineering structures are susceptible to ageing degradation under various attacks which may affect the mechanical characteristics of the structures. Whether the aged mechanical structures can still withstand the challenges from hostile environments and natural events is of great concern to engineers. Therefore, time-dependent degradation effects should be included when structural safety and reliability are evaluated for mechanical structures with age-related degradation.

In the past many investigators have studied the effect of cracking on the dynamic response of engineering structures using the concept of fracture mechanics. The concept of fracture mechanics requires complete details of initiation and propagation of cracks within the structure and the location. Besides, the numerical modelling of such individual crack propagation requires special techniques such as quarter-point element, remeshing, etc. [Murti and Valliappan 1986]. Therefore the application of fracture mechanics is limited and for cases in which extensive microcracking may develop, it may not be suitable, especially in dynamic analysis.

The concept of continuum damage mechanics can be used to study the effect of microcracking on the dynamic responses of engineering structures [Valliappan and Zhang 1996]. Damage mechanics provides an average measure of material degradation due to microcracking, interfacial debonding, nucleation, and coalescence of voids. In the microcracking of brittle materials under tensile stress, damage is regarded as elastic degradation. This material degradation is reflected in the nonlinear behaviour of the structures.

2.2.1. Finite element equations of motion for aged mechanical structures. Modelling of mechanical structures can be done using the two-dimensional finite element method. The equation of motion for the dynamic analysis including damage can be written as

$$\mathbf{M}\ddot{\vec{U}} + \mathbf{C}^*\dot{\vec{U}} + \vec{P}^*(\vec{U}) = \vec{F}_s + \vec{F}_d, \quad (3)$$

where \mathbf{M} is the mass matrix of the system and consists of element mass matrices \mathbf{m}^e

$$\mathbf{m}^e = \int_{\Omega_e} \rho^{(e)} \mathbf{N}^T \mathbf{N} d\Omega,$$

where $\rho^{(e)}$ and \mathbf{N} represent mass density and shape function matrix for an element, respectively, \mathbf{C}^* is the damping matrix of the system, $\vec{P}^*(\vec{U})$ represents the vector of restoring forces, and \vec{F}_s and \vec{F}_d are static and dynamic loading vectors, respectively. $\vec{P}^*(\vec{U})$ is a nonlinear function of displacement and stress-strain history depending on the constitutive law. It can be given by

$$\vec{P}^*(\vec{U}) = \mathbf{K}^* \vec{U},$$

where \mathbf{K}^* is the system stiffness and is obtained from the assemblage of an element stiffness matrices \mathbf{k}^e

$$\mathbf{k}^e = \int_{\Omega_e} \mathbf{B}^T \mathbf{T}_\sigma \tilde{\mathbf{E}}^{*(e)} \mathbf{T}_\sigma^T \mathbf{B} d\Omega,$$

where \mathbf{T}_σ is the coordinate transformation matrix, $\tilde{\mathbf{E}}^*$ is the damaged constitutive matrix taking into account the age-related degradation in the orthotropic damage space, and \mathbf{B} is the strain-displacement matrix.

2.2.2. Damage model and damage evolution. The formulation of a damage model first requires the definition of threshold of damage, which is the condition that initiates the damage. Secondly, the evolution of damage with loading must be also defined, and it is a function of a measure of strains, stresses, or energy. This damage evolution can be any of the following forms

$$\dot{D} = \dot{D}(\sigma_{ij}(\varepsilon_{ij}), D, \dots) \quad \text{or} \quad D = D(\sigma_{ij}(\varepsilon_{ij}), \dots), \quad (4)$$

where σ_{ij} is the state of stress at a particular point and D is the damage tensor at that point. Also \dot{D} represents the rate of damage. The most common damage kinetic equation that is used widely is based on a power function of tensile normal stress and was introduced first by [Kachanov \[1980\]](#):

$$\dot{D} = \begin{cases} A_L \left(\frac{\sigma}{1-D} \right)^n, & \text{for } \sigma > \sigma_d, \\ 0, & \text{for } \sigma \leq \sigma_d, \end{cases}$$

where $A_L > 0$ and $n > 1$ are material constants depending on the rate of loading, σ is the uniaxial tensile stress, and σ_d is the stress at damage threshold. For this model one needs experimental results to obtain parameters A_L and n , but these results are not available for all kinds of loading. As proposed by [Bazant and Lin \[1988\]](#) and applied by [Ghrib and Tinawi \[1995\]](#), a second model based on [Equation \(4\)](#) (right) can be used for dynamic analysis.

In the materials, which eventually exhibit strain softening that leads to a complete loss of strength, the secant modulus decreases with increasing strain [\[Lubliner et al. 1989\]](#). A widely used assumption is a triangular stress-strain diagram for uniaxial loading. This gives a linear strain softening relationship. But various experimental evidences indicate that it is more realistic to assume a strain-softening curve with a steep initial decline followed by an extended tail [\[Lubliner et al. 1989\]](#). Then an exponential

strain-softening model can be given by

$$\sigma(\varepsilon) = \begin{cases} E\varepsilon, & \text{for } \varepsilon \leq \varepsilon_0, \\ f'_t(2e^{-a(\varepsilon-\varepsilon_0)} - e^{-2a(\varepsilon-\varepsilon_0)}), & \text{for } \varepsilon_0 < \varepsilon < \varepsilon_{cr}, \\ 0, & \text{for } \varepsilon \geq \varepsilon_{cr} \end{cases} \quad (5)$$

in which f'_t is the tensile strength and ε_0 is the corresponding strain threshold, E is the modulus of elasticity, a is a dimensionless constant, and ε_{cr} is the maximum strain. For aged mechanical structures, E and f'_t in Equation (5) are given by Equation (1) due to ageing degradation. In this study the value ε_{cr} is calculated when its corresponding stress is equal to $0.02f'_t$. Then

$$\varepsilon_{cr} = \varepsilon_0 + \frac{\ln\left(\frac{2+\sqrt{4-4\lambda}}{2\lambda}\right)}{a}.$$

When $\lambda = 0.02$, the maximum strain ε_{cr} is calculated by

$$\varepsilon_{cr} = \varepsilon_0 + \frac{4.6}{a}.$$

The fracture energy per unit area, G_f , is defined as $G_f = l_{ch}g_t$, where g_t is total area under stress-strain curve

$$g_t = \int_0^{\infty} \sigma(\varepsilon) d\varepsilon = \frac{3f'_t}{2a} + \frac{f'_t}{2E},$$

and l_{ch} is the characteristic length. From the above two equations the constant a can be given by

$$a = \frac{3}{\varepsilon_0 \left(\frac{2EG_f}{l_{ch}f'^2_t} - 1 \right)} \geq 0.$$

Based on the hypothesis of strain energy equivalence, the anisotropic damage parameters can be defined in terms of Young's modulus [Valliappan et al. 1990]

$$D_i = 1 - \sqrt{\frac{E_i^*}{E_i}},$$

and hence from Equation (5), the proper definition of damage for the uniaxial case is

$$D_i = 1 - \sqrt{\left(\frac{\varepsilon_0}{\varepsilon}\right) (2e^{-a(\varepsilon-\varepsilon_0)} - e^{-2a(\varepsilon-\varepsilon_0)})}.$$

In the two equations above i represents the i -th principal direction.

3. Numerical analysis

Two examples – a notched bar and a plate with a central hole – are used for the numerical analysis to validate the proposed method for safety assessment of aged mechanical structures.

Figure 1 shows the model of the notched bar and its finite element mesh discretization. The dimension of the bar is 10 cm × 30 cm. Distributed step loading of 1560 kN/cm⁻¹, which is shown in Figure 2, is applied at one end of the bar in longitudinal direction. The notched bar is modeled as a two-dimensional

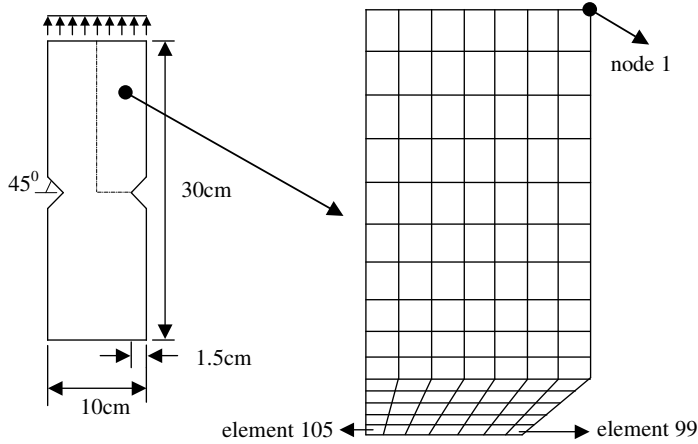


Figure 1. Notched bar and its finite element mesh discretization.

plane stress case and is discretized with four noded isoparametric elements. Because of the symmetries of geometry and loading, the notched bar is discretized with 105 elements and 128 nodes. The material properties of the bar are chosen as follows: modulus of elasticity $E = 2.0 \times 10^{11}$ Pa; Poisson’s ratio $\nu = 0.28$; density $\rho = 7850.0 \text{ kg/m}^{-3}$; tensile strength $f_t' = 4.0 \times 10^8$ Pa, and fracture energy for unit area $G_f = 2.6 \times 10^6 \text{ N/m}^{-1}$.

To include ageing degradation effect in the numerical analysis, a degradation function given by Equation (2) is used to modify the modulus of elasticity and tensile strength of the material. Parameters A and B in Equation (2) are the two constants that define the ageing degradation effect. In order to determine their effect on the system responses and damages, in the present study parameter A is considered to be a fuzzy variable, while parameter B is considered to be a deterministic parameter. It was found that B is more sensitive to the ageing degradation. Therefore the values of 0.125 and 0.25 were assigned to parameter B in the numerical analysis to simulate the degradation processes under different environmental and working conditions. The value of A is set to 100. Figure 3 shows the deterioration curves of different B values used in the numerical analysis.

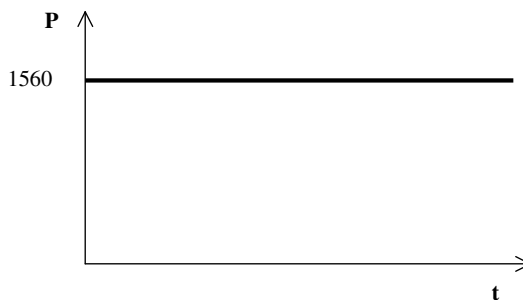


Figure 2. Step loading: $P = 1560 \text{ kN/cm}$.

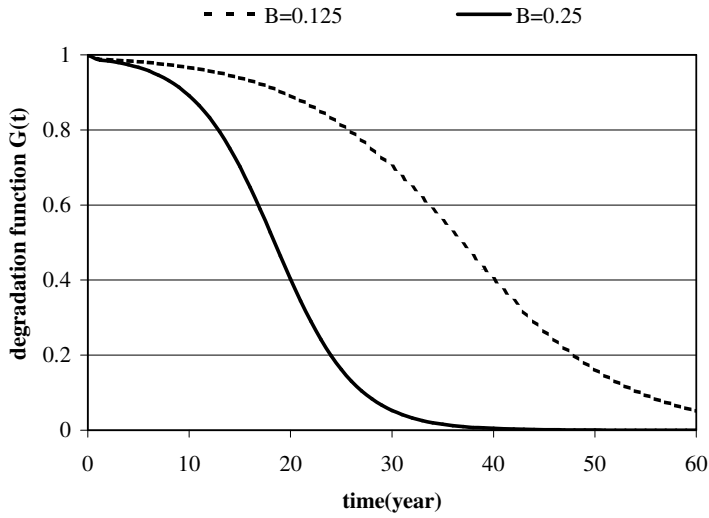


Figure 3. Degradation function of steel.

In this study the equation of motion (Equation (3)) in the time domain is solved using Newmark’s integration method, which is unconditionally convergent. In selecting the time step the natural frequency of the structure and the type of loading must be considered. However, in the present case, because of the step loading, it is necessary to consider only the loading, and hence the time step is set as 0.01 s to check the system responses and damages. Structural responses and damage parameters were obtained for both cases of $B = 0.125$ (up to 40 years) and $B = 0.25$ (up to 20 years) to check the effect of ageing degradation on the behaviour of the notched bar.

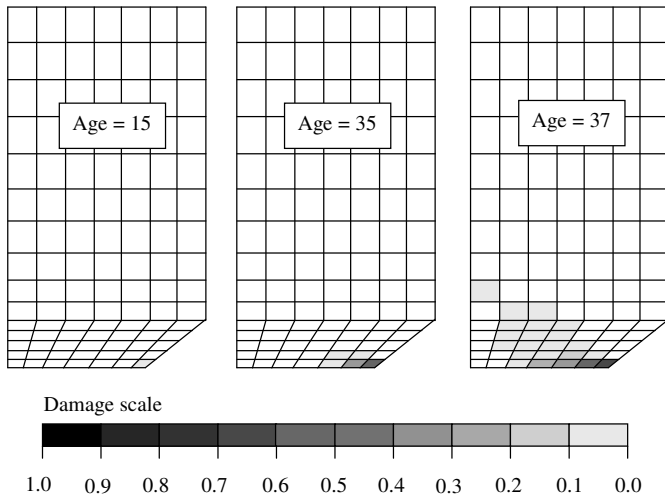


Figure 4. Damage patterns of the notched bar ($B = 0.125$).

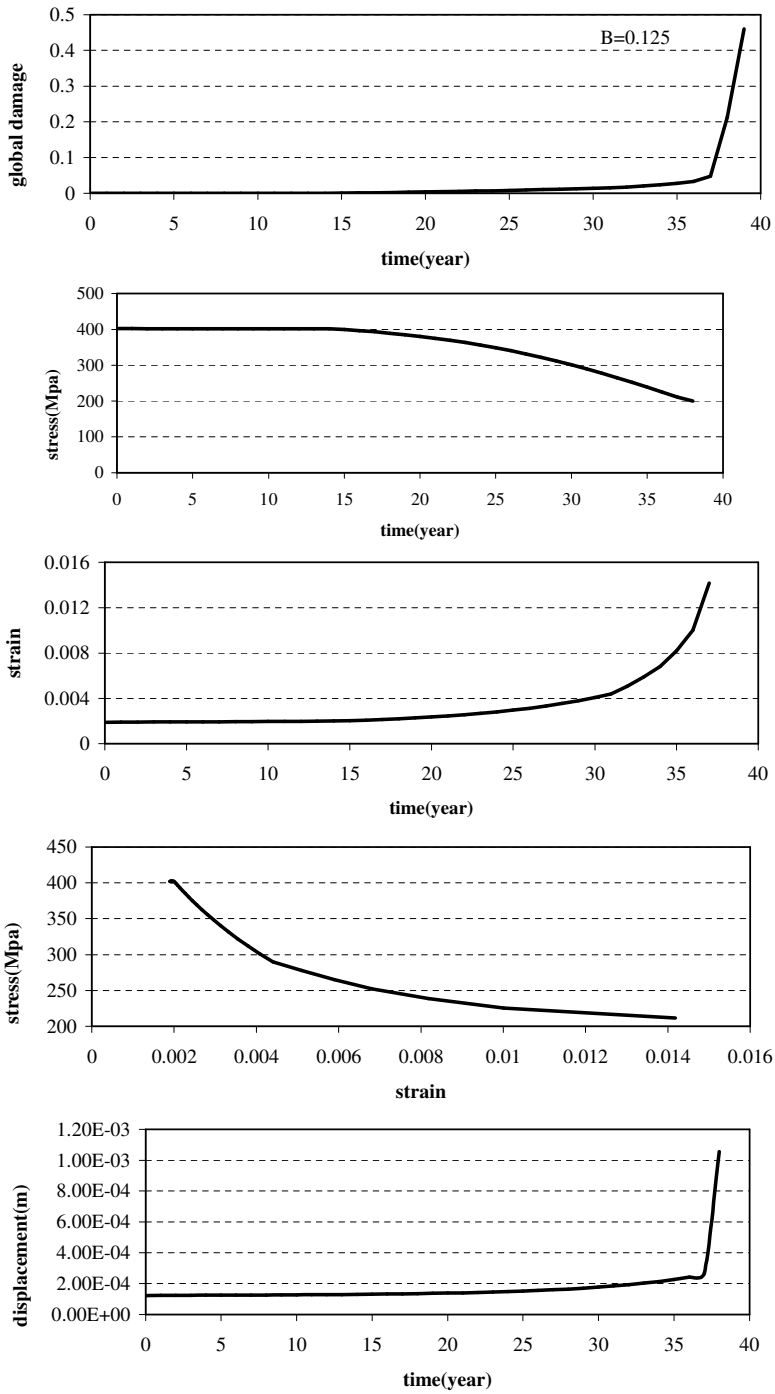


Figure 5. Global damage, displacement of node 1, and major principal stress, major principal strain, and stress-strain relationship of element 99, respectively, of the notched bar ($B = 0.125$).

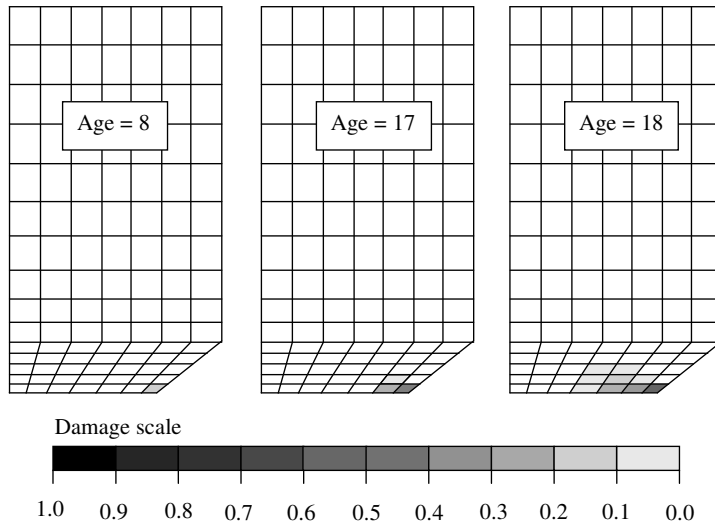


Figure 6. Damage patterns of the notched bar ($B = 0.25$).

For the case of $B = 0.125$ Figure 4 shows the damage pattern of the notched bar at times of 15, 35, and 37 years, and Figure 5 shows the global damage index. The global damage index is defined by the following equation

$$D_{\text{global}} = \sqrt{\sum_{e=1}^{\text{nel}} \int_{\Omega_e} (D^{(e)})^2 d\Omega_e} / \sqrt{\sum_{e=1}^{\text{nel}} \int_{\Omega_e} d\Omega_e} \quad (6)$$

in which $D^{(e)}$ is the damage of the e -th element and ‘nel’ represents the total number of the damaged elements. In determining the damage to the entire structure, it is desirable to take into account the cumulative effect of the damage occurring in parts of the structure, which are individual elements in the finite element method. It is well known that there is a size effect when discretization techniques are used. In the present study this cumulative effect is represented by the expression given in Equation (6) for the purpose of illustrating the damage to the structure due to ageing degradation. If one desires, any other alternative expression can be developed for this purpose.

These two figures show that the damage occurs when the bar is 15 years of age and then extends gradually to the direction of 45° as the age of the bar increases. After 37 years, the damage increases significantly which leads to the failure of the notched bar. Figure 5 shows the displacement at node 1. As the age of the notched bar increases, the strength of the material decreases which results in an increase of displacement and damage. Also shown in Figure 5 are the major principal stress, strain, and their relationship of element 99, respectively.

Figure 6 shows the damage pattern of the notched bar at 8, 17, and 18 years for the case of $B = 0.25$, and Figure 7 shows the global damage index. Because the notched bar has suffered more ageing degradation than the case of $B = 0.125$, the damage initiates at the age of 8 years and increases dramatically to total failure after 18 years. Also shown in Figure 7 are the displacement of node 1, the major principal stress, strain, and their relationship of element 99, respectively.

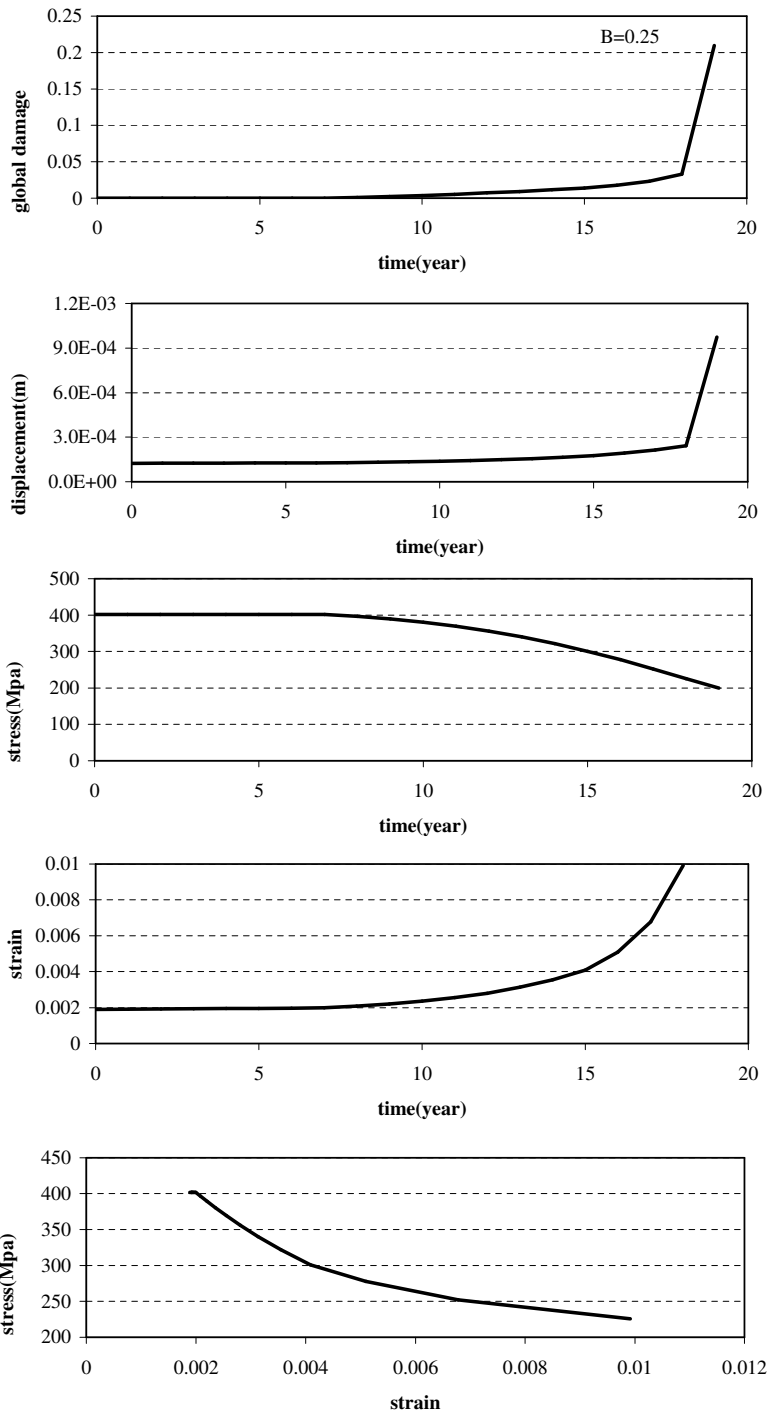


Figure 7. Global damage, displacement of node 1, and major principal stress, major principal strain, and stress-strain relationship of element 99, respectively, of the notched bar ($B = 0.25$).

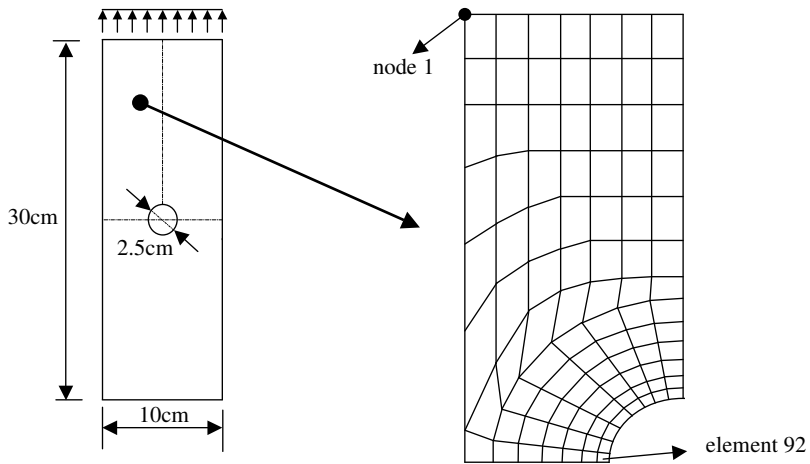


Figure 8. A plate with a central hole and its finite element mesh discretization.

Figure 8 shows the plate model and its finite element mesh. The dimension of the plate is $10 \text{ cm} \times 30 \text{ cm}$, and the diameter of the central hole is 2.5 cm . Distributed step loading is also used in the analysis of which the amplitude is 1380 kN/cm^{-1} . Four noded isoparametric elements are used in finite element discretization, and the plate is discretized into 92 elements and 120 nodes due to the symmetries of geometry and loading. The material properties of the plate are assumed to be the same as those of the notched bar. The analysis is carried out for the two different deterioration rate $B = 0.125$ and $B = 0.25$, respectively.

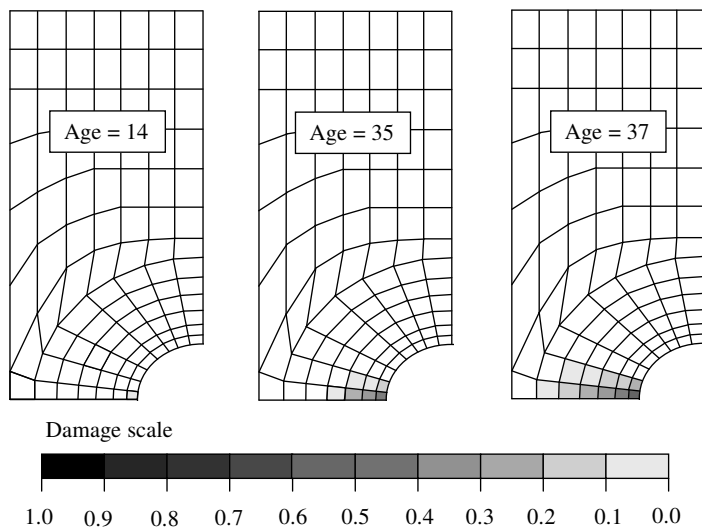


Figure 9. Damage patterns of the plate ($B = 0.125$).

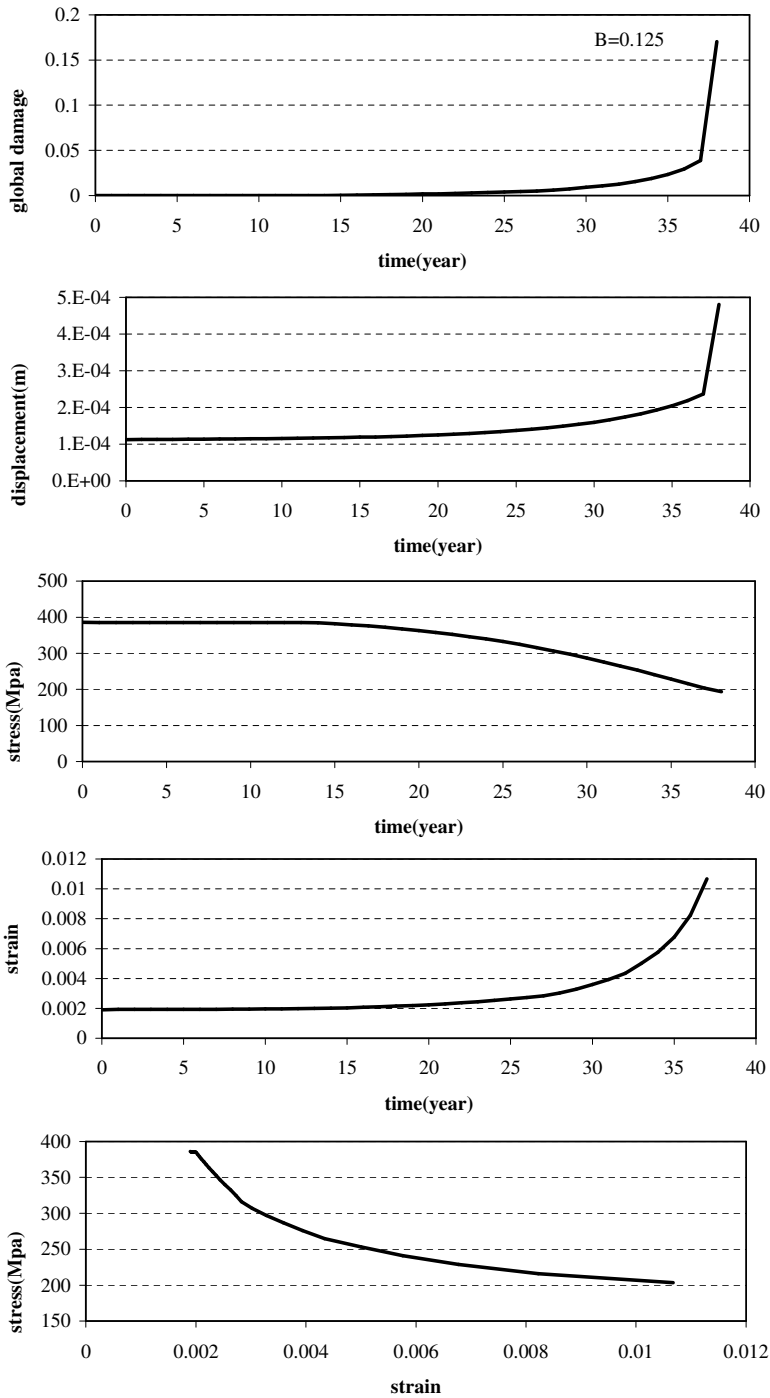


Figure 10. Global damage, displacement of node 1, and major principal stress, major principal strain, and stress-strain relationship of element 92, respectively, of the notched bar ($B = 0.125$).

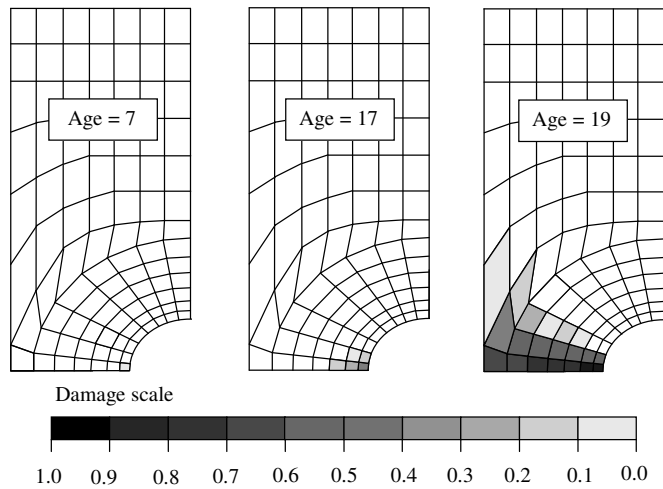


Figure 11. Damage patterns of the plate ($B = 0.25$).

Figure 9 shows the damage pattern of the plate model at 14, 35, and 37 years and Figure 10 shows the global damage index for the case of $B = 0.125$. Damage occurs firstly in element 92 at 14 years and then extends in the direction orthogonal to the loading as the plate suffers more ageing deterioration. Damage increases significantly after 37 years and leads to total failure of the plate. Figure 10 shows the displacement of node 1 at different times and the major principal stress, strain, and their relationship of element 92, respectively.

For the case of $B = 0.25$ Figures 11 and 12 show the damage pattern of the plate and the global damage index at 7, 17 and 19 years. Because of more severe ageing degradation for this case, the plate is damaged initially in element 92 at 7 years and the damage increases gradually up to 18 years. The damage increases sharply at 19 years which then leads to total failure. The displacement at node 1 is shown in Figure 12. It shows the same trend as the global damage index. Figure 12 also shows the major principal stress, strain, and their relationship of element 92, respectively.

4. Conclusions

Ageing is a natural phenomenon via a slow process for mechanical structures due to environmental attacks and operation conditions. Age-related degradation can reduce the strength, change physical properties of the mechanical structures, which may result in the decrease of the their capacity to withstand operation conditions and hostile natural events.

The method presented in this paper is for numerical analysis of mechanical structures with ageing degradation effect. Using techniques such as the finite element method, damage mechanics, and ageing degradation evaluation methods, this method can be used for safety assessment of aged mechanical structures by obtaining initiation and propagation of structural damage over a long period of time. The proposed method was validated by numerical analyses of a notched bar and a plate with a central hole. Under step loading condition, structural responses, damage initiation and propagation were studied in detail for different levels of degradation over a period of several decades. Numerical results show ageing

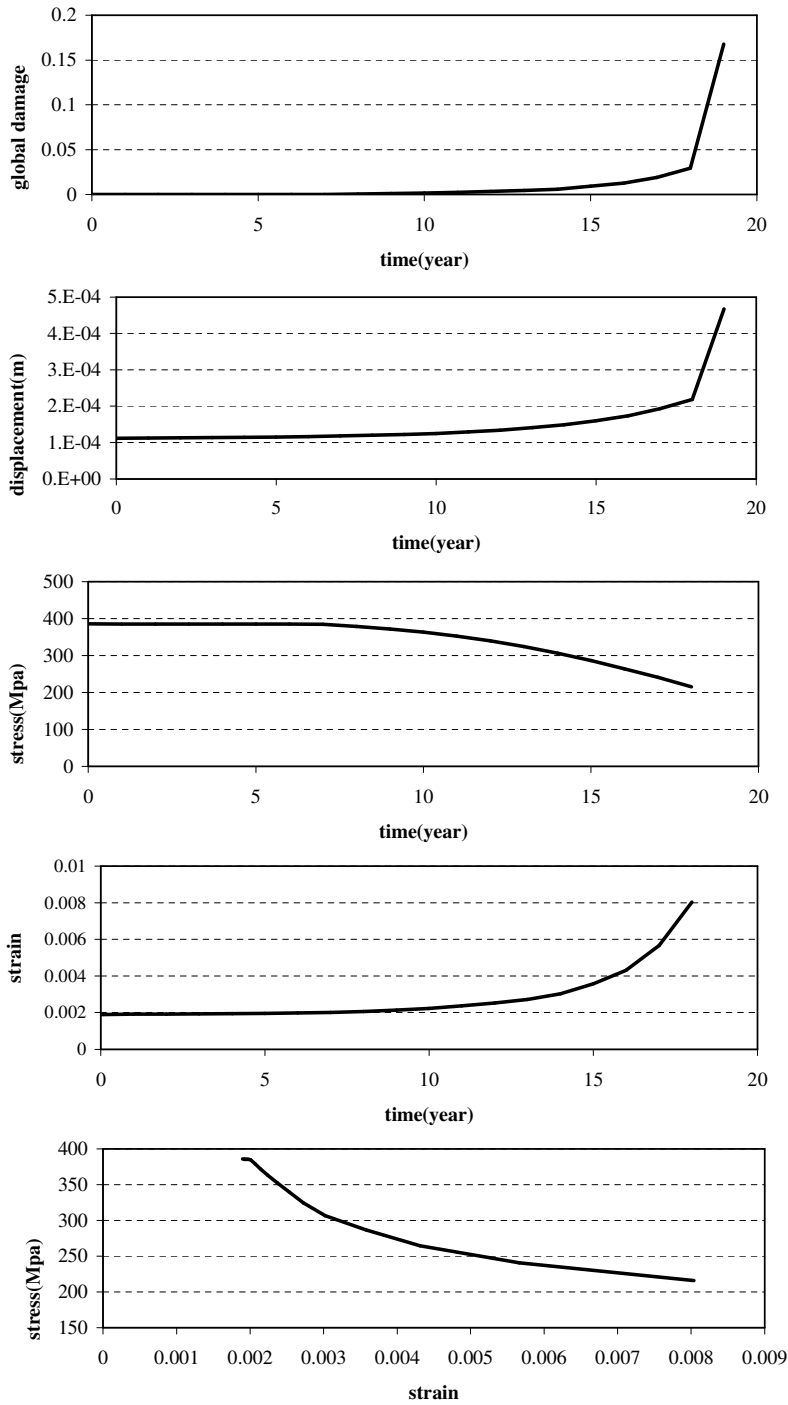


Figure 12. Global damage, displacement of node 1, and major principal stress, major principal strain, and stress-strain relationship of element 92, respectively, of the notched bar ($B = 0.25$).

degradation can significantly affect structural performance and more severe damages occur for mechanical structures when ageing degradation is included.

References

- [Bazant and Lin 1988] Z. P. Bazant and F. B. Lin, “Non-local smeared cracking model for concrete fracture”, *J. Struct. Eng. (ASCE)* **114**:11 (1988), 2493–2510.
- [Braverman et al. 2004] J. I. Braverman, C. A. Miller, C. H. Hofmayer, B. R. Ellingwood, D. J. Naus, and T. Y. Chang, “Degradation assessment of structures and passive components at nuclear power plants”, *Nucl. Eng. Des.* **228**:1–3 (2004), 283–304.
- [Broomfield 1997] J. P. Broomfield, *Corrosion of steel in concrete: Understanding, investigation, and repair*, E & FN Spon, London, 1997.
- [Ellingwood 1998] B. R. Ellingwood, “Issues related to structural aging in probabilistic risk assessment of nuclear power plants”, *Reliab. Eng. Syst. Saf.* **62**:3 (1998), 171–183.
- [Ghrib and Tinawi 1995] F. Ghrib and R. Tinawi, “An application of damage mechanics for seismic analysis of concrete gravity dams”, *Earthquake Eng. Struct. Dyn.* **24**:2 (1995), 157–173.
- [Kachanov 1980] L. M. Kachanov, “Continuum model of medium with cracks”, *J. Eng. Mech. Div. (ASCE)* **106**:5 (1980), 1039–1051.
- [Lubliner et al. 1989] J. Lubliner, J. Oliver, S. Oller, and E. Onate, “A plastic-damage model for concrete”, *Int. J. Solids Struct.* **25**:3 (1989), 299–326.
- [Mori and Ellingwood 1993] Y. Mori and B. R. Ellingwood, “Probability-based service-life assessment of aging concrete structures”, *J. Struct. Eng. (ASCE)* **119**:5 (1993), 1600–1621.
- [Murti and Valliappan 1986] V. Murti and S. Valliappan, “The use of quarter point element in dynamic crack analysis”, *Eng. Fract. Mech.* **23**:3 (1986), 585–614.
- [Naus et al. 1999] D. J. Naus, C. B. Oland, B. R. Ellingwood, C. J. Hookham, and H. L. Graves, III, “Summary and conclusions of a program addressing aging of nuclear power plant concrete structures”, *Nucl. Eng. Des.* **194**:1 (1999), 73–96.
- [Shinozuka 1983] M. Shinozuka, “Basic analysis of structural safety”, *J. Struct. Eng. (ASCE)* **109**:3 (1983), 721–740.
- [Tekie and Ellingwood 2003] P. B. Tekie and B. R. Ellingwood, “Seismic fragility assessment of concrete gravity dams”, *Earthquake Eng. Struct. Dyn.* **32**:14 (2003), 2221–2240.
- [Valliappan and Zhang 1996] S. Valliappan and W. Zhang, “Analysis of structural components based on damage mechanics concept”, pp. 265–280 in *Current advances in mechanical design and production, VI: Proceedings of the Sixth Cairo University International MDP Conference (Cairo)*, edited by M. E. Elarabi and A. S. Wifi, Pergamon Press, Oxford, 1996.
- [Valliappan et al. 1990] S. Valliappan, V. Murti, and W. Zhang, “Finite element analysis of anisotropic damage mechanics problems”, *Eng. Fract. Mech.* **35**:6 (1990), 1061–1071.
- [Wang et al. 1997] M. R. Wang, M. R. Chowdhury, and A. Haldar, “System reliability evaluation considering strength and serviceability requirements”, *Comput. Struct.* **62**:5 (1997), 883–896.
- [Zhang and Valliappan 1998a] W. Zhang and S. Valliappan, “Continuum damage mechanics theory and application, I: Theory”, *Int. J. Damage Mech.* **7**:3 (1998), 250–273.
- [Zhang and Valliappan 1998b] W. Zhang and S. Valliappan, “Continuum damage mechanics theory and application, II: Application”, *Int. J. Damage Mech.* **7**:3 (1998), 274–297.

Received 21 May 2007. Revised 21 Feb 2008. Accepted 23 Feb 2008.

SOMASUNDARAM VALLIAPPAN: somaval@bigpond.net.au

School of Civil & Environmental Engineering, The University of New South Wales, Sydney NSW 2052, Australia

<http://www.civeng.unsw.edu.au/staff/somasundaram.valliappan>

CALVIN K. CHEE: ck.chee@unsw.edu.au

School of Civil & Environmental Engineering, The University of New South Wales, Sydney NSW 2052, Australia

NUMERICAL SIMULATION OF TSUNAMI PROPAGATION USING THE CHARACTERISTIC-BASED SPLIT METHOD

GUNAWAN BUDI WIJAYA, TAM THANH BUI AND WORSAK KANOK-NUKULCHAI

A disastrous tsunami struck North Sumatra, Indonesia and many other countries on December 26, 2004. In response to this disaster, we develop a two-dimensional numerical model to simulate tsunami propagation on the open sea. Tsunami propagation — a process during which the wave has a relatively small height compared to its breadth — is modeled using the shallow water equations. To solve these equations, our model employs the characteristic-based split method first introduced by Zienkiewicz. Four case studies are proposed to verify the numerical model, and our results show that the present numerical model is both accurate and efficient. The numerical model is then used to model the propagation of the tsunami of December 26, 2004, and gives a relatively close result.

1. Introduction

During the last decades, several tsunamis have occurred, striking coastlines and causing devastating property damage and loss of life. The 1992 Flores Tsunami killed more than 264 people in Indonesia, the 1993 Hokkaido tsunami in Japan killed 239 people. One of the worst on record is the December 26, 2004 tsunami, which struck North Sumatra, Indonesia and many other countries, killing more than 289,000 people.

Basically, tsunami can be generated when the sea floor abruptly deforms and vertically displaces the overlying water. Earthquakes are the most frequent triggers, although in some cases a tsunami is generated by a landslide, volcanic eruption, explosion, or the impact of a meteorite or asteroid. When an earthquake occurs beneath the sea, it can cause the water above the deformed area to displace from its equilibrium position. Waves are formed as the displaced water mass, under the influence of gravity, moves to regain its equilibrium. When a large enough area of the sea floor suddenly changes elevation, a tsunami forms.

Tsunami propagation on the open sea is characterized as a shallow-water wave with long period and small height compared to its breadth. Shallow-water waves move at a speed that is equal to the square root of the product of the acceleration of gravity (9.8 m/s^2) and the water depth. Thus, the deeper the water, the faster the wave. And since waves lose energy at a rate inversely related to their wavelength, tsunami can travel at high speeds for long periods of time, losing very little energy in the process. As a tsunami leaves the deep water of the open ocean and travels into shallower water near a coast, it transforms. The tsunami's energy flux, which is dependent on both its wave speed and wave height, remains nearly constant. Consequently, as the tsunami travels into the shallower water, its speed is reduced and its height

Keywords: tsunami propagation, shallow water equations, finite element method, characteristic-based split method.

The authors acknowledge support from the Royal Thai Government Joint Research Program, which has provided funds for *Tsunami Tracking and Alert System* projects.

grows. As a result, tsunamis grow to be several meters or more in height near the coast, and may appear as a rapidly changing tide, a series of breaking waves, or even a bore.

When a tsunami reaches land, it will start to lose some energy due to reflection from the shore, bottom friction, and turbulence. Although there are energy losses, many tsunami waves don't break. They simply surge, flooding low-lying areas, and destroying vegetation, houses, and other coastal structures before rebounding off of cliffs or hills. Often, this flow back into the ocean causes as much damage as the initial onslaught.

This physical phenomenon of tsunami propagation can be mathematically modeled using the Shallow Water Equations (SWE), which are based on the Navier–Stokes equations. In the early days of using computers to find the numerical solutions of fluid flows, finite difference methods were the main tools used by researchers. Various finite difference models have been developed for tsunami wave propagation analysis, such as FUNWAVE, which was developed based on the extended Boussinesq model [Wei and Kirby 1995], TUNAMI which uses linear shallow water theory in a spherical coordinate system [Imamura 1996], SWAN, a model for shallow water and long waves, ZUNI, which uses a two dimensional incompressible Navier–Stokes formulation, and SOLA-3D, a three dimensional incompressible Navier–Stokes model for solving water wave problems of all types. Numerous examples and discussion on the applications of SWAN, ZUNI and SOLA-3D models are presented in [Mader 2004].

In recent years, finite element methods have been widely considered as an alternative choice to finite difference methods because of their flexibility in accurately representing arbitrary topography and complex boundary conditions. Several finite element models have been formulated to study shallow water wave propagation. Grotkop [1973] presents a space-time finite element model for long-period water wave analysis, however this model requires more computer storage and running time than an explicit difference model. For tsunami analysis, Houston [1978] uses a hybrid finite element method to study the interaction of tsunamis with the Hawaiian Islands. Sklarz et al. [1979] simulated the November 29, 1975 tsunami that hit the Hawaiian Islands. Considerable effort has been devoted to improving the performance of finite element models. In the realm of time integration techniques, Kawahara et al. [1978] implemented a two step explicit method which is modified from the Lax–Wendroff finite difference method. Malone and Kuo [1981] proposed semiimplicit time integration schemes that allow the choice of a time step based on accuracy, rather than some Courant-type restriction. Peraire et al. [1986] presented a general explicit formulation which requires little computer storage and can be used on mini- and microcomputers.

The main difficulty of using finite element methods for flow problems is due to the convection terms in the governing equations of fluid. The solutions of convection-dominated problems are often destroyed by spurious oscillations if certain parameters exceed a critical value. Severe mesh and time step refinement are required to remove these oscillations. Zienkiewicz and Codina [1995] introduced a new finite element algorithm which precludes oscillations without the requirement of mesh or time step refinement. This finite element algorithm is named the *characteristic-based split* (CBS) method, and combines the characteristic Galerkin method to deal with advection-dominated flows with a splitting technique to make the system equations become self-adjoint. Such a system of equations can be solved optimally by using the Galerkin formulation. In semiimplicit form, the algorithm requires a critical time step dependent only on the current velocity rather than on the wave celerity. Many studies using the CBS method have been conducted to solve more general fluid problems [Zienkiewicz et al. 1999; Nithiarasu et al. 2004; Ortiz

et al. 2004]. Here, the CBS method is used to develop a two-dimensional numerical model to simulate the propagation of the December 26, 2004 tsunami.

2. Review on shallow water equations

The governing equations for general fluid dynamics problems are the Navier–Stokes equations, which are derived from fluid’s characteristic conservation of mass and momentum, as shown below:

$$\text{Continuity Equation: } \frac{\partial \rho}{\partial t} + \frac{\partial}{\partial x_i}(\rho u_i) = 0 \tag{1}$$

$$\text{Momentum Equation: } \frac{\partial(\rho u_i)}{\partial t} + \frac{\partial}{\partial x_j}[(\rho u_i)u_j] - \frac{\partial}{\partial x_j}[\tau_{ji}] + \frac{\partial p}{\partial x_i} + Q_i = 0, \tag{2}$$

where $i, j = 1, 2, 3$ represent the coordinate directions, ρ is the water density, u_i is the velocity vector, p is the water pressure, and Q_i is a source vector term that includes Coriolis force, surface and bottom shear stresses, and atmospheric gradient.

2.1. Shallow water flow characteristic. Shallow water flow is a nearly horizontal flow. This allows a considerable simplification in the mathematical formulation and numerical simulation allowing the assumption that the pressure distribution is hydrostatic. However, shallow water flow is not exactly two-dimensional. Density stratification due to differences in temperature or salinity cause variations in the vertical direction. In many shallow water flows, these three-dimensional effects are not essential and it is sufficient to consider the depth-averaged form, which is two-dimensional in the horizontal plane.

The basic assumption in shallow-water theory is that vertical scales are much smaller than horizontal ones. The vertical parameters include the water depth H , the variation in the bottom level, and the variation in water height h . The horizontal ones include the physical dimensions of the basin (length, width) and the wavelength λ (Figure 1). From linear wave theory, the ratio of water depth to wavelength must be less than about 0.05 [Le Méhauté 1976]. This can be considered as the upper limit of shallow water theory. In shallow water flow, the horizontal velocities are of primary importance, and are defined

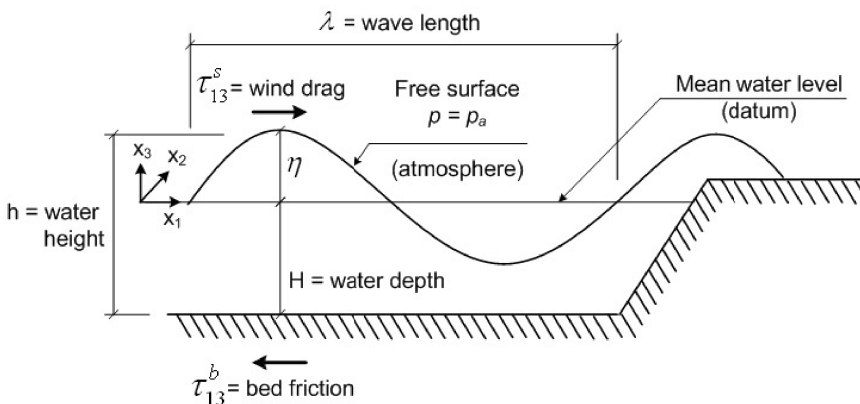


Figure 1. Shallow water flow profile.

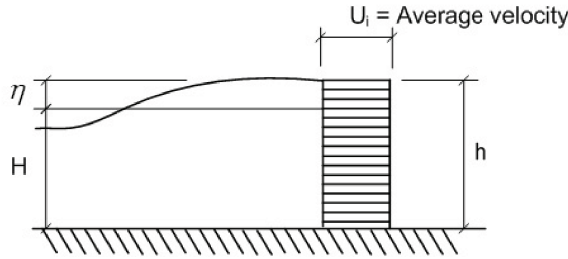


Figure 2. Velocity distribution of shallow water flow.

as the average velocity:

$$\int_{-H}^{\eta} u_i dx_3 = U_i(H + \eta) = U_i \cdot h, \tag{3}$$

where U_i is the average velocity vector (Figure 2).

In general shallow water flow, there are two types of boundary conditions governing the fluid at its top and bottom:

- A kinematic boundary condition, which states that water particles cannot cross either boundary, further requires that,
 - along the solid bottom ($z = -H$), velocities normal to the surface must vanish:

$$-u_1 \frac{\partial H}{\partial x} - u_2 \frac{\partial H}{\partial y} - u_3 = 0, \tag{4a}$$

- along the free top surface ($z = \eta$), since the surface must not move away from itself, the fluid’s relative normal velocity must vanish:

$$\frac{\partial \eta}{\partial t} + u_1 \frac{\partial \eta}{\partial x} + u_2 \frac{\partial \eta}{\partial y} - u_3 = 0. \tag{4b}$$

- A dynamic boundary condition, which defines the forces acting at each boundary:
 - Along the bottom, it is assumed that the viscous fluid sticks to the surface (no slip condition):

$$u_1 = u_2 = 0. \tag{4c}$$

- Along the top, it is assumed that the stress in the fluid just below the free surface is the same as that in the air just above, namely the atmospheric pressure:

$$p = p_a. \tag{4d}$$

2.2. Shallow water continuity equation. The equation for the free surface is derived by an integration of the continuity equation (1) over the depth coordinate x_3 :

$$\int_{-H}^{\eta} \frac{\partial u_1}{\partial x} dz + \int_{-H}^{\eta} \frac{\partial u_2}{\partial y} dz + \int_{-H}^{\eta} \frac{\partial u_3}{\partial z} dz = 0. \tag{5}$$

By using the Leibniz rule of integrals, Equation (5) can be written as

$$\frac{\partial h}{\partial t} + \frac{\partial(hU_j)}{\partial x_j} = 0. \tag{6}$$

With $j = 1, 2$, Equation (6) can also be written as

$$\frac{\partial h}{\partial t} + \frac{\partial(hU_1)}{\partial x} + \frac{\partial(hU_2)}{\partial y} = 0. \tag{7}$$

2.3. Shallow water momentum equations. In shallow water flow, the vertical velocity (u_3) is very small, and the corresponding acceleration can be neglected. So the vertical momentum equation becomes:

$$\frac{1}{\rho} \frac{\partial p}{\partial x_3} + g = 0. \tag{8}$$

After integration, we can determine the pressure as

$$p = \rho g(\eta - z) + p_a. \tag{9}$$

The other momentum equations for horizontal velocities are also integrated over the depth:

$$\int_{-H}^{\eta} \left[\frac{\partial(u_i)}{\partial t} + \frac{\partial}{\partial x_j}(u_i u_j) + \frac{1}{\rho} \frac{\partial p}{\partial x_i} - \frac{1}{\rho} \frac{\partial \tau_{ji}}{\partial x_j} - Q_i \right] dx_3 = 0. \tag{10}$$

Using the definition of p from Equation (9), and with $i = 1, 2$, Equation (10) can be written as the conservative form of the depth-averaged equations:

$$\begin{aligned} \frac{\partial(hU_i)}{\partial t} + \frac{\partial}{\partial x_j} \left[(hU_i U_j) + \delta_{ij} \frac{1}{2} g(h^2 - H^2) \right] \\ + \frac{\partial}{\partial x_j} \left[-\frac{h}{\rho} \bar{\tau}_{ji} \right] + \left[-\frac{1}{\rho} (\tau_{3i}^s - \tau_{3i}^b) - h f i - g(h - H) \frac{\partial H}{\partial x_i} + \frac{h}{\rho} \frac{\partial P_a}{\partial x_i} \right] = 0. \end{aligned} \tag{11}$$

The term τ_{ij}^s is the surface shear stress which is caused by the wind stress. The magnitude and direction of the wind stress on the sea surface are determined by the flow in the atmosphere. A semiempirical formula to calculate the magnitude of the wind stress is given by Gill [1982] as

$$\tau_{ij}^s = c_d \cdot \rho \cdot W_i^2, \tag{12}$$

where

$$c_d = \text{drag coefficient} \quad \text{and} \quad W_i = \text{wind speed}.$$

The term τ_{ij}^b is the bottom shear stress due to the no-slip boundary condition. This stress is influenced by the roughness of the bottom layer. A simple approximation to calculate this bottom stress is given by Groen and Groves [1962] as

$$\tau_{3j}^b = c_f \cdot \rho \cdot |U| U_i, \tag{13}$$

where

$$|U| = \sqrt{U_i U_i} \quad \text{and} \quad c_f = \text{standard friction coefficient}.$$

The term $\partial P_a/\partial x_i$ is the atmospheric pressure gradient. This may be important for the simulation of storm surges [Heaps 1967]. The value of this gradient can be obtained, for example, from a meteorological forecast.

2.4. Shallow water equations. From the continuity and momentum equation, the complete form of the Shallow Water Equations can be written in the conservative forms as

$$\frac{\partial \Phi}{\partial t} + \frac{\partial F_i}{\partial x_i} + \frac{\partial G_i}{\partial x_i} + Q = 0, \tag{14}$$

where

$$\begin{aligned} \Phi &= \begin{bmatrix} h \\ hU \\ hV \end{bmatrix} = \text{independent variable vector,} \\ F_i &= \begin{bmatrix} hU_i \\ hUU_i + \delta_{1i} \frac{1}{2} g(h^2 - H^2) \\ hVU_i + \delta_{2i} \frac{1}{2} g(h^2 - H^2) \end{bmatrix} = \text{convective flux vector,} \\ G_i &= \begin{bmatrix} 0 \\ -(h/\rho)\bar{\tau}_{1i} \\ -(h/\rho)\bar{\tau}_{2i} \end{bmatrix} = \text{diffusion fluxes,} \\ Q &= \begin{bmatrix} 0 \\ -h\hat{f}V - g(h - H)\frac{\partial H}{\partial x} - \frac{h}{\rho}\frac{\partial P_a}{\partial x} - \frac{1}{\rho}\tau_{31}^s + c_f \cdot U\sqrt{U^2 + V^2} \\ h\hat{f}U - g(h - H)\frac{\partial H}{\partial y} - \frac{h}{\rho}\frac{\partial P_a}{\partial y} - \frac{1}{\rho}\tau_{32}^s + c_f \cdot V\sqrt{U^2 + V^2} \end{bmatrix} = \text{source terms.} \end{aligned}$$

For a general shallow water flow, the value of the stress $\bar{\tau}_{ji}$, the surface stress τ_{ij}^s , the bottom stress τ_{ij}^b , and the atmospheric pressure gradient $\partial P_a/\partial x_i$ are very small and can be neglected, so the shallow water equations can be simplified as

$$\frac{1}{c^2} \frac{\partial p}{\partial t} + \frac{\partial U_i}{\partial x_i} = 0, \quad \frac{\partial U_i}{\partial t} + \frac{\partial}{\partial x_j} (u_j U_i) + \frac{\partial p}{\partial x_i} + Q = 0, \tag{15}$$

with

$$\begin{aligned} U_i &= \text{average velocity over the depth,} \\ p &= \frac{1}{2}(h^2 - H^2) = \text{pressure,} \\ c &= \sqrt{gh} = \text{wave celerity,} \\ Q &= -g(h - H)\frac{\partial H}{\partial x_i} + f_i = \text{source term,} \end{aligned}$$

in which f_i is the Coriolis force.

3. Review on characteristic-based split method

The numerical method used in this study is the characteristic-based split (CBS) algorithm, which was first proposed by Zienkiewicz and Codina [1995]. It can be applied to solve both compressible and incompressible flows, and is efficient and accurate. The main concept of this method is to split the shallow water equations into two parts:

- A set of simple scalar equations of convective-diffusion type that can be solved using a much bigger time step.
- A set of equations that are self-adjoint and can be discretized optimally by the Galerkin procedure, which can be solved implicitly and is unconditionally stable.

3.1. CBS time discretization. The time discretization in this scheme will treat the pressure gradient of the momentum equation (15)₂ as a source term, and will evaluate it differently in $t = t^n + \theta \Delta t$ at time increments Δt as shown below:

$$\frac{\partial p^{n+\theta_2}}{\partial x_i} = (1 - \theta_2) \frac{\partial p^n}{\partial x_i} + \theta_2 \frac{\partial p^{n+1}}{\partial x_i}. \quad (16)$$

This equation yields

$$\begin{aligned} \Delta U_i = \Delta t \left[-\frac{\partial}{\partial x_j} (u_j U_i) - Q + \frac{\Delta t}{2} u_k \frac{\partial}{\partial x_k} \left(\frac{\partial}{\partial x_j} (u_j U_i) + Q \right) \right]^n \\ - (1 - \theta_2) \Delta t \left[\frac{\partial p}{\partial x_i} - \frac{\Delta t}{2} u_k \frac{\partial}{\partial x_k} \left(\frac{\partial p}{\partial x_i} \right) \right]^n - \theta_2 \Delta t \left[\frac{\partial p}{\partial x_i} \right]^{n+1}. \end{aligned} \quad (17)$$

This can be split into two parts:

$$\Delta U_i = \Delta U_i^* + \Delta U_i^{**}, \quad (18)$$

where

$$\Delta U_i^* = \Delta t \left[-\frac{\partial}{\partial x_j} (u_j U_i) - Q + \frac{\Delta t}{2} u_k \frac{\partial}{\partial x_k} \left(\frac{\partial}{\partial x_j} (u_j U_i) + Q \right) \right]^n, \quad (19)$$

$$\begin{aligned} \Delta U_i^{**} &= -(1 - \theta_2) \Delta t \left[\frac{\partial p}{\partial x_i} - \frac{\Delta t}{2} u_k \frac{\partial}{\partial x_k} \left(\frac{\partial p}{\partial x_i} \right) \right]^n - \theta_2 \Delta t \left[\frac{\partial p}{\partial x_i} \right]^{n+1} \\ &= -\Delta t \left[\frac{\partial p^n}{\partial x_i} + \theta_2 \frac{\partial \Delta p}{\partial x_i} \right] + (1 - \theta_2) \frac{\Delta t^2}{2} u_k \frac{\partial}{\partial x_k} \frac{\partial p^n}{\partial x_i}, \end{aligned} \quad (20)$$

$$\Delta p = p^{n+1} - p^n. \quad (21)$$

With the same procedure, the shallow water continuity equation can also be discretized in time as

$$\left(\frac{1}{c^2} \right)^n \Delta p = -\Delta t \left[\frac{\partial U_i}{\partial x_i} + \theta_1 \frac{\partial \Delta U_i}{\partial x_i} \right] = -\Delta t \left[\frac{\partial U_i}{\partial x_i} + \theta_1 \frac{\partial \Delta U_i^*}{\partial x_i} + \theta_1 \frac{\partial \Delta U_i^{**}}{\partial x_i} \right]. \quad (22)$$

Neglecting third-order terms, this can be written as

$$\left(\frac{1}{c^2} \right)^n \Delta p = -\Delta t \left[\frac{\partial U_i}{\partial x_i} + \theta_1 \frac{\partial \Delta U_i^*}{\partial x_i} - \Delta t \theta_1 \left(\frac{\partial^2 p^n}{\partial x_i \partial x_i} + \theta_2 \frac{\partial^2 \Delta p}{\partial x_i \partial x_i} \right) \right]. \quad (23)$$

This algorithm can be applied to both explicit and semiimplicit schemes, and depends on the selection of the values θ_1 and θ_2 . The stability criteria will depend on the scheme selected. For the fully explicit scheme, we have

$$1/2 \leq \theta_1 \leq 1, \quad \theta_2 = 0. \tag{24}$$

Stability is obtained when the time increment is less than the time limit, defined as

$$\Delta t \leq \Delta t_\sigma = \frac{a}{c + |u|}, \tag{25}$$

where

$$a = \text{element size}, \quad c = \sqrt{g \cdot h} = \text{wave celerity}, \quad |u| = \sqrt{U_i U_i}.$$

In semiimplicit form, the quantities of θ_1 and θ_2 are defined as

$$1/2 \leq \theta_1 \leq 1, \quad 1/2 \leq \theta_2 \leq 1. \tag{26}$$

This algorithm is conditionally stable. Three time limits have to be considered to assure stability:

$$\Delta t \leq \Delta t_\sigma = \frac{a}{|u|}, \quad \Delta t \leq \Delta t_\nu = \frac{a^2}{2\nu}, \quad \Delta t \leq \frac{\Delta t_\sigma \cdot \Delta t_\nu}{\Delta t_\sigma + \Delta t_\nu}, \tag{27}$$

where $\nu =$ kinematic viscosity.

3.2. CBS spatial discretization. The finite element methods (FEM) is used to discretize the space. FEM is an approximate method for solving differential equations of boundary and initial value problems. The basic concept of FEM is to divide a continuum into many smaller elements of convenient shapes — triangle, quadrilateral, and so on. Choosing suitable points (‘nodes’) within the elements, the variable in the differential equation is written as a linear combination of appropriately selected interpolation functions describing the variable. The governing equations are then transformed into a set of *finite element equations* for each element, and assembled into a global system based on the connectivity of the nodes. The nodal values of the variable are determined from this system of equations.

The spatial discretizations used in these formulations are

$$U_i = N(\bar{U}_i), \quad \Delta U_i = \Delta U_i^* + \Delta U_i^{**} = N(\Delta \bar{U}_i^*) + N \cdot (\Delta \bar{U}_i^{**}), \quad p = N \cdot (\bar{p}), \tag{28}$$

where

$$\begin{aligned} \bar{U}_i &= [\bar{U}_i^1 \ \bar{U}_i^2 \ \dots \ \bar{U}_i^k] = \text{Nodal velocities of a } k\text{-node element,} \\ N_i &= [N^1 \ N^2 \ \dots \ N^k] = \text{Galerkin shape function of a } k\text{-node element.} \end{aligned}$$

Equations (19), (20) and (23) are then discretized in space using the standard Galerkin finite element method. By writing the pressure p in terms of total water height h , these equations can be solved in three steps, as illustrated by Figure 3.

STEP 1

$$\mathbf{K}_1 \{ \Delta U_i^* \} = \mathbf{F}_1 (U_i^n, h^n, \Delta t)$$

$$\begin{bmatrix} \text{Diagonal Matrix} \\ \text{Diagonal Matrix} \end{bmatrix} \begin{Bmatrix} \Delta U^* \\ \Delta V^* \end{Bmatrix} = \begin{Bmatrix} \mathbf{F}u^* \\ \mathbf{F}v^* \end{Bmatrix}$$

Diagonal Matrix

STEP 3

$$\mathbf{K}_3 \{ \Delta U_i^{**} \} = \mathbf{F}_3 (U_i^n, h^n, h^{n+1}, \Delta t, \theta_2)$$

$$\begin{bmatrix} \text{Diagonal Matrix} \\ \text{Diagonal Matrix} \end{bmatrix} \begin{Bmatrix} \Delta U^{**} \\ \Delta V^{**} \end{Bmatrix} = \begin{Bmatrix} \mathbf{F}u^{**} \\ \mathbf{F}v^{**} \end{Bmatrix}$$

Diagonal Matrix

STEP 2

$$\mathbf{K}_2 (h^n, \Delta t, \theta_1, \theta_2) \{ \Delta h \} = \mathbf{F}_2 (\Delta U_i^*, \Delta U_i^n, h^n, \Delta t, \theta_1)$$

$$\begin{bmatrix} \text{Band Matrix} \end{bmatrix} \begin{Bmatrix} \Delta h \end{Bmatrix} = \begin{Bmatrix} \mathbf{F}h \end{Bmatrix}$$

Band Matrix

$$h^{n+1} = h^n + \Delta h$$

Figure 3. CBS solution algorithm.

Step 1: Intermediate momentum equation. We have

$$\int_{\Omega} N \cdot \Delta U_i^* d\Omega = \Delta t \left[- \int_{\Omega} N \frac{\partial}{\partial x_j} (u_j U_i) d\Omega - \int_{\Omega} N \cdot Q_i d\Omega - \frac{\Delta t}{2} \int_{\Omega} \frac{\partial}{\partial x_k} (u_k N) \frac{\partial}{\partial x_j} (u_j U_i) d\Omega \right. \\ \left. + \frac{\Delta t}{2} \int_{\Omega} (u_k \cdot N) \frac{\partial Q_i}{\partial x_k} d\Omega + \frac{\Delta t}{2} \int_{\partial\Omega} (N \cdot u_k) \frac{\partial}{\partial x_j} (u_j U_i) n_k d\Gamma \right]^n, \quad (29)$$

whose solution is

$$\Delta \bar{U}_i^* = -M^{-1} \Delta t [C \cdot \bar{U} + \Delta t \cdot K_u \bar{U} - (f + \Delta t \cdot f_s) - \Delta t \cdot K_b], \quad (30)$$

where

$$M = \int_{\Omega} N^T N d\Omega, \quad f = \int_{\Omega} N^T Q d\Omega,$$

$$C = \int_{\Omega} N^T \frac{\partial}{\partial x_j} (u_j N) d\Omega, \quad f_s = -\frac{1}{2} \int_{\Omega} \frac{\partial}{\partial x_i} (u_i N^T) Q d\Omega,$$

$$K_u = \frac{1}{2} \int_{\Omega} \frac{\partial}{\partial x_k} (u_k N^T) \frac{\partial}{\partial x_j} (u_j N) d\Omega, \quad K_b = \frac{1}{2} \int_{\partial\Omega} (u_k N^T) \frac{\partial}{\partial x_j} (u_j N) n_k d\Gamma.$$

Step 2: Total water depth calculation.

$$\begin{aligned} & \int_{\Omega} N(\Delta h)d\Omega + \Delta t^2\theta_1\theta_2 \int_{\Omega} \frac{\partial N}{\partial x_i}(\bar{c}^2)\frac{\partial(\Delta h)}{\partial x_i}d\Omega \\ &= -\Delta t \left[\int_{\Omega} N \frac{\partial U_i^n}{\partial x_i}d\Omega + \theta_1 \int_{\Omega} \frac{\partial N}{\partial x_i} \left(\Delta U_i^* - \Delta t(c^2)^n \frac{\partial h^n}{\partial x_i} \right) d\Omega \right. \\ & \quad \left. - \theta_1 \int_{\partial\Omega} N \left[\Delta U_i^* - \Delta t \left((c^2)^n \frac{\partial h^n}{\partial x_i} + \theta_2(\bar{c}^2)\frac{\partial(\Delta h)}{\partial x_i} \right) \right] n_i d\Gamma \right], \end{aligned} \quad (31)$$

whose solution is

$$\begin{aligned} \Delta \bar{h} &= (\tilde{M} + \Delta t^2 \cdot \theta_1\theta_2\bar{c}^2(H - Q_b))^{-1} \Delta t \\ & \quad \times \left[Q(-\bar{U}_i + \theta_1 \Delta \bar{U}_i^*) - \Delta t\theta_1 c^2 H \cdot \bar{h} + \theta_1(\Delta t \cdot c^2 Q_b \bar{h} - M_b \Delta \bar{U}_i^*) \right]^n, \end{aligned} \quad (32)$$

where

$$\begin{aligned} \tilde{M} &= \int_{\Omega} N^T N d\Omega, & M_b &= \int_{\partial\Omega} N^T N \cdot n_i \cdot d\Gamma, \\ Q &= \int_{\Omega} \frac{\partial N^T}{\partial x_i} N \cdot d\Omega, & H &= \int_{\Omega} \frac{\partial N^T}{\partial x_i} \frac{\partial N}{\partial x_i} \cdot d\Omega, & Q_b &= \int_{\partial\Omega} \frac{\partial N^T}{\partial x_i} N \cdot n_i d\Gamma. \end{aligned}$$

Step 3: Velocity correction.

$$\begin{aligned} \int_{\Omega} N \Delta U_i^{**} d\Omega &= -\Delta t \cdot (1 - \theta_2) \int_{\Omega} N(c^2)^n \frac{\partial h^n}{\partial x_i} d\Omega - \Delta t\theta_2 \int_{\Omega} N(c^2)^{n+1} \frac{\partial h^{n+1}}{\partial x_i} d\Omega \\ & \quad - (1 - \theta_2) \frac{\Delta t^2}{2} \int_{\Omega} \frac{\partial N}{\partial x_k} u_k \left((c^2)^n \frac{\partial h^n}{\partial x_i} \right) d\Omega - (1 - \theta_2) \frac{\Delta t^2}{2} \int_{\Omega} N \frac{\partial u_k}{\partial x_k} \left((c^2)^n \frac{\partial h^n}{\partial x_j} \right) d\Omega \\ & \quad + (1 - \theta_2) \frac{\Delta t^2}{2} \int_{\partial\Omega} N u_k \left((c^2)^n \frac{\partial h^n}{\partial x_j} \right) \cdot n_i \cdot d\Gamma. \end{aligned} \quad (33)$$

The solution of Equation (33) is

$$\Delta(\bar{U}_i)^{**} = -M \cdot^{-1} \Delta t \cdot \left[Q^T [(1 - \theta_2)(c^2)^n \bar{h}^n + \theta_2(c^2)^{n+1} \bar{h}^{n+1}] + \frac{\Delta t}{2} P(c^2)^n \bar{h}^n - \frac{\Delta t}{2} P_b(c^2)^n \bar{h}^n \right], \quad (34)$$

where

$$\begin{aligned} M &= \int_{\Omega} N^T N d\Omega, & P &= (1 - \theta_2) \int_{\Omega} \frac{\partial}{\partial x_i} (u_i N^T) \frac{\partial N^T}{\partial x_i} d\Omega, \\ Q &= \int_{\Omega} \frac{\partial N^T}{\partial x_i} N \cdot d\Omega, & P_b &= (1 - \theta_2) \int_{\partial\Omega} (u_k N^T) \frac{\partial N^T}{\partial x_i} n_k d\Gamma, \end{aligned}$$

and where $i, j, k = 1, 2$, and N is the standard finite element shape function. The variable \bar{c} is the average value of the celerity over the time step, while Ω is the flow domain bounded by $\partial\Omega$, and n_k is the outward normal of the boundary $\partial\Omega$. Step 1 and Step 3 can be solved explicitly, while Step 2 needs to be solved implicitly. The velocity is computed in two stages by the characteristic Galerkin method as shown in Step 1 and Step 3. In Step 2, the pressure, or elevation of the free surface, is solved from a

self-adjoint Laplacian-type equation, which can be discretized optimally by the Galerkin procedure. In this semiimplicit form, the algorithm's time step depends only on the current velocity, rather than on the wave celerity. By now it should be clear why the CBS method is very efficient.

4. Review on exact solution

The exact solution for water elevation is achieved by solving the continuity equation above. By defining η as the water elevation, we can get

$$\eta(x, t) = \frac{H}{2} \cos(kx - \sigma t), \tag{35}$$

where

$$k = \frac{2\pi}{L} = \text{the wave number}, \tag{36}$$

$$\sigma^2 = \frac{2\pi}{T} = gk * \tanh(kh) = \text{the circular frequency}, \tag{37}$$

$$c = \frac{\sigma}{k} = \frac{2\pi/T}{2\pi/L} = \frac{L}{T} = \text{the wave celerity}. \tag{38}$$

For shallow water waves, where kh is very small ($kh < \pi/10$), the hyperbolic function $\tanh(kh)$ can be approximated as kh . With this simplification, the dispersion relationship for shallow water reduces in such a way that the wave celerity for shallow water wave can be defined as

$$\sigma^2 = gk * \tanh(kh) = gk^2h, \quad \frac{\sigma^2}{k^2} = c^2 = gh, \quad c = \sqrt{gh}. \tag{39}$$

From the linearized frictionless momentum equations, we have

$$\frac{\partial U}{\partial t} = -g \frac{\partial \eta}{\partial x}. \tag{40}$$

Substituting Equation (35) into Equation (40), we get

$$\frac{\partial U}{\partial t} = g \frac{H}{2} k \sin(kx - \sigma t),$$

or

$$U = g \frac{H}{2\sigma} k \cos(kx - \sigma t) = \frac{c}{h} \eta. \tag{41}$$

If we further examine the change in wave height due to changes in water depth and channel width, we find that

$$H_2 = H_1 \left(\frac{h_1}{h_2} \right)^{1/4} \left(\frac{b_1}{b_2} \right)^{1/2}, \tag{42}$$

where subscript 1 indicates the location at the reference point, and subscript 2 indicates the location at the examined point. For a special case where the channel width is uniform ($b_1 = b_2$), this relationship is called Green's Law. This formula implies that a change in water depth or channel width can change the water height.

5. Model verification and demonstration

The element used in this study is a standard linear triangular element with three unknowns to be solved in each node, as shown in Figure 4. These unknowns are h , U , and V which determine the water elevation and the mass flow in x and y directions. The area and line integrations are calculated numerically using one Gauss point, as show in Figure 5.

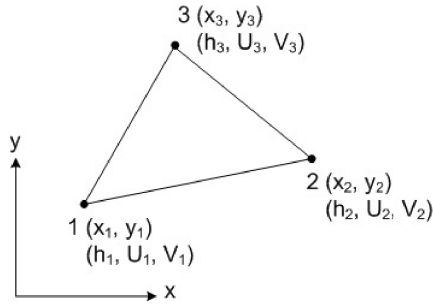


Figure 4. Triangular element.

The wave parameters will be defined based on the characteristic of shallow water wave states where the ratio of the vertical scale h to the horizontal scale L is very small. Our shallow water condition is:

$$h/L < 0.05 \quad \text{or} \quad kh < \pi/10. \tag{43}$$

In this study, water depth is kept constant at the level $h = 0.5$ m. Using this water depth, we can compute the wave celerity simply by using Equation (39):

$$c = \sqrt{gh} = 2.214 \text{ m/s}. \tag{44}$$

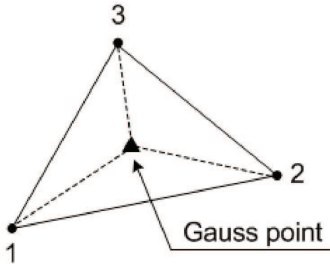
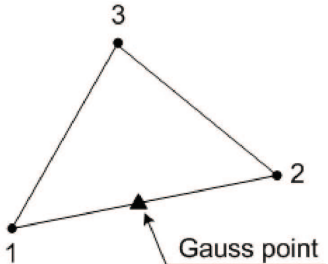
Numerical Area integration	Numerical Line integration
 $\int_{\Omega} N_1 d\Omega = \int_{\Omega} N_2 d\Omega = \int_{\Omega} N_3 d\Omega = \frac{1}{3} * \text{Area}$	 $\int_{\partial\Omega} N_1 d\Gamma = \int_{\partial\Omega} N_2 d\Gamma = \frac{1}{2} * \text{Length}$ $\int_{\partial\Omega} N_3 d\Gamma = 0$

Figure 5. Numerical integration.

Parameter:	Symbol	Value used
Water depth	H	0.5 m
Wave amplitude	A	0.02 m
Wave period	T	10 s
Time stepping parameter	θ_1 and θ_2	0.5
Time increment	Δt	0.0625 s
Lumping parameter	B	0.9

Table 1. Parameters used in this study.

Using Equations (36) and (38) with $k = 2\pi/L$ and $L = c \cdot T$, we can compute the wave period by

$$kh < \frac{\pi}{10} \rightarrow \frac{2\pi}{c \cdot T}h < \frac{\pi}{10} \rightarrow T > 4.52 \text{ s.} \tag{45}$$

To satisfy this condition, the wave period is set to 10 s, and the wave amplitude is set at 0.02 m. The wavelength is computed using Equation (38) and is equal to 22.14 m. For the sake of stability, the time stepping parameters θ_1 and θ_2 are set to 0.5, following the Crank–Nicolson scheme. The time step increment, Δt , is set to be 0.0625 s, and the lumping parameter β is set at 0.9. These parameters, used throughout this study, are summarized in Table 1.

The model will be verified and demonstrated by solving and analyzing four case studies. The analysis is done by performing a convergence test and, where possible, comparing the numerical results with exact solutions and laboratory experiments. In cases where the exact solution is not available, the analysis is based only on the physical characteristics of the water flow. These cases serve as demonstrations of the capability of the model.

Case 1: Flow in rectangular channel with constant depth. A simple experiment of shallow water wave propagation is done in a frictionless channel with a length and depth of 50 m and 10 m respectively. The purpose of this case is to verify that the FEM solution for water elevation, velocity, and pressure converge well as our mesh gets finer. Other wave parameters will also be verified.

A series of waves are generated on one side, such that they will propagate to the other side and reflect back. The boundary conditions we apply to the model are the normal velocity on the boundary B-C, C-D, and A-D is assumed to be zero, while a sinusoidal wave is imposed on the boundary A-B with an amplitude of 0.02 m and a period of 10 s.

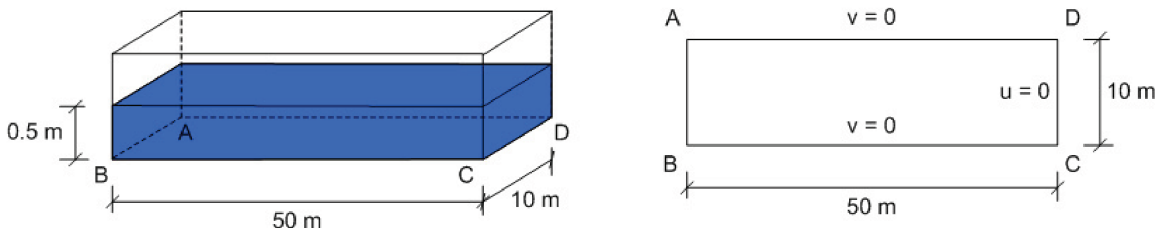


Figure 6. Rectangular profile with constant depth.

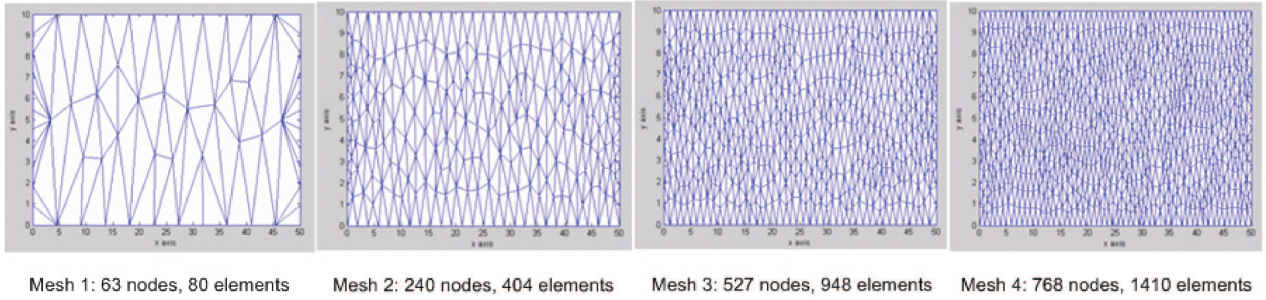


Figure 7. Four types of mesh used in Case 1.

We will study convergence of solutions across four successively refined meshes, as shown in Figure 7. The convergence test is conducted at regular 5 m intervals within the channel. Figure 8 compares water elevations in the FEM and exact solutions, at time = 20 s and $x = 5, 10, 15, 20, 25$ and 30 m.

Looking to Figure 8, we see that the FEM solution using meshes 2, 3, and 4 give results close to the exact solution. The exact solution given here is for a wave in a steady state. Looking to our results, the error seems to be increasing as x increases. This can be explained by the fact that, when the wave is generated, it will first propagate in a transient state, only reaching the steady state after quite some time. Furthermore, the exact solution gives no wall boundary condition around the channel. If we look at the steady state region, $x \leq 15$ m, the FEM with mesh 4 gives pretty good results. By contrast, at $x = 50$ m we see a clear difference between the FEM and exact solutions. The wave in the numerical solution has yet to arrive, while the wave in the exact solution is already in its steady state. Results from successively refined meshes do not converge very well, and sometimes the least error is found with a mesh other than mesh 4, which is the most refined mesh. This is likely the result of the irregular shape and location of the triangles used in the meshing scheme.

To further confirm our method, we examine the accuracy of the physical results got using mesh 4. Looking to Figure 9, which shows the wave at time = 25 s, we see that the amplitude of the wave

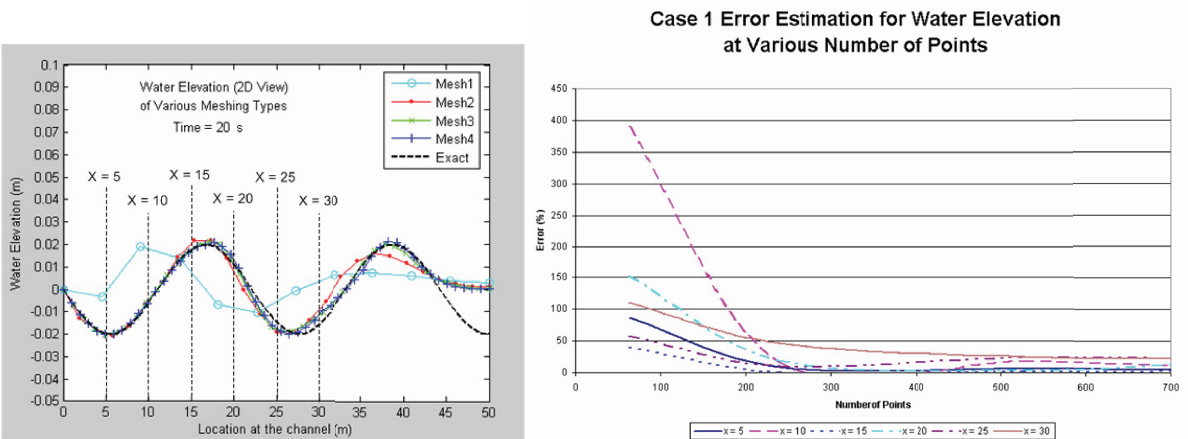
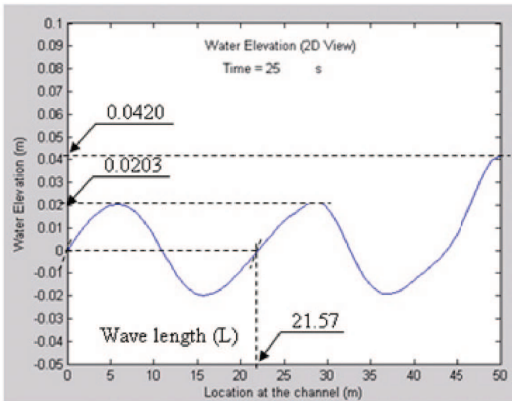


Figure 8. Water elevation result of Case 1 at time = 20 s.



	FEM	Exact	Error
Wave Length	21.57 m	22.14 m	2.58 %
Amplitude	0.0203 m	0.02 m	1.50 %
Maximum water elevation on the wall	0.0420 m	0.04 m	5.00 %

Figure 9. Wave properties at time = 25 s.

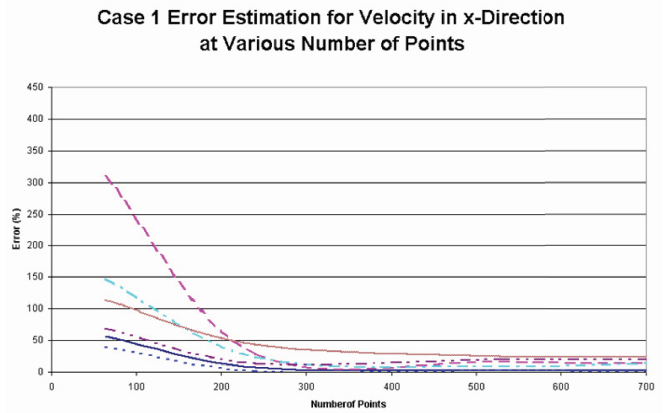
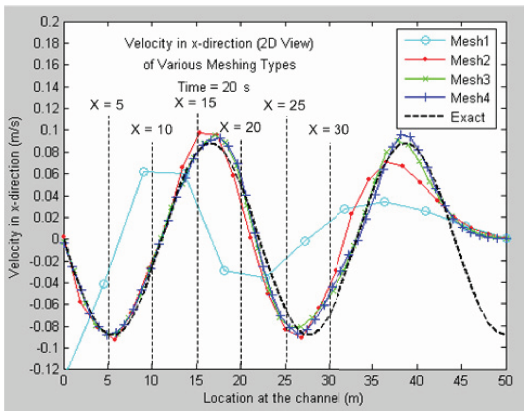


Figure 10. Velocity in x-direction of Case 1 at time = 20 s.

is consistently 0.0203 m. This is a 1.5% error relative to the initial amplitude of 0.02 m. The FEM wavelength is computed to be 21.57 m, which is 2.58% in excess of the exact solution 22.14 m. When the wave hits the wall (at time ≈ 25 s), the maximum water elevation will double, to 0.04 m. The FEM solution gives this elevation as 0.0420 m, a 5.00% error.

Since the water pressure is derived directly from water elevation ($p = 0.5g(h^2 - H^2)$), it has exactly the same behavior as water elevation. The velocity in the x -direction for both FEM and exact solutions at time = 20 s are presented in Figure 10. The convergence test is again conducted at the same 5 m intervals.

The behavior of the velocity is similar to that of the water elevation. FEM solutions of velocity using meshes 3 and 4 give results close to the exact solution in the steady state region, $x < 15$ m. Velocity in the y -direction is zero for all time throughout the channel. This is as expected, as the imposed wave is symmetrical. Again, the results converge poorly due to the irregular triangular meshing. The maximum velocity in the x -direction is 0.0952 m/s which has 7.25% error from exact solution 0.0883 m/s.

Case 2: Flow in rectangular channel with irregular depth. Next, we pursue a variation on Case 1, a rectangular channel with irregular depth as shown in Figure 11. Again, we assume no normal velocity

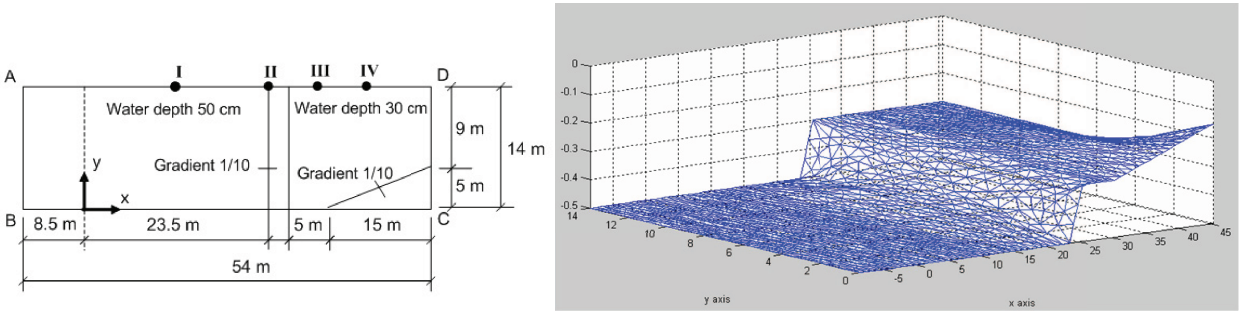


Figure 11. Channel profile of Case 2.

along boundaries B-C, C-D, and A-D, with a sinusoidal wave imposed on boundary A-B. The wave’s amplitude is 0.02 m and its period of 10 s. The water elevation will be computed on the edge of the channel ($y = 14$ m) at four different points ($x_I = 11.5$ m, $x_{II} = 23.5$ m, $x_{III} = 29.5$ m, and $x_{IV} = 35.5$ m).

We compare the results of this case study with experimental data, and other numerical result previously done by Cheng and Kawahara [1991] using the combination of the explicit and quasi explicit standard Galerkin finite element method.

The water elevations at our four reference points are plotted against time in Figure 12. The dotted line shows observed experimental data, the solid line shows the numerical result using the standard Galerkin finite element method, and the dashed line is the numerical result using the CBS method. From the figure

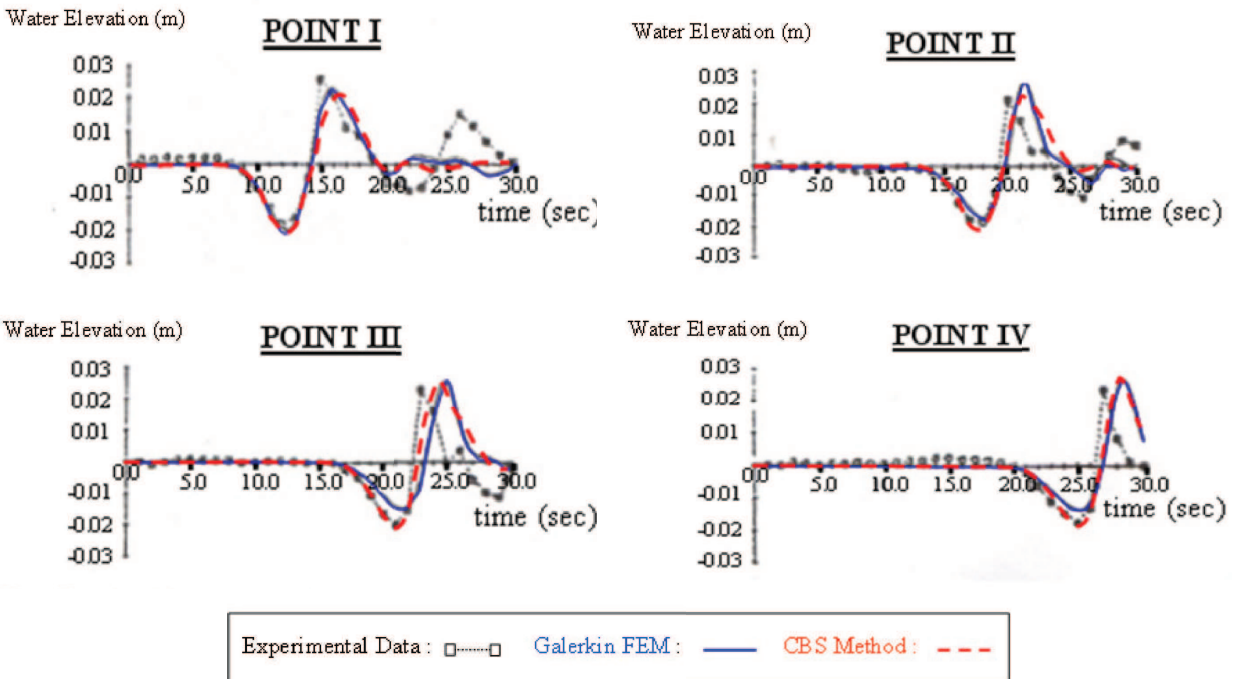


Figure 12. Numerical results of Case 2.

we see that the values obtained using the CBS method are the better of the numerical results, closer to the experimental data.

Snapshots of the three-dimensional view of water elevation are shown in [Figure 13](#). From the simulation, it can be seen that when the wave enters the shallower area, its height increases. This corresponds with the characteristic of tsunami propagation.

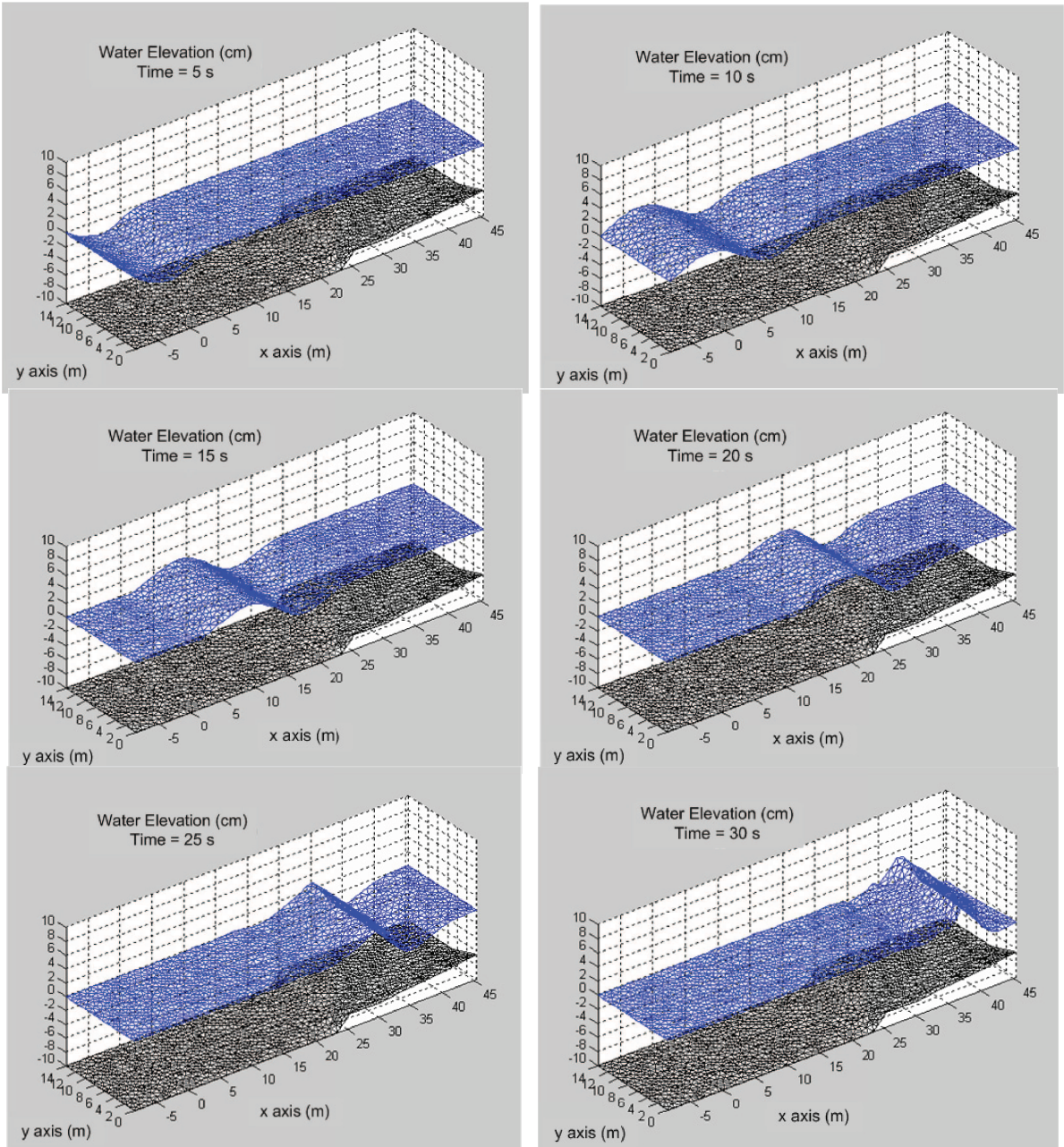


Figure 13. Water elevation of [Case 2](#) at various time steps.

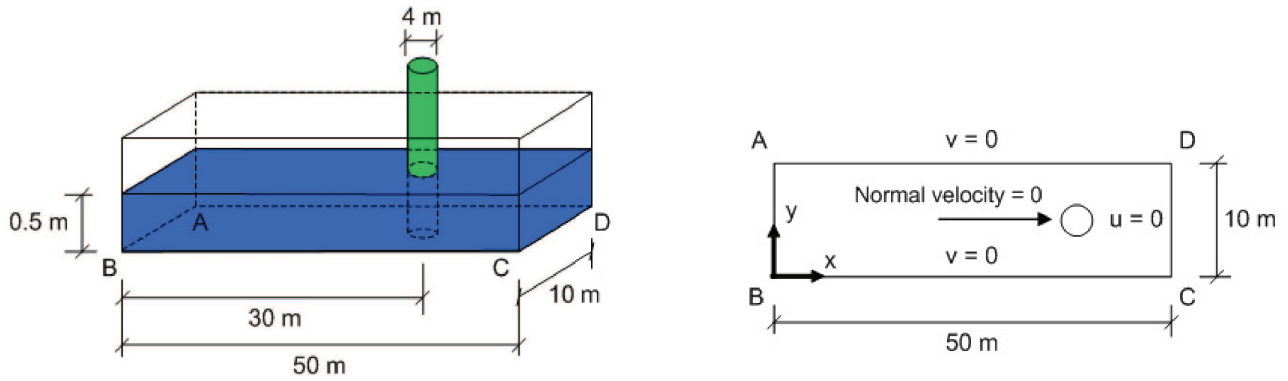


Figure 14. Channel profile for Case 3.

Case 3. Flow passing a solid barrier. In Case 3, a cylindrical barrier with a diameter of 4 m is placed in the middle of the channel at $x = 30$ m, as shown in Figure 14. The purpose of this case is to model and study the behavior of the tsunami wave passing a solid barrier, such as an offshore structure. Again, we set the normal velocity along boundaries B-C, C-D, and A-D to zero, and propagate a sinusoidal wave with an amplitude of 0.02 m and a period of 10 s from boundary A-B.

Snapshots of the wave’s elevation at two times are plotted in Figure 15. The solid lines show the water elevation in the middle of the channel ($y = 5$ m), while the dashed lines show the water elevation in the edge of the channel ($y = 0$ m).

If we look at Figure 15, at time = 15 s there is a difference in water elevation between the water in the middle of the channel ($y = 5$ m), which starts to hit the barrier, and the water on the edge of the channel ($y = 0$ m), which still propagates with the same amplitude. At time $t = 25$ s, the maximum water elevation at the wall is about 0.035 m. In Case 1 where there is no barrier, the maximum water

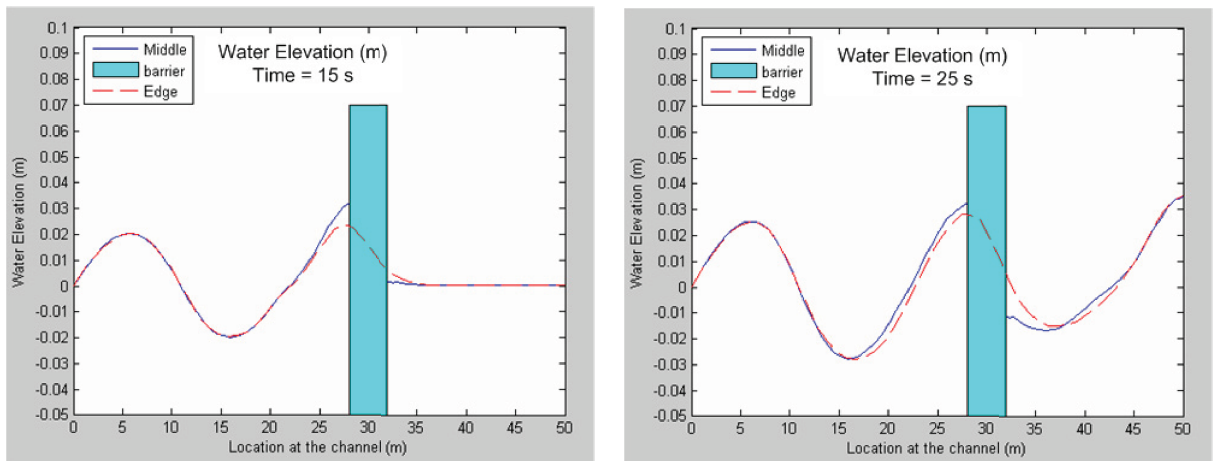


Figure 15. Water elevation of Case 3 at $t = 15$ s and $t = 25$ s.

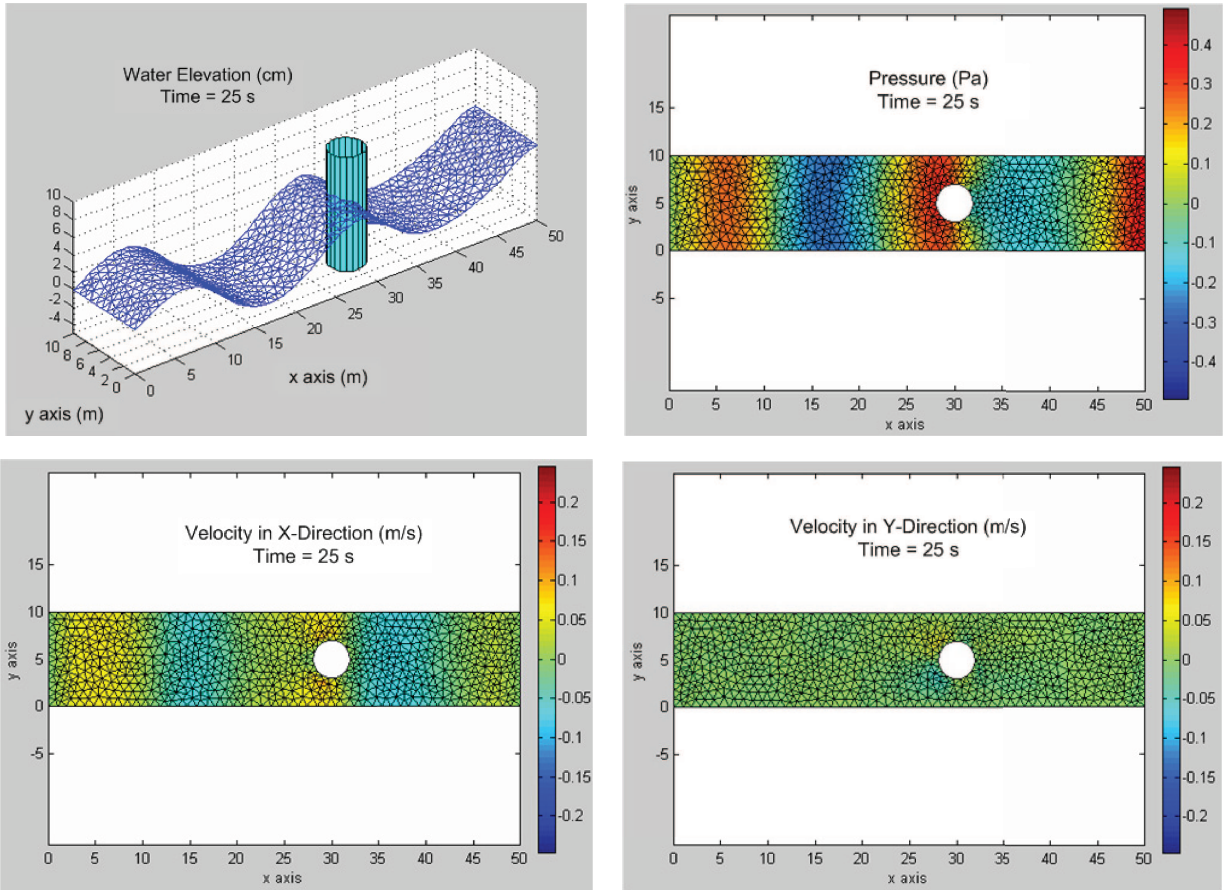


Figure 16. Water elevation, pressure, and velocity of Case 3 at $t = 25$ s.

elevation at the wall is 0.04 m. So in this case, it is shown that the barrier has reduced the maximum water elevation by up to 12.5%.

Figure 16 shows the water elevation as a three-dimensional view, along with water pressure and also velocity in x and y directions. From this figure, we can see that the velocity and pressure propagate in the same manner as the water elevation, which means the higher the water elevation, the higher the velocity and the pressure. The only difference appears at the wall boundary condition. The water elevation and pressure are maximized due to the reflecting wave, but the velocity is zero.

Case 4: Flow in circular channel with constant depth. Tsunami propagation due to an earthquake on the open sea is modeled using a circular channel with a diameter of 50 m and constant depth of 0.5 m, as shown in Figure 17. The land surrounding the sea is modeled by assuming the normal velocity around the channel to be zero. The earthquake is modeled by imposing a sinusoidal wave with amplitude of 0.02 m and period of 10 s in a small circular area with a radius of 1 m in the center of the channel.

Figure 18 represents the water elevation in the middle of the channel ($y = 0$ m) where we can see that the initial bottom deformation of 0.02 m generates an initial wave with amplitude of 0.02 m. The wave

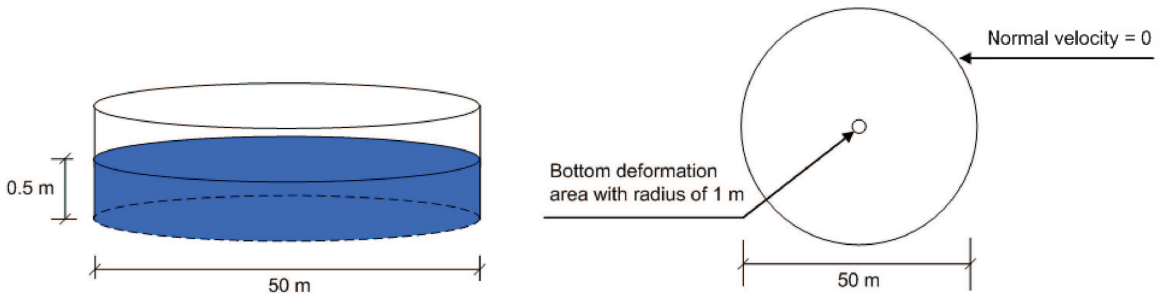


Figure 17. Channel profile of Case 4.

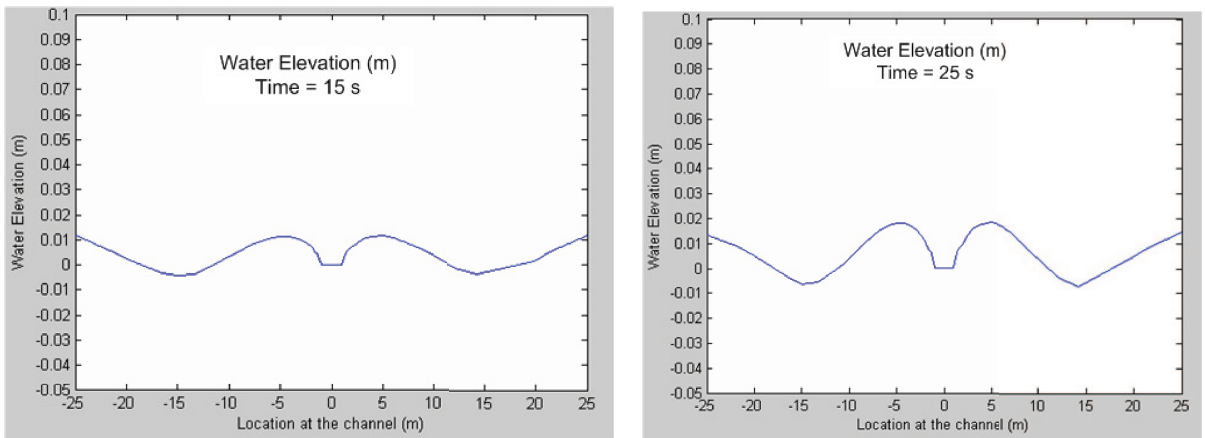


Figure 18. Water elevation of Case 3 in the middle of the channel ($y = 0$ m) at $t = 15$ s and $t = 215$ s.

then propagates symmetrically with a decreased amplitude. When the first wave reaches the wall around the circular channel, the maximum water elevation is only 0.012 m. This means that while propagating out to a radius of 25 m, the wave loses up to 70% of its height, or about 2.8% per meter travelled. Three-dimensional snapshots of the water elevation, pressure, and velocity are shown as Figure 19.

6. Tsunami simulation

In this section, we use the presented finite element method to model the propagation of the December 26, 2004 tsunami. Figure 20 presents the tsunami propagation model in the domain of 10° S – 20° N and 80° E – 100° E.

To be able to perform analysis of real tsunami propagation, appropriate wave sources for tsunamis must be employed. These wave sources will have to be derived from earthquakes that occur in the problem domain. An appropriate wave source model for tsunami propagation problems is still in development. To illustrate the capability of the present finite element model in predicting tsunami wave traveling time, our simulation uses a simple wave source in the form of sinusoidal wave with an amplitude of 1 m and period of 300 seconds.

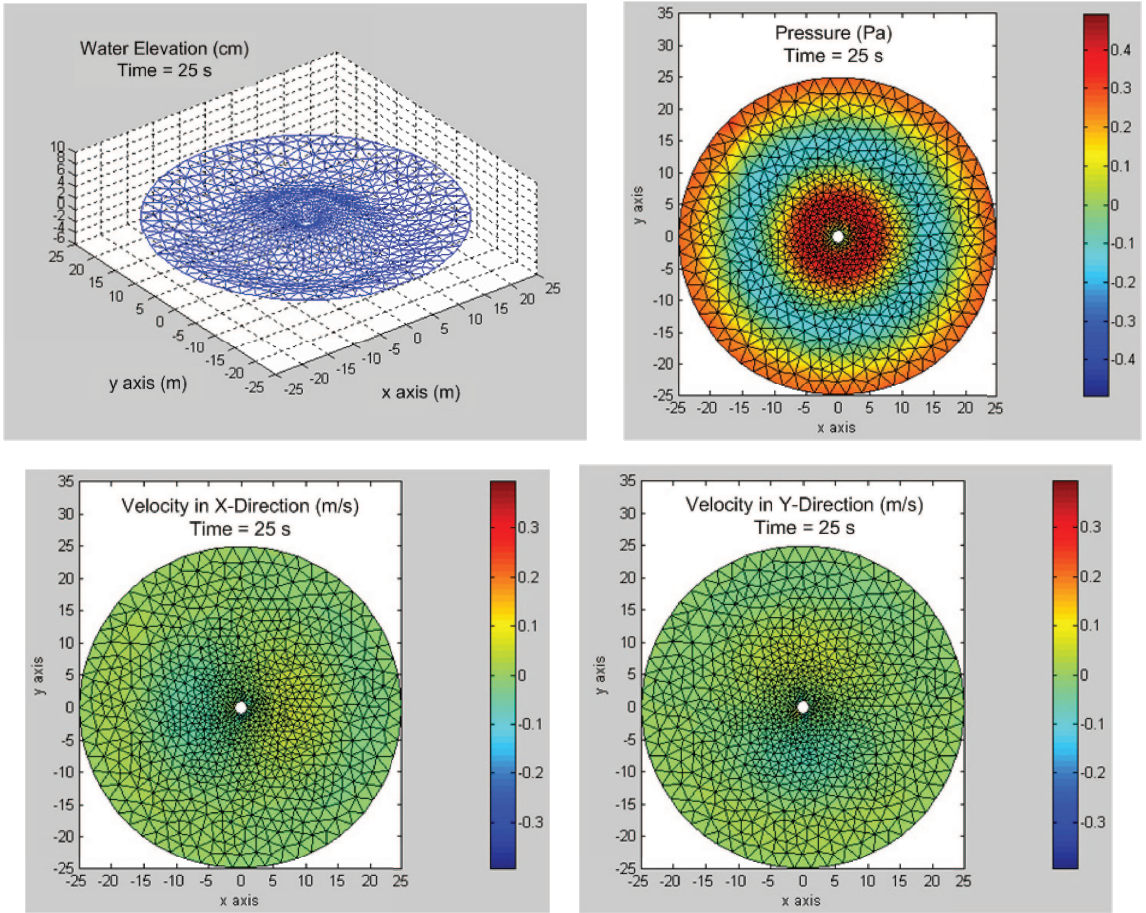


Figure 19. Water elevation, pressure, and velocity of **Case 4** at $t = 25$ s.

Figure 21, left, shows the first simulation, estimating wave speed in deep water. In deep water, tsunami waves move at a speed that is equal to the square root of the product of the acceleration of gravity and the water depth. In the studied domain, with an average water depth of 6000 m, the analytical tsunami wave speed is calculated as 240 m/s. The simulation is conducted up to 6000 seconds with the sinusoidal wave at the left boundary as shown in the same figure. As derived from wave’s ultimate translation, our model estimates a deep water tsunami wave speed of 225 m/s.

The second simulation serves as a tool to predict tsunami wave traveling time to the shoreline. The sinusoidal wave source is excited at the island shown in **Figure 21**, right. From numerical simulation, the time of tsunami wave traveling from the excited island to Phuket area in the figure is 1 hour and 14 minutes. The result is relatively close to the real observation obtained from the December 26, 2004 Tsunami. This important feature of the present model has been implemented in the Tsunami tracking and alert system currently under development at Thailand’s Asian Institute of Technology, School of Engineering and Technology.

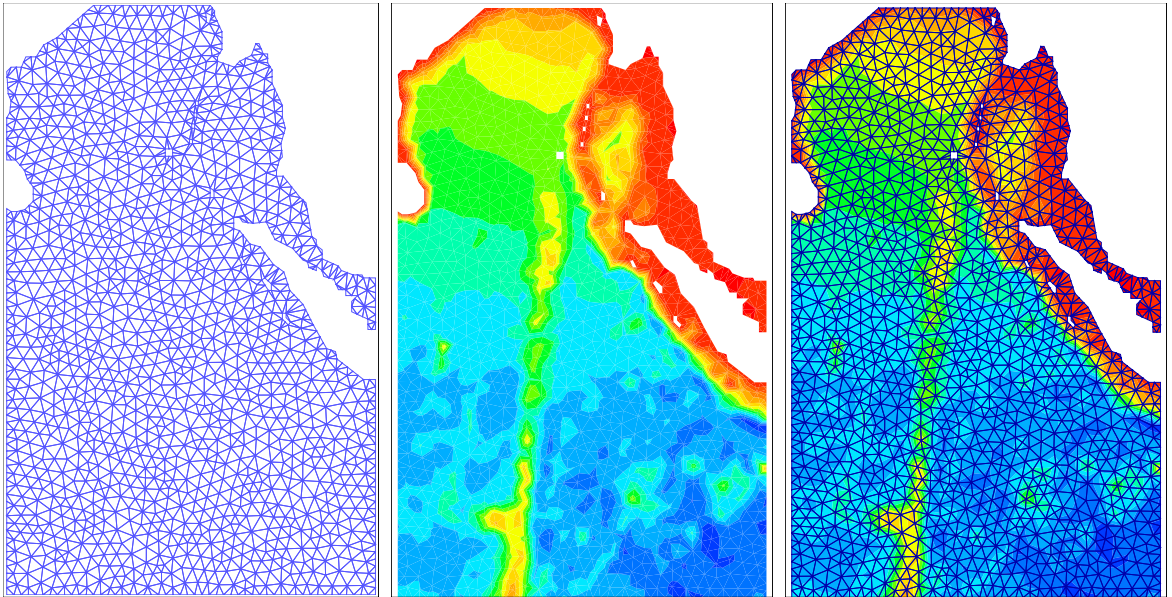


Figure 20. Finite element model for the propagation of the December 26, 2004 tsunami. Left: mesh created for the domain; middle: bathymetry data; right: composite of both.

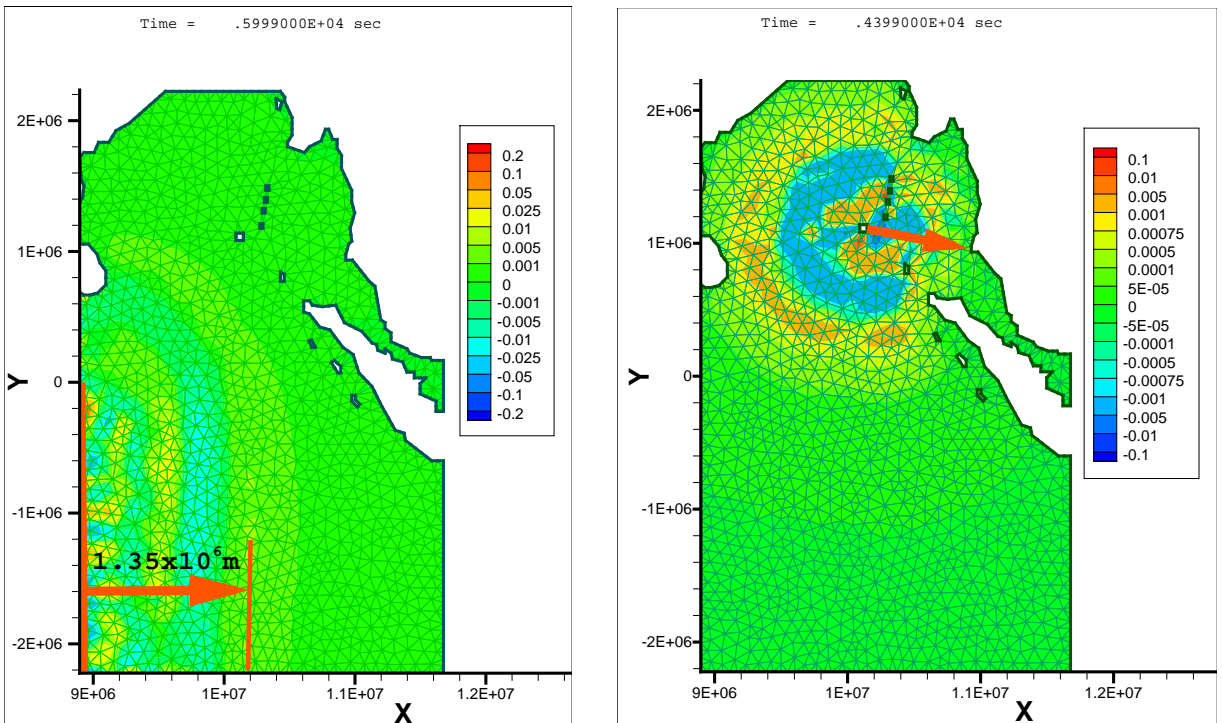


Figure 21. Estimating wave speed in deep water (left) and traveling time to shoreline (right). Labels are in meters.

7. Conclusions

This paper presented the characteristic-based split as a method for the solution of the shallow water equations. The main advantages of this method are its efficiency and accuracy. The efficiency is obtained from the split procedure, which enables us to solve some equations explicitly. From the numerical results in [Case 2](#), it is shown that the CBS solution is very accurate, giving results closer to the experimental data than those given by the standard Galerkin method. The numerical model can also be used to model tsunami propagation passing a solid barrier, as shown in [Case 3](#), and tsunami propagation due to an earthquake on the open sea, as shown in [Case 4](#). Using these case studies, we showed the method's facility in modeling the characteristics of real tsunami propagation, namely that water elevation increases as a tsunami enters shallower areas, and that, in general, the higher the water elevation, the higher the water velocity and pressure. The exception to this correspondence between water velocity and water elevation appears at the wall boundary, where the water elevation doubles and the wave is reflected from the wall with zero velocity. Finally, the propagation of the December 26, 2004 tsunami is modeled using the CBS method. The numerical simulation gives relatively close results compared to actual data from the event. However, this correspondence is limited due to the lack of an appropriate wave source. The result using an arbitrary wave source is designed to illustrate the capability of the model, and motivate its use when appropriate wave sources can be supplied. This analysis of a truly real tsunami will be addressed in a future paper, after the development of a wave source model for tsunami propagation is complete.

Acknowledgement

The authors acknowledge the advice of R. L. Taylor and P. Nithiarasu on the coding of the CBS algorithm.

References

- [Cheng and Kawahara 1991] J. Y. Cheng and M. Kawahara, "Finite element method for shallow water wave analysis", pp. 1679–1683 in *Computational mechanics: Proceedings of the Asian Pacific Conference on Computational Mechanics* (Hong Kong, 1991), vol. 2, edited by Y. K. Cheung et al., Balkema, Rotterdam, 1991.
- [Gill 1982] A. E. Gill, *Atmosphere-ocean dynamics*, Academic Press, 1982.
- [Groen and Groves 1962] P. Groen and G. W. Groves, "Surges", pp. 611–646 in *The sea*, vol. I, edited by M. N. Hill, Interscience, 1962.
- [Grotkop 1973] G. Grotkop, "Finite element analysis of long-period water waves", *Comput. Methods Appl. Mech. Eng.* **2:2** (1973), 147–157.
- [Heaps 1967] N. S. Heaps, "Storm surges oceanography and marine biology", *Oceanogr. Mar. Biol.* **5** (1967), 11–47.
- [Houston 1978] J. R. Houston, "Interaction of tsunamis with the Hawaiian islands calculated by a finite-element numerical model", *J. Phys. Oceanogr.* **8:1** (1978), 93–102.
- [Imamura 1996] F. Imamura, "Review of tsunami simulation with a finite difference method", pp. 25–42 in *Long-wave runup models* (Friday Harbor, WA, 1995), edited by H. Yeh et al., World Scientific, Singapore, 1996.
- [Kawahara et al. 1978] M. Kawahara, N. Takeuchi, and T. Yoshida, "Two step explicit finite element method for tsunami wave propagation analysis", *Int. J. Numer. Methods Eng.* **12:2** (1978), 331–351.
- [Le Méhauté 1976] B. Le Méhauté, *An introduction to hydrodynamics and water waves*, Springer, New York, 1976. [MR 57 #11286](#)
- [Mader 2004] C. L. Mader, *Numerical modelling of water waves*, 2nd ed., CRC Press, Boca Raton, FL, 2004.

- [Malone and Kuo 1981] F. D. Malone and J. T. Kuo, “Semi-implicit finite element methods applied to the solution of the shallow water equations”, *J. Geophys. Res.* **86**:C5 (1981), 4029–4040.
- [Nithiarasu et al. 2004] P. Nithiarasu, J. S. Mathur, N. P. Weatherill, and K. Morgan, “Three-dimensional incompressible flow calculations using the characteristic based split (CBS) scheme”, *Int. J. Numer. Methods Fluids* **44**:11 (2004), 1207–1229. MR 2043786
- [Ortiz et al. 2004] P. Ortiz, O. C. Zienkiewicz, and J. Szmelter, “CBS finite element modelling of shallow water and transport problems”, in *European Congress on Computational Methods in Applied Sciences and Engineering* (Jyväskylä, 2004), edited by P. Neittaanmäki et al., University of Jyväskylä, Jyväskylä, 2004.
- [Peraire et al. 1986] J. Peraire, O. C. Zienkiewicz, and K. Morgan, “Shallow water problems: A general explicit formulation”, *Int. J. Numer. Methods Eng.* **22**:3 (1986), 547–574. MR 87e:76029
- [Sklarz et al. 1979] M. A. Sklarz, L. Q. Spielvogel, and H. G. Loomis, “Numerical simulation of the 29 November 1975 island of Hawaii tsunami by the finite-element method”, *J. Phys. Oceanogr.* **9**:5 (1979), 1022–1031.
- [Wei and Kirby 1995] G. Wei and J. T. Kirby, “Time-dependent numerical code for extended Boussinesq equations”, *J. Waterw. Port C. (ASCE)* **121**:5 (1995), 251–261.
- [Zienkiewicz and Codina 1995] O. C. Zienkiewicz and R. Codina, “A general algorithm for compressible and incompressible flow, I: The split, characteristic-based scheme”, *Int. J. Numer. Methods Fluids* **20**:8–9 (1995), 869–885. MR 96d:76060a
- [Zienkiewicz et al. 1999] O. C. Zienkiewicz, P. Nithiarasu, R. Codina, M. Vázquez, and P. Ortiz, “The characteristic-based-split procedure: An efficient and accurate algorithm for fluid problems”, *Int. J. Numer. Methods Fluids* **31**:1 (1999), 359–392. MR 2000g:76084

Received 15 Jun 2007. Revised 19 Feb 2008. Accepted 21 Feb 2008.

GUNAWAN BUDI WIJAYA: gunawan_sipil@yahoo.co.uk

School of Engineering and Technology, Asian Institute of Technology, P.O. Box 4 Klong Luang, Pathumthani 12120, Thailand

TAM THANH BUI: loantam@ait.ac.th

School of Engineering and Technology, Asian Institute of Technology, P.O. Box 4 Klong Luang, Pathumthani 12120, Thailand

WORSAK KANOK-NUKULCHAI: worsak@ait.ac.th

School of Engineering and Technology, Asian Institute of Technology, P.O. Box 4 Klong Luang, Pathumthani 12120, Thailand

WAVE PROPAGATION IN A PRESTRESSED COMPRESSIBLE ELASTIC LAYER WITH CONSTRAINED BOUNDARIES

ANIL C. WIJEYEWICKREMA, YOSUKE USHIDA AND PRIZA KAYESTHA

The dynamic motion of a prestressed *compressible* elastic layer having constrained boundaries is considered. The dispersion relations which relate wave speed and wave number are obtained for both symmetric and antisymmetric motions. Both motions can be considered by formulating the incremental boundary-value problem based on the theory of incremental elastic deformations, and using the propagator matrix technique. The limiting phase speed at the low wave number limit of symmetric and antisymmetric waves is obtained. At the low wave number limit, depending on the prestress, for symmetric motion with slipping boundaries and for antisymmetric motion with vertically unconstrained boundaries, a finite phase speed may exist for the fundamental mode. Numerical results are presented for a Blatz–Ko material. The effects of the constrained boundaries are clearly seen in the dispersion curves.

1. Introduction

In general, wave propagation in prestressed *incompressible* elastic media has been studied before the analysis of waves in prestressed *compressible* elastic media. Surface wave propagation in an incompressible elastic half-space was studied in [Dowaikh and Ogden 1990] and the corresponding problem for a compressible elastic half-space was considered in [Dowaikh and Ogden 1991b]. Interfacial wave propagation in two joined incompressible elastic half-spaces was analyzed in [Dowaikh and Ogden 1991a] and the problem of compressible elastic half-spaces was considered in [Sotiropoulos 1998]. Vibration and stability analysis of a prestressed elastic layer was reported in [Ogden and Roxburgh 1993] for incompressible elastic materials and in [Roxburgh and Ogden 1994] for compressible elastic materials. Guided waves in a layered half-space were studied in [Ogden and Sotiropoulos 1995; 1996] for incompressible and compressible materials, respectively. Analyses of waves in an elastic layer bonded to two half-spaces were conducted in [Sotiropoulos and Sifniotopoulos 1995] for incompressible elastic materials and in [Sotiropoulos 2000] for compressible elastic materials. Propagation and reflection of plane waves in an incompressible elastic half-space has been considered in [Ogden and Sotiropoulos 1997], while the corresponding compressible elastic half-space problem has been reported in [Ogden and Sotiropoulos 1998].

The dispersive behavior of time harmonic in-plane waves in a prestressed *incompressible* symmetric layered composite with imperfect interface conditions has been analyzed for symmetric waves in [Leungvichcharoen and Wijeyewickrema 2003] and for antisymmetric waves in [Leungvichcharoen et al. 2004]. The corresponding problems for the perfectly bonded interface case were analyzed by [Rogerson and Sandiford 1997; 2000]. In the present paper, the effect of constrained boundaries on both symmetric

Keywords: wave propagation, prestress, dispersion curves, nonlinear elasticity.

and antisymmetric time harmonic plane waves in a prestressed *compressible* symmetric elastic layer are considered.

The basic equations of infinitesimal time harmonic wave propagation in prestressed, compressible, elastic media are given in Section 2. Using the propagator matrix, the dispersion relations for symmetric and antisymmetric motions are obtained in Section 3. The dispersion relation is analyzed in Section 4 and numerical results using Blatz–Ko material are presented in Section 5.

2. Basic equations

The equations for infinitesimal time-harmonic wave propagation in prestressed compressible elastic media are given in this section [Roxburgh and Ogden 1994; Ogden and Sotiropoulos 1998]. Consider a homogeneous, compressible, isotropic elastic body with an initial unstressed state \mathfrak{B}_u , which after being subjected to pure homogeneous strains has the new configuration \mathfrak{B}_e , the prestressed equilibrium state. A Cartesian coordinate system $Ox_1x_2x_3$, with axes coincident with the principal axes of strain is chosen for configuration \mathfrak{B}_e . Let \mathbf{u} be a small, time dependent displacement superimposed on \mathfrak{B}_e . For the plane strain incremental problem considered here, the nonzero displacement components u_1 and u_2 are independent of x_3 . The incremental equations of motion can be expressed as

$$\alpha_{11}u_{1,11} + \gamma_2u_{1,22} + \delta u_{2,12} = \rho\ddot{u}_1, \quad \gamma_1u_{2,11} + \alpha_{22}u_{2,22} + \delta u_{1,12} = \rho\ddot{u}_2, \tag{1}$$

where ρ is the current material density, the superimposed dot and comma indicate differentiation with respect to time t and the spatial coordinate component in \mathfrak{B}_e , respectively, and $\alpha_{ij} = \mathcal{A}_{0iij}$ ($i = 1, 2$), $\gamma_1 = \mathcal{A}_{01212}$, $\gamma_2 = \mathcal{A}_{02121}$, $\delta = \alpha_{12} + \gamma_2 - \sigma_2 = \alpha_{12} + \gamma_1 - \sigma_1$, in which \mathcal{A}_{0ijkl} are the components of the fourth-order tensor of first-order instantaneous moduli of isotropic elastic material which relates the nominal stress increment tensor and the deformation gradient increment tensor and σ_i are the principal Cauchy stress in x_i -direction. The instantaneous elastic moduli α_{ij} , γ_i and the principal Cauchy stress σ_i can be expressed in terms of the strain energy function W per unit reference volume and principal stretches λ_i as in [Ogden and Sotiropoulos 1998]:

$$J\alpha_{ij} = \lambda_i\lambda_jW_{ij}, \quad J\gamma_i = \frac{\lambda_1W_1 - \lambda_2W_2}{\lambda_1^2 - \lambda_2^2}\lambda_i^2, \quad J\sigma_1 = \lambda_1W_1, \quad J\sigma_2 = \lambda_2W_2, \tag{2}$$

where $W_i = \partial W/\partial\lambda_i$, $W_{ij} = \partial^2 W/\partial\lambda_i\partial\lambda_j$ ($i, j = 1, 2$) and $J = \lambda_1\lambda_2\lambda_3$. Note that the properties $\alpha_{12} = \alpha_{21}$ and $\gamma_1 - \sigma_1 = \gamma_2 - \sigma_2$ have been used in obtaining (1). In the case of equibiaxial deformation when $\lambda_1 = \lambda_2$, (2) reduces to

$$\begin{aligned} J\alpha_{11} = J\alpha_{22} &= \lambda_1^2W_{11}, & J\alpha_{12} &= \lambda_1^2W_{12}, \\ J\gamma_1 = J\gamma_2 &= \frac{1}{2}\lambda_1(\lambda_1W_{11} - \lambda_1W_{12} + W_1), & J\sigma_1 = J\sigma_2 &= \lambda_1W_1, \end{aligned}$$

that is $\alpha_{11} = \alpha_{22} = \alpha_{12} + 2\gamma_2 - \sigma_2$. In addition, in the configuration \mathfrak{B}_u , $\alpha_{11} = \lambda + 2\mu$, $\alpha_{12} = \lambda$, $\gamma_1 = \gamma_2 = \mu$, where λ and μ are the classical Lamé moduli of the material. In the analysis of wave propagation, the strong ellipticity conditions given by [Ogden and Sotiropoulos 1998] are assumed, that is, $\alpha_{ii} > 0$, $\gamma_i > 0$ ($i = 1, 2$), $\beta_c + \sqrt{\alpha_{11}\alpha_{22}\gamma_1\gamma_2} > 0$, where $2\beta_c = \alpha_{11}\alpha_{22} + \gamma_1\gamma_2 - \delta^2$.

The relevant components of the nominal stress increment tensor in the configuration \mathfrak{B}_e can be expressed as

$$\begin{aligned} s_{021}(x_1, x_2, t) &= \gamma_2 u_{1,2} + (\gamma_2 - \sigma_2) u_{2,1}, \\ s_{022}(x_1, x_2, t) &= \alpha_{12} u_{1,1} + \alpha_{22} u_{2,2}. \end{aligned} \tag{3}$$

3. Formulation of problem and dispersion relations

The prestressed isotropic compressible elastic layer with constrained boundaries is shown in Figure 1. The Cartesian coordinate system is chosen such that x_1 and x_2 -axes are coincident with the principal axes, the x_2 -direction is normal to the midplane of the layer, the time harmonic wave propagation is in x_1 -direction and the origin O lies at the midplane of the layer. The thickness of the layer is $2h$. The homogeneous layer has material parameters $\alpha_{11}, \alpha_{12}, \alpha_{22}, \gamma_1, \gamma_2$ and mass density ρ .

The superimposed infinitesimal displacements may be expressed as

$$(u_1, u_2) = (A_1, A_2) e^{\tilde{q} k x_2} e^{i k (x_1 - vt)}, \tag{4}$$

where k is the wave number, v is the phase speed, A_1 and A_2 are arbitrary constants, and the parameter \tilde{q} is to be determined. (This is the notation we use for the compressible case; q and q^* were used in [Leungvicharoen and Wijeyewickrema 2003; Leungvicharoen et al. 2004] for related problems in the incompressible case.)

Substituting (4) into (1) yields a system of homogeneous equations for which a nontrivial solution exists provided that

$$\alpha_{22} \gamma_2 \tilde{q}^4 - (\alpha'_{11} \alpha_{22} + \gamma'_1 \gamma_2 - \delta^2) \tilde{q}^2 + \alpha'_{11} \gamma'_1 = 0, \tag{5}$$

where $\alpha'_{11} = \alpha_{11} - \rho v^2$ and $\gamma'_1 = \gamma_1 - \rho v^2$. Let \tilde{q}_1^2 and \tilde{q}_2^2 be the roots of the quadratic equation (5); then

$$\tilde{q}_1^2 + \tilde{q}_2^2 = \frac{\alpha'_{11} \alpha_{22} + \gamma'_1 \gamma_2 - \delta^2}{\alpha_{22} \gamma_2}, \quad \tilde{q}_1^2 \tilde{q}_2^2 = \frac{\alpha'_{11} \gamma'_1}{\alpha_{22} \gamma_2}.$$

Define the *squared phase speed* as the nondimensional quantity $\xi = \rho v^2 / \gamma_2$, and set

$$\bar{\alpha}_{ij} = \frac{\alpha_{ij}}{\gamma_2} \quad (i, j = 1, 2), \quad \bar{\alpha}'_{11} = \frac{\alpha'_{11}}{\gamma_2}, \quad \bar{\delta} = \frac{\delta}{\gamma_2}, \quad \bar{\gamma}_1 = \frac{\gamma_1}{\gamma_2}, \quad \bar{\sigma}_2 = \frac{\sigma_2}{\gamma_2}. \tag{6}$$

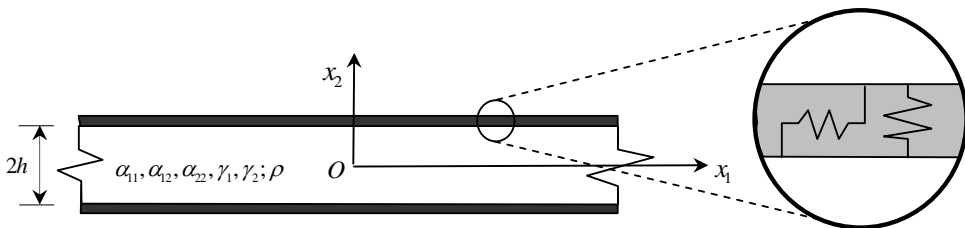


Figure 1. Prestressed compressible elastic layer with constrained boundaries.

To obtain the propagator matrix, the incremental displacements and stresses in (3) and (4) are written in the form of a 4×1 vector as

$$(u_1, u_2, s_{021}, s_{022})^T = [U_1(x_2), U_2(x_2), S_{021}(x_2), S_{022}(x_2)]^T e^{ik(x_1-vt)}. \tag{7}$$

From (7) it can be shown after some manipulation that

$$\mathbf{y}(x_2) = \mathbf{H} \tilde{\mathbf{E}}(x_2) \mathbf{a}, \tag{8}$$

where

$$\mathbf{y}(x_2) = \left[-iU_1(x_2), U_2(x_2), \frac{S_{021}(x_2)}{ik}, \frac{S_{022}(x_2)}{k} \right]^T$$

is the displacement-stress increment vector,

$$\tilde{\mathbf{E}}(x_2) = \text{diag}(e^{\tilde{q}_1 k x_2}, e^{-\tilde{q}_1 k x_2}, e^{\tilde{q}_2 k x_2}, e^{-\tilde{q}_2 k x_2}),$$

is a diagonal matrix,

$$\mathbf{a} = \left[\frac{iA_1^{(1)}}{\tilde{q}_1 \bar{\delta}}, \frac{-iA_1^{(2)}}{\tilde{q}_1 \bar{\delta}}, \frac{iA_1^{(3)}}{\tilde{q}_2 \bar{\delta}}, \frac{-iA_1^{(4)}}{\tilde{q}_2 \bar{\delta}} \right]^T$$

is a vector of constants, and \mathbf{H} is a 4×4 matrix independent of x_2 and defined by

$$\mathbf{H} = \begin{bmatrix} -\tilde{q}_1 \bar{\delta} & \tilde{q}_1 \bar{\delta} & -\tilde{q}_2 \bar{\delta} & \tilde{q}_2 \bar{\delta} \\ \tilde{f}(\tilde{q}_1) & \tilde{f}(\tilde{q}_1) & \tilde{f}(\tilde{q}_2) & \tilde{f}(\tilde{q}_2) \\ -\gamma_2 \tilde{f}(\tilde{q}_1) \tilde{g}(\tilde{q}_2) / \bar{\delta} & -\gamma_2 \tilde{f}(\tilde{q}_1) \tilde{g}(\tilde{q}_2) / \bar{\delta} & -\gamma_2 \tilde{f}(\tilde{q}_2) \tilde{g}(\tilde{q}_1) / \bar{\delta} & -\gamma_2 \tilde{f}(\tilde{q}_2) \tilde{g}(\tilde{q}_1) / \bar{\delta} \\ \gamma_2 \tilde{q}_1 \tilde{g}(\tilde{q}_1) & -\gamma_2 \tilde{q}_1 \tilde{g}(\tilde{q}_1) & \gamma_2 \tilde{q}_2 \tilde{g}(\tilde{q}_2) & -\gamma_2 \tilde{q}_2 \tilde{g}(\tilde{q}_2); \end{bmatrix}$$

with

$$\tilde{f}(\tilde{q}_m) = \tilde{q}_m^2 - \bar{\alpha}'_{11}, \quad \tilde{g}(\tilde{q}_m) = \bar{\alpha}_{22} \tilde{f}(\tilde{q}_m) + \bar{\delta} \bar{\alpha}_{12} \quad (m = 1, 2). \tag{9}$$

The vector \mathbf{a} is eliminated from (8) by introducing the vector $\mathbf{y}(\bar{x}_2)$ at an arbitrary location $x_2 = \bar{x}_2$ and finally obtain the expression

$$\mathbf{y}(x_2) = \mathbf{H} \tilde{\mathbf{E}}(x_2 - \bar{x}_2) \mathbf{H}^{-1} \mathbf{y}(\bar{x}_2) = \mathbf{P}(x_2 - \bar{x}_2) \mathbf{y}(\bar{x}_2). \tag{10}$$

involving the propagator matrix \mathbf{P} , whose entries are given by

$$\begin{aligned} P_{11} &= P_{33} = \tilde{q}_1 \tilde{q}_2 \bar{\delta}^2 \tilde{f}(\tilde{q}_1) \tilde{f}(\tilde{q}_2) [\tilde{g}(\tilde{q}_1) \tilde{C}_2 - \tilde{g}(\tilde{q}_2) \tilde{C}_1] \tilde{\kappa}^{-1}, \\ P_{12} &= \tilde{q}_1 \tilde{q}_2 \bar{\delta}^3 [\tilde{q}_2 \tilde{f}(\tilde{q}_1) \tilde{g}(\tilde{q}_2) \tilde{S}_2 - \tilde{q}_1 \tilde{f}(\tilde{q}_2) \tilde{g}(\tilde{q}_1) \tilde{S}_1] \tilde{\kappa}^{-1}, \\ P_{13} &= \tilde{q}_1 \tilde{q}_2 \bar{\delta}^4 [\tilde{q}_2 \tilde{f}(\tilde{q}_1) \tilde{S}_2 - \tilde{q}_1 \tilde{f}(\tilde{q}_2) \tilde{S}_1] (\gamma_2 \tilde{\kappa})^{-1}, \\ P_{14} &= -P_{23} = \tilde{q}_1 \tilde{q}_2 \bar{\delta}^3 \tilde{f}(\tilde{q}_1) \tilde{f}(\tilde{q}_2) [\tilde{C}_2 - \tilde{C}_1] (\gamma_2 \tilde{\kappa})^{-1}, \\ P_{21} &= -P_{34} = \bar{\delta} \tilde{f}(\tilde{q}_1) \tilde{f}(\tilde{q}_2) [\tilde{q}_2 \tilde{f}(\tilde{q}_1) \tilde{g}(\tilde{q}_2) \tilde{S}_1 - \tilde{q}_1 \tilde{f}(\tilde{q}_2) \tilde{g}(\tilde{q}_1) \tilde{S}_2] \tilde{\kappa}^{-1}, \\ P_{22} &= P_{44} = \tilde{q}_1 \tilde{q}_2 \bar{\delta}^2 \tilde{f}(\tilde{q}_1) \tilde{f}(\tilde{q}_2) [\tilde{g}(\tilde{q}_1) \tilde{C}_1 - \tilde{g}(\tilde{q}_2) \tilde{C}_2] \tilde{\kappa}^{-1}, \\ P_{24} &= \bar{\delta}^2 \tilde{f}(\tilde{q}_1) \tilde{f}(\tilde{q}_2) [\tilde{q}_2 \tilde{f}(\tilde{q}_1) \tilde{S}_1 - \tilde{q}_1 \tilde{f}(\tilde{q}_2) \tilde{S}_2] (\gamma_2 \tilde{\kappa})^{-1}, \end{aligned}$$

$$\begin{aligned}
 P_{31} &= \gamma_2 \tilde{f}(\tilde{q}_1) \tilde{f}(\tilde{q}_2) [\tilde{q}_1 \tilde{f}(\tilde{q}_2) \tilde{g}(\tilde{q}_1)^2 \tilde{S}_2 - \tilde{q}_2 \tilde{f}(\tilde{q}_1) \tilde{g}(\tilde{q}_2)^2 \tilde{S}_1] \tilde{\kappa}^{-1}, \\
 P_{32} &= -P_{41} = \gamma_2 \tilde{q}_1 \tilde{q}_2 \delta \tilde{f}(\tilde{q}_1) \tilde{f}(\tilde{q}_2) \tilde{g}(\tilde{q}_1) \tilde{g}(\tilde{q}_2) [\tilde{C}_2 - \tilde{C}_1] \tilde{\kappa}^{-1}, \\
 P_{42} &= \gamma_2 \tilde{q}_1 \tilde{q}_2 \delta^2 [\tilde{q}_1 \tilde{f}(\tilde{q}_2) \tilde{g}(\tilde{q}_1)^2 \tilde{S}_1 - \tilde{q}_2 \tilde{f}(\tilde{q}_1) \tilde{g}(\tilde{q}_2)^2 \tilde{S}_2] \tilde{\kappa}^{-1}, \\
 P_{43} &= \tilde{q}_1 \tilde{q}_2 \delta^3 [\tilde{q}_1 \tilde{f}(\tilde{q}_2) \tilde{g}(\tilde{q}_1) \tilde{S}_1 - \tilde{q}_2 \tilde{f}(\tilde{q}_1) \tilde{g}(\tilde{q}_2) \tilde{S}_2] \tilde{\kappa}^{-1},
 \end{aligned}$$

where

$$\begin{aligned}
 \tilde{S}_m &= \sinh[\tilde{q}_m kh], \quad \tilde{C}_m = \cosh[\tilde{q}_m kh] \quad (m = 1, 2), \\
 \tilde{\kappa} &= \tilde{q}_1 \tilde{q}_2 \delta^2 \tilde{f}(\tilde{q}_1) \tilde{f}(\tilde{q}_2) [\tilde{g}(\tilde{q}_1) - \tilde{g}(\tilde{q}_2)].
 \end{aligned} \tag{11}$$

For in-plane wave propagation in the x_1 -direction, since the wave motion can be decoupled into symmetric and antisymmetric modes, it is convenient to analyze the *symmetric* and *antisymmetric* waves separately, and it is sufficient to consider only the upper half of the layer ($0 \leq x_2 \leq h$).

The midplane conditions for symmetric and antisymmetric waves can be written as

$$\text{symmetric waves: } U_2(0) = S_{021}(0) = 0, \tag{12}$$

$$\text{antisymmetric waves: } U_1(0) = S_{022}(0) = 0. \tag{13}$$

At the boundary ($x_2 = h$), the shear stress increment is assumed to be proportional to the displacement increment in the x_1 -direction and the normal stress increment is assumed to be proportional to the displacement increment in the x_2 -direction, that is,

$$S_{021}(h) = \frac{k_1 \gamma_2}{h} U_1(h), \quad S_{022}(h) = \frac{k_2 \gamma_2}{h} U_2(h), \tag{14}$$

where k_1, k_2 are the nondimensional spring parameters.

Substituting the boundary conditions (14) and the midplane conditions, (12), into (10) with $x_2 = h$ and $\tilde{x}_2 = 0$, the dispersion relation for symmetric waves in a layer with constrained boundaries is obtained as

$$\begin{aligned}
 \{P_{31} P_{44} - P_{34} P_{41}\} + \frac{\gamma_2 k_1}{kh} \{P_{11} P_{44} - P_{14} P_{41}\} \\
 + \frac{\gamma_2 k_2}{kh} \{P_{31} P_{24} - P_{34} P_{21}\} + \frac{\gamma_2 k_1}{kh} \frac{\gamma_2 k_2}{kh} \{P_{11} P_{24} - P_{14} P_{21}\} = 0. \tag{15}
 \end{aligned}$$

Similarly the dispersion relation for antisymmetric waves can be obtained as

$$\begin{aligned}
 \{P_{32} P_{43} - P_{33} P_{42}\} + \frac{\gamma_2 k_1}{kh} \{P_{12} P_{43} - P_{13} P_{42}\} \\
 + \frac{\gamma_2 k_2}{kh} \{P_{23} P_{32} - P_{22} P_{33}\} + \frac{\gamma_2 k_1}{kh} \frac{\gamma_2 k_2}{kh} \{P_{12} P_{23} - P_{13} P_{22}\} = 0. \tag{16}
 \end{aligned}$$

For symmetric waves we substitute the elements of $\mathbf{P}(h)$ into (15) and remove the common factor $\gamma_2 \tilde{q}_1 \tilde{q}_2 \delta^2 [\tilde{g}(\tilde{q}_1) - \tilde{g}(\tilde{q}_2)]$ from the denominator. The removal of this common factor leads to spurious roots in the resulting relation

$$\begin{aligned}
 \delta^2 (\tilde{q}_1 \tilde{f}(\tilde{q}_2) \tilde{S}_2 \tilde{C}_1 - \tilde{q}_2 \tilde{f}(\tilde{q}_1) \tilde{S}_1 \tilde{C}_2) + \frac{kh}{k_1} \tilde{f}(\tilde{q}_1) \tilde{f}(\tilde{q}_2) \tilde{S}_1 \tilde{S}_2 (\tilde{g}(\tilde{q}_2) - \tilde{g}(\tilde{q}_1)) \\
 + \frac{kh}{k_2} \delta^2 \tilde{q}_1 \tilde{q}_2 \tilde{C}_1 \tilde{C}_2 (\tilde{g}(\tilde{q}_2) - \tilde{g}(\tilde{q}_1)) + \frac{(kh)^2}{k_1 k_2} (\tilde{q}_2 \tilde{f}(\tilde{q}_1) \tilde{g}(\tilde{q}_2)^2 \tilde{S}_1 \tilde{C}_2 - \tilde{q}_1 \tilde{f}(\tilde{q}_2) \tilde{g}(\tilde{q}_1)^2 \tilde{S}_2 \tilde{C}_1) = 0, \tag{17}
 \end{aligned}$$

where $\tilde{f}(\tilde{q}_m)$ and $\tilde{g}(\tilde{q}_m)$ are defined in (9) and \tilde{C}_m and \tilde{S}_m are defined in (11).

The dispersion relation for antisymmetric waves can be similarly obtained as

$$\begin{aligned} &\delta^2(\tilde{q}_2\tilde{f}(\tilde{q}_1)\tilde{S}_2\tilde{C}_1 - \tilde{q}_1\tilde{f}(\tilde{q}_2)\tilde{S}_1\tilde{C}_2) + \frac{kh}{k_1}\tilde{f}(\tilde{q}_1)\tilde{f}(\tilde{q}_2)\tilde{C}_1\tilde{C}_2(\tilde{g}(\tilde{q}_1) - \tilde{g}(\tilde{q}_2)) \\ &+ \frac{kh}{k_2}\delta^2\tilde{q}_1\tilde{q}_2\tilde{S}_1\tilde{S}_2(\tilde{g}(\tilde{q}_1) - \tilde{g}(\tilde{q}_2)) + \frac{(kh)^2}{k_1k_2}(\tilde{q}_1\tilde{f}(\tilde{q}_2)\tilde{g}(\tilde{q}_1)^2\tilde{S}_1\tilde{C}_2 - \tilde{q}_2\tilde{f}(\tilde{q}_1)\tilde{g}(\tilde{q}_2)^2\tilde{S}_2\tilde{C}_1) = 0, \end{aligned} \tag{18}$$

where the common factor removed from the denominator of (16) after substitution of the components of the propagator matrix is $\gamma_2\tilde{f}(\tilde{q}_1)\tilde{f}(\tilde{q}_2)[\tilde{g}(\tilde{q}_1) - \tilde{g}(\tilde{q}_2)]$.

The dispersion relations for the fixed boundary case and traction free boundary case can be deduced from the dispersion relations for the constrained boundary case.

When $k_1, k_2 \rightarrow \infty$, the dispersion relation for waves propagating in a layer with fixed boundaries is obtained for symmetric waves from (17) as

$$\delta^2(\tilde{q}_1\tilde{f}(\tilde{q}_2)\tilde{S}_2\tilde{C}_1 - \tilde{q}_2\tilde{f}(\tilde{q}_1)\tilde{S}_1\tilde{C}_2) = 0, \tag{19}$$

and for antisymmetric waves propagating from (18) as

$$\delta^2(\tilde{q}_2\tilde{f}(\tilde{q}_1)\tilde{S}_2\tilde{C}_1 - \tilde{q}_1\tilde{f}(\tilde{q}_2)\tilde{S}_1\tilde{C}_2) = 0.$$

When $k_1, k_2 \rightarrow 0$, the dispersion relation for waves propagating in a layer with traction free boundaries is obtained for symmetric waves from (17) as

$$(\tilde{q}_2\tilde{f}(\tilde{q}_1)\tilde{g}(\tilde{q}_2)^2\tilde{S}_1\tilde{C}_2 - \tilde{q}_1\tilde{f}(\tilde{q}_2)\tilde{g}(\tilde{q}_1)^2\tilde{S}_2\tilde{C}_1) = 0, \tag{20}$$

and for antisymmetric waves propagating from (18) as

$$(\tilde{q}_1\tilde{f}(\tilde{q}_2)\tilde{g}(\tilde{q}_1)^2\tilde{S}_1\tilde{C}_2 - \tilde{q}_2\tilde{f}(\tilde{q}_1)\tilde{g}(\tilde{q}_2)^2\tilde{S}_2\tilde{C}_1) = 0. \tag{21}$$

After some manipulation (20) and (21) can be rewritten respectively as

$$\frac{\tanh[kh\tilde{q}_1]}{\tanh[kh\tilde{q}_2]} = \frac{\tilde{q}_1[\bar{\alpha}'_{11}(\gamma'_1 - (1 - \bar{\sigma}_2)^2) - \tilde{q}_2^2(\bar{\alpha}_{12}^2 - \bar{\alpha}'_{11}\bar{\alpha}_{22})]}{\tilde{q}_2[\bar{\alpha}'_{11}(\gamma'_1 - (1 - \bar{\sigma}_2)^2) - \tilde{q}_1^2(\bar{\alpha}_{12}^2 - \bar{\alpha}'_{11}\bar{\alpha}_{22})]}, \tag{22}$$

and

$$\frac{\tanh[kh\tilde{q}_1]}{\tanh[kh\tilde{q}_2]} = \frac{\tilde{q}_2[\bar{\alpha}'_{11}(\gamma'_1 - (1 - \bar{\sigma}_2)^2) - \tilde{q}_1^2(\bar{\alpha}_{12}^2 - \bar{\alpha}'_{11}\bar{\alpha}_{22})]}{\tilde{q}_1[\bar{\alpha}'_{11}(\gamma'_1 - (1 - \bar{\sigma}_2)^2) - \tilde{q}_2^2(\bar{\alpha}_{12}^2 - \bar{\alpha}'_{11}\bar{\alpha}_{22})]}. \tag{23}$$

These agree with [Roxburgh and Ogden 1994, (4.24) and (4.22)].

4. Analysis of dispersion relations

The similarity of the dispersion relation for symmetric and antisymmetric waves shown in Section 3 results in similar behavior for these two kinds of waves, as will be discussed in this section. Equation (5) can be rewritten in nondimensional form as

$$\bar{\alpha}_{22}\tilde{q}^4 - (\bar{\alpha}'_{11}\bar{\alpha}_{22} + \bar{\gamma}'_1 - \bar{\delta}^2)\tilde{q}^2 + \bar{\alpha}'_{11}\bar{\gamma}'_1 = 0, \tag{24}$$

where $\bar{\gamma}'_1 = \gamma'_1/\gamma_2 = \bar{\gamma}_1 - \bar{\zeta}$ in the notation of (6). The roots of the quadratic (24) can be written as

$$\tilde{q}_1^2, \tilde{q}_2^2 = \frac{1}{2\bar{\alpha}_{22}} \left[\bar{\alpha}'_{11}\bar{\alpha}_{22} + \bar{\gamma}'_1 - \bar{\delta}^2 \mp \sqrt{(\bar{\alpha}'_{11}\bar{\alpha}_{22} + \bar{\gamma}'_1 - \bar{\delta}^2)^2 - 4(\bar{\alpha}_{22}\bar{\alpha}'_{11}\bar{\gamma}'_1)} \right]. \tag{25}$$

For symmetric waves, the common factor $\gamma_2\tilde{q}_1\tilde{q}_2\bar{\delta}^2[\tilde{g}(\tilde{q}_1) - \tilde{g}(\tilde{q}_2)]$ taken out from the denominator of (15) leads to spurious roots of (17) given by

$$\begin{aligned} \bar{\zeta} &= \bar{\zeta}_{S1}, & \bar{\zeta}_{S2} &= \bar{\alpha}_{11}, \bar{\gamma}_1, \text{ when } \tilde{q}_1 = 0 \text{ or } \tilde{q}_2 = 0, & \bar{\zeta} &= \bar{\zeta}_{S3}, \\ \bar{\zeta}_{S4} &= \frac{(\bar{\alpha}_{22} - 1)(\bar{\alpha}_{11}\bar{\alpha}_{22} - \bar{\gamma}_1) - \bar{\delta}^2(1 + \bar{\alpha}_{22})}{(\bar{\alpha}_{22} - 1)^2} \pm \frac{2\sqrt{\bar{\alpha}_{22}\bar{\delta}^2[\bar{\delta}^2 - (\bar{\alpha}_{22} - 1)(\bar{\alpha}_{11} - \bar{\gamma}_1)]}}{(\bar{\alpha}_{22} - 1)^2}, \text{ when } \tilde{g}(\tilde{q}_1) = \tilde{g}(\tilde{q}_2). \end{aligned}$$

Similarly for antisymmetric waves the common factor $\gamma_2\tilde{f}(\tilde{q}_1)\tilde{f}(\tilde{q}_2)[\tilde{g}(\tilde{q}_1) - \tilde{g}(\tilde{q}_2)]$ taken out from the denominator of (16) leads to spurious roots of (18) given by

$$\bar{\zeta} = \bar{\zeta}_{S1}, \text{ when } \tilde{f}(\tilde{q}_1)\tilde{f}(\tilde{q}_2) = 0, \quad \bar{\zeta} = \bar{\zeta}_{S3}, \bar{\zeta}_{S4}, \text{ when } \tilde{g}(\tilde{q}_1) = \tilde{g}(\tilde{q}_2).$$

Low wave number limit $kh \rightarrow 0$. When $kh \rightarrow 0$ the thickness of the layer is very small compared to the wavelength. By considering small argument expansions of the hyperbolic functions, the squared phase speeds for symmetric waves for the slipping boundary ($k_1 = 0$) are obtained from (17) as

$$\bar{\zeta}^S = \bar{\alpha}_{11} - \frac{\bar{\alpha}_{12}^2}{k_2 + \bar{\alpha}_{22}}, \tag{26a}$$

and when $k_2 = 0$ or $k_2 = \infty$ the squared phase speeds for (26a) can be obtained as

$$\bar{\zeta}_{00}^S = \bar{\alpha}_{11} - \frac{\bar{\alpha}_{12}^2}{\bar{\alpha}_{22}}, \quad \bar{\zeta}_{0\infty}^S = \bar{\alpha}_{11}. \tag{26b}$$

For antisymmetric waves for the vertically unconstrained boundary ($k_2 = 0$) the limiting squared phase speed as $kh \rightarrow 0$ can be obtained from (18) as

$$\bar{\zeta}^A = \bar{\gamma}_1 - \frac{(1 - \bar{\sigma}_2)^2}{k_1 + 1}, \tag{27a}$$

and when $k_1 = 0$ or $k_1 = \infty$ the squared phase speeds for (27a) can be obtained as

$$\bar{\zeta}_{00}^A = \bar{\gamma}_1 - (1 - \bar{\sigma}_2)^2, \quad \bar{\zeta}_{\infty 0}^A = \bar{\gamma}_1. \tag{27b}$$

Equations (26) and (27) are the finite squared phase speeds of the lowest branches of the dispersion curves, which have frequencies that tend to zero as $kh \rightarrow 0$. The frequencies of higher modes which have infinite squared phase speeds ($\bar{\zeta} \rightarrow \infty$) when $kh \rightarrow 0$ are considered next. When $\bar{\zeta} \rightarrow \infty$ expressions for \tilde{q}_1^2 and \tilde{q}_2^2 can be obtained from (25) as

$$\tilde{q}_1^2 = -1 + \frac{-\bar{\delta}^2 + \bar{\alpha}_{11}(\bar{\alpha}_{22} - 1)}{(\bar{\alpha}_{22} - 1)\bar{\zeta}} + O(\bar{\zeta}^{-2}), \quad \tilde{q}_2^2 = -\frac{1}{\bar{\alpha}_{22}} + \frac{\bar{\delta}^2 + \bar{\gamma}_1(\bar{\alpha}_{22} - 1)}{(\bar{\alpha}_{22} - 1)\bar{\alpha}_{22}\bar{\zeta}} + O(\bar{\zeta}^{-2}). \tag{28}$$

It can be seen that \tilde{q}_1 and \tilde{q}_2 are imaginary when $\bar{\zeta} \rightarrow \infty$. By substituting (28) into (17) and (19), introducing the nondimensional parameter $\Omega = kh\sqrt{\bar{\zeta}}$ and considering small argument expansions of the

hyperbolic functions, the equation for cut-off frequencies of symmetric waves is obtained as

$$\omega_1^S(\Omega_C^{(S)})\omega_2^S(\Omega_C^{(S)}) = 0, \tag{29}$$

where

$$\begin{aligned} \omega_1^S(\Omega_C^{(S)}) &= \left(k_1 \cos(\Omega_C^{(S)}) - \Omega_C^{(S)} \sin(\Omega_C^{(S)})\right), \\ \omega_2^S(\Omega_C^{(S)}) &= \left(k_2 \sin(\Omega_C^{(S)}/\sqrt{\bar{a}_{22}}) + \sqrt{\bar{a}_{22}}\Omega_C^{(S)} \cos(\Omega_C^{(S)}/\sqrt{\bar{a}_{22}})\right). \end{aligned} \tag{30}$$

Similarly for antisymmetric waves, the equation for cut-off frequencies is obtained as,

$$\omega_1^A(\Omega_C^{(A)})\omega_2^A(\Omega_C^{(A)}) = 0, \tag{31}$$

where

$$\begin{aligned} \omega_1^A(\Omega_C^{(A)}) &= \left(k_1 \sin(\Omega_C^{(A)}) + \Omega_C^{(A)} \cos(\Omega_C^{(A)})\right), \\ \omega_2^A(\Omega_C^{(A)}) &= \left(-k_2 \cos(\Omega_C^{(A)}/\sqrt{\bar{a}_{22}}) + \sqrt{\bar{a}_{22}}\Omega_C^{(A)} \sin(\Omega_C^{(A)}/\sqrt{\bar{a}_{22}})\right). \end{aligned} \tag{32}$$

It can be seen that term $\omega_1^S(\Omega_C^{(S)})$ and $\omega_1^A(\Omega_C^{(A)})$ depend only on nondimensional spring parameter k_1 while $\omega_2^S(\Omega_C^{(S)})$ and $\omega_2^A(\Omega_C^{(A)})$ depend on nondimensional parameters \bar{a}_{22} and k_2 .

5. Numerical results

The effects of constrained boundaries on wave propagation in a prestressed compressible elastic layer discussed in the previous sections are illustrated by considering a numerical example in this section. Here compressible material with a Blatz–Ko strain energy function is considered.

The strain energy function $W_c^{(BK)}$ of Blatz–Ko material [Roxburgh and Ogden 1994] is

$$W_c^{(BK)} = \frac{\mu}{2}(\lambda_1^{-2} + \lambda_2^{-2} + \lambda_3^{-2} + 2\lambda_1\lambda_2\lambda_3 - 5),$$

and parameters α_{11} , α_{12} , α_{22} , γ_1 , and γ_2 for this material are

$$\alpha_{11} = \frac{3\mu}{J\lambda_1^2}, \quad \alpha_{12} = \mu, \quad \alpha_{22} = \frac{3\mu}{J\lambda_2^2}, \quad \gamma_1 = \frac{\mu}{J\lambda_2^2}, \quad \gamma_2 = \frac{\mu}{J\lambda_1^2},$$

which yields

$$\bar{\alpha}_{11} = 3, \quad \bar{\alpha}_{12} = J\lambda_1^2, \quad \bar{\alpha}_{22} = \frac{3\lambda_1^2}{\lambda_2^2}, \quad \bar{\gamma}_1 = \frac{\lambda_1^2}{\lambda_2^2}, \tag{33}$$

and the principal Cauchy stresses are

$$\sigma_i = \frac{\mu(\lambda_i^2 J - 1)}{\lambda_i^2 J} \quad (i = 1, 2, 3).$$

The compressible layer is equibiaxially deformed in the (x_1, x_2) -plane, that is, $\lambda_1 = \lambda_2$. The nondimensional parameters prescribed are $\bar{\alpha}_{11} = 3$ (from (33)), $\bar{\alpha}_{12} = 1$, and $\bar{\gamma}_1 = 1$; the computed ones are $\bar{\alpha}_{22} = 3$, $\bar{\sigma}_2 = 0$, and $\bar{\delta} = 2$. The nondimensional squared phase speeds ζ of the fundamental mode and the next ten modes for symmetric and antisymmetric waves ($\zeta_S^{(n)}$, $\zeta_A^{(n)}$, $n = 1, 2, \dots, 11$) are shown, using linear plots as well as log-log plots to clearly show the low wave number limits, in Figures 2 and 3 for

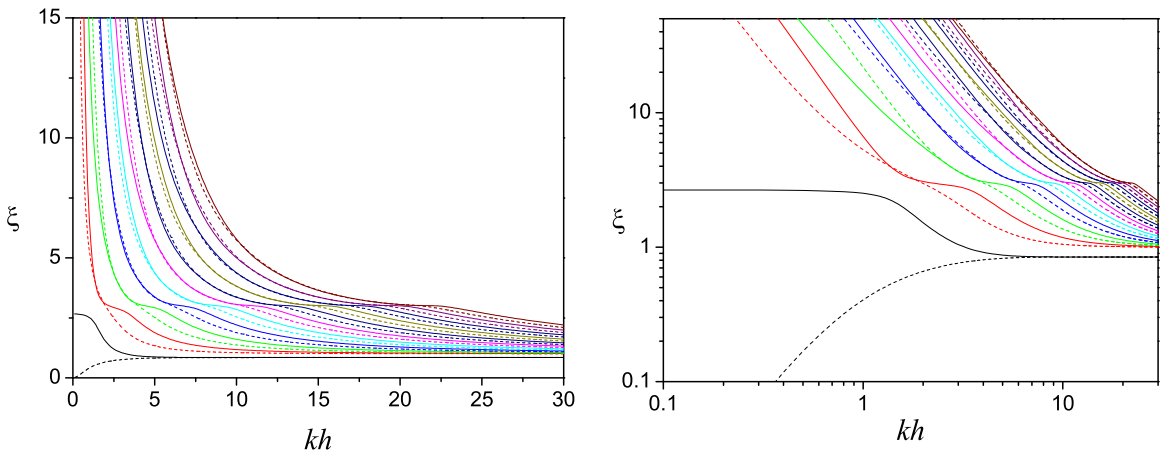


Figure 2. Dispersion curves of the fundamental mode and next ten modes for $k_1 = 0, k_2 = 0$ (traction free boundary). Linear scale plot (left) and logarithmic scale plot (right); solid lines for symmetric waves and dashed lines for antisymmetric waves.

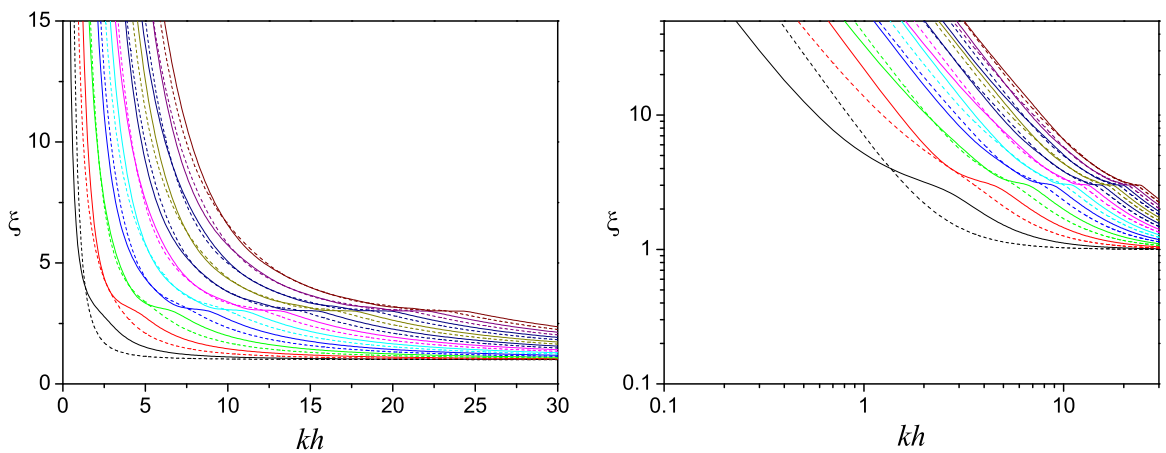


Figure 3. Dispersion curves of the fundamental mode and next ten modes for $k_1 = \infty, k_2 = \infty$ (fixed boundary). Linear scale plot (left) and logarithmic scale plot (right); solid lines for symmetric waves and dashed lines for antisymmetric waves.

the two extreme cases $k_1 = 0, k_2 = 0$ (corresponding to traction free boundaries) and $k_1 = \infty, k_2 = \infty$ (corresponding to fixed boundaries). When $kh \rightarrow 0$, it can be seen from Figure 2 for the traction free case ($k_1 = 0, k_2 = 0$) that the squared phase speed of the fundamental mode for symmetric waves tends to a finite limit, that is, $\xi_S^{(1)} \rightarrow \xi_{00}^S = 2.667$ while the squared phase speed of the fundamental mode of antisymmetric waves $\xi_A^{(1)}$ tends to zero and the other higher modes have infinite squared phase speeds, that is, $\xi_S^{(n)}, \xi_A^{(n)} \rightarrow \infty$ ($n = 2, 3, \dots$). For the fixed boundary case ($k_1 = \infty, k_2 = \infty$) when $kh \rightarrow 0$, it can be seen from Figure 3 that both symmetric and antisymmetric modes have infinite squared phase speeds, that is, $\xi_S^{(n)}, \xi_A^{(n)} \rightarrow \infty$ ($n = 1, 2, \dots$).

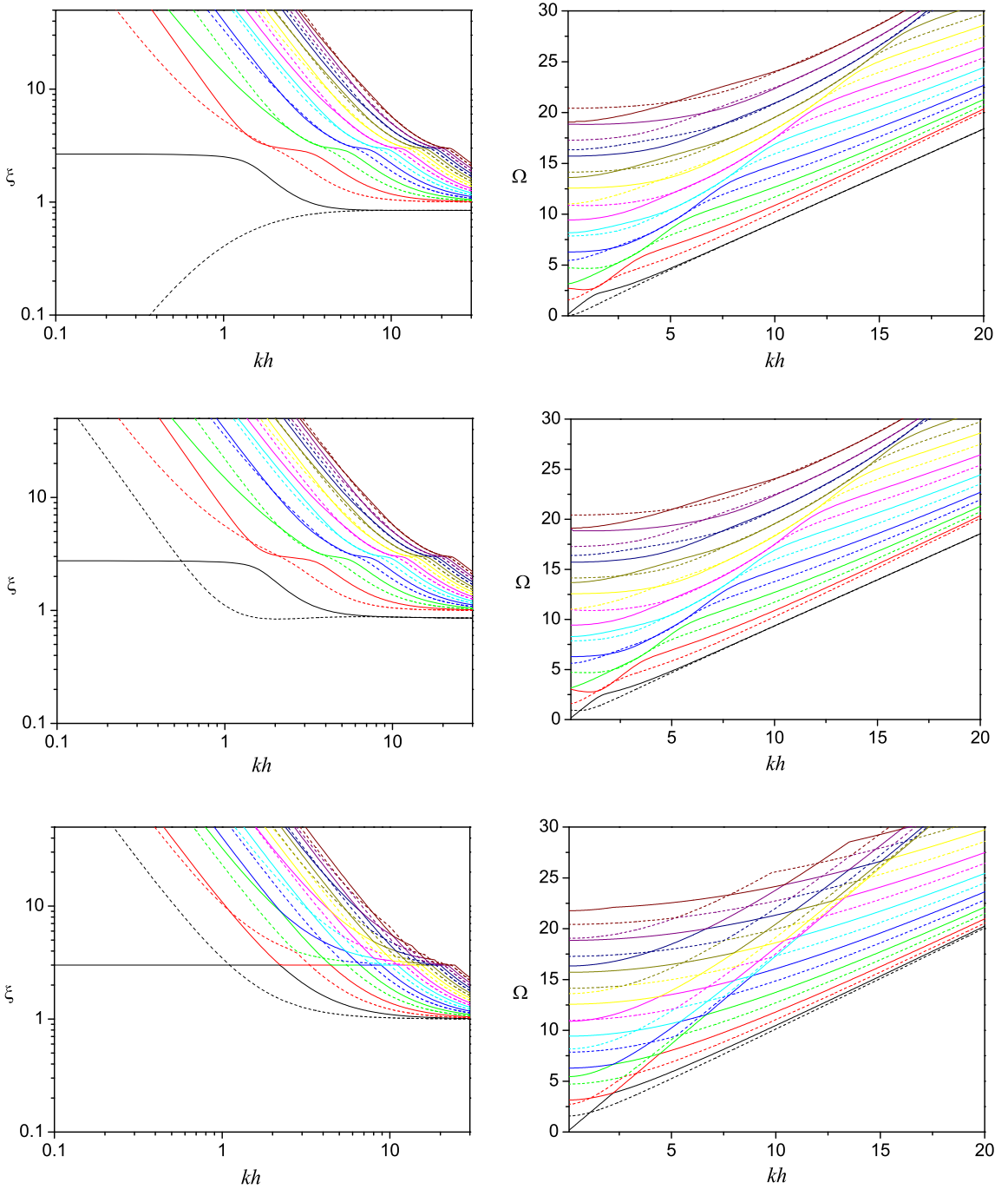


Figure 4. Dispersion curves of the fundamental mode and next ten modes for $k_1 = 0$, $k_2 = 0, 1, \infty$ (slipping boundary). Nondimensional squared phase speed ζ (left column) and nondimensional frequency Ω (right column); solid lines for symmetric waves and dashed lines for antisymmetric waves.

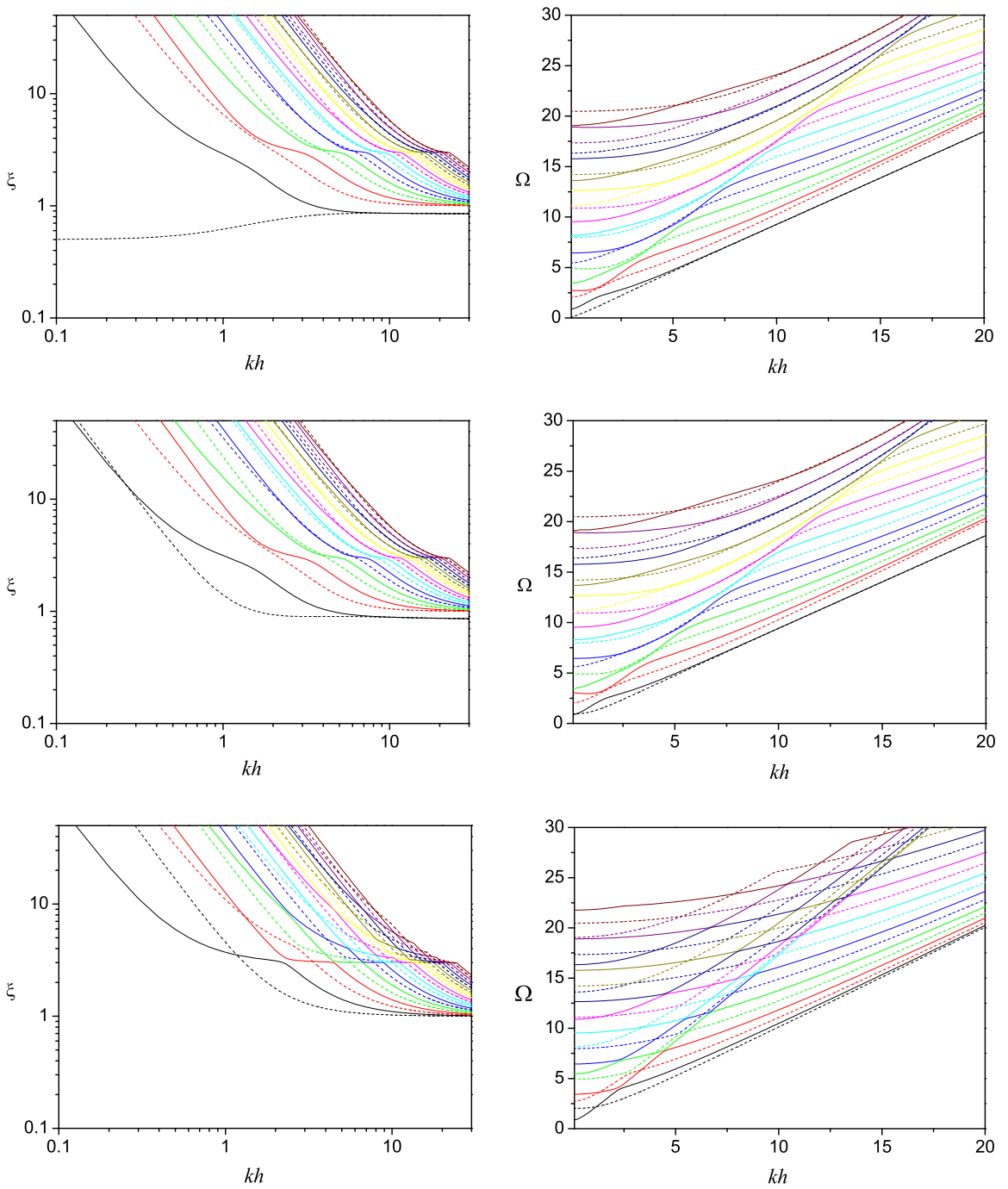


Figure 5. Dispersion curves of the fundamental mode and next ten modes for $k_1 = 1$, $k_2 = 0, 1, \infty$ (partially constrained slipping boundary). Nondimensional squared phase speed ξ (left column) and nondimensional frequency Ω (right column); solid lines for symmetric waves and dashed lines for antisymmetric waves.

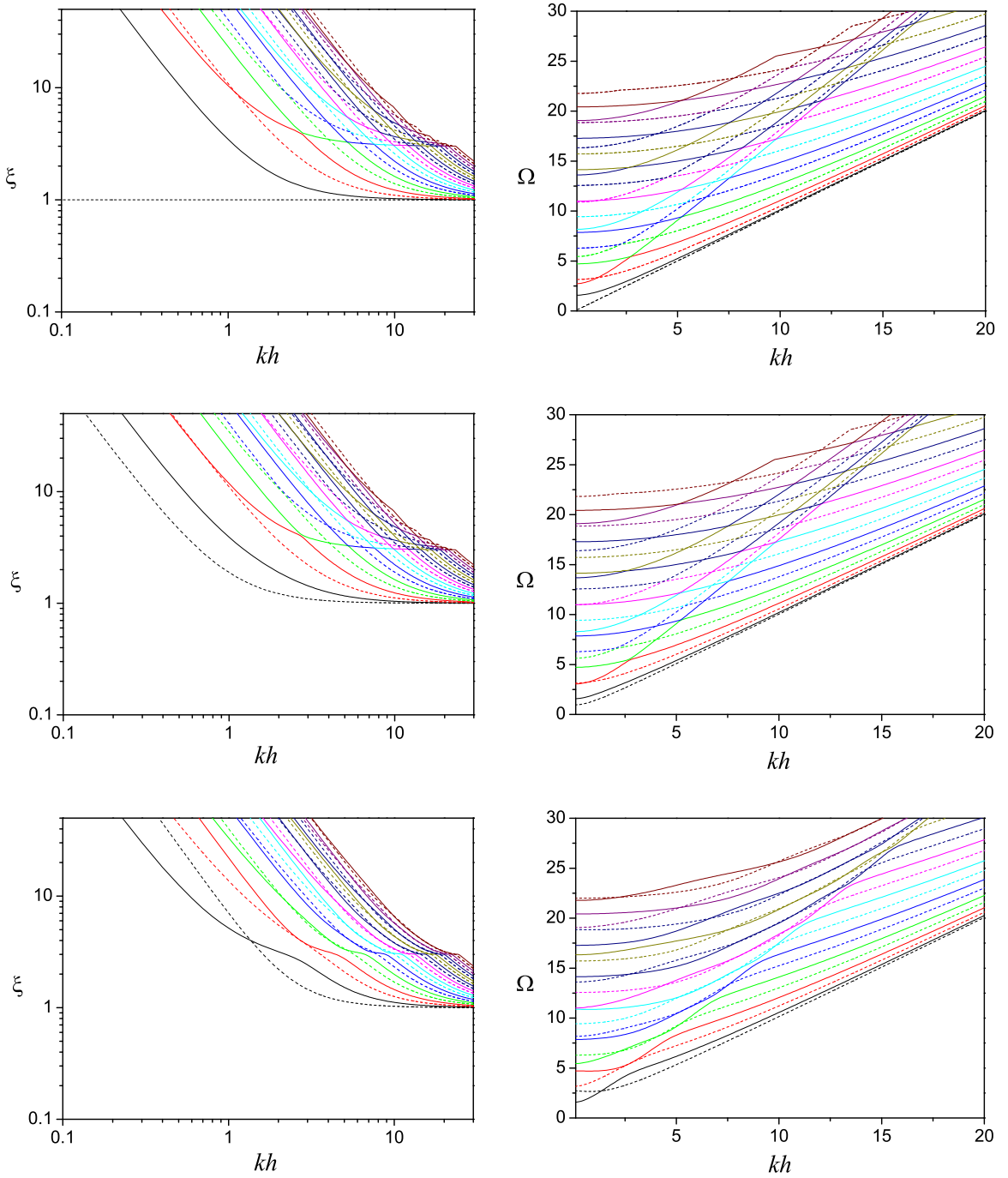


Figure 6. Dispersion curves of the fundamental mode and next ten modes for $k_1 = \infty$, $k_2 = 0, 1, \infty$ (no slip boundary). Nondimensional squared phase speed ζ (left column) and nondimensional frequency Ω (right column); solid lines for symmetric waves and dashed lines for antisymmetric waves.

The effect of the spring parameters k_1 and k_2 are seen in the next three figures. Figure 4 corresponds to a slipping boundary ($k_1 = 0$), Figure 5 to a partially constrained slipping boundary ($k_1 = 1$) and Figure 6 to a no slip boundary ($k_1 = \infty$), for $k_2 = 0, 1, \infty$. From the left column of Figure 4 it can be seen that, when $kh \rightarrow 0$, for the slipping boundary ($k_1 = 0$), the squared phase speed of the fundamental mode for symmetric waves tends to a finite limit, $\zeta_{00}^S = 2.667$, $\zeta_{01}^S = 2.75$, $\zeta_{0\infty}^S = 3.0$, while the fundamental mode for antisymmetric waves $\zeta_A^{(1)}$ tends to zero for $k_2 = 0$ but has infinite squared phase speeds for $k_2 = 1, \infty$. For the partially constrained slipping boundary ($k_1 = 1$), when $kh \rightarrow 0$, it can be seen from the left column of Figure 5 that the fundamental mode for antisymmetric waves $\zeta_A^{(1)}$ tends to a finite limit, meaning $\zeta_A^{(1)} \rightarrow \zeta_{10}^A = 0.5$, for $k_2 = 0$, while the fundamental mode for symmetric waves $\zeta_S^{(1)}$ and the other higher modes have infinite squared phase speeds, that is, $\zeta_S^{(n)}, \zeta_A^{(n)} \rightarrow \infty$ ($n = 2, 3, \dots$). For the no slip boundary ($k_1 = \infty$), when $kh \rightarrow 0$, it can be seen from the left column of Figure 6 that the behavior of the different modes are similar to the partially constrained slipping boundary case, the fundamental mode for antisymmetric waves $\zeta_A^{(1)}$ tends to a finite limit, that is, $\zeta_A^{(1)} \rightarrow \zeta_{\infty 0}^A = 1$ for $k_2 = 0$. From the right columns in Figures 4, 5, and 6, it can be seen that the modes that have finite limiting phase speeds when $kh \rightarrow 0$, have frequencies that tend to zero. The frequencies of the other modes tend to the cut-off frequencies calculated from (29)–(32).

6. Summary and conclusions

In the present analysis, the dispersive behavior of in-plane time harmonic waves in a prestressed compressible layer with constrained boundaries is considered. The dispersion relations for both symmetric and antisymmetric waves are obtained. From the asymptotic analysis of the dispersion relations the limiting squared phase speed at the low wave number limit is obtained. The equations for cut-off frequencies of the modes that have infinite phase speeds at the low wave number limit are also obtained.

The behavior of the dispersion curves for symmetric and antisymmetric waves are similar at the low wave number limit. At low wave number limit, depending on the prestress, at most only one finite limiting squared phase speed may exist.

Acknowledgements. The authors are pleased to acknowledge financial support from Monbukagakusho (Ministry of Education, Culture, Sports, Science and Technology), Japan, under Grant-in-Aid for Scientific Research (C) No. 19560075.

References

- [Dowaikh and Ogden 1990] M. A. Dowaikh and R. W. Ogden, "On surface waves and deformations in a pre-stressed incompressible elastic solid", *IMA J. Appl. Math.* **44**:3 (1990), 261–284.
- [Dowaikh and Ogden 1991a] M. A. Dowaikh and R. W. Ogden, "Interfacial waves and deformations in pre-stressed elastic media", *Proc. R. Soc. Lond. A* **433**:1888 (1991), 313–328.
- [Dowaikh and Ogden 1991b] M. A. Dowaikh and R. W. Ogden, "On the surface waves and deformations in compressible elastic half space", *Stab. Appl. Anal. Cont. Media* **1** (1991), 27–44.
- [Leungvichcharoen and Wijeyewickrema 2003] S. Leungvichcharoen and A. C. Wijeyewickrema, "Dispersion effects of extensional waves in pre-stressed imperfectly bonded incompressible elastic layered composites", *Wave Motion* **38**:4 (2003), 311–325.
- [Leungvichcharoen et al. 2004] S. Leungvichcharoen, A. C. Wijeyewickrema, and T. Yamamoto, "Anti-symmetric waves in pre-stressed imperfectly bonded incompressible elastic layered composites", *Int. J. Solids Struct.* **41**:24–25 (2004), 6873–6894.

- [Ogden and Roxburgh 1993] R. W. Ogden and D. G. Roxburgh, “The effect of pre-stress on the vibration and stability of elastic plates”, *Int. J. Eng. Sci.* **31**:12 (1993), 1611–1639.
- [Ogden and Sotiropoulos 1995] R. W. Ogden and D. A. Sotiropoulos, “On interfacial waves in pre-stressed layered incompressible elastic solids”, *Proc. R. Soc. Lond. A* **450**:1939 (1995), 319–341.
- [Ogden and Sotiropoulos 1996] R. W. Ogden and D. A. Sotiropoulos, “The effect of pre-stress on guided ultrasonic waves between a surface layer and a half-space”, *Ultrasonics* **34**:2–5 (1996), 491–494.
- [Ogden and Sotiropoulos 1997] R. W. Ogden and D. A. Sotiropoulos, “The effect of pre-stress on the propagation and reflection of plane waves in incompressible elastic solids”, *IMA J. Appl. Math.* **59**:1 (1997), 95–121.
- [Ogden and Sotiropoulos 1998] R. W. Ogden and D. A. Sotiropoulos, “Reflection of plane waves from the boundary of a pre-stressed compressible elastic half-space”, *IMA J. Appl. Math.* **61**:1 (1998), 61–90.
- [Rogerson and Sandiford 1997] G. A. Rogerson and K. J. Sandiford, “Flexural waves in incompressible pre-stressed elastic composites”, *Q. J. Mech. Appl. Math.* **50**:4 (1997), 597–624.
- [Rogerson and Sandiford 2000] G. A. Rogerson and K. J. Sandiford, “The effect of finite primary deformations on harmonic waves in layered elastic media”, *Int. J. Solids Struct.* **37**:14 (2000), 2059–2087.
- [Roxburgh and Ogden 1994] D. G. Roxburgh and R. W. Ogden, “Stability and vibration of pre-stressed compressible elastic plates”, *Int. J. Eng. Sci.* **32**:3 (1994), 427–454.
- [Sotiropoulos 1998] D. A. Sotiropoulos, “Interfacial waves in pre-stressed compressible elastic media”, *Comput. Mech.* **21**:4–5 (1998), 293–299.
- [Sotiropoulos 2000] D. A. Sotiropoulos, “Guided elastic waves in a pre-stressed compressible interlayer”, *Ultrasonics* **38**:1–8 (2000), 821–823.
- [Sotiropoulos and Sifniotopoulos 1995] D. A. Sotiropoulos and C. G. Sifniotopoulos, “Interfacial waves in pre-stressed incompressible elastic interlayers”, *J. Mech. Phys. Solids* **43**:3 (1995), 365–387.

Received 17 Jul 2008. Accepted 8 Sep 2008.

ANIL C. WIJEYEWICKREMA: wijeyewickrema.a.aa@m.titech.ac.jp

Department of Civil Engineering, Tokyo Institute of Technology, M1-19, 2-12-1, O-okayama, Meguro-ku, Tokyo, 152-8552, Japan

<http://www.cv.titech.ac.jp/~anil-lab/>

YOSUKE USHIDA: yushida@cv.titech.ac.jp

Department of Civil Engineering, Tokyo Institute of Technology, M1-19, 2-12-1, O-okayama, Meguro-ku, Tokyo, 152-8552, Japan

PRIZA KAYESTHA: kayestha.p.aa@m.titech.ac.jp

Department of Civil Engineering, Tokyo Institute of Technology, M1-19, 2-12-1, O-okayama, Meguro-ku, Tokyo, 152-8552, Japan

NONLINEAR LOCAL BENDING OF FGM SANDWICH PLATES

JIE YANG, SRITAWAT KITIPORNCHAI AND KIM MEOW LIEW

This paper investigates the nonlinear local bending of a sandwich plate consisting of two composite laminated face sheets and a graded core subjected to a lateral patch load. It is assumed that the material composition of the graded layer varies symmetrically along the thickness direction according to a power law distribution. The present analysis is based on the first order shear deformation plate theory and von Karman nonlinear kinematics, with the interaction between the loaded face sheet and the graded core being modeled as an elastic plate resting on a Vlasov-type elastic foundation. A perturbation technique and Galerkin method are used to determine the nonlinear local bending response. Numerical results show that compared with conventional sandwich plates with a homogeneous soft core, the use of a functionally graded core can effectively reduce both the local deformation and interfacial shear stresses. A parametric study is performed to show the influences of the volume fraction index, Young's modulus ratio, thickness of the graded core, boundary condition, and load position.

1. Introduction

Due to their high specific stiffness, light weight, exceptional impact energy absorption, and excellent thermal and acoustical insulation characteristics, sandwich structures are widely used in many engineering applications such as infrastructures, marine constructions, automobiles, and the aerospace industry. A typical sandwich structure consists of two stiff face sheets and a thick intermediate core of low-density and low-modulus material sandwiched in between. One of the major concerns in using such a structure is the so-called "interface problem" (possible crack and delamination at the face sheet/core interfaces caused by the transverse shear stress concentration) that arises from large stiffness differences between the face sheets and the core which may result in a significant deterioration in structure reliability.

Functionally graded materials (FGMs) constitute a new class of inhomogeneous composites whose material composition and physical properties change continuously and smoothly in one or more spatial coordinates so that the interface problem can be effectively mitigated or eliminated. Rapid advances in manufacturing techniques have enabled the fabrication of bulk FGMs that can be used in large-scale structural systems [Ichikawa 2001]. This provides an advantageous degree of freedom in incorporating FGMs into a sandwich structure to achieve a smooth variation in the material property profile. Recent theoretical and experimental investigations [Apetre et al. 2002; Anderson 2003; Venkataraman and Sankar 2003; Venkataraman et al. 2004; Kirugulige et al. 2005; Pollien et al. 2005; Das et al. 2006; Apetre et al. 2006; Zhu and Sankar 2007] have shown that the use of an FGM core can significantly reduce the interfacial shear stresses.

Keywords: local bending, sandwich structure, functionally graded materials, nonlinear behavior, laminates.

This work described in this paper was fully funded by a research grant from City University of Hong Kong (Project No. 7002211).

It is known that under a highly localized lateral load such as a point or a patch load, a sandwich structure tends to fail not by overall bending but more often by excessive bending deformation or indentation into the soft core layer around the loaded area. In such a case, the local deformation can be regarded as the relative deflection of the loaded face sheet against the unloaded face sheet. Quite a few theoretical and experimental studies have been conducted to address this issue [Corbett and Reid 1993; Thomsen 1993; Thomsen 1995; Frostig and Baruch 1996; Abrate 1997; da Silva and Santos 1998; Polyakov 2001; Koissin et al. 2004; Hohe and Librescu 2004; Carrera and Ciuffreda 2005], among many others. For sandwich plate structures with a continuous core layer, the relative deflection can be determined by using an approximate approach in which the core layer is modeled as an elastic foundation. Weissman-Berman et al. [1996] treated the loaded face sheet as a Kirchhoff plate resting on a Winkler-type elastic foundation whose equivalent foundation stiffness was dependent on the material properties of the core. For a thick core whose shearing effect is important, Thomsen [1993; 1995] suggested a modified Vlasov-type elastic foundation model and studied the local bending behavior of simply supported rectangular sandwich panels with thin orthotropic face layers. By modeling the sandwich panel as an infinite orthotropic elastic plate resting on a rigid-plastic foundation, Türk and Fatt [1999] investigated the local damage response of a composite sandwich panel induced by static indentation of a hemispherical-nose indenter. It is noted that all of the aforementioned studies were based on the linear displacement-strain relationship only and did not take into account the geometric nonlinearity which is inevitable when a sandwich structure is subjected to a localized load of high density. The only work including this effect was reported by Yang et al. [2001] who presented a nonlinear local bending analysis of composite laminated sandwich plates with a flexible core under a combination of lateral strip load and uniform edge forces by using the classical plate theory and a differential quadrature based semi analytical method. Their results showed that the nonlinear local bending response is considerably different from linear predictions.

This paper investigates the geometrically nonlinear bending response of a rectangular FGM sandwich plate subjected to a lateral patch load within the framework of von Karman-type geometric nonlinearity and the first order shear deformation plate theory. The sandwich plate consists of a thick symmetrically graded core layer bonded by two composite face sheets. The Vlasov-type elastic foundation model is used to describe the supporting action of the graded core to the loaded face sheet. The nonlinear governing partial differential equations are first transformed into a group of linear equations through the use of a perturbation technique and then solved by the Galerkin procedure. Illustrative examples are analyzed to gain an insight into the effects of the Young's modulus ratio, the thickness ratio, the boundary condition as well as the load position on the nonlinear local bending response.

2. Analytical formulations

2.1. Vlasov-type elastic foundation model. Figure 1 shows a rectangular sandwich plate of length a and width b consisting of an isotropic inhomogeneous thick core of thickness H_c and two composite laminated face sheets of equal thickness H_f . Let (x, y, z) be a set of coordinates with the x - and y -axes located in the middle plane of the upper face sheet and the z -axis pointing upwards. The material profile of the core changes continuously along the thickness direction according to a power law distribution and is compositionally symmetric about its midplane. The effective Young's modulus at an arbitrary point

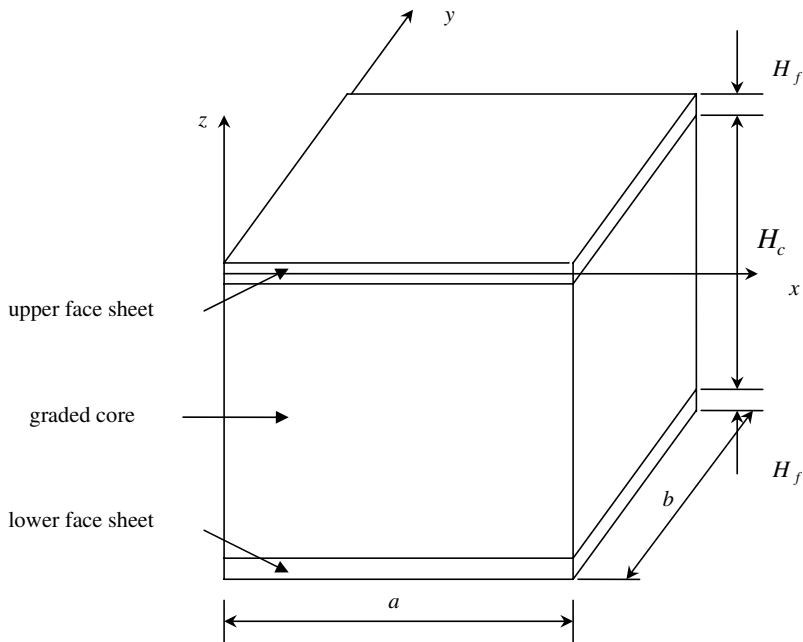


Figure 1. Schematic configuration of an FGM sandwich plate.

within the core layer can be determined by

$$E_{\text{core}} = \begin{cases} (E_1 - E_0) \left(2 \frac{z+h}{H_c} \right)^n + E_0 & -h \leq z \leq -0.5H_f, \\ (E_1 - E_0) \left(-2 \frac{z+h}{H_c} \right)^n + E_0 & -h - 0.5H_c \leq z \leq -h, \end{cases} \quad (1)$$

where $h = (H_c + H_f)/2$, n is the non-negative volume fraction index, E_0 denotes the Young's modulus in the mid-plane of the core and is much smaller than the Young's modulus E_1 at the face sheet/core interface. Poisson's ratio is taken to be constant throughout the core ($\nu_{\text{core}} = \nu_0 = \nu_1$).

It is assumed in this study that

- (1) the face sheets and the graded core are perfectly bonded so that no separation takes place,
- (2) the graded core and the face sheet have the same Young's modulus, that is, $E_1 = E_f$ at the face sheet/core interfaces to achieve a smooth variation in material properties, and
- (3) a large value of n is used to obtain a graded soft core whose E_{core} in the majority of the cross section is much smaller than E_f .

Suppose that the upper face sheet is subjected to a lateral patch load $q(x, y) = q_0\varphi(x, y)$ distributed over a small area $2a_q \times 2b_q$ with its center located at (x_q, y_q) . q_0 and $\varphi(x, y)$ denote the magnitude and the distribution function of the load. To take into account the shearing effect in the graded core, the interaction between the loaded face sheet and the core layer is modeled by a Vlasov-type two-parameter

foundation as

$$p = K_1 w(x, y) - K_2 \nabla^2 w(x, y), \tag{2}$$

where $w(x, y)$ is the relative deflection of the upper face sheet against the lower face sheet, p is the foundation reaction per unit area provided by the graded core, $\nabla^2 = \partial^2/\partial x^2 + \partial^2/\partial y^2$ is the Laplace operator, K_1 and K_2 are the equivalent spring stiffness and shear stiffness of the foundation which can be derived using Lagrange’s principle of virtual work [Selvadurai 1979] as

$$K_1 = \int_{-(h_f/2+H_c)}^{-h_f/2} \frac{\tilde{E}(z)}{[1 - \tilde{\nu}^2]} \left(\frac{d\phi(z)}{dz} \right)^2 dz, \quad K_2 = \int_{-(h_f/2+H_c)}^{-h_f/2} \frac{\tilde{E}(z)}{4[1 + \tilde{\nu}]} \phi(z)^2 dz, \tag{3}$$

in which $\tilde{E} = E_{\text{core}}/(1 - \nu_{\text{core}}^2)$, $\tilde{\nu} = \nu_{\text{core}}/(1 - \nu_{\text{core}})$, and $\phi(z)$ is the deformation distribution of the core layer that is considered to be in the plane strain state and takes the exponential form

$$\phi(z) = \frac{\sinh[1.5(H_c - z - h)/b]}{\sinh(1.5 H_c/b)}. \tag{4}$$

It can be seen from the calculations based on Equations (3) and (4) that both K_1 and K_2 fall sharply and then remain almost constant as the volume fraction index n and the modulus ratio E_1/E_0 increase. The variation of K_1 with the core thickness H_c follows almost the same pattern. The value of K_2 , however, increases steadily as H_c increases, implying that the shearing effect of the core material tends to be more important for sandwich plates with a thick core.

At the interface between the loaded upper face sheet and the graded core ($z = -0.5H_f$), the stress components σ_z , τ_{zx} , and τ_{zy} can be calculated by

$$\sigma_z|_{z=-0.5H_f} = K_1 w(x, y) - K_2 \nabla^2 w(x, y), \tag{5a}$$

$$\tau_{zx}|_{z=-0.5H_f} = K_2 u(x, y, -0.5H_f), \tag{5b}$$

$$\tau_{zy}|_{z=-0.5H_f} = K_2 v(x, y, -0.5H_f), \tag{5c}$$

where u and v are in-plane displacement components of the loaded face sheet at the interface.

2.2. Governing equations. The face sheet considered in this study may be one of the following: (1) an antisymmetrically angle-ply laminated plate; (2) a symmetrically cross-ply laminated plate; or (3) a symmetric angle-ply laminated plate with more than 15 plies. In these cases, the plate stiffness elements $A_{16} = A_{26} = D_{16} = D_{26} = 0$. Both isotropic and orthotropic plates can be treated as special cases.

The first order shear deformation theory is used to account for the transverse shear deformation of the face sheet. Hence, the displacement field (u, v, w) of the loaded face sheet takes the form

$$\begin{Bmatrix} u(x, y, z) \\ v(x, y, z) \\ w(x, y, z) \end{Bmatrix} = \begin{Bmatrix} \bar{u}(x, y) \\ \bar{v}(x, y) \\ \bar{w}(x, y) \end{Bmatrix} + z \begin{Bmatrix} \psi_x(x, y) \\ \psi_y(x, y) \\ 0 \end{Bmatrix}, \tag{6}$$

where $(\bar{u}, \bar{v}, \bar{w})$ are the displacements of a point on the midplane of the face sheet ($z = 0$) and (ψ_x, ψ_y) are cross sectional rotations about the y - and x -axes, respectively.

The partial differential equations governing the nonlinear flexural response of the loaded face sheet in the sense of von Karman-type nonlinear kinematics [Liew et al. 2004] can be written in dimensionless form as

$$L_{11}(U) + L_{12}(V) + L_{14}(\psi_x) + L_{15}(\psi_y) + \mu L_{16}(W, W) = 0, \tag{7}$$

$$L_{21}(U) + L_{22}(V) + L_{24}(\psi_x) + L_{25}(\psi_y) + \mu\beta L_{26}(W, W) = 0, \tag{8}$$

$$L_{33}(W) + L_{34}(\psi_x) + L_{35}(\psi_y) + \mu^2 L_{36}(W, W) + \mu L_{37}[(U, V, \psi_x, \psi_y), W] = \lambda_q \varphi(x, y) / \mu, \tag{9}$$

$$L_{41}(U) + L_{42}(V) - L_{43}(W) + L_{44}(\psi_x) + L_{45}(\psi_y) + \mu L_{46}(W, W) = 0, \tag{10}$$

$$L_{51}(U) + L_{52}(V) - L_{53}(W) + L_{54}(\psi_x) + L_{55}(\psi_y) + \mu L_{56}(W, W) = 0, \tag{11}$$

where the linear partial differential operators L_{ij} ($i, j \leq 5$), the nonlinear partial differential operators L_{i6} ($i = 1, \dots, 5$), and L_{37} are given in the Appendix. The dimensionless quantities in (7)–(11) are

$$\xi = x/a,$$

$$\eta = y/b,$$

$$\beta = a/b,$$

$$\mu = H_f/a,$$

$$(U, V, W) = (\bar{u}, \bar{v}, \bar{w})/H_f,$$

$$(k_1, k_2) = (K_1 a^2, K_2)/A_{11},$$

$$\lambda_q = q_0 a / A_{11},$$

$$(\gamma_1, \gamma_2, \gamma_3) = [A_{44}, A_{45}, A_{55}] H_f^2 / D_{11},$$

$$(\gamma_{11}, \gamma_{12}, \gamma_{13}, \gamma_{14}) = [A_{66}, A_{12} + A_{66}, A_{12}, A_{22}] / A_{11},$$

$$(\gamma_{15}, \gamma_{16}, \gamma_{17}, \gamma_{18}, \gamma_{19}, \gamma_{110}, \gamma_{111}) = [B_{11}, B_{16}, B_{66}, B_{12} + B_{66}, B_{26}, B_{22}, B_{12}] / (A_{11} H_f),$$

$$(\gamma_{41}, \gamma_{42}) = [D_{66}, D_{12} + D_{66}] / D_{11},$$

$$(\gamma_{43}, \gamma_{44}, \gamma_{45}, \gamma_{46}, \gamma_{47}, \gamma_{48}) = [B_{11}, B_{16}, B_{66}, B_{12} + B_{66}, B_{26}, B_{22}] H_f / D_{11},$$

in which A_{ij} , B_{ij} and D_{ij} are the stiffness elements of the face sheet

$$(A_{ij}, B_{ij}, D_{ij}) = \sum_{k=1}^{N_L} \int_{z_k}^{z_{k+1}} Q_{ij}^{(k)}(1, z, z^2) dz \quad (i, j = 1, 2, 4, 5, 6), \tag{12}$$

where $Q_{ij}^{(k)}$ are the reduced stiffnesses for the k th layer of the N_L -ply laminated face sheet and are functions of fiber orientation of that layer. Their expressions are available in many references; see, for example, the book by Reddy [1997].

The edges of the loaded face sheet may be either simply supported or clamped with the boundary conditions

$$W = 0, \quad \psi_s = 0, \quad M_n = 0, \quad N_n = 0, \quad U_s = 0, \tag{13a}$$

for a simply supported edge, and

$$W = 0, \quad \psi_s = 0, \quad \psi_n = 0, \quad U_n = 0, \quad U_s = 0, \tag{13b}$$

for a clamped edge. The subscripts n and s refer to the normal and tangential directions of the edge, and $N_n, N_{ns}, M_n, M_{ns}, Q_n$ are the in-plane forces, moments, and transverse shear force, respectively.

3. Analytical methodology

3.1. Perturbation technique. To determine the local response of the loaded face sheet, a perturbation technique [Yang et al. 2001; Yang and Shen 2003a; Yang and Shen 2003b] is used, and the unknown displacement components (U, V, W, ψ_x, ψ_y) are expanded in an ascending power series up to the R th order for a small perturbation parameter λ_q as

$$(U, V, W, \psi_x, \psi_y) = \sum_r^R (\lambda_q)^r (U^{(r)}, V^{(r)}, W^{(r)}, \psi_x^{(r)}, \psi_y^{(r)}). \tag{14}$$

Following a standard perturbation technique, a set of equations can be obtained in terms of $U^{(r)}, V^{(r)}, W^{(r)}, \psi_x^{(r)}$, and $\psi_y^{(r)}$:

$$L_{11}(U^{(r)}) + L_{12}(V^{(r)}) + L_{14}(\psi_x^{(r)}) + L_{15}(\psi_y^{(r)}) = R_1^{(r)}, \tag{15}$$

$$L_{21}(U^{(r)}) + L_{22}(V^{(r)}) + L_{24}(\psi_x^{(r)}) + L_{25}(\psi_y^{(r)}) = R_2^{(r)}, \tag{16}$$

$$L_{33}(W^{(r)}) + L_{34}(\psi_x^{(r)}) + L_{35}(\psi_y^{(r)}) = R_3^{(r)}, \tag{17}$$

$$L_{41}(U^{(r)}) + L_{42}(V^{(r)}) - L_{43}(W^{(r)}) + L_{44}(\psi_x^{(r)}) + L_{45}(\psi_y^{(r)}) = R_4^{(r)}, \tag{18}$$

$$L_{51}(U^{(r)}) + L_{52}(V^{(r)}) - L_{53}(W^{(r)}) + L_{54}(\psi_x^{(r)}) + L_{55}(\psi_y^{(r)}) = R_5^{(r)}, \tag{19}$$

where

$$R_1^{(1)} = R_2^{(1)} = R_4^{(1)} = R_5^{(1)} = 0, \quad R_3^{(1)} = \varphi(x, y)/\mu, \tag{20}$$

$$R_i^{(r)} = -\mu \sum_{s=1}^{i-1} L_{i6}(W^{(r-s)}, W^{(s)}) \quad (r = 2, i = 1, 2, 4, 5),$$

$$R_3^{(2)} = -\mu^2 \sum_{s=1}^{i-1} L_{37}[(U^{(r-s)}, V^{(r-s)}, \psi_x^{(r-s)}, \psi_y^{(r-s)}), W^{(s)}],$$

$$R_3^{(r)} = -\mu R_{31}^{(r)} - \mu^2 \sum_{s=1}^{i-1} L_{37}[(U^{(r-s)}, V^{(r-s)}, \psi_x^{(r-s)}, \psi_y^{(r-s)}), W^{(s)}] \quad (r \geq 3). \tag{21}$$

Obviously, the right-hand terms $R_i^{(r)}$ ($i = 1, \dots, 5$) have already been determined in the previous perturbation step and can be treated as “pseudoloads” at the current step. In (21), the terms $R_{31}^{(r)}$ ($r \geq 3$), up to the fifth-order perturbation, are

$$R_{31}^{(3)} = \left(\frac{\partial^2 W^{(1)}}{\partial \xi^2} + \gamma_{13} \beta^2 \frac{\partial^2 W^{(1)}}{\partial \eta^2} \right) \left(\frac{\partial W^{(1)}}{\partial \xi} \right)^2 + 2\gamma_{11} \beta \frac{\partial^2 W^{(1)}}{\partial \xi \partial \eta} \frac{\partial W^{(1)}}{\partial \xi} \frac{\partial W^{(1)}}{\partial \eta} + \beta^2 \left(\gamma_{13} \frac{\partial^2 W^{(1)}}{\partial \xi^2} + \beta^2 \gamma_{14} \frac{\partial^2 W^{(1)}}{\partial \eta^2} \right) \left(\frac{\partial W^{(1)}}{\partial \eta} \right)^2, \tag{22}$$

$$\begin{aligned}
 R_{31}^{(4)} = & \left(\frac{\partial^2 W^{(2)}}{\partial \xi^2} + \gamma_{13} \beta^2 \frac{\partial^2 W^{(2)}}{\partial \eta^2} \right) \left(\frac{\partial W^{(1)}}{\partial \xi} \right)^2 \\
 & + 2\gamma_{11} \beta \left(\frac{\partial^2 W^{(2)}}{\partial \xi \partial \eta} \frac{\partial W^{(1)}}{\partial \xi} \frac{\partial W^{(1)}}{\partial \eta} + \frac{\partial^2 W^{(1)}}{\partial \xi \partial \eta} \frac{\partial W^{(2)}}{\partial \xi} \frac{\partial W^{(1)}}{\partial \eta} + \frac{\partial^2 W^{(1)}}{\partial \xi \partial \eta} \frac{\partial W^{(1)}}{\partial \xi} \frac{\partial W^{(2)}}{\partial \eta} \right) \\
 & + \beta^2 \left(\gamma_{13} \frac{\partial^2 W^{(2)}}{\partial \xi^2} + \beta^2 \gamma_{14} \frac{\partial^2 W^{(2)}}{\partial \eta^2} \right) \left(\frac{\partial W^{(1)}}{\partial \eta} \right)^2, \quad (23)
 \end{aligned}$$

$$\begin{aligned}
 R_{31}^{(5)} = & \left(\frac{\partial^2 W^{(1)}}{\partial \xi^2} + \gamma_{13} \beta^2 \frac{\partial^2 W^{(1)}}{\partial \eta^2} \right) \left(\frac{\partial W^{(2)}}{\partial \xi} \right)^2 + \left(\frac{\partial^2 W^{(3)}}{\partial \xi^2} + \gamma_{13} \beta^2 \frac{\partial^2 W^{(3)}}{\partial \eta^2} \right) \left(\frac{\partial W^{(1)}}{\partial \xi} \right)^2 \\
 & + 2\gamma_{11} \beta \left(\frac{\partial^2 W^{(3)}}{\partial \xi \partial \eta} \frac{\partial W^{(1)}}{\partial \xi} \frac{\partial W^{(1)}}{\partial \eta} + \frac{\partial^2 W^{(1)}}{\partial \xi \partial \eta} \frac{\partial W^{(3)}}{\partial \xi} \frac{\partial W^{(1)}}{\partial \eta} + \frac{\partial^2 W^{(1)}}{\partial \xi \partial \eta} \frac{\partial W^{(1)}}{\partial \xi} \frac{\partial W^{(3)}}{\partial \eta} \right. \\
 & \quad \left. + \frac{\partial^2 W^{(2)}}{\partial \xi \partial \eta} \frac{\partial W^{(2)}}{\partial \xi} \frac{\partial W^{(1)}}{\partial \eta} + \frac{\partial^2 W^{(2)}}{\partial \xi \partial \eta} \frac{\partial W^{(1)}}{\partial \xi} \frac{\partial W^{(2)}}{\partial \eta} + \frac{\partial^2 W^{(1)}}{\partial \xi \partial \eta} \frac{\partial W^{(2)}}{\partial \xi} \frac{\partial W^{(2)}}{\partial \eta} \right) \\
 & + \beta^2 \left(\gamma_{13} \frac{\partial^2 W^{(1)}}{\partial \xi^2} + \beta^2 \gamma_{14} \frac{\partial^2 W^{(1)}}{\partial \eta^2} \right) \left(\frac{\partial W^{(2)}}{\partial \eta} \right)^2 + \beta^2 \left(\gamma_{13} \frac{\partial^2 W^{(3)}}{\partial \xi^2} + \beta^2 \gamma_{14} \frac{\partial^2 W^{(3)}}{\partial \eta^2} \right) \left(\frac{\partial W^{(1)}}{\partial \eta} \right)^2. \quad (24)
 \end{aligned}$$

3.2. Solution procedure. The solutions of the perturbation equations (15)–(19) under the associated boundary conditions in (13) can be expanded in series form:

$$U^{(r)} = \sum_{m=1}^M \sum_{n=1}^N a_{mn}^{(r)} \bar{U}_m(\xi) \tilde{U}_n(\eta), \quad V^{(r)} = \sum_{m=1}^M \sum_{n=1}^N b_{mn}^{(r)} \bar{V}_m(\xi) \tilde{V}_n(\eta), \quad (25a)$$

$$W^{(r)} = \sum_{m=1}^M \sum_{n=1}^N c_{mn}^{(r)} \bar{W}_m(\xi) \tilde{W}_n(\eta), \quad \psi_x^{(r)} = \sum_{m=1}^M \sum_{n=1}^N d_{mn}^{(r)} \bar{\psi}_{xm}(\xi) \tilde{\psi}_{xn}(\eta), \quad (25b)$$

$$\psi_y^{(r)} = \sum_{m=1}^M \sum_{n=1}^N e_{mn}^{(r)} \bar{\psi}_{ym}(\xi) \tilde{\psi}_{yn}(\eta), \quad (25c)$$

where $(a_{mn}^{(r)}, b_{mn}^{(r)}, c_{mn}^{(r)}, d_{mn}^{(r)}, e_{mn}^{(r)})$ are constants to be determined, $(\bar{U}_m^{(r)}, \bar{V}_m^{(r)}, \bar{W}_m^{(r)}, \bar{\psi}_{xm}^{(r)}, \bar{\psi}_{ym}^{(r)})$ and $(\tilde{U}_n^{(r)}, \tilde{V}_n^{(r)}, \tilde{W}_n^{(r)}, \tilde{\psi}_{xn}^{(r)}, \tilde{\psi}_{yn}^{(r)})$ are the analytical functions that satisfy boundary conditions at edges $\xi = 0, 1$ and $\eta = 0, 1$, respectively. For example, when the face sheet is simply supported at $\xi = 0, 1$,

$$\bar{V}_m^{(r)}(\xi) = \bar{W}_m^{(r)}(\xi) = \bar{\psi}_{ym}^{(r)}(\xi) = \sin(m\pi \xi), \quad \bar{U}_m^{(r)}(\xi) = \bar{\psi}_{xm}^{(r)}(\xi) = \cos(m\pi \xi), \quad (26)$$

and when the face sheet is clamped at $\xi = 0, 1$,

$$\bar{U}_m^{(r)}(\xi) = \bar{W}_m^{(r)}(\xi) = \bar{\psi}_{ym}^{(r)}(\xi) = X_m(\xi), \quad \bar{V}_m^{(r)}(\xi) = \bar{\psi}_{xm}^{(r)}(\xi) = \frac{dX_m(\xi)}{d\xi}, \quad (27)$$

where

$$\begin{aligned} X_m(\xi) &= \sin \mu_m \xi - \sinh \mu_m \xi - \theta_m (\cos \mu_m \xi - \cosh \mu_m \xi), \\ \theta_m &= (\sin \mu_m - \sinh \mu_m) / (\cos \mu_m - \cosh \mu_m), \\ \mu_m &= (2m + 1)\pi / 2. \end{aligned}$$

Substituting (25) into the perturbation equations (15)–(19) and applying the Galerkin approach to minimize the residual within the face sheet domain leads to a system of linear algebraic equations from which the constants $(a_{mn}^{(r)}, b_{mn}^{(r)}, c_{mn}^{(r)}, d_{mn}^{(r)}, e_{mn}^{(r)})$ can be determined step by step. Finally, the nonlinear load-deflection relationship for a given point p can be obtained by using the relationship in (14) as

$$W_p = \lambda_q W_p^{(1)} + \lambda_q^2 W_p^{(2)} + \dots + \lambda_q^R W_p^{(R)}, \quad (28)$$

where W_p refers to the dimensionless deflection at point p .

4. Numerical results and discussions

In the following computations, we use third order perturbation and the condition that $M = N = 5$ in the solution series in Equation (25). These conditions were chosen based on the convergence study implemented by means of varying the total number of series terms and increasing the perturbation order.

To validate the present analysis, the linear local bending of a clamped sandwich plate with a PVC core and orthotropic face sheets subjected to a point load $P = 1$ kN at the plate center is considered. This example was previously analyzed by Thomsen [1993] based on the classical plate theory as well. The geometry and material properties are $a = b = 500$ mm, $H_f = 3$ mm, $E_{11}^f = 33.6$ GPa, $E_{22}^f = 8.4$ GPa, $G_{12}^f = 3.1$ GPa, $\nu_{12}^f = 0.32$ for the orthotropic face sheet and $H_c = 30$ mm, $E_c = 0.1$ GPa, $\nu_c = 0.35$ for the PVC core. Figure 2 displays the lateral deflection profile at the midspan ($y = b/2$) of the plate. Severe deformation localization can be observed. The deflection reaches its peak value at the center of the plate, and then decays steeply as the distance from the center increases. Good agreement is achieved between the present solution and the finite element method (FEM) results [Thomsen 1993].

The second comparison example concerns the nonlinear bending of a simply supported functionally graded square plate ($a = b = 200$ mm, $h = 10$ mm) under a uniform lateral pressure of intensity q . The plate is made of a mixture of aluminum ($E = 70$ GPa, $\nu = 0.3$) and zirconia ($E = 151$ GPa, $\nu = 0.3$). Figure 3 presents the curves of dimensionless central deflection $w_0 = w/h$ versus load parameter $q^* = qa^4/E_m h^4$ for plates with different material compositions where E_m is the Young's modulus of aluminum. The FEM results [Reddy 2000] based on the higher-order shear deformation plate theory are also provided for direct comparison. Again, good agreement is observed. The discrepancy in the above comparisons is due to the different numerical solution methods used in the present analysis and existing studies [Thomsen 1993; Reddy 2000].

Figures 4–9 give the numerical results for square sandwich plates with a symmetrically graded core and 4-layer ($-45^\circ/45^\circ/-45^\circ/45^\circ$) antisymmetric angle-ply Kevlar/epoxy face sheets of equal ply thickness. Unless stated otherwise, the plate is assumed to be simply supported at all sides and subjected to a uniformly distributed patch load over an area $(2a_q, 2b_q) = (2 \times 0.05a, 2 \times 0.05b)$ in the vicinity of the center of the plate $(x_q, y_q) = (0.5a, 0.5b)$. The material properties and geometrical parameters are: $E_{11}^f = 76$ GPa, $E_{22}^f = 5.5$ GPa, $G_{12}^f = 2.3$ GPa, $\nu_{12}^f = 0.34$, $H_f = 5$ mm, $a = b = 500$ mm for the face

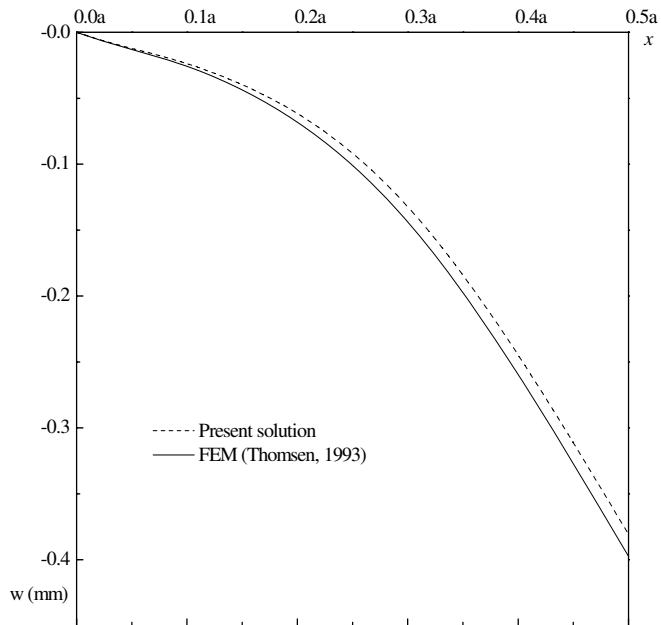


Figure 2. Comparison of the linear deflection profile $w|_{y=0.5b}$ of an orthotropic loaded face sheet under a point load at the plate center.

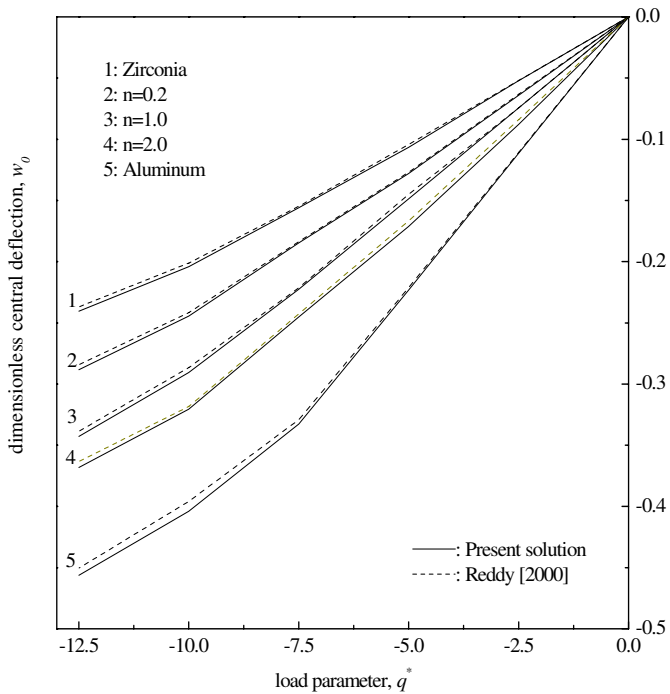


Figure 3. Nonlinear load-deflection curves of simply supported FGM square plates under uniform lateral pressure.

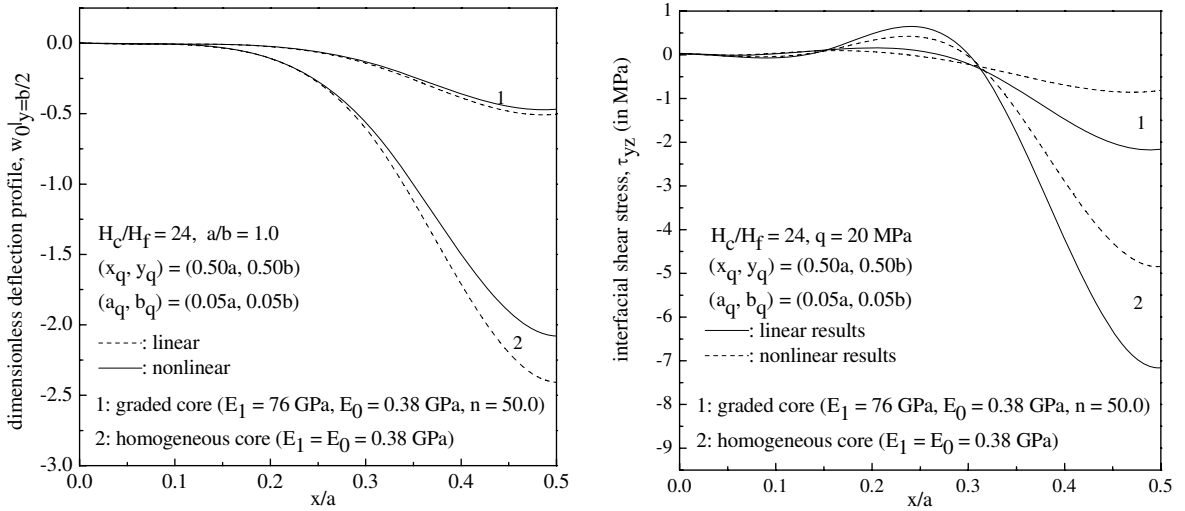


Figure 4. Comparison of the nonlinear local bending response of square sandwich plates with a homogeneous core and a graded core: (left) deflection profile $w_0|_{y=b/2}$; (right) interface shear stress $\tau_{yz}|_{y=b/2}$.

sheet, and $E_1 = 76$ GPa, $E_1/E_0 = 200$, $\nu = 0.08$, $H_c/H_f = 24$, $n = 50.0$ for the graded core. The load intensity is $q = 20$ MPa in Figures 4 and 9 and can vary up to $q = 40$ MPa in other examples. Numerical results of normalized deflection $w_0 = w/H_f$ and stresses (in MPa) at the loaded upper face sheet/graded core interface are provided.

We first compare the local deflection profiles and interfacial transverse shear stress distributions of sandwich plates with a graded core ($E_1 = 76$ GPa, $E_0 = 0.38$ GPa, $n = 50.0$) and with a homogeneous soft core ($E_1 = E_0 = 0.38$ GPa) subjected to a patch load $q = 20$ MPa. Due to the symmetry in both structural configuration and loading condition, only the deformed shape and shear stress τ_{yz} at the midspan $y = b/2$ on the left half of the plate are displayed in Figure 4 where nonlinear and linear results are represented by solid and dashed curves, respectively. The local deflection and the interfacial shear stress τ_{yz} are maximal at the plate center and decay rapidly towards the plate edge. It is important to note that both deflection and interfacial shear stress τ_{yz} are greatly reduced when a graded core is used. This is because the equivalent supporting stiffnesses K_1 and K_2 of the graded core are significantly higher than those of a homogeneous core. This observation is of particular importance since it indicates that the structural performance of a sandwich plate can be effectively improved through the use of a graded core that is capable of alleviating the local deformation and lowering the interfacial shear stress responsible for debonding failure at the face sheet/core interface.

Figure 5 displays the load-central deflection curves and the load-central interfacial stress curves for sandwich plates with a homogeneous soft core ($E_1 = E_0 = 0.38$ GPa) and a graded core with varying volume fraction index ($E_1/E_0 = 200$, $E_1 = 76$ GPa, $n = 20, 50$). It should be noted that under the power law defined in Equation (1), the graded core becomes stiffer as the volume fraction index n decreases, while $n = \infty$ corresponds to a core that is roughly homogeneous. Because of this, the sandwich plate with a graded core of $n = 20$ has the lowest central deflection. An increase in n leads to a higher τ_{yz} but

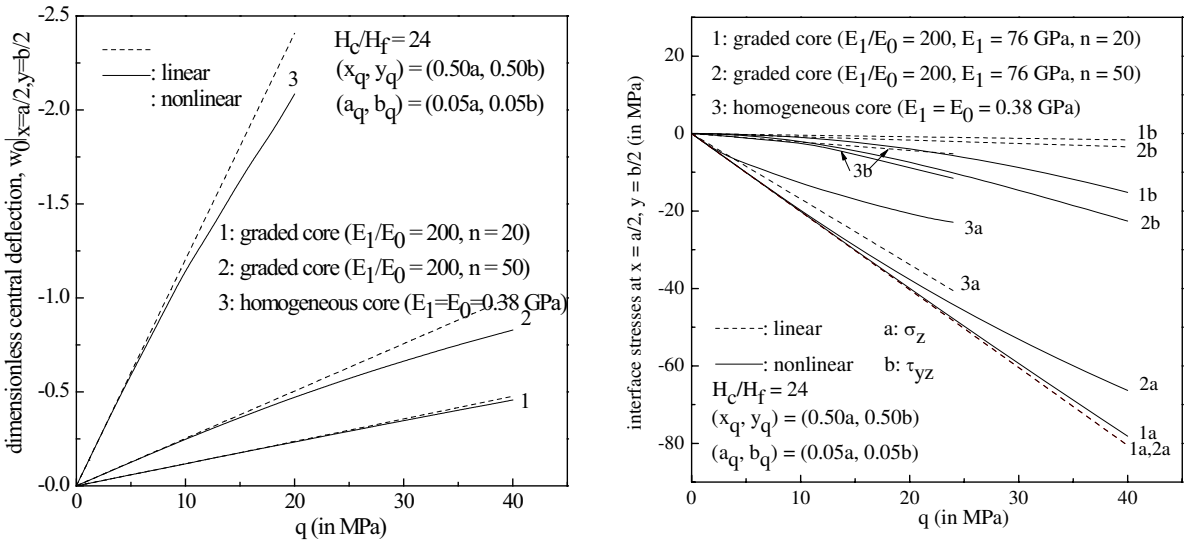


Figure 5. Comparison of the nonlinear local bending response of square sandwich plates with a homogeneous core and a graded core: (left) load-central deflection curves; (right) load-central interface stress curves.

a lower σ_z . As can be observed in Figures 4 and 5, linear solutions greatly overpredict the deflection and interfacial normal stress σ_z but on the other hand, considerably underestimate the interfacial shear stress τ_{yz} . This discrepancy becomes even more significant when a graded core with a larger value of n is used. Note that for the sandwich plate with $n = 20$, the load-central interfacial normal stress σ_z relationship is basically linear. This is due to the fact that its load-central deflection curve is almost linear and the first term in Equation (5a), which has a much higher weighing than the second term, is directly proportional to the deflection.

To investigate the effect of modulus ratio E_1/E_0 of the graded core, the nonlinear load-central deflection and load-central interfacial stress curves for sandwich plates containing a graded core ($n = 50$) with $E_1/E_0 = 100, 500$, and 1000 are given in Figure 6. The Young's modulus at the face sheet/core interface E_1 is kept constant, while that at the core center E_0 is varied. Therefore, a larger E_1/E_0 ratio in fact indicates a softer graded core with a smaller E_0 . The nonlinear deflection and interfacial shear stress τ_{yz} increase, whereas the interfacial normal stress σ_z decreases as the E_1/E_0 ratio is increased. It is worth noting that the results for $E_1/E_0 = 500$ and 1000 are quite close, implying that the nonlinear local response will almost not be affected by the change of E_1/E_0 beyond a certain value, say, $E_1/E_0 \geq 500$ in this example.

Figure 7 examines the influence of the thickness ratio H_c/H_f on the nonlinear local bending behavior of FGM sandwich plates. It is assumed that only the core thickness H_c is changed, while the face sheet thickness remains constant. Both the central deflection and central interfacial stresses follow a nonmonotonic variation with the core thickness. A sandwich plate with $H_c/H_f = 30$ has the greatest

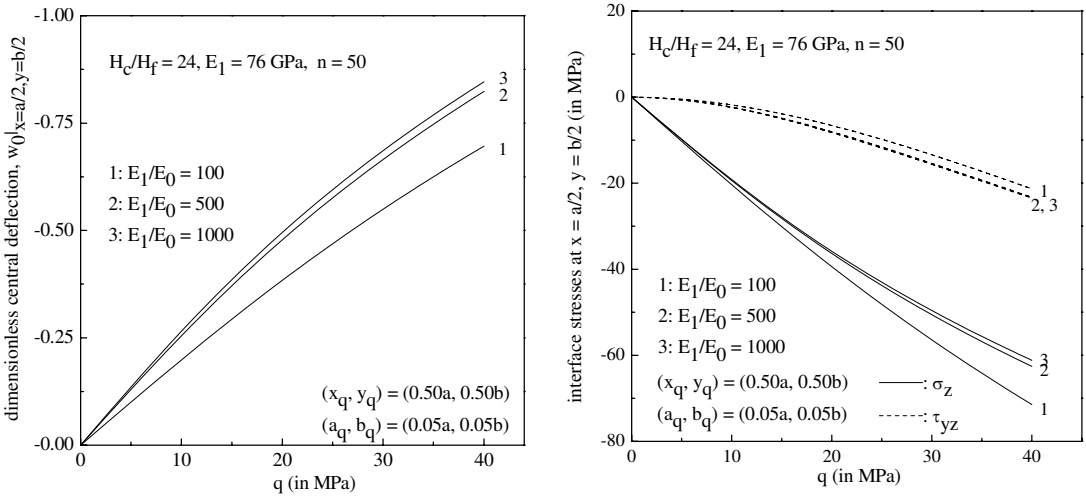


Figure 6. Nonlinear local bending response of square FGM sandwich plates with different E_1/E_0 ratios: (left) load-central deflection curves; (right) load-central interface stress curves.

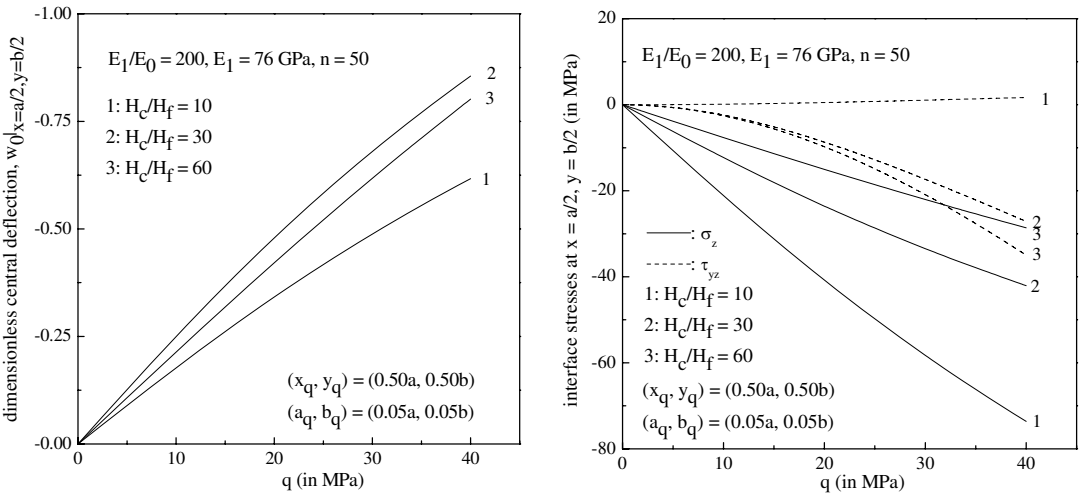


Figure 7. Nonlinear local bending response of square FGM sandwich plates with different H_c/H_f ratios: (left) load-central deflection curves; (right) load-central interface stress curves.

central deflections, but its central interfacial stresses are intermediate to those of the plates with $H_c/H_f = 10$ and $H_c/H_f = 60$. The reason is that as the graded core becomes thicker the spring stiffness K_1 becomes smaller but the shear stiffness K_2 becomes larger, and the local bending behavior of the plate depends largely on the combined effects of foundation stiffnesses K_1 and K_2 .

The nonlinear local bending responses of FGM sandwich plates under different boundary conditions are depicted in [Figure 8](#) in which notations “SSSS”, “CCCC” and “SCSC” stand for, respectively, a simply

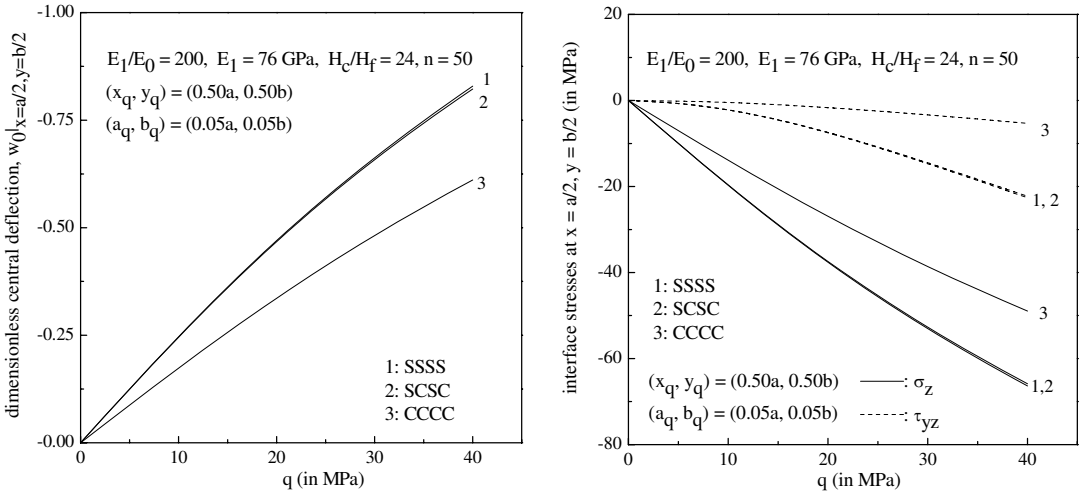


Figure 8. Nonlinear local bending response of square FGM sandwich plates with different boundary conditions: (left) load-central deflection curves; (right) load-central interface stress curves.

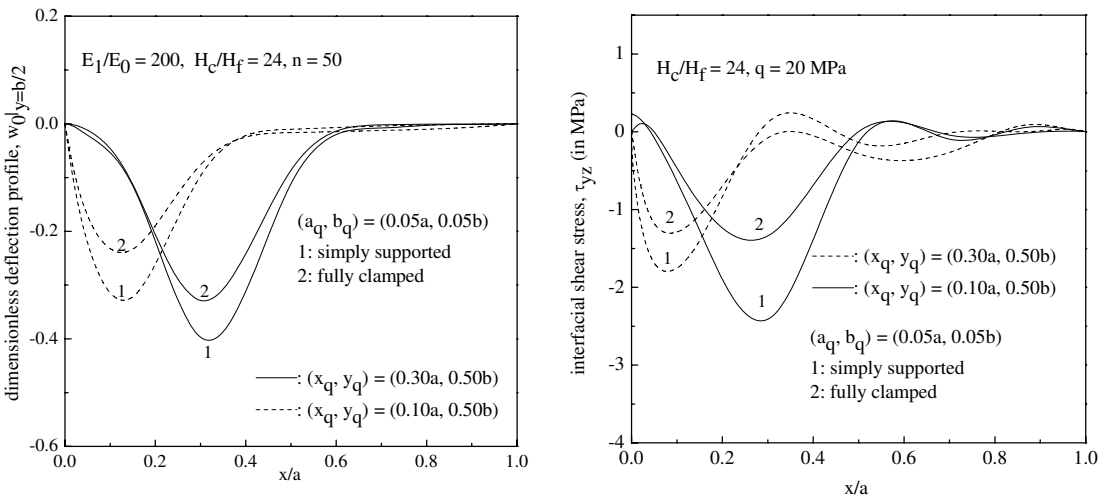


Figure 9. Effect of load position on: (left) the dimensionless central deflection profile $w_0|_{y=b/2}$; and (b) the interface shear stress $\tau_{yz}|_{y=b/2}$ of a square FGM sandwich plate.

supported sandwich plate, a clamped sandwich plate, and a sandwich plate clamped at edges $x = 0, a$ and simply supported at edges $y = 0, b$. The results show that the boundary constraints have a significant effect on the nonlinear local bending response. The fully clamped plate undergoes the lowest nonlinear deflection and interfacial stresses. The nonlinear local responses of the SSSS and SCSC sandwich plates are almost identical.

Figure 9 gives the deflection profiles and interfacial shear stress distributions for simply supported and clamped FGM sandwich plates under a patch load $q = 20$ MPa centered some distance away from the

plate center ($x_q = 0.1a, 0.3a, y_q = 0.50b$). As can be observed, both the deflection and interface shear stress are affected by the load location. In particular, their peak values, which are of the greatest interest in engineering design, are sensitive to both load location and the boundary conditions. As the load center moves towards the support, both the deformed zone and the peak of interfacial stress distributions shift towards the support accordingly.

5. Concluding remarks

The nonlinear local bending response of a composite sandwich plate containing a functionally graded core under a lateral patch load is investigated based on the first order shear deformation plate theory and von Karman type geometric nonlinearity. The analysis employs a Vlasov-type elastic foundation model including the shear effect in the flexible core to model the interaction between the loaded face sheet and the supporting core, and makes use of a perturbation technique and Galerkin approach to obtain the numerical solutions. It is found that the deformation localization and interfacial transverse shear stress concentration can be effectively reduced by using a core with smooth gradient in material properties. The geometrical nonlinear effect is pronounced at high load levels and must be taken into consideration for a reliable analysis. The use of a graded core with a smaller volume fraction index and a lower modulus ratio E_1/E_0 helps suppress both the nonlinear local deflection and interfacial transverse shear stress but leads to a higher interfacial normal stress. The nonlinear response is significantly influenced by the thickness ratio in a nonmonotonic way and is sensitive to boundary conditions as well.

Appendix

Let $\kappa = \frac{5}{6}$ be the shear correction factor. The linear and nonlinear partial differential operators in Equations (7)–(11) are

$$\begin{aligned}
 L_{11} &= \frac{\partial^2}{\partial \xi^2} + \beta^2 \gamma_{11} \frac{\partial^2}{\partial \eta^2}, & L_{12} &= L_{21} = \gamma_{12} \beta \frac{\partial^2}{\partial \xi \partial \eta}, \\
 L_{14} &= \gamma_{15} \frac{\partial^2}{\partial \xi^2} + 2\gamma_{16} \beta \frac{\partial^2}{\partial \xi \partial \eta} + \gamma_{17} \beta^2 \frac{\partial^2}{\partial \eta^2}, & L_{15} &= L_{24} = \gamma_{16} \frac{\partial^2}{\partial \xi^2} + \gamma_{18} \beta \frac{\partial^2}{\partial \xi \partial \eta} + \gamma_{19} \beta^2 \frac{\partial^2}{\partial \eta^2}, \\
 L_{16}(W, W) &= \left(\frac{\partial^2 W}{\partial \xi^2} + \gamma_{11} \beta^2 \frac{\partial^2 W}{\partial \eta^2} \right) \frac{\partial W}{\partial \xi} + \gamma_{12} \beta^2 \frac{\partial W}{\partial \xi \partial \eta} \frac{\partial W}{\partial \eta}, & L_{22} &= \gamma_{11} \frac{\partial^2}{\partial \xi^2} + \beta^2 \gamma_{14} \frac{\partial^2}{\partial \eta^2}, \\
 L_{25} &= \gamma_{17} \frac{\partial^2}{\partial \xi^2} + 2\gamma_{19} \beta \frac{\partial^2}{\partial \xi \partial \eta} + \gamma_{110} \beta^2 \frac{\partial^2}{\partial \eta^2}, & L_{26}(W, W) &= \left(\gamma_{11} \frac{\partial^2 W}{\partial \xi^2} + \beta^2 \frac{\partial^2 W}{\partial \eta^2} \right) \frac{\partial W}{\partial \eta} + \gamma_{12} \frac{\partial W}{\partial \xi \partial \eta} \frac{\partial W}{\partial \xi}, \\
 L_{33} &= \kappa^2 \left(\gamma_3 \frac{\partial^2}{\partial \xi^2} + 2\gamma_2 \beta \frac{\partial^2}{\partial \xi \partial \eta} + \gamma_1 \beta^2 \frac{\partial^2}{\partial \eta^2} \right) + k_1 - k_2 \left(\frac{\partial^2}{\partial \xi^2} + \beta^2 \frac{\partial^2}{\partial \eta^2} \right), \\
 L_{34} &= L_{43} = \frac{\kappa^2}{\mu} \left(\gamma_3 \frac{\partial}{\partial \xi} + \gamma_2 \beta \frac{\partial}{\partial \eta} \right), & L_{35} &= L_{53} = \frac{\kappa^2}{\mu} \left(\gamma_2 \frac{\partial}{\partial \xi} + \gamma_1 \beta \frac{\partial}{\partial \eta} \right), \\
 L_{36}(W, W) &= \left(\frac{\partial^2 W}{\partial \xi^2} + \gamma_{13} \beta^2 \frac{\partial^2 W}{\partial \eta^2} \right) \left(\frac{\partial W}{\partial \xi} \right)^2 + 2\gamma_{11} \beta \frac{\partial^2 W}{\partial \xi \partial \eta} \frac{\partial W}{\partial \xi} \frac{\partial W}{\partial \eta} + \beta^2 \left(\gamma_{13} \frac{\partial^2 W}{\partial \xi^2} + \beta^2 \gamma_{14} \frac{\partial^2 W}{\partial \eta^2} \right) \left(\frac{\partial W}{\partial \eta} \right)^2,
 \end{aligned}$$

$$L_{37}[(U, V, \psi_x, \psi_y), W] = \left(\frac{\partial U}{\partial \xi^2} + \gamma_{13}\beta \frac{\partial V}{\partial \eta} + \gamma_{15} \frac{\partial \psi_x}{\partial \xi} + \gamma_{16}\beta \frac{\partial \psi_x}{\partial \eta} + \gamma_{16} \frac{\partial \psi_y}{\partial \xi} + \gamma_{111}\beta \frac{\partial \psi_y}{\partial \eta} \right) \frac{\partial^2 W}{\partial \xi^2} \\ + 2\beta \left(\gamma_{11}\beta \frac{\partial U}{\partial \eta} + \gamma_{11} \frac{\partial V}{\partial \xi} + \gamma_{16} \frac{\partial \psi_x}{\partial \xi} + \gamma_{17}\beta \frac{\partial \psi_x}{\partial \eta} + \gamma_{17} \frac{\partial \psi_y}{\partial \xi} + \gamma_{19}\beta \frac{\partial \psi_y}{\partial \eta} \right) \frac{\partial^2 W}{\partial \xi \partial \eta} \\ + \beta^2 \left(\gamma_{13} \frac{\partial U}{\partial \xi} + \gamma_{14}\beta \frac{\partial V}{\partial \eta} + \gamma_{111} \frac{\partial \psi_x}{\partial \xi} + \gamma_{19}\beta \frac{\partial \psi_x}{\partial \eta} + \gamma_{19} \frac{\partial \psi_y}{\partial \xi} + \gamma_{110}\beta \frac{\partial \psi_y}{\partial \eta} \right) \frac{\partial^2 W}{\partial \eta^2},$$

$$L_{41} = \gamma_{44} \frac{\partial^2}{\partial \xi^2} + 2\gamma_{45}\beta \frac{\partial^2}{\partial \xi \partial \eta} + \gamma_{46}\beta^2 \frac{\partial^2}{\partial \eta^2}, \quad L_{42} = L_{51} = \gamma_{45} \frac{\partial^2}{\partial \xi^2} + \gamma_{47}\beta \frac{\partial^2}{\partial \xi \partial \eta} + \gamma_{48}\beta^2 \frac{\partial^2}{\partial \eta^2},$$

$$L_{44} = \frac{\partial^2}{\partial \xi^2} + \beta^2 \gamma_{41} \frac{\partial^2}{\partial \eta^2} - \left(\frac{\kappa}{\mu} \right)^2 \gamma_3, \quad L_{45} = L_{54} = \gamma_{42}\beta \frac{\partial^2}{\partial \xi \partial \eta} - \left(\frac{\kappa}{\mu} \right)^2 \gamma_2,$$

$$L_{46}(W, W) = \left(\gamma_{44} \frac{\partial^2 W}{\partial \xi^2} + 2\gamma_{45}\beta \frac{\partial^2 W}{\partial \xi \partial \eta} + \gamma_{46}\beta^2 \frac{\partial^2 W}{\partial \eta^2} \right) \frac{\partial W}{\partial \xi} + \beta \left(\gamma_{45} \frac{\partial^2 W}{\partial \xi \partial \eta} + \gamma_{47}\beta \frac{\partial^2 W}{\partial \xi \partial \eta} + \gamma_{48}\beta^2 \frac{\partial^2 W}{\partial \eta^2} \right) \frac{\partial W}{\partial \eta},$$

$$L_{52} = \gamma_{46} \frac{\partial^2}{\partial \xi^2} + 2\gamma_{48}\beta \frac{\partial^2}{\partial \xi \partial \eta} + \gamma_{49}\beta^2 \frac{\partial^2}{\partial \eta^2}, \quad L_{55} = \gamma_{41} \frac{\partial^2}{\partial \xi^2} + \beta^2 \gamma_{43} \frac{\partial^2}{\partial \eta^2} - \left(\frac{\kappa}{\mu} \right)^2 \gamma_1,$$

$$L_{56}(W, W) = \left(\gamma_{45} \frac{\partial^2 W}{\partial \xi^2} + \gamma_{47}\beta \frac{\partial^2 W}{\partial \xi \partial \eta} + \gamma_{48}\beta^2 \frac{\partial^2 W}{\partial \eta^2} \right) \frac{\partial W}{\partial \xi} + \beta \left(\gamma_{46} \frac{\partial^2 W}{\partial \xi \partial \eta} + 2\gamma_{48}\beta \frac{\partial^2 W}{\partial \xi \partial \eta} + \gamma_{49}\beta^2 \frac{\partial^2 W}{\partial \eta^2} \right) \frac{\partial W}{\partial \eta}.$$

References

- [Abrate 1997] S. Abrate, "Localized impact on sandwich structures with laminated facings", *Appl. Mech. Rev.* **50** (1997), 69–82.
- [Anderson 2003] T. A. Anderson, "A 3-D elasticity solution for a sandwich composite with functionally graded core subjected to a transverse loading by a rigid sphere", *Compos. Struct.* **60**:3 (2003), 265–274.
- [Apetre et al. 2002] N. A. Apetre, B. V. Sankar, and S. Venkataraman, "Indentation of a sandwich beam with functionally graded core", in *Proceedings of the 43rd AIAA/ASME/ASCE/AHS/ASC Structures, Structural Dynamics and Materials Conference* (Denver, CO, 2002), AIAA, Reston, VA, 22–25 April 2002. AIAA-2002-1683.
- [Apetre et al. 2006] N. A. Apetre, B. V. Sankar, and D. R. Ambur, "Low-velocity impact response of sandwich beams with functionally graded core", *Int. J. Solids Struct.* **43**:9 (2006), 2479–2496.
- [Carrera and Ciuffreda 2005] E. Carrera and A. Ciuffreda, "Bending of composites and sandwich plates subjected to localized lateral loadings: A comparison of various theories", *Compos. Struct.* **68**:2 (2005), 185–202.
- [Corbett and Reid 1993] G. G. Corbett and S. R. Reid, "Local loading of simply-supported steel-grout sandwich plates", *Int. J. Impact Eng.* **13**:3 (1993), 443–461.
- [Das et al. 2006] M. Das, A. Barut, E. Madenci, and D. R. Ambur, "A triangular plate element for thermo-elastic analysis of sandwich panels with a functionally graded core", *Int. J. Numer. Methods Eng.* **68**:9 (2006), 940–966.
- [Frostig and Baruch 1996] Y. Frostig and M. Baruch, "Localized load effects in high-order bending of sandwich panels with flexible core", *J. Eng. Mech. (ASCE)* **122**:11 (1996), 1069–1076.
- [Hohe and Librescu 2004] J. Hohe and L. Librescu, "Advances in the structural modeling of elastic sandwich panels", *Mech. Adv. Mater. Struct.* **11**:4–5 (2004), 395–424.
- [Ichikawa 2001] K. Ichikawa (editor), *Functionally graded materials in the 21st century: A workshop on trends and forecasts* (Tsukuba, 2000), Kluwer, Dordrecht, 2001.
- [Kirugulige et al. 2005] M. S. Kirugulige, R. Kitey, and H. V. Tippur, "Dynamic fracture behavior of model sandwich structures with functionally graded core: A feasibility study", *Compos. Sci. Technol.* **65**:7–8 (2005), 1052–1068.

- [Koissin et al. 2004] V. Koissin, V. Skvortsov, S. Krahmalev, and A. Shilpsha, “The elastic response of sandwich structures to local loading”, *Compos. Struct.* **63**:3–4 (2004), 375–385.
- [Liew et al. 2004] K. M. Liew, J. Yang, and S. Kitipornchai, “Thermal post-buckling of laminated plates comprising functionally graded materials with temperature-dependent properties”, *J. Appl. Mech. (ASME)* **71**:6 (2004), 839–850.
- [Pollien et al. 2005] A. Pollien, Y. Conde, L. Pambaguian, and A. Mortensen, “Graded open cell aluminum foam core sandwich beams”, *Mater. Sci. Eng. A* **404**:1–2 (2005), 9–18.
- [Polyakov 2001] V. Polyakov, “Local effects at bending of nonsymmetric sandwich of composite and soft filler”, *Compos. Struct.* **54**:2–3 (2001), 325–330.
- [Reddy 1997] J. N. Reddy, *Mechanics of laminated composite plates: Theory and analysis*, CRC Press, Boca Raton, FL, 1997.
- [Reddy 2000] J. N. Reddy, “Analysis of functionally graded plates”, *Int. J. Numer. Methods Eng.* **47**:1–3 (2000), 663–684.
- [Selvadurai 1979] A. P. S. Selvadurai, *Elastic analysis of soil-foundation interaction*, Developments in Geotechnical Engineering **17**, Elsevier, Amsterdam, 1979.
- [da Silva and Santos 1998] L. A. P. S. da Silva and J. M. C. Santos, “Localised formulations for thick ‘sandwich’ laminated and composite structures”, *Comput. Mech.* **22**:3 (1998), 211–224.
- [Thomsen 1993] O. T. Thomsen, “Analysis of local bending effects in sandwich plates with orthotropic face layers subjected to localised loads”, *Compos. Struct.* **25**:1–4 (1993), 511–520.
- [Thomsen 1995] O. T. Thomsen, “Theoretical and experimental investigation of local bending effects in sandwich plates”, *Compos. Struct.* **30**:1 (1995), 85–101.
- [Türk and Fatt 1999] M. H. Türk and M. S. H. Fatt, “Localized damage response of composite sandwich plates”, *Compos. B Eng.* **30**:2 (1999), 157–165.
- [Venkataraman and Sankar 2003] S. Venkataraman and B. V. Sankar, “Elasticity solution for stresses in a sandwich beam with functionally graded core”, *AIAA J.* **41**:12 (2003), 2501–2505.
- [Venkataraman et al. 2004] S. Venkataraman, R. T. Haftka, B. V. Sankar, H. Zhu, and M. L. Blosser, “Optimal functionally graded metallic foam thermal insulation”, *AIAA J.* **42**:11 (2004), 2355–2363.
- [Weissman-Berman et al. 1996] D. Weissman-Berman, S. Lahiri, and R. Marrey, “Flexural response of sandwich plates with core as elastic foundation”, *Trans. Soc. Naval Arch. Marine Eng.* **104** (1996), 491–518.
- [Yang and Shen 2003a] J. Yang and H. S. Shen, “Non-linear analysis of functionally graded plates under transverse and in-plane loads”, *Int. J. Non-Linear Mech.* **38**:4 (2003), 467–482.
- [Yang and Shen 2003b] J. Yang and H. S. Shen, “Nonlinear bending analysis of shear deformable functionally graded plates subjected to thermo-mechanical loads and under various boundary conditions”, *Compos. B Eng.* **34**:2 (2003), 103–115.
- [Yang et al. 2001] J. Yang, H. S. Shen, and L. Zhang, “Nonlinear local response of foam-filled sandwich plates with laminated faces under combined transverse and in-plane loads”, *Compos. Struct.* **52**:2 (2001), 137–148.
- [Zhu and Sankar 2007] H. Zhu and B. V. Sankar, “Analysis of sandwich TPS panel with functionally graded foam core by Galerkin method”, *Compos. Struct.* **77**:3 (2007), 280–287.

Received 19 May 2007. Revised 16 Nov 2007. Accepted 6 Dec 2007.

JIE YANG: j.yang@rmit.edu.au

School of Aerospace, Mechanical and Manufacturing Engineering, RMIT University, PO Box 71, Bundoora, VIC 3083, Australia

SRITAWAT KITIPORNCHAI: bcskit@cityu.edu.hk

Department of Building and Construction, City University of Hong Kong, Tat Chee Avenue, Kowloon, Hong Kong

KIM MEOW LIEW: kmliew@cityu.edu.hk

Department of Building and Construction, City University of Hong Kong, Tat Chee Avenue, Kowloon, Hong Kong

SUBMISSION GUIDELINES

ORIGINALITY

Authors may submit manuscripts in PDF format on-line. Submission of a manuscript acknowledges that the manuscript is *original and has neither previously, nor simultaneously, in whole or in part, been submitted elsewhere*. Information regarding the preparation of manuscripts is provided below. Correspondence by email is requested for convenience and speed. For further information, write to:

[Marie-Louise Steele](#)

Division of Mechanics and Computation
Durand Building, Room 262
Stanford University
Stanford CA 94305

LANGUAGE

Manuscripts must be in English. A brief abstract of about 150 words or less must be included. The abstract should be self-contained and not make any reference to the bibliography. Also required are keywords and subject classification for the article, and, for each author, postal address, affiliation (if appropriate), and email address if available. A home-page URL is optional.

FORMAT

Authors are encouraged to use L^AT_EX and the standard article class, but submissions in other varieties of T_EX, and, exceptionally in other formats, are acceptable. Electronic submissions are strongly encouraged in PDF format only; after the refereeing process we will ask you to submit all source material.

REFERENCES

Bibliographical references should be listed alphabetically at the end of the paper and include the title of the article. All references in the bibliography should be cited in the text. The use of B^IB_T_EX is preferred but not required. Tags will be converted to the house format (see a current issue for examples), however, in the manuscript, the citation should be by first author's last name and year of publication, e.g. "as shown by Kramer, et al. (1994)". Links will be provided to all literature with known web locations and authors are encouraged to provide their own links on top of the ones provided by the editorial process.

FIGURES

Figures prepared electronically should be submitted in Encapsulated PostScript (EPS) or in a form that can be converted to EPS, such as GnuPlot, Maple, or Mathematica. Many drawing tools such as Adobe Illustrator and Aldus FreeHand can produce EPS output. Figures containing bitmaps should be generated at the highest possible resolution. If there is doubt whether a particular figure is in an acceptable format, the authors should check with production by sending an email to:

production@mathscipub.org

Each figure should be captioned and numbered so that it can float. Small figures occupying no more than three lines of vertical space can be kept in the text ("the curve looks like this:"). It is acceptable to submit a manuscript with all figures at the end, if their placement is specified in the text by means of comments such as "Place Figure 1 here". The same considerations apply to tables.

WHITE SPACE

Forced line breaks or page breaks should not be inserted in the document. There is no point in your trying to optimize line and page breaks in the original manuscript. The manuscript will be reformatted to use the journal's preferred fonts and layout.

PROOFS

Page proofs will be made available to authors (or to the designated corresponding author) at a web site in PDF format. Failure to acknowledge the receipt of proofs or to return corrections within the requested deadline may cause publication to be postponed.

Journal of Mechanics of Materials and Structures

Volume 3, N^o 10 December 2008

- Preface** **R. K. NIMAL D. RAJAPAKSE, ANIL C. WIJEYEWICKREMA,
WORSAK KANOK-NUKULCHAI AND TEERAPONG SENJUNTICHAI** 1809
- Finite element simulation of strain rate effects on localized unstable pseudoelastic response of
shape memory alloys**
 B. AZADI BORUJENI, DAAN M. MAIJER AND R. K. NIMAL D. RAJAPAKSE 1811
- Elastodynamic reciprocity relations for wave scattering by flaws in fiber-reinforced composite
plates** **WARNA KARUNASENA** 1831
- Simulations of micro and nanoindentations**
 ZISHUN LIU, SOMSAK SWADDIWUDHIPONG AND QINGXIANG PEI 1847
- Numerical implementation of a constitutive model for soil creep**
 M. A. K. M. MADURAPPERUMA AND U. G. A. PUSWEWALA 1857
- On a Winkler ligament contact between a rigid disc and an elastic halfspace**
 A. P. S. SELVADURAI, T. SCARPAS AND N. KRINGOS 1875
- Dynamic response of multiple flexible strips on a multilayered poroelastic half-plane**
 TEERAPONG SENJUNTICHAI AND WICHAIRAT KAEWJUEA 1885
- Time-domain thin layer method for computing transient response due to sudden/moving
loads** **HIROKAZU TAKEMIYA** 1903
- Aging degradation of mechanical structures**
 SOMASUNDARAM VALLIAPPAN AND CALVIN K. CHEE 1923
- Numerical simulation of tsunami propagation using the characteristic-based split method**
 GUNAWAN BUDI WIJAYA, TAM THANH BUI AND WORSAK KANOK-NUKULCHAI 1939
- Wave propagation in a prestressed compressible elastic layer with constrained boundaries**
 ANIL C. WIJEYEWICKREMA, YOSUKE USHIDA AND PRIZA KAYESTHA 1963
- Nonlinear local bending of FGM sandwich plates**
 JIE YANG, SRITAWAT KITIPORNCHAI AND KIM MEOW LIEW 1977